Characteristics of Clinical Electron Beams: Current and Optimal

Martin Andrew Ebert, BSc (Hons), Dip. Ed.

Supervisors:

Dr P. W. Hoban

Dr J. R. Patterson

UNIVERSITY OF ADELAIDE

DEPARTMENT OF PHYSICS AND MATHEMATICAL PHYSICS

A thesis submitted in fulfilment

of the requirements for the

degree of Doctor of Philosophy.

December, 1996

ABSTRACT

This thesis presents the results of two investigations into the characteristics of electron beams for application in radiation therapy. The first investigation involves the modelling of the interactions between the tertiary collimation system (applicator) of a Siemens Mevatron KD2 linear accelerator, and the electron beam produced by that accelerator. EGS4 Monte Carlo code is used to simulate the transport of 6 MeV, 12 MeV and 18 MeV electron beams from the accelerator waveguide, through the electron scattering foils and air to the applicator assembly, in order to determine primary beam electron and photon spectra. Narrow beams are then simulated incident on sections of applicator trimming plate edges (edge elements) in order to investigate the characteristics of scattering off these edges. It is found that electron scattering is dependent on the energy of the primary beam and the material of which the edges are made, as well as the angle of incidence of the primary beam to the edge. Primary beam photons are scattered minimally. A model for scatter from irregular apertures is developed based on a superposition of scatter *kernels* from edge elements. This model is evaluated using several regular and a single irregular applicator/cutout combinations, and found to give central-axis depth dose and profile data consistent with measured results. The model is also used to obtain detailed information of the characteristics of particles scattered from the electron applicator.

The second investigation involves evaluating the characteristics of electrons in an electron beam which would produce dose distributions in homogeneous media which most closely approximate specified dose distributions. For this purpose, optimal electron beam properties are determined by inversion of desired dose distributions using a simulated annealing optimisation method. This technique is used for several regular desired dose distributions, and various intuitive results are obtained regarding the effects electron energy and angular modulation have on resulting dose distributions. The technique is also used for several complex desired dose distribution, indicating the relative influence energy and angular modulation can have on dose conformation with electrons. For a suitably selected electron energy, modulation of electron incidence angle can be used to control the variation in dose with depth in order to increase dose conformity, and to reduce dose deposition within desired low-dose regions adjacent to and underlying desired high-dose regions.

Published and submitted papers related to work presented in this thesis

Ebert, M.A. and Hoban, P.W. (1995) A Monte Carlo investigation of electron beam applicator scatter, *Med. Phys.*, **22**, 1431-1435

Ebert, M.A. and Hoban, P.W. (1995) A model for electron beam applicator scatter, *Med. Phys.*, **22**, 1419-1429

Ebert, M.A. and Hoban, P.W. (1996) Some characteristics of tumour control probability for heterogeneous tumours, *Phys. Med. Biol.*, **41**, 2125-2133

Ebert, M.A. and Hoban, P.W. (1996) The energy and angular characteristics of the applicator scattered component of an electron beam, *Aust. Phys. Eng. Sci. Med.*, **19**, 151-159

Ebert, M.A., Hoban, P.W. and Keall, P.J. (1996) Modelling clinical accelerator beams: A review, *Aust. Phys. Eng. Sci. Med.*, **19**, 131-150

Ebert, M.A. (1996) An overview of optimisation techniques in conformal radiotherapy, Submitted to *Aust. Phys. Eng. Sci. Med.*, November, 1996

Ebert, M.A. and Hoban, P.W. (1996) Possibilities for tailoring dose distributions through the manipulation of electron beam characteristics, Submitted to *Phys. Med. Biol.*, December, 1996

Presentations related to work presented in this thesis

Ebert, M.A. and Hoban, P.W. (1994) Interactions of high energy electron beams with electron beam applicators, EPSM '94, Perth, WA

Ebert, M.A. and Hoban, P.W. (1995) A model for electron beam applicator scatter, 1995 Meeting of the AAPM, Boston, MA

Ebert, M.A. and Hoban, P.W. (1995) Consequences for tumour control of dose heterogeneity, 1995 IEAust (SA Branch of Biomedical division) student paper night

Ebert, M.A. and Hoban, P.W. (1996) Mathematical characteristics of TCP including optimal dose distribution for heterogeneous tumours, 1996 Meeting of the AAPM, Philadelphia, PA

Ebert, M.A. and Hoban, P.W. (1996) The potential for conformity through the manipulation of electron beam characteristics, 1996 Meeting of the AAPM, Philadelphia, PA

Ebert, M.A. and Hoban, P.W. (1996) Characteristics of electron beam applicator-scattered particles, 1996 Meeting of the COMP, Vancouver, BC

Ebert, M.A. and Hoban, P.W. (1996) Optimisation of electron beam characteristics by simulated annealing, EPSM '96, Canberra, ACT

Ebert, M.A. and Hoban, P.W. (1996) Consequences for tumour control of dose heterogeneity, EPSM '96, Canberra, ACT

DECLARATION

This work contains no material which has been accepted for the award of any other degree or diploma in any university or other tertiary institution and, to the best of my knowledge and belief, contains no material previously published or written by another person, except where due reference has been made in the text.

I give consent for this copy of my thesis, when deposited in the University Library, being available for loan and photocopying.

Signed: ..

Date: ..... 20/12/96 .....

ACKNOWLEDGMENTS

I am not entirely responsible for the work presented in this thesis - it would never have been written were it not for the invaluable assistance of the following organisations and individuals, and many others; Siemens Corp. for providing information on the construction of their accelerators; the Royal Adelaide Hospital (RAH), particularly the Cancer Services section and its helpful staff; the University of Adelaide (U of A) for providing financial assistance as well as an efficient research environment; the Australasian College of Physical Scientists and Engineers in Medicine for financial and professional assistance; the multitude of international medical physics researchers who helped educate me, who allowed me to visit their institutions and who provided much helpful discussion; all members of the RAH Department of Medical Physics who supplied a friendly and helpful work environment, particularly the lunch crew; Mr Kurt Byas (RAH), who I had the privilege of sharing a room with for over two years - thanks Kurt for Déja Vu and Dixie Chicken, for strengthening and expanding my faith, for your persistent sense of humour, and your open nature; Mr Ralph Nicholls (RAH), for providing consistent assistance and friendship; the Atomix; Dr John Patterson (U of A), for providing much assistance and for taking on a poor lost orphan; Dr Alun Beddoe of the Queen Elizabeth Medical Center, Birmingham, for providing the initial incentive for this research, and for being a true mentor; all my past teachers and lecturers who inspired and encouraged me, particularly Dr Fred Menk of the University of Newcastle who provided invaluable guidance and friendship during my undergraduate years, and Dr Tomas Kron of the University of Newcastle who provided me with my initial experience with the truly worthy field of medical physics; my church family who provided me with the acceptance and love that everyone needs; Dr Paul Keall of the Queensland University of Technology, with whom I have shared this stage of my life - Paul, thanks for your enthusiasm, ingenuity, the willingness to share your knowledge, ardour for life, and friendship; my primary supervisor Dr Peter Hoban - thanks Pete for encouragement all the way, for making research even more fun, and for becoming a good friend - I look forward to working together for many more years; special thanks to the family we left 'back east', who support us in all we do, especially my parents who provided me with the upbringing and freedom necessary for pursuing the career I have chosen.

I am unable to fully express my gratitude to that person for whom I owe the most appreciation. The fact that the years spent preparing this thesis have been amongst my most memorable is mainly due to the support and unconditional love of my wife, and because of the events we have shared during this time. I can only repay Jane with my endless devotion to her and our children (in heaven and on earth).

For my wonderful family;
my wife Jane, our beautiful daughter Adehlia,
and the child we never got to meet.

"Who is wise and understanding among you? Let him show it by his good life, by deeds done in the humility that comes from wisdom."

James 3:16 (NIV)

CONTENTS

FIGURES

CHAPTER 2

CHAPTER 3

CHAPTER 4

CHAPTER 5

TABLES

CHAPTER 2

CHAPTER 4

CHAPTER 5

SYMBOLS USED (IN MAIN TEXT)

$\boldsymbol{A}$	Matrix of dose points defining a set of dose constraints
A_l	lth scattering moment
a	Operator such that $\boldsymbol{aI}$ corresponds to the inverse of the dose distribution-Hessian matrix
$\boldsymbol{b}$	Vector of real values
c	Speed of light in a vacuum; scalar coefficient
$\boldsymbol{c}$	Matrix of coefficients
$\boldsymbol{C}$	Positivity operator
D	Absorbed dose
$\overline{D}$	Average absorbed dose to a specified region
$\overline{D}_e$	Mean absorbed dose to a phantom below a collimator edge due to scatter from the edge
$\boldsymbol{d}$	Desired or objective dose distribution matrix
d_{max}	Depth of maximum dose build-up
E	Electron energy
E_i	Energy of particle in phase space
E_γ	Photon energy
E_{en}	Energy imparted to matter by radiation
E_p	Most probable electron energy
$E_{p,0}$	Most probable incident electron energy
E_{tr}	Energy transferred from uncharged to charged particles
$\overline{\overline{E}}$	Mean energy of collimator-scattered electrons
$\overline{E}_0$	Mean energy of incident electrons
f	Value of optimisation objective function
f_θ	Back-projected irradiation profile at angle θ
g	Fraction of energy of secondary particles lost to bremsstrahlung
$\boldsymbol{I}$	Identity matrix
I_0	Relative incident beam intensity
i	x dimension (cross-plane) voxel index
j	Iteration number or y direction voxel index

K	Kerma (Kinetic energy released per unit mass)
K_c	Collision kerma
k	z dimension (depth) voxel index
k_B	Boltzmann constant
L	Distance from collimator edge/applicator face to calculation plane
$\boldsymbol{M}$	Dose-kernel matrix
m	Radiation beam modality descriptor
m_e	Electron rest mass
N	Total number of elements in beam phase space; number of particles
N_e	Number of energies defining phase space
n	nth dimension of N-space
P	Optimisation potential or cost function value
P_j	Position of particle in phase space
P_+	Probability of patient survival without severe complication
q	Low pass Fourier filter
R	Radiant energy
R_α^e	Edge scatter geometry operator for element e of aperture α
R_{50}	Depth of 50% isodose for a dose distribution
R_{80}	Depth of 80% isodose for a dose distribution
R_p	Electron beam practical range
R_T	Rate of variation of simulated annealing temperature
R_w	Rate of variation of simulated annealing grain-size amplitude
$\boldsymbol{r}$	Generic position vector
r	Singular value decomposition solution residual
r_{eff}	Effective radius of trimmer edge
s	Fourier-conjugate to position vector
S_{col}	Linear collisional stopping power
$(S/\varrho)_{col}$	Mass collisional stopping power
S_{rad}	Linear radiative stopping power
$(S/\varrho)_{rad}$	Mass radiative stopping power
$(S/\varrho)_{tot}$	Total mass stopping power
t	Thickness of collimator/trimmer edge

T	Linear scattering power; also used for simulated annealing temperature measure
T	Transpose operator
T/ϱ	Mass scattering power
T_0	Initial simulated annealing temperature
w	Beam element weighting vector
w	Component of weighting vector w
w_{est}	Estimated value of weighting vector w
W	Amplitude of simulated annealing grain-size distribution
x	Vector of variables
X_0	Radiation length
Z	Atomic number
z	Depth in dose deposition phantom
$\bar{\theta}_x^2$	Mean square angular deflection of electrons in the x direction
$\bar{\theta}_0^2$	Mean square angle of incident electrons
$\sigma_{\theta_x}^2$	Standard deviation of electron Gaussian spread in the x direction
σ_x	Lateral standard deviation of electrons in the x direction
Ω_α^E	Edge scatter kernel element at energy E of aperture α
Φ_{CA}^p	Central-axis primary beam fluence
Φ_s^p	Primary beam off-axis fluence variation
Φ^p	Primary beam fluence distribution
Φ_{Scatt}	Applicator scatter fluence
$\mathcal{F}$	Fourier transform
∇	Gradient operator
Φ	Particle fluence
Ψ	Energy fluence
ϱ	Mass density
τ	Photoelectric interaction cross section
$\varkappa$	Pair production cross section
φ	Primary beam incidence angle to trimmer edge

ψ	Primary beam obliquity angle to trimmer edge
ϕ	Generic energy (dose) deposition kernel
Δ	Fourier transform of dose distribution
ΔP	Change in optimisation potential
Δw	Grain size or beam element perturbation
Γ	Fourier transform of space-invariant kernel
Ω	Radiation source position descriptor
Ω_k	Direction of particle in phase space
ζ	Random variate
ν_ω	Number of elements describing fluence profile
ν_Ω	Number of allowed source positions
ν_m	Number of allowed beam modalities
ν_E	Number of allowed beam energies
μ/ϱ	Total mass attenuation coefficient (linear coefficient μ)
μ_{en}/ϱ	Mass energy absorption coefficient (linear coefficient μ_{en})
μ_{other}/ϱ	Mass attenuation coefficient for non-specific interactions
μ_{tr}/ϱ	Mass energy transfer coefficient (linear coefficient μ_{tr})
σ_c	Compton scattering cross section
σ_{coh}	Coherent scattering cross section

ABBREVIATIONS USED

AAPM	**A**merican **A**ssociation of **P**hysicists in **M**edicine
ACPSEM	**A**ustralasian **C**ollege of **P**hysical **S**cientists & **E**ngineers in **M**edicine
AE	EGS4 γ-ray production energy threshold
AP	EGS4 secondary photon energy threshold
COMP	**C**anadian **O**rganisation of **M**edical **P**hysicists
CPU	**C**entral **P**rocessing **U**nit
ECUT	EGS4 low energy electron cutoff
EGS4	**E**lectron **G**amma **S**hower version **4** Monte Carlo code
EPSM	**E**ngineering and **P**hysical **S**ciences in **M**edicine
ESTEPE	EGS4 fractional energy loss maximum
LMPA	**L**ow **M**elting **P**oint **A**lloy
MMC	**M**acro **M**onte **C**arlo
NTCP	**N**ormal **T**issue **C**omplication **P**robability
PCUT	EGS4 low energy photon cutoff
PDF	**P**robability **D**istribution **F**unction
PLC	**P**ath **L**ength **C**orrection
RONSC	**R**andom **O**ptimisation with **N**on-linear **S**core functions and **C**onstraints
SMC	**S**uper **M**onte **C**arlo
SSD	Effective radiation **S**ource to current **S**urface **D**istance
TCP	**T**umour **C**ontrol **P**robability
UTCP	**U**ncomplicated **T**umour **C**ontrol **P**robability

1. GENERAL INTRODUCTION

1.1. Radiotherapy - Contemporary Philosophy

The aim of radiotherapy of any modality is the killing of neoplasmic cells via interactions with delivered radiation. In a holistic approach, radiotherapy is optimised when radiation can be delivered to the entire radiation-treatable population with the largest probability of complication free control of the tumour. This process may involve consideration of patient and community psychology, the aptitude of clinical staff, economic and engineering aspects of radiation delivery, general physiology, the radiobiology of the dose response of various tissues, and the manner in which our knowledge of radiation processes is used to ensure accuracy in dose delivery. It is the latter which is the primary concern of this investigation.

Of the two principle external beam modalities in contemporary use, photons and electrons, it is the characteristics of electron beams that have proven the most difficult to accurately model. Considerable effort has been made in establishing electron beam dose calculation models, despite the fact that electron therapy represents a minor treatment modality when compared to photon methods. To achieve accurate dose delivery with electron beams requires modelling all stages of the beam's path; from the beam's source, to the eventual absorption of energy within patient tissues or elsewhere. The accuracy required is governed by the differential response of tumour and normal tissue cells to a given regime of dose delivery and by the latitude in dose between a small and large probability of tumour control.

The path of particles in an electron beam can be separated into two principle stages, divided by the surface of the patient. Before reaching the patient, the beam must be created by the radiation device, filtered and collimated in order to possess some approximately

known set of characteristics and pass through other extraneous media (eg., air). Subsequent dose deposition in the patient can be calculated with models for electron beam dose deposition, which are limited by the knowledge of the patient geometry, beam characteristics, particle transport processes and computational capabilities.

To efficiently implement radiotherapy, a compromise must be made between treatment practicality and accuracy. However, contemporary trends in radiotherapy development, spurred by technological advancements (particularly in computation, electronics and engineering), have been towards increasingly complex treatment techniques, with more degrees of freedom in radiation manipulation, combined with increasingly accurate dose calculation and optimisation methods.

The areas investigated in this thesis concern three main themes raised above; electron beam radiotherapy, the characteristics of the incident radiation beam, and the optimal use of degrees of freedom in radiation manipulation.

1.2. Aims of Current Investigation

The efficiency of attempted complication free treatment is influenced by many stages of patient treatment. These stages include initial diagnosis, localisation of tumours and anatomical structures, treatment machine calibration and reliability, patient positioning and temporal organ movement, and dose calculation accuracy. Accuracy of dose calculation can be improved when the algorithms used incorporate detailed knowledge of the treatment situation such as body composition and structure information, and the characteristics of the radiation being used. The latter is dependent on the treatment device being employed, and how the device's properties determine the type, energy, spatial and directional characteristics of the radiation.

In electron beam treatments, spatial definition (collimation) of a suitable beam is often achieved using apertures composed of metals and alloys. The efficiency with which this occurs depends on the specific materials and their geometry, and it has been found

experimentally that currently used collimators (applicators) can have measurable effects on the properties of the electron beams, manifest in the dose distributions they produce.

For electron beam dose calculations to be of greatest efficiency, the effects of applicators must be incorporated into beam descriptions. Thus, a principle aim of the research presented here was to investigate the manner in which applicators perturb electron beams, and then to develop a model for calculating the properties of these perturbations for arbitrary configurations of applicator apertures. Such a model had to be accurate enough to describe the principle effects of applicators on dose distributions, and efficient enough to perform such calculations within the time requirements of contemporary clinical situations.

An alternative to viewing electron beam radiotherapy in terms of the beams that are currently available, their properties, and the restrictions they place on achievable dose distributions is to examine the properties of beams that would deliver dose distributions which approximate desired distributions as closely as possible. Although the means of producing such beams do not yet exist, treatment machines capable of limited beam manipulation with multiple degrees of freedom are being developed. The determination of the desired properties of optimal beams allows evaluation of feasible degrees of freedom *a priori* to the development of technologically complex treatment machines. For this purpose, an inverse process was required for performing an optimisation of beam properties with minimal constraints.

1.3. Thesis Outline

The two main investigations presented in this thesis are elaborated in Chapters 4 and 5. Chapters 2 and 3 are intended to supply general background knowledge which supports understanding of the radiotherapy physics used in discussion in Chapters 4 and 5.

Chapter 2 concentrates on relevant aspects of radiation transport, including scattering, energy loss and particle creation interactions and the dependence of these processes on the radiation energy and the characteristics of the irradiated medium. These aspects are then

incorporated into a brief discussion of radiation transport simulations, in particular, as applied to Monte Carlo methods of particle transport, used extensively in this thesis. The Monte Carlo code used, EGS4, is described together with the particular implementation employed in the simulations performed.

Chapter 3 discusses general aspects of electron beam therapy. The production and manipulation of electron beams at therapeutic energies is described, together with how the characteristics of the beams so produced affect dose distributions within phantoms and patients. The properties of these dose distributions which may be employed for clinical advantage are then described, including methods of achieving the optimal use of these properties.

Following an overview of techniques used in linear accelerator-generated beam modelling, Chapter 4 involves elaboration of the investigation made into electron beam applicator scatter, and the model developed to determine the characteristics of applicator scattered particles. This model is evaluated through comparison with measured dose distributions, and predictions for the characteristics of applicator scattered particles are discussed.

The investigation of the optimal characteristics for pure electron beams is presented in Chapter 5. An overview of the motivation for and techniques used in radiotherapy optimisation is presented, including a discussion of the simulated annealing technique used in the current investigation. The method used and results obtained in the study are then presented, and results discussed in terms of the effects various degrees of freedom in electron manipulation.

Chapter 6 highlights and summarises the main findings of the work presented in this thesis, and suggests areas where the investigation could be extended.

In conjunction with the work presented in this thesis, an investigation was undertaken into the mathematical characteristics of tumour control probability relationships. This work has been published in the journal *Physics in Medicine and Biology*, and is presented in Appendix H.

2. MODELLING PARTICLE TRANSPORT

2.1. Particle Transport

The processes leading to energy deposition in a medium due to irradiation with photons and electrons (or positrons) can be described in terms of interactions between primary radiation particles, the electrons and atomic nuclei of the irradiated medium, and secondary particles generated in such interactions. Due to the different physical nature of photons and electrons, they undergo different interaction processes though it is electrons which deposit energy through ionisations and excitations. The interaction processes that occur, and their relative probabilities of occurrence, depend on the energy of incident photons and electrons and the composition of the medium as shall be described.

2.1.1. Fundamental Quantities

Several quantities, universal to photon and electron transport, are frequently used in radiation physics discussion. Fluence, Φ, relates to the number of particles, dN, entering a sphere of cross sectional area da irrespective of direction;

$$\Phi = \frac{dN}{da}. \tag{2.1}$$

The planar fluence is the corresponding quantity for a plane of area da with a fixed orientation with particle numbers being positive when incident from one side of the plane and negative when incident from the other.

The energy fluence, Ψ, is defined as

$$\Psi = \frac{dR}{da}, \tag{2.2}$$

where dR is the radiant energy entering a sphere of cross sectional area da.

Absorbed dose (D) relates the energy deposited by radiation in a medium to its mass density. Thus, when a mean energy of dE_{en} is imparted by ionising radiation to material of mass dm the absorbed dose is

$$D = \frac{dE_{en}}{dm}. \tag{2.3}$$

The accepted unit of absorbed dose is the Gray (Gy), with 1 Gy being equal to 1 Joule per kilogram.

A quantity useful for describing the transfer of energy from uncharged particles to charged particles in an irradiated medium is Kerma, K, defined as the kinetic energy released per unit mass:

$$K = \frac{dE_{tr}}{dm}, \tag{2.4}$$

where E_{tr} is the energy transferred from uncharged to charged particles at the interaction site in a volume element of mass dm. The relationship between Kerma and absorbed dose shall be discussed in §2.1.4.

2.1.2. Electron Transport

Electron interactions with particles composing an irradiated medium can be classified as energy loss interactions or scattering interactions, with further classification then occurring according to the particular type of interaction that occurs. However, it is important to remember that energy deposition and scattering are not necessarily independent events; it is simply convenient for the description of electron transport. When calculating energy deposition and particle distributions due to such interactions, it is the resulting statistical distributions that we are ultimately concerned with in terms of the investigations presented in this study. As such, only a brief discussion of the most important generalised processes shall be presented. The following discussion also applies to the transport of positrons, which are generated in pair production processes as discussed in §2.1.3.

2.1.2.1. Collisional Losses

Electrons in motion within a medium with some kinetic energy (in addition to the electron rest mass energy equivalent of $m_e c^2 \approx 0.511$ MeV where m_e is the electron rest mass and c the speed of light in a vacuum), interact with bound electrons leading to the excitation of the bound electrons. If the energy transfer is sufficient to ionise the respective atom, the bound electron is ejected and deposits energy locally via subsequent interactions. Occasionally the ejected electron has sufficient energy to cause subsequent ionisations in which case it is called a secondary electron or δ-ray.

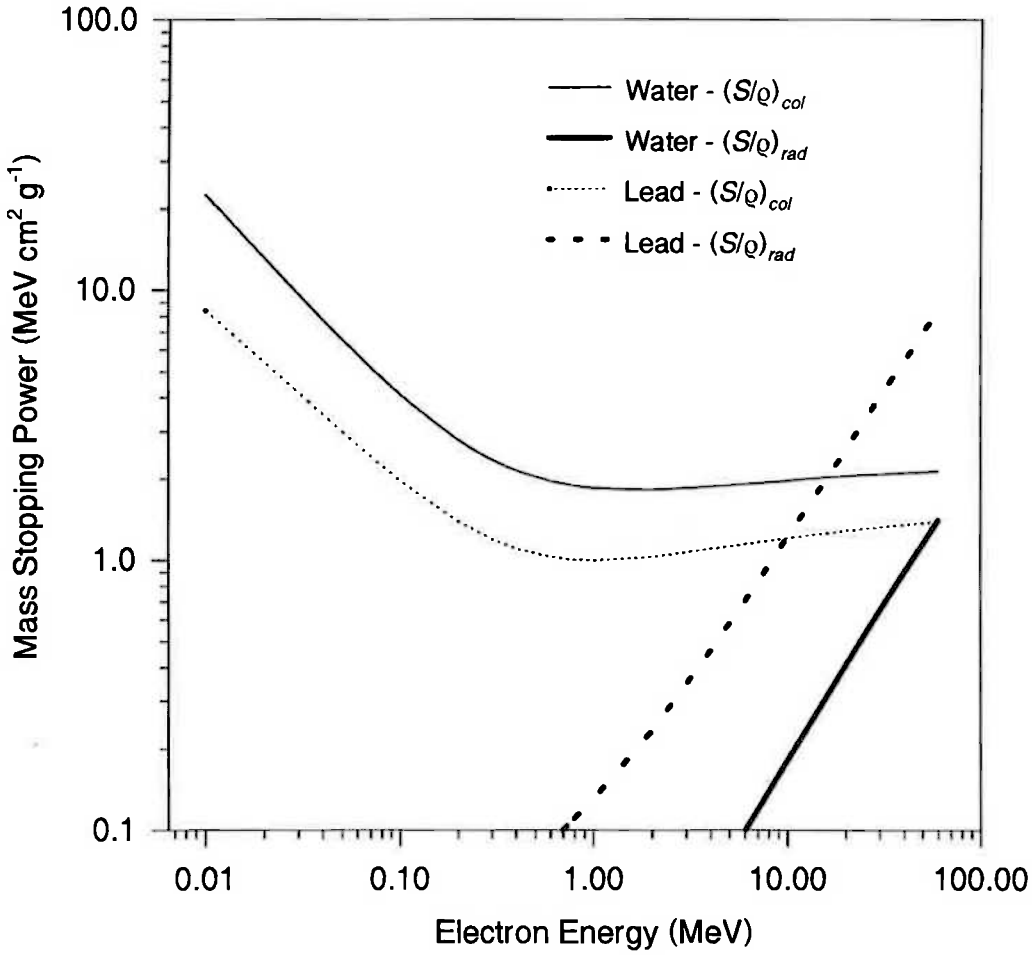

Figure 2-1: Variation in mass collisional and radiative stopping powers with electron energy for water and lead. (Data from Berger and Seltzer, 1982).

The energy lost by an electron per unit effective path length via interactions leading to ionisation and excitation is called the collision stopping power, S_{col}. If ϱ is the mass density of the irradiated medium, $(S/\varrho)_{col}$ is termed the mass collision stopping power. $(S/\varrho)_{col}$ can be calculated using theoretical results obtained by Bethe (1930, 1932; Nelms 1956, 1958; Berger and Seltzer 1964; Pages *et al.,* 1972; ICRU 1984). Collisional energy losses vary slowly with the atomic number of irradiated material due to the influence of electron-electron interactions (resulting in an electron density dependence), and increase approximately logarithmically with energy above approximately 1 MeV. Figure 2-1 illustrates the variation in $(S/\varrho)_{col}$ with electron energy. Collisional energy losses form the dominant energy loss processes at low energies ($<< m_e c^2$) and in low atomic number materials.

2.1.2.2. Radiative Losses

As shown in Figure 2-2, an electron passing close to an atomic nucleus will be decelerated due to the resulting Coulomb force between the two charged particles. The energy lost via deceleration of the electron is released as electromagnetic radiation, with the resulting photon called a bremsstrahlung photon. The probability of nuclear-bremsstrahlung interaction varies with approximately the square of atomic number of irradiated material (ICRU 1984; Khan 1994). Electron-electron interactions can also generate bremsstrahlung with probability of occurrence being proportional to atomic number of irradiated material (Klevenhagen, 1985).

Radiation can also be emitted as characteristic emissions from excited or ionised atoms. The energy transferred by an electron to radiation per unit effective path length in a material is called the radiative stopping power , S_{rad}, with the corresponding mass radiative stopping power,$(S/\varrho)_{rad}$. The variation of mass radiative stopping power with electron energy is also displayed in Figure 2-1. Radiative energy losses are dominant at high electron energies ($>> m_e c^2$).

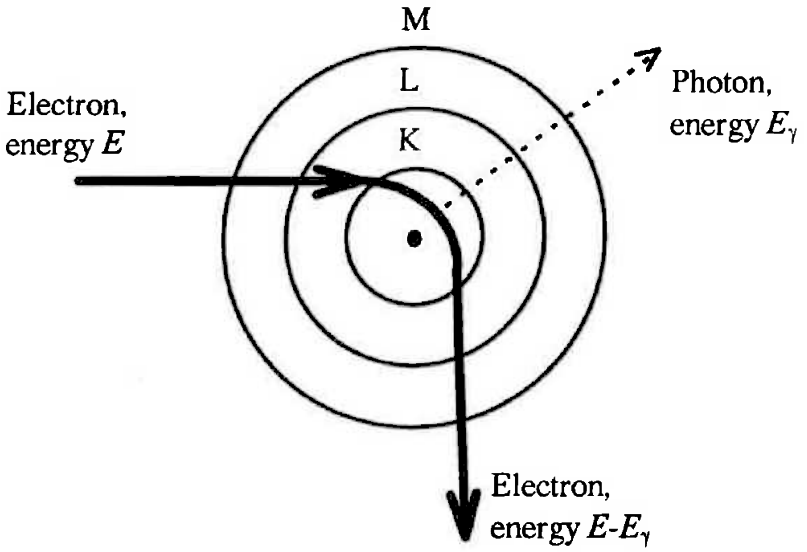

Figure 2-2: Illustration of bremsstrahlung generation by deceleration of an electron in the electrostatic field of an atomic nucleus.

2.1.2.3. Total Losses

The total mass stopping power, $(S/\varrho)_{tot}$, is the energy lost by an electron via collisional and radiative interactions and is given by the sum of collisional and radiative stopping powers;

$$(S/\varrho)_{tot} = (S/\varrho)_{col} + (S/\varrho)_{rad}. \tag{2.5}$$

The value of $(S/\varrho)_{tot}$ varies from 1.87 MeVcm^{2}g^{-1} to 2.47 MeVcm^{2}g^{-1} for electron energies 1 MeV to 20 MeV in water (Johns and Cunningham, 1983).

The ratio of radiative to collisional mass stopping powers varies approximately linearly with electron energy (E) and atomic number (Z) of irradiated material, yielding a simple approximate expression (Klevenhagen, 1985);

$$\frac{(S/\varrho)_{rad}}{(S/\varrho)_{col}} = E\left(\frac{Z+1.2}{800}\right). \tag{2.6}$$

For more detailed discussion of the theoretical basis of stopping powers and for tables of values see Berger and Seltzer (1982) or ICRU (1984).

If the emphasis of electron interactions under examination is local energy deposition (local to the interaction site) as opposed to energy carried away by secondary particles, then the concept of restricted stopping power is used (Klevenhagen, 1985). Thus, restricted stopping power is calculated by ignoring all energy losses leading to δ-rays with energies in excess of a specific value. This is because energy deposited along a path by an electron should not include energy transferred to other electrons that travel away from the original electron's path.

2.1.2.4. Scattering

Electrons undergo extremely large numbers of scattering events when traversing dense media (tens of thousands before stopping, at therapeutic energies), and so it is convenient to discuss electron scattering in terms of single scattering processes and multiple scattering, where the single scattering is to be associated with large-angle scattering events, and multiple scattering with small-angle deflections. Both electron-nuclear (Rutherford) and electron-electron (Møller) scattering is possible, though electron-nuclear scattering dominates (Klevenhagen, 1985). Due to the small mass of the electron relative to an atomic nucleus, such scattering tends to be elastic. Theoretical descriptions of electron scattering cross sections (eg. Rossi, 1952; Brahme, 1971) include relativistic effects as well as the screening effects of bound electrons. Other interaction possibilities include annihilation (production of two photons of energy 0.511 MeV by mutual annihilation of a positron and electron), Bhabha scattering (interaction of an electron and positron without annihilation), and Cerenkov emission (emission of radiation from fast electrons).

The mean square angle of deflection of electrons from their path ($\bar{\theta}^2$) is found to increase approximately linearly with the thickness of material traversed (Rossi, 1952; ICRU, 1984). The increase in $\bar{\theta}^2$ ($d\bar{\theta}^2$) per unit density and thickness traversed (dl) is called the linear scattering power (T) which also varies with electron energy and material composition. In analogy with mass stopping powers, we define the mass scattering power

$$T/\varrho = \frac{1}{\varrho}\frac{d\bar{\theta}^2}{dl}. \qquad (2.7)$$

Statistical models for multiple scattering have been proposed for predicting scattering angles (eg., Goudsmit and Saunderson, 1940; Moliére, 1947; Scott, 1963; Marion and Zimmerman, 1967; Berger and Wang, 1988; Jette, 1996). To be truly accurate, such models must include the effects of energy loss straggling as well as variation in lateral displacement with distance (Klevenhagen, 1985; Berger and Wang, 1988). The application of multiple scattering models to explicit electron transport shall be discussed more in §2.2.

One approach to multiple scattering which is worth greater discussion because of the simple predictions it makes is the Gaussian approximation (Fermi, 1940; Eyges, 1948; Brahme, 1975; Jette, 1988; Zheng-Ming and Brahme, 1993). Fermi (1940) formulated a scattering theory for small-angle scattering (thus excluding large-angle events) which was refined by Eyges (1948) to include the effects of energy losses. Using the scattering moments (A_0, A_1 and A_2) comprising Eyges' solution to Fermi's transport equation (Eyges, 1948; Hogstrom *et al.*, 1981), a series of recursive relationships can be set up to describe the variation in the properties of an electron beam as it propagates through a series of media with varying scattering power;

$$A_0(z_k) = A_0(z_{k-1}) + \frac{\Delta z_k}{2} T_k \tag{2.8}$$

$$A_1(z_k) = A_1(z_{k-1}) + \Delta z_k A_0(z_{k-1}) + \frac{(\Delta z_k)^2}{4} T_k \tag{2.9}$$

$$A_2(z_k) = A_2(z_{k-1}) + 2\Delta z_k A_1(z_{k-1}) + (\Delta z_k)^2 A_0(z_{k-1}) + \frac{(\Delta z_k)^3}{6} T_k \tag{2.10}$$

(Keall, 1996). Here, T_k and Δz_k are the scattering power and thickness of layer k respectively. From these moments, several parameters can be calculated such as the x (arbitrarily) component of the lateral standard deviation of electrons at depth z,

$$\sigma_x = \sqrt{A_2}, \tag{2.11}$$

the mean x component of electrons relative to the initial direction at lateral position x,

$$\bar{\theta}_x = \frac{A_1}{A_2} x, \tag{2.12}$$

and the x component of the angular standard deviation about $\bar{\theta}_x$ at depth z and lateral position x,

$$\sigma_{\theta_x} = \sqrt{A_0 - A_1^2 / A_2} \,. \tag{2.13}$$

Equation 2.13 has been used to determine the variation in σ_x with depth in water for several incident beam energies, and this result is displayed in Figure 2-3. This formalism can be used to describe the distribution of electrons resulting from irradiation of a medium by a narrow 'pencil beam' (ICRU, 1984; Zheng-Ming and Brahme, 1993), pertinent to Chapter 5 of this thesis.

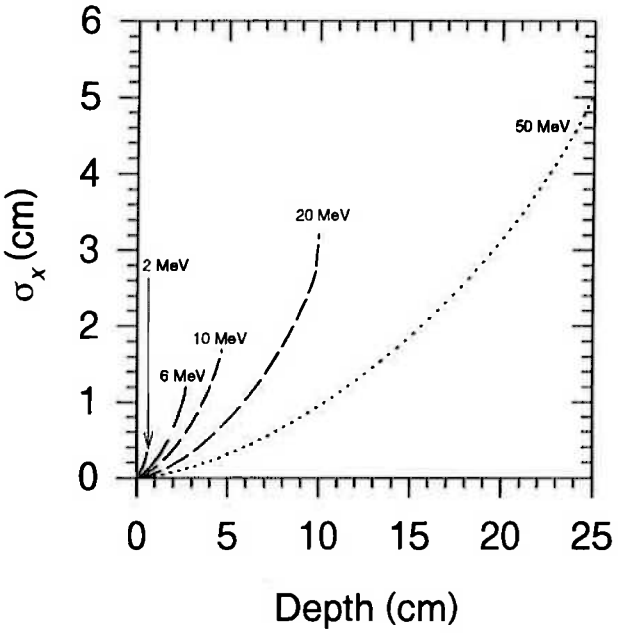

Figure 2-3: Approximate variation in σ_x with depth in water for several incident electron beam energies, as calculated using the recursive relations of equations 2.8 to 2.10, and equation 2.11. The variation in mean energy with depth has been approximated by $E(z) = E_0\left(1 - z/R_p\right)$, where E_0 is the incident beam energy, and R_p the practical range (see §3.2.1.1), approximated by $R_p = (E_0 - 0.48)/1.95$ (ICRU, 1984). The scattering power has been approximated by $T(z) = T_0\left(\frac{E_0}{E(z)}\right)^2$, where T_0 is the scattering power at the surface taken from tables in ICRU (1984).

2.1.3. Photon Transport

Although the research presented in this thesis concentrates on characteristics of electron beams, photon transport must also be considered because of the radiative processes discussed above in §2.1.2.2. Thus, an electron irradiation will generally give rise to a photon component which must also be considered for faithful modelling of physical situations. A major difference for photon transport relative to electron transport is the smaller size of interaction cross sections, leading to significantly longer path lengths for photons than electrons of similar energies. Also, photons deposit energy by first transferring energy to electrons and positrons. Again, the discussion of photon transport shall be kept extremely brief, and mention only made of principle relevant processes.

2.1.3.1. Photon Interaction Processes

Photons incident on a medium, or those generated within a medium, undergo interactions with atomic nuclei and electrons within that medium with relative probabilities governed by photon energies, the composition of the medium, and the resulting interaction cross sections. A photon which has not interacted in a medium and which was generated outside of the medium is called a primary photon. Primary photons that have interacted at least once are subsequently known as scattered photons.

At therapeutic energies, the principle interaction processes are the photoelectric effect, Compton scattering and pair production. Coherent (Rayleigh) scattering constitutes a minor process at low energies in water (< 100 keV; Johns and Yaffe, 1983). In this type of scattering, the incident photon collides with a bound electron and, unable to cause ionisation, forces the atom to oscillate and re-emit the energy as a photon of the same wavelength as the incident one, and so without energy loss. The cross section (probability of interaction per unit particle fluence) for coherent scattering of a photon is labelled σ_{coh}.

In the photoelectric process, the incident photon imparts all of its energy to an inner shell electron which is ejected from the atom. The remaining vacancy can be filled by an outer

shell electron with the emission of characteristic radiation or another (Auger) electron. The cross section for photoelectric interaction is labelled τ. For water (tissue), the photoelectric effect is negligible above approximately 100 keV (Johns and Cunningham, 1983).

Compton scattering involves the collision of a photon with a 'free' electron in the irradiated medium. The photon transfers some of its energy to the electron, and both particles recoil as secondary particles. Compton scattering is the principal photon interaction process for photons in water with energies between approximately 200 keV and 2 MeV (Johns and Cunningham, 1983), and the cross section for Compton interaction is labelled σ_c.

Pair production may occur when an incident photon interacts with the intense field of an atomic nucleus. The energy of the photon is converted into the mass of an electron and a positron, and the energy with which they mutually recoil. The minimum energy of a photon which can undergo pair production is thus the rest-mass energy of the electron and positron ($\approx$1.02 MeV). In water, pair production becomes an important interaction process for photons with energies above approximately 5 MeV (Johns and Cunningham, 1983). The cross section for pair production is labelled $\varkappa$.

2.1.3.2. Attenuation, Energy Absorption, and Energy Transfer

All of the above mentioned interaction cross sections vary with the energy of the incident photon and composition of the irradiated medium. For details of these variations, there are summaries in Johns and Cunningham (1983) and Greening (1985). The probability of interaction by *any* one process per unit path length in terms of mass/area gives the total mass attenuation coefficient, μ/ϱ, for a given photon energy and medium;

$$\frac{\mu}{\varrho} = \frac{\tau}{\varrho} + \frac{\sigma_c}{\varrho} + \frac{\varkappa}{\varrho} + \frac{\sigma_{coh}}{\varrho} + \frac{\mu_{other}}{\varrho}, \qquad (2.14)$$

where μ_{other} represents the cross section due to all other unmentioned interaction processes. The total mass attenuation coefficient determines the likelihood of interaction per unit

effective path length in a medium, and thus how rapidly the photon fluence is exponentially attenuated with distance through the irradiated medium.

The fraction of energy transferred to charged particles in interactions per unit density and effective path length is given by the mass energy transfer coefficient, $\frac{\mu_{tr}}{\varrho}$. The fraction of this energy deposited in the irradiated medium by charged particles is given by the mass energy absorption coefficient, $\frac{\mu_{en}}{\varrho}$. Some of the energy of the charged particles (a fraction g), will be re-radiated in bremsstrahlung processes. The mass energy transfer and absorption coefficients are then related by

$$\frac{\mu_{en}}{\varrho} = \frac{\mu_{tr}}{\varrho}(1-g). \tag{2.15}$$

2.1.4. Relating Absorbed Dose to Kerma

As mentioned above, photons transfer energy to charged particles (electrons and positrons) in a medium, which then deposit energy within the medium. A useful parameter is the collision kerma which is related to kerma through

$$K_c = K(1-g), \tag{2.16}$$

where g is defined as above. If charged particle equilibrium is present (the same number, energy and direction of charged particles enter a region as leaves it), then it can be shown (Attix, 1979) that absorbed dose and collision kerma are equal. Because of the finite range of electrons set in motion by incident photons, this is not necessarily the case in photon beam irradiations and the absorbed dose at depth is greater than the collision kerma. For a more thorough discussion, see Greening (1985).

2.2. Monte Carlo Particle Transport - EGS4

2.2.1. Monte Carlo Particle Transport

Describing the transport (interactions, energy depositions) of electrons through media analytically is extremely difficult, and resort is often made to generalised macroscopic statistical results to predict dose distributions due to irradiation (such as the Fermi-Eyges multiple scattering theory described in §2.1.2.4). A more feasible alternative is to simulate the transport of individual particles through matter, making use of theoretical and statistical results of scattering and energy deposition on a more microscopic scale. Such simulation is the objective of Monte Carlo methods which allow transport simulations of an arbitrary number of particles through media of varying composition. Monte Carlo methods are used extensively in the research presented in this thesis. The structure and operation of the Monte Carlo code used, EGS4 (Electron Gamma Shower Version 4; Nelson *et al.,* 1985), shall be briefly outlined.

2.2.2. EGS4 Monte Carlo

The EGS4 code system was developed at the Stanford Linear Accelerator Center (SLAC). Its development, structure and application are well documented (eg., Nelson and Jenkins, 1980; Nelson *et al.,* 1985, Chapters 12 - 14 in Jenkins *et al.,* 1988). The functions and distributions sampled in EGS4 Monte Carlo and the techniques used for transporting photons and electrons are well documented in these references and shall only be briefly discussed in the next section, with a brief overview of the code system following. Of primary interest is the method of implementation in the current study, how geometries are described, and the particle characteristics and dose distributions obtained. A discussion of these points is given in §2.2.3.

2.2.2.1. Particle Transport in EGS4

The principle of particle transport in EGS4 is to follow the history of every particle considered (electrons, positrons and photons in the EGS4 system), including secondary particles, until they are either stopped in the medium of interest (the *phantom*) due to their energy falling below a predetermined value, or are discarded because of their geometrical location. The motion of the particle during its history is determined by the sampling of random variables, which are random numbers controlling factors such as step size and interaction parameters.

The cross sections elaborated in §2.1.3.1 are all small enough in most materials that it is feasible to model *all* photon interactions a photon undergoes before being discarded. That is , photons deposit their energy in relatively few interactions. Given a photon then, with a specific energy, location and direction in a medium of known characteristics, and given known interaction cross sections, it is straightforward to determine a feasible location for the next interaction of the photon from the expected mean free path (Nelson *et al.,* 1985; Murray, 1990). The relative cross sections of each interaction type for the photon are known, and the type of interaction can be determined by random number sampling. For example, if there are n types of interaction possible with cross sections σ_j (j=1,..,n), then we can create a function F which divides a unit interval into n divisions;

$$F(i) = \frac{\sum_{j=1}^{i} \sigma_j}{\sum_{j=1}^{n} \sigma_j}. \qquad (2.17)$$

Given a random number ζ on the interval [0,1], the actual interaction to occur at each interaction site is then found by finding $F(i)$ such that

$$F(i-1) < \zeta < F(i). \qquad (2.18)$$

Once an interaction type has been selected, the resulting scattering angles, energy losses and particles generated in the interaction can be sampled in a similar way from theoretical interaction coefficients (see Nelson *et al.,* 1985). The result is a set of product particles

with their individual energies and directions ready to be transported *from* the interaction site.

In order to determine the actual distribution of energy deposition within the irradiated medium, it is necessary to perform the explicit transport of electrons. EGS4 employs what is known as a Class II transport scheme (Rogers and Bielajew, 1986; Murray, 1990) where small energy losses are simulated using Moliére multiple scattering theory (Bethe, 1930, 1932; Moliére, 1947; Scott, 1963), and large-angle events (ie., catastrophic collisional and radiative interactions) are considered individually.

The occurrence of a large energy loss event can be decided upon by considering the amount of energy lost during an electron step. If the energy loss is over a specified value, then a discrete interaction is considered and secondary particles are created for subsequent transport. The appropriate amount and type of energy loss can be determined using the mass stopping powers discussed in §2.1.2. Fluctuations in such energy loss allow authentic simulation of energy loss straggling, which is required for obtaining realistic dose distributions. For smaller energy losses, multiple scattering is employed along with restricted stopping powers (see §2.1.2.3) to determine local energy deposition due to low energy secondary products (assuming a relatively local deposition of all the energy of secondaries).

In order to accurately account for variations in energy loss, it is necessary to establish a threshold for division between discrete and multiple scattering events which allows fast simulation (ie., with fewer discrete events) with sufficient inclusion of energy loss straggling. Control of such transport parameters is by variation in the parameters listed in Table 2-I. Compromise in discrete and multiple event simulation through variation in the parameters AE and AP can lead to inaccurate simulation. The PRESTA algorithm developed by Bielajew and Rogers (1987) helps to provide efficient simulation of energy losses at each particle step.

Table 2-I: User selected energy parameters for control of EGS4 particle transport.

Parameter	*Purpose*
AE	Energy loss threshold for secondary electron production. δ rays with energy below AE are not transported though their effect is included via use of the restricted collisional stopping power.
AP	Energy loss threshold for secondary photon production. Secondary photons with energy below AP are not transported though their effect is included via use of the restricted radiative stopping power.
ECUT	Low energy cutoff for explicit transport of positrons and electrons (energy deposited locally below this value).
PCUT	Low energy cutoff for explicit transport of photons (energy deposited locally below this value).

Due to the fact that discrete particles are simulated in this Monte Carlo approach, the accuracy in results (energy deposition distributions, particle characteristics) will depend on (other then the selection of energy parameters) the actual numbers of particles simulated due to statistical variations. Statistical uncertainties in Monte Carlo results are proportional to the square root of the number of particle histories (Shreider, 1966; Nelson and Rogers, 1988), and also depend on such factors as the size of voxels describing a phantom, and particle energy cutoff parameters as listed in Table 2-I. However, it is because Monte Carlo methods simulate individual particle histories that, given a sufficiently large number of histories and accurate cross sectional representation of particle interactions, Monte Carlo methods will provide the most accurate radiation transport results short of an explicit analytical solution obtained without approximations.

2.2.2.2. EGS4 Code Structure

The actual execution of the particle transport described in §2.2.2.1 is performed with FORTRAN programs which comprise the EGS4 system. Administration of particles, parameters to be scored, simulation geometries and program execution is performed by a *usercode* written to allow characterisation of specific situations. In order to allow efficient sampling of interaction parameters for materials involved in a simulation, a preprocessor (PEGS4) is used to establish tables of cross sections based on user-defined cutoff energies and the composition of phantom materials. These elements combine to form an executable simulation as shown in Figure 2-4.

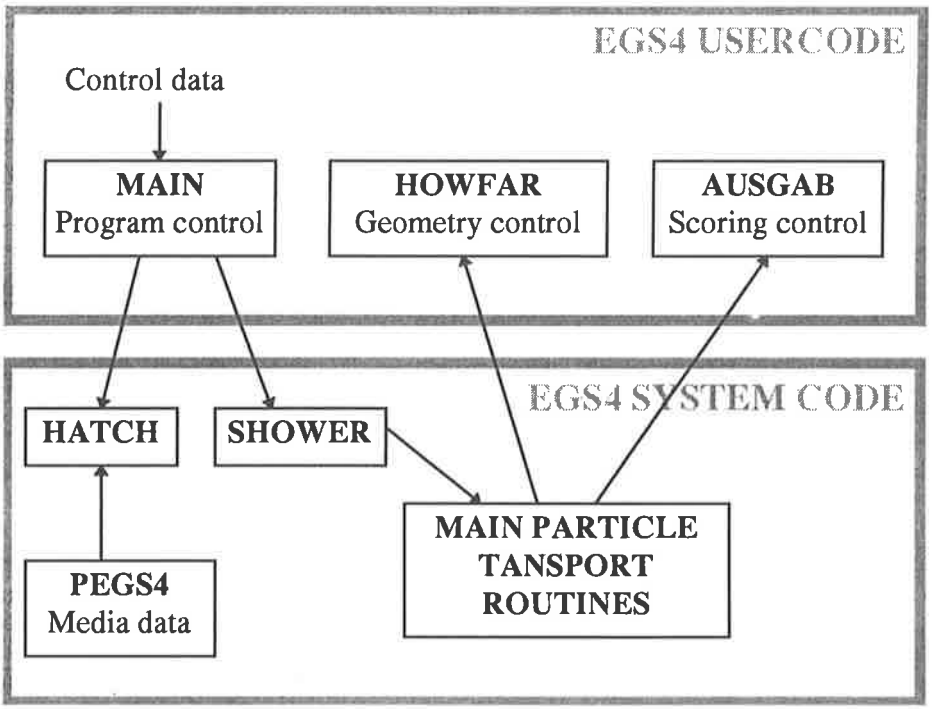

Figure 2-4: Relationship of principle components in the EGS4 code system.

The MAIN part of the usercode establishes the media and geometry of the phantom, establishes initial particle parameters and cut-off energies, and performs final collation of desired information. It also outputs collated dose distributions, energy spectra, particle histories etc to appropriate files.

HOWFAR establishes the location of a particle at any time relative to phantom *boundaries* (locations of voxels within the phantom which separate out different geometrical and

media-type regions), and is called each time EGS4 is about to transport a particle near to a region boundary (as governed by the PRESTA algorithm). It evaluates the distance of a particle to the boundaries of voxels composing the phantom and can modify a potential step length accordingly. AUSGAB scores simulation parameters as directed by the user, such as energy deposition (translatable to dose), particle types, energies and directions etc. Calls to AUSGAB are also made each time EGS4 is about to transport a particle by a step. Information from a simulation is collated during execution by successive calls to AUSGAB.

The HATCH routine reads in the data generated by PEGS4, whereas the SHOWER routine takes the characteristics of an initial particle and the medium it is in from MAIN, and performs the transport of the particle and any particles it generates until they are stopped or discarded.

2.2.3. Characteristics of Current Implementation

In order to perform simulations which formed part of the research presented here, several specific features in EGS4 simulation were required. These involved specific characterisation of geometries, and specialised scoring routines. Two user codes, originally written by Murray (1991), were modified accordingly, one (RTPCYL) utilising a cylindrical description of the phantom geometry and the other (RTPCART_XYZ) utilising a Cartesian geometry. Only the features of these usercodes pertinent to the current application shall be discussed.

2.2.3.1. Usercode RTPCYL

RTPCYL is used for modeling beams of various types incident on phantoms described by cylindrical geometries, with particles typically incident near to the direction of the principle axis. The main features of this code employed in the current application (simulation of electron beam scattering foils, obtaining dose distributions due to pencil beams, obtaining depth dose distributions due to broad beams) are:

- Definition of cylindrical layers in the phantom of arbitrary width, and radial regions of arbitrary width
- Use of point sources of particles at some distance from the phantom, collimated to a rectangle at the phantom surface
- Use of parallel pencil beams of particles incident on the phantom surface
- Possibility for entering particle energies as sampled from given spectra
- Scoring of particle energy spectra at any plane in the geometry
- Scoring of energy deposition within a cylindrical geometry

An input file ('Control data' in Figure 2-4) is read in by this code at simulation commencement containing parameters required for the simulation. An example of such an input file is shown in Appendix A.

2.2.3.2. Usercode RTPCART_XYZ

RTPCART_XYZ is used for simulating beams incident on phantoms described by Cartesian geometries, with particles usually incident from one side of a plane defining the phantom. This code was used for several purposes in the research presented here (simulation of applicator scattering, obtaining dose distributions due to arbitrarily configured radiation fields, obtaining dose distributions due to broad fields), and use was made of the following features:

- Possibility for sampling incident particle energies from given spectra
- Possibility for sampling incident particle angles from a Gaussian distribution with specified standard deviation
- Possible use of point sources of particles incident from one side of the phantom, collimated to a rectangular region anywhere on the phantom surface
- Scoring of particle numbers normalised to incident fluence across all voxels of any plane in the phantom
- Establishment of *scatter kernels* with specific file format as described in §4.3.2
- Scoring of particle energy spectra at any plane, region or voxel in the phantom
- Collimation of incident particle beams to an arbitrary field shape (using the polygon clipping routine described in Appendix C).

- Possibility to input individual particle characteristics (type, energy, location, direction) through reading *phase space* characteristics (see §4.3.3)

Again, an input file was created for each simulation type in order to establish simulation parameters, and an example is shown in Appendix B.

3. ELECTRON BEAM RADIOTHERAPY

3.1. Generation of Electron Beams

High energy (1 to 50 MeV) electron beams have been used for treating tumours since the 1950/60's, (Harvey *et al.,* 1952; Hseih and Uhlmann, 1956; Ovadia and Uhlmann, 1960; Zatz *et al.,* 1961; Klevenhagen, 1985). Obtaining high energy beams which are useful for controlled treatment processes means accelerating electrons to relativistic speeds (>0.95*c*) in beams with controllable spatial and temporal properties. Such a beam has greatest utility when it can be manipulated through collimation or explicit directional control. By far the most currently popular and affordable means of obtaining high energy electron beams is with linear accelerators, as modelled in the investigation presented in Chapter 4.

3.1.1. Linear Accelerators

The principle of operation of linear accelerators for therapeutic use is outlined in detail in many sources (eg., Johns and Cunningham, 1983; Klevenhagen, 1985; Karzmark and Morton, 1989; Khan, 1994), though a brief description shall be given here. The description of electron acceleration in a waveguide in §3.1.1.1 also applies to the generation of megavoltage photon beams with linear accelerators. This similarity in electron/photon beam generation implies that linear accelerators are often used as dual modality devices, capable of delivering either sort of beam at discrete energies.

3.1.1.1. Electron Acceleration

Figure 3-1 shows the generic arrangement of a linear accelerator used for generating electron beams. Several components such as beam monitors, mirrors, focusing and other auxiliary control systems are not shown. Electron acceleration is achieved by the transfer of energy from microwaves in a waveguide to electrons injected into the guide. Both standing and travelling wave propagation modes have been employed, with microwave power delivered by a klystron or magnetron.

Electrons are injected into the waveguide (in phase with microwave pulses) from an electron gun. After acceleration along the guide, the electrons are transmitted through a thin window and may have their direction modified for clinical purposes. At this stage, electrons are usually entering what is known as the *treatment head* of the accelerator, where final beam formation occurs prior to incidence on the patient. If the bending of the accelerated electrons is required, this can be achieved using a *bending magnet* as shown in Figure 3-1, which changes electron direction by either a 90^{o} or 270^{o} (as shown) rotation. A 270^{o} rotation allows recombination of all energy components after the change in direction which allows for chromatic tuning (Klevenhagen, 1985). This is not achievable with a 90^{o} rotation.

3.1.1.2. Electron Beam Formation

The result of electron propagation at this point is a narrow (several mm^2 in cross section) quasi-monoenergetic, quasi-parallel electron beam directed down towards the patient plane. Such a beam has little clinical utility unless it is modified. A useful clinical beam can be broadened to field sizes of many cm^2, with electron intensity, direction and energy being sufficiently uniform across the full field, and subject to long term stability in fluence and energy (Klevenhagen, 1985). Such effect may be obtained by scanning the narrow beam across the field as discussed in §3.1.2. Also (as shown in §3.2.2.2), electron beams produce

more well defined dose distributions when characterised by a single maximum energy rather then a broader energy spectrum*, with as little photon contamination as possible.

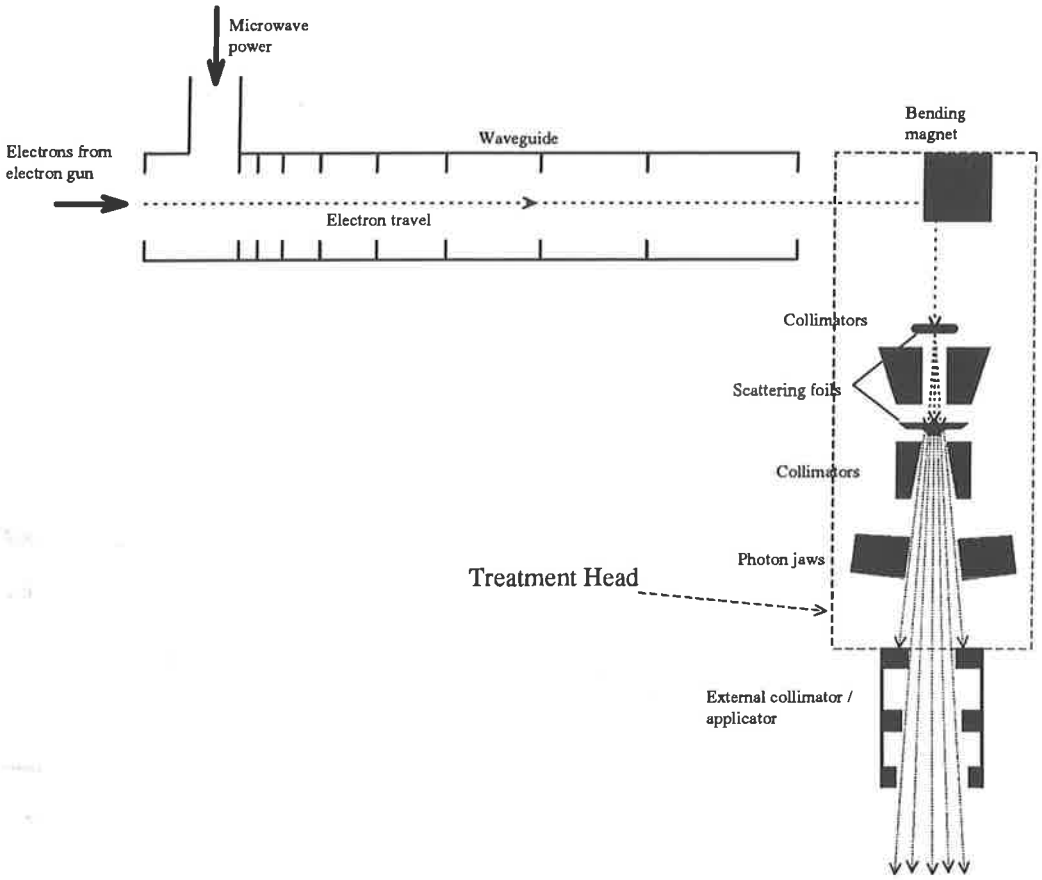

Figure 3-1: Generic construction of a linear accelerator for producing broad electron beams for therapy (not to scale).

Beam broadening is most commonly achieved using a combination of *scattering foils* (Loevinger *et al.,* 1961; ICRU, 1984; Klevenhagen, 1985) upon which the beam from the waveguide is incident as shown in Figure 3-1. The optimisation of scattering foil arrangement requires consideration of the amount of scattering (and hence lateral spread and intensity flatness), attenuation and energy straggling electrons undergo, and the amount of bremsstrahlung generated in the foil. All of these factors are controlled by the choice of scattering foil arrangement in the following ways (Svensson, 1971; Marbach and Almond, 1981; Klevenhagen, 1985; Desobry and Boyer, 1994; Klein *et al.,* 1995):

- ***Composition*** - In order to achieve greater scattering efficiency, the material used for foils must optimise the mass scattering power relative to the mass collisional

* Known energy modulations can be clinically advantageous as shown in §3.2.2.2 and Chapter 5.

stopping power, which is achieved with high atomic number materials, promoting scattering relative to energy loss. However, bremsstrahlung generation is increased in higher atomic number materials (see §2.1.2.3) and leads to greater photon contamination, although the increase in energy degradation with smaller atomic number (and greater thickness of scatterer required) generally means a high atomic number material is selected for foils (Loevinger *et al.,* 1961; Brahme and Svensson, 1979; ICRU, 1984).

- ***Thickness and Geometry*** - The degree of scatter in a beam increases with depth in the scattering material (see equation 2.6), and so thicker foils will generate flatter, broader beams. However, with more material to traverse, electrons will suffer energy loss and a broader energy spectrum will result, together with a decrease in intensity due to greater scattering. The greater thickness also means increased bremsstrahlung production. The shape of scattering foils can also influence beam flatness for beams that have already been partially spread. Thus, dual scattering foil systems are often employed (separated by an air gap which allows electrons scattered in the first foil to be projected to a wider lateral distance as they enter the second foil), with the shape of the second foil calculated for optimal beam flatness as shown in Figure 3-2. This allows preferential scattering at the central part of the beam, which will emerge from the first foil with greater intensity in the central region due to the Gaussian nature of scattering (see §2.1.2.4). The same degree of scattering can be achieved with dual foils with total foil thickness an order of magnitude smaller then with a single foil (ICRU, 1984), which reduces energy loss and spread.

All factors mentioned above require mutual consideration in foil design, and have formed the basis for many studies in foil optimisation (eg., Okumura *et al.*, 1969; Svensson, 1971; Brahme, 1972; Sandberg, 1973; Bjärngard *et al.,* 1976; Kozlov and Shisov, 1976; Abou-Mandour and Harder, 1978; Berger and Seltzer, 1978; Brahme and Svensson, 1979; Marbach and Almond, 1981; Desobry and Boyer, 1994; Klein *et al.,* 1995). Furthermore, for accelerators capable of generating beams of varying energies, scattering foil systems must be designed for each energy to be used (Karzmark *et al.,* 1993).

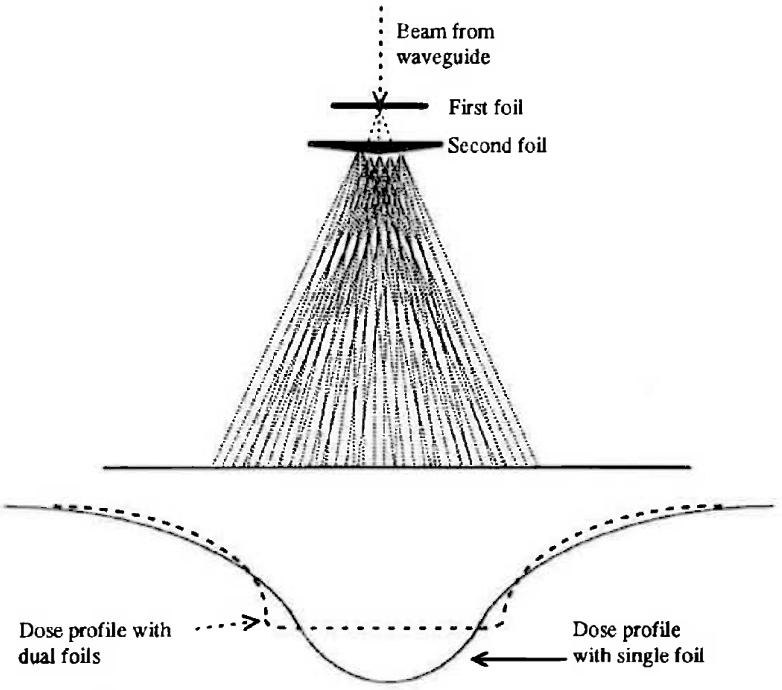

Figure 3-2: Influence of double scattering foil system on electron beam flatness (adapted from Klevenhagen, 1985, and Brahme, 1977).

3.1.1.3. Final Beam Collimation

Electrons in electron beams undergo considerable scattering in the air column between the scattering foils and the patient surface (Hogstrom, 1995). This scattering results in a continual increase in the angular spread of electrons with distance through air and, if collimated near to the scattering foils, a beam will not be sufficiently defined at the patient plane resulting in broad penumbral regions in the dose distribution (see §3.2.1). To obtain a uniformly high dose across the target volume, and low dose elsewhere, it is essential in electron beam therapy therefore, that the beam be collimated as near as is reasonable to the irradiated surface.

Many designs for final collimation systems (*applicators* or *cones*) have been proposed, generally based on either closed wall devices (Loevinger *et al.*, 1961; Beattie *et al.*, 1962; Bradshaw and Maysent, 1964; Svensson, 1971; Lax and Brahme, 1980) or as a series of trimming apertures (Svensson and Hittinger, 1967; Svensson, 1971; van der Laarse, 1978; Goede *et al.*, 1977; Biggs *et al.*, 1979; Muller-Runkel *et al.*, 1985; Pennington *et al.*, 1988;

Das *et al.,* 1990). Whatever technique is used, scatter from collimation systems can lead to perturbations in dose distributions (Bradshaw and Maysent, 1964; van der Laarse *et al.,* 1978; Lax and Brahme, 1980; Kassaee *et al.,* 1994; see §4.1.1.2) which can be used to advantage if the scatter can assist in beam flattening. However, this contribution is usually kept to a minimum as optimisation of the scattering foil system is likely to be of more useful advantage for achieving flatness (Lax and Brahme, 1980).

The contribution of scatter from collimators to the electron beam is strongly dependent on the materials used in collimator construction (ICRU, 1984). In applicators composed of trimming plates, the plates must be sufficiently thick to stop electrons of the maximum energy employed (Giarratano *et al.,* 1975; Purdy *et al.,* 1980) without undesired photon generation. If the trimming plates are composed of high-atomic number and low-density material, then considerable scattering of low energy electrons back into the beam will result, degrading the energy and angular characteristics of the electron beam (Lax and Brahme, 1980; see §4.1.1.1).

For static or dynamic (arced) electron fields, it is useful if beam definition can be made of arbitrary field shapes rather then fixed rectangular or circular standards. This allows the shielding of organs-at-risk within the patient, and selective irradiation of the target region. For this purpose, patient-specific low melting point alloy (LMPA) *cutouts* are often used which perform the final collimation of the beam before incidence on the patient surface (Biggs *et al.,* 1979; Choi *et al.,* 1979; Nair *et al.,* 1983; Muller-Runkel *et al.*, 1985; Kurup *et al.,* 1995). Such cutouts are often mounted at the base of the applicator, on or several centimetres above the irradiated surface. The use of low melting point materials allows specific field shapes to be formed easily for individual patients.

The general combination of scattering foils and collimators determines the characteristics of the electron beam produced including the beam quality (Bjärngard *et al.,* 1976; Brahme and Svensson, 1976), the photon contamination properties (Rustgi and Rodgers, 1987; Das *et al.,* 1994), and the general intensity and angular variations. These characteristics all influence the dose distribution and clinical applicability of an electron beam as shall be discussed in §3.2.

3.1.2. Other Accelerators and Developing Techniques

Whereas linear accelerators have presented the most common and affordable means of accelerating electrons for clinical purposes, other methods are possible. One method involves cycling electrons through a single section of accelerating cavity to a desired energy. This is the basis for the *racetrack microtron*, and allows high electron energies (> 50 MeV) and a large number of discrete energies to be achieved in a smaller spatial volume than in a linear accelerator (Brahme *et al.,* 1975; Johns and Cunningham, 1983; Brahme, 1987; Karlsson *et al.,* 1992; Lind and Brahme, 1995). Another method involves accelerating electrons in circular orbits within an evacuated chamber using alternating magnetic fields of increasing strength. This method, used in *betatrons*, is relatively inefficient for generating electron beams relative to linear accelerators due to low electron yield and energy limits (Johns and Cunningham, 1983).

Alternatives also exist for achieving broad, flat electron beams from high energy narrow (pencil) beams other than using flattening filters. Electron energy losses and bremsstrahlung production would be eliminated if the electron beam were broadened without having to pass through high atomic number scattering materials. This can be done using magnetic fields to defocus the beam from the guide (Hsieh and Uhlmann, 1956), as well as other defocusing methods including physical motion of the accelerator treatment head (ICRU, 1984).

A particularly elegant technique uses magnetic fields to scan the initially accelerated beam over the treatment field. This *scanning beam* technique can be used to achieve very high geometric definition with electrons (Lind and Brahme, 1987; Lief *et al.,* 1994, 1995; Lind and Brahme, 1995; Lief *et al.,* 1996), with the lack of energy straggling in scattering foils minimising energy spread and allowing accurate definition of treatment depth (see §3.2.1).

Scanning beams would be used optimally if the intensity of the scanned pencil beam could be varied across a treatment field by variation in the speed of beam scanning to produce non-uniform dose distributions (Carpender *et al.,* 1963; Lind and Brahme, 1995). This could be combined with the ability to vary the energy of the incident beam and the ability

to move the effective location of the beam's source (or just generally move the location of the target region relative to the source) via translation and rotation to achieve electron beams with arbitrary characteristics (ie., beams with electrons of varying energy, location, and direction) for achieving some desired distribution in dose (as investigated in Chapter 5). These electron beam characteristics may not resemble those of traditional flat beams. A general source position would be achieved if the accelerator is robotically mounted (Lind and Brahme, 1995), or if electrons were guided to the irradiation site using magnetic guidance along a *magnetic electron hose*.

3.2. Clinical Applications and Limitations

The clinical application of electron beams depends on many factors, such as the dose distributions that electron beams produce, clinical situations where such distributions are useful, and the efficient use and potential modification of the dose distributions. These factors shall now be respectively considered.

3.2.1. Electron Beam Dose Distributions

When a patient or phantom is irradiated by an electron beam, the resulting distribution of absorbed dose depends on the initial characteristics of the particles in the beam, and the subsequent transport in the patient/phantom medium. There are several ways of representing the three-dimensional distribution of dose as shown below. Examination of these representations can indicate how properties of electron energy, spatial and angular variation, and photon contamination can influence electron beam dose distributions.

3.2.1.1. Depth Dose Curves

A depth dose curve is a plot of absorbed dose with depth in a medium (usually normalised to 100% at the maximum dose). For static fields, the depth axis is conventionally taken as

that along the beam's principal axis. An example of a depth dose curve, measured at the centre of a 6x6 cm^2 12 MeV beam with a diode detector, is shown in Figure 3-3. When depth dose curves (or any dose distribution) are measured, the raw data is usually the amount of ionisation measured in a radiation detector, which can be converted to absorbed dose in the medium of interest by taking account of variations in stopping power for the medium and the detector material with depth (ICRU, 1984).

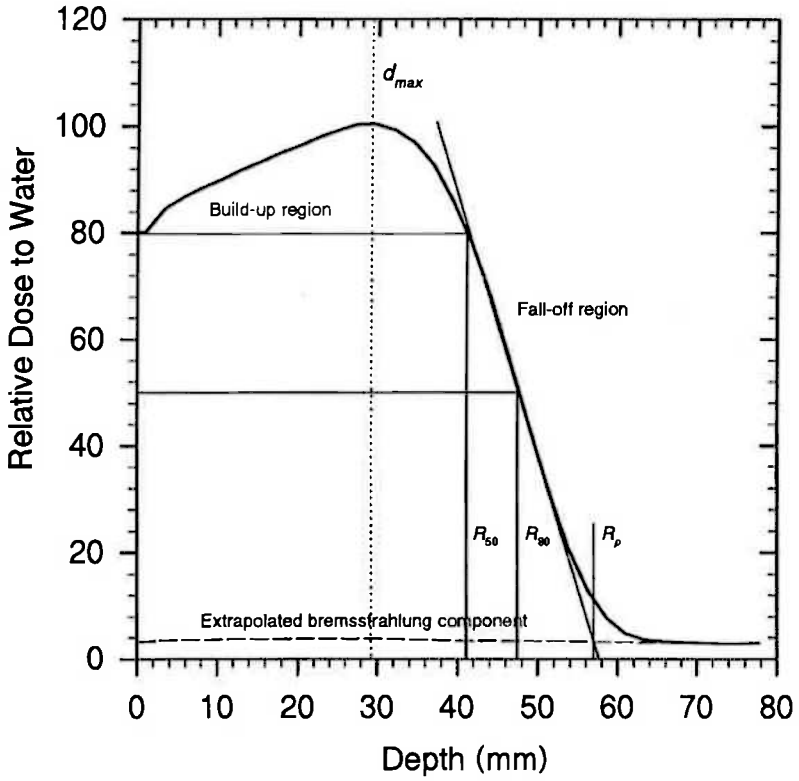

Figure 3-3: 12 MeV, 6x6cm^2 depth dose curve (heavy line) measured with a diode detector, showing some major parameters used to describe the curve.

Figure 3-3 also shows some parameters which can be used to describe the depth dose curve for a certain beam. These parameters, and the general shape of the curve itself, depend on the characteristics of the electron beam such as energy spectrum, angular distribution, and spatial distribution including field size. When the electron beam enters the irradiated surface, the electrons begin scattering according to their energies, and the composition of the medium (assumed water-equivalent for this discussion), and the electron directions

become progressively more oblique to the initial direction with depth. The resulting increasing electron fluence leads to the build-up region shown, which extends to a point at which further scattering cannot increase the electron fluence. The depth in the irradiated medium at which the resulting maximum dose (100% in Figure 3-3) occurs is termed d_{max} After d_{max}, the reduction in dose due to electrons stopping is greater then the increase due to increasing electron obliquity producing the fall-off region. Electrons continue to deposit energy over the fall-off region until they are completely stopped at the depth known as the practical range, R_p. The shape and extent of the build-up region in a depth dose curve does depend on the actual size of the electron field as well as the energy spectrum of incident electrons as shall be explained below.

In Figure 3-3, R_{50} and R_{80} are the depths on the depth dose curve where the dose level in the fall-off region has dropped to 50% and 80% of the maximum dose respectively. These measures allow characterisation of the depth dose curve, and also the estimation of mean and most probable energies in the electron beam (ICRU, 1984). R_{80} also defines arbitrarily, the beginning of the steep fall-off region and the limit of the clinically useful part of the dose distribution (see §3.2.2), and constitutes the *therapeutic range* for the given beam. The therapeutic range may also be taken as some other shallower depth, such as R_{85} or R_{90} (Klevenhagen, 1985).

As mentioned above in §3.1.1, the electron beam produced by an accelerator will have a photon contamination component, and this is manifest in depth dose curves as a tail region past R_p. Dose due to photons also constitutes a small fraction of the total dose at shallower depths. This dose is also due to photons generated in the irradiated medium itself, though Rustgi and Rodgers (1987), using magnets to sweep electrons out of an electron beam, showed that the principle source of photon dose in an electron beam irradiation of water is from treatment head-generated photons. An estimation of the magnitude of dose due to photons at depths less than R_p can be obtained by extrapolating the tail curve back to shallower depths as shown in Figure 3-3. Due to the preferential bremsstrahlung production of electrons in treatment head materials with increasing electron energy (see equation 2.4), higher energy beams have greater levels of photon contamination and hence larger relative photon dose contributions.

Increasing incident energy in an electron beam will significantly affect a dose distribution due to the increased electron range, and the decreased scattering power (ICRU, 1984; see §2.1.2.4). Higher energy electrons are scattered proportionally less than lower energy electrons when entering water so that the increase in electron fluence due to scattering is much less marked for high energy electron beams. Thus, the build-up region is less pronounced for higher energy electron beams, with high dose levels maintained to greater depths (R_{50} moving to greater depths). Thus, R_p also increases in depth with increasing energy, and the fall-off region becomes less steep.

The shallower depth of d_{max} for lower energy electrons has ramifications for depth dose curves when a beam contains a spectrum of electron energies rather than a single energy. Low energy components will increase the dose at shallower depths relative to a monoenergetic beam, move d_{max} closer to the surface and increase doses at depths less then d_{max}.

Similarly, if electrons are incident obliquely to the irradiated surface, then the fluence at shallow depths will be increased relative to a normally incident beam, resulting in higher doses at shallow depths. Since electron beams will have electrons obliquely incident to the irradiated surface (due to scattering in air and treatment head components, and divergence from electron sources), then clinical depth dose curves will have higher doses near the surface than theoretical normally incident beams. The angular distribution of electrons in a beam must thus be accounted for in beam models for authentic replication of the physical situation. If the increase of dose near the surface is a *desired* feature, then low-energy or oblique electrons can be introduced into the beam (Alasti and Galbraith, 1995; Hyödynmaa *et al.,* 1996; see §3.2.2.2).

For dose to be able to *build up* as much as possible as measured in a depth dose curve, electrons must be available to the region where the curve was measured (usually the beam's central-axis) from all surrounding regions of the irradiated medium, within the maximum lateral range of the electrons considered. If not, then an increase in the size of the electron field will provide more electrons to central-axis due to the finite range of

scattered electrons, resulting in a larger amount of build-up. This is displayed in Figure 3-4. In figure a), electrons incident at the outside of the field have sufficient maximum lateral range in the irradiated medium to reach central axis before stopping This situation is known as having *lateral electron disequilibrium* at central-axis. If the field size is increased past this range as in Figure 3-4b), then the maximum possible dose is achieved at central axis. This corresponding situation is known as having *lateral electron equilibrium* at central-axis. Since higher-energy electrons have longer ranges, then field sizes must increase with beam energy for lateral electron equilibrium to be maintained.

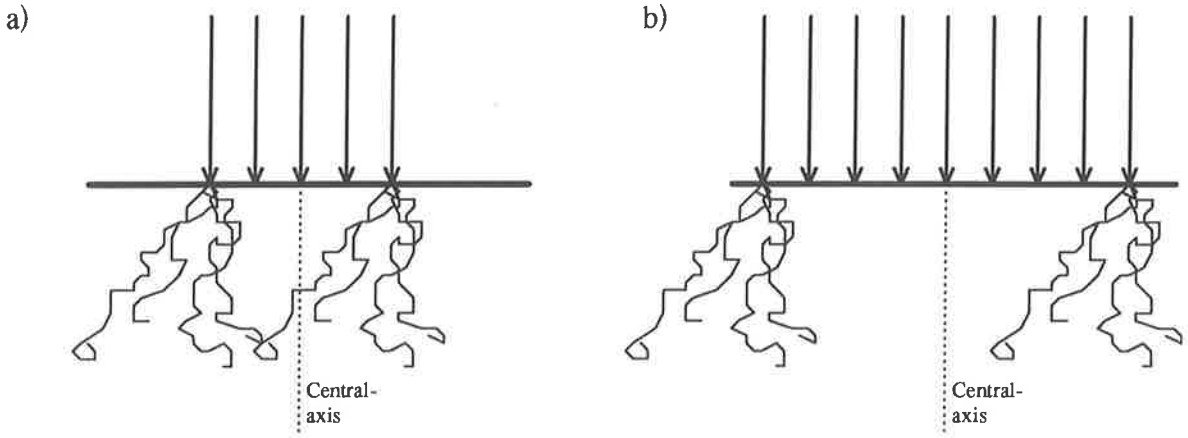

Figure 3-4: Illustration of how electron beam field size varies the degree of lateral electron equilibrium. In a), the distance to the beam boundary from central axis is less then the maximum lateral range of electrons in the beam, and lateral electron equilibrium does not exist. Thus, an increase in field size will result in an increase in dose at central axis until the lateral electron range is exceeded. This is the situation in b), where equilibrium does exist, and electrons incident at the beam boundary cannot traverse the distance to central axis.

Below the field size which provides equilibrium at central-axis for a given beam energy, several aspects of the depth dose curve become field size dependent. The main observations with decreasing field size are (ICRU, 1984);

- the maximum dose decreases and moves to shallower depths;
- the percentage dose at the irradiated surface increases;
- the gradient of the fall-off region decreases; and
- the linearity of the fall-off region decreases and consequently R_p becomes more difficult to specify.

These observations are all epitomised when the field size becomes infinitesimally small in the case of an incident pencil beam, discussed in §3.2.1.4.

3.2.1.2. Dose Profiles

Whereas depth dose curves are measured along the direction of the incident beam, dose profiles represent a one-dimensional distribution of relative dose along a line transverse to the incident beam, at some depth in the irradiated medium. Examples of profiles at several depths (for a 6x6 cm^2 12 MeV electron beam incident on water) are shown in Figure 3-5.

The beam profile extends from central-axis out to the *penumbral* region, which falls off gradually due to the long range of high-energy electrons, the angular spread of electrons before incidence (affected by the distance from the end of the external collimator to the irradiated surface; Klevenhagen, 1985), and the variation of angular spread after incidence. The increase in lateral spread with depth also reduces the penumbral slope with depth. This point can be more easily understood by considering a broad beam to be composed of a superposition of narrow pencil beams (Lillicrap *et al.,* 1975; see §3.2.1.4), as shown in Figure 3-6. According to the Gaussian approximation for electron spread with penetration into a medium (see §2.1.2.4), the dose profile for pencil beams will be approximately Gaussian, with the Gaussian spread increasing with depth. The superposition of a series of Gaussians leads to a dose profile with an extended penumbra, with the penumbral slope decreasing with depth as seen in comparison of Figure 3-6a) and Figure 3-6b).

A measure of the consistency of an electron beam is the *flatness* of the dose profile at some specified depth. The flatness of a specific beam has a range of definitions such as the difference between maximal and minimal dose values. Another figure of merit is the *uniformity* of the dose distribution, defined by Svensson and Hettinger (1971) as the ratio of the area inside the 90% isodose line in the plane (perpendicular to the beam axis) through d_{max} to the area of the geometrical field on a phantom's surface (ICRU, 1984).

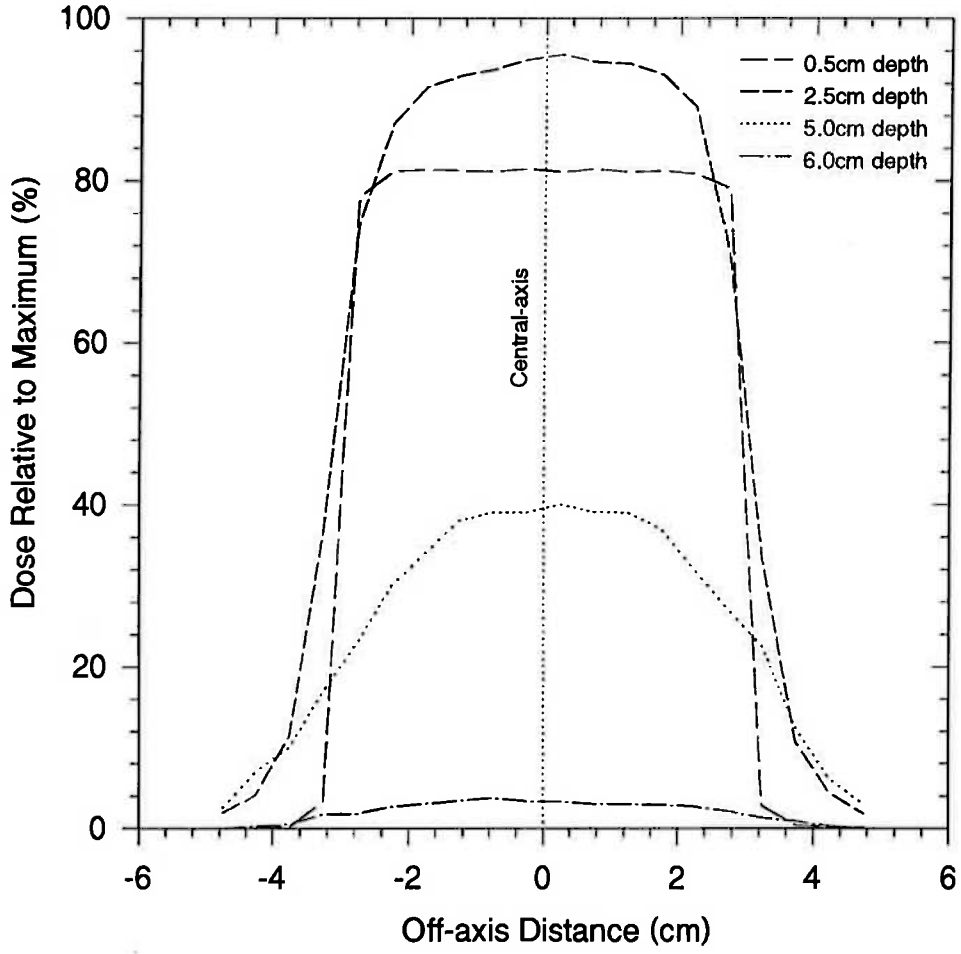

Figure 3-5: Dose profiles calculated using EGS4 Monte Carlo (usercode RTPCART_XYZ) for a 12 MeV electron beam incident on water. Profiles are at discrete depths.

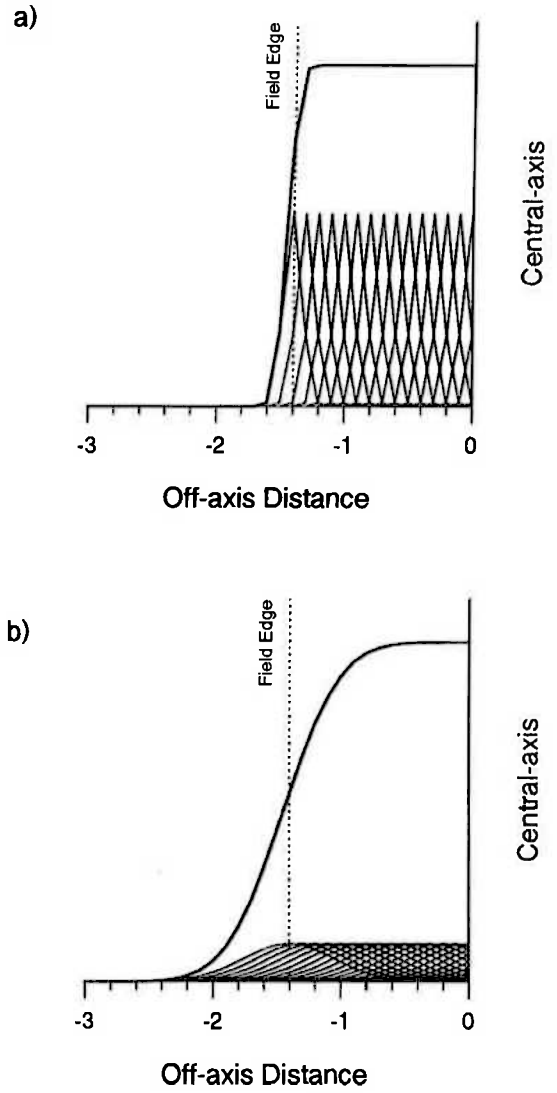

Figure 3-6: Illustration of the formation of electron beam profile shape by considering the incident beam as a superposition of pencil beams, with individual profiles being Gaussian in shape. In a), the lateral standard deviation of each Guassian distribution is 0.1, with individual Gaussians separated by 0.1 on the off-axis distance axis. In b), the lateral standard deviation is 0.5, representing the pencil beams at a greater depth, which produces a penumbral region which is much less steep then in a). The darker line in each case is the superposed profile (sum of all Gaussians) for a half-field, and the vertical scale is arbitrary.

3.2.1.3. Contour and Surface Plots

In order to observe the distribution of dose in an irradiated medium in a two-dimensional plane, a contour plot of isodoses in that plane can be formed, as shown in Figure 3-7. Alternatively, dose can be used as a third-dimension in the plane of interest and the dose distribution viewed as a surface plot. The dose distribution shown as a contour plot in Figure 3-7 is shown as a surface plot in Figure 3-8.

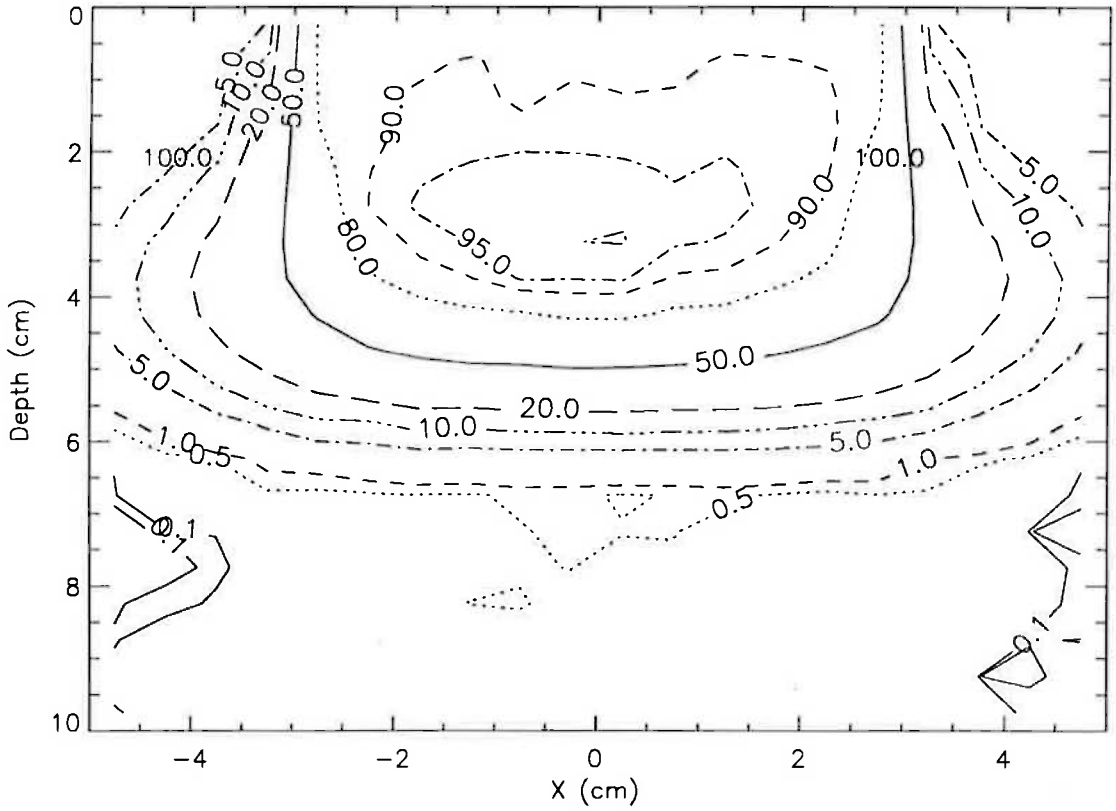

Figure 3-7: Contour plot of dose in water percentage normalised to maximum for a 12 MeV 6x6cm^2 irradiation. Calculation performed using EGS4 Monte Carlo.

3.2.1.4. Pencil Beam Dose Distributions

Of special interest in electron beam calculations is the concept of a *pencil beam*, since it is convenient to represent a broad electron beam by a superposition of pencil beams (as shown in §3.2.1.2 above). Pencil beam dose distributions represent the limit as broad-beam

widths are contracted. In homogeneous media, the dose distribution due to a uniform irradiation can be obtained by the superposition of pencil beam dose distributions (of some finite width) calculated in that same media type (Lillicrap *et al.,* 1975; Hogstrom *et al.,* 1981). This method is exploited in the calculations presented in Chapter 5. Pencil beam dose calculation algorithms (discussed briefly in §3.3.1) also employ such a superposition, with depth doses forced to agree with experimentally obtained ones, and pencil beam dose distributions modified to account for inhomogeneities in the irradiated medium.

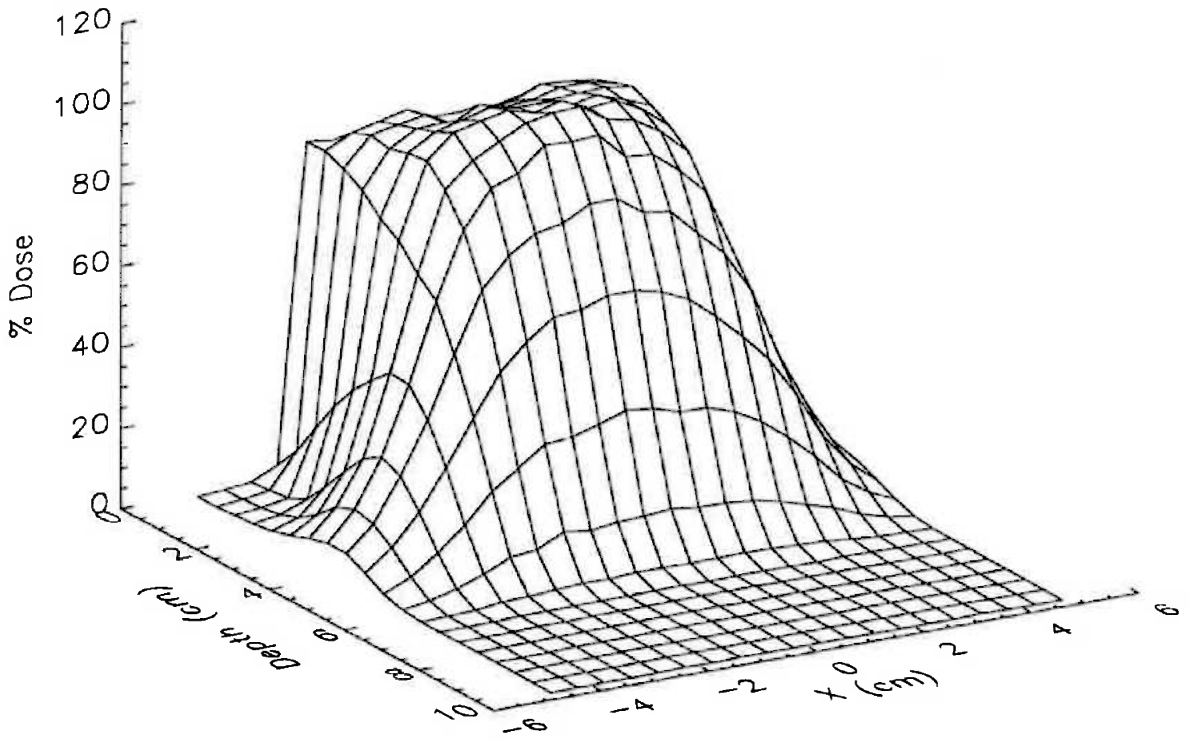

Figure 3-8: Dose distribution of Figure 3-7 shown as a surface plot.

Pencil beam dose distributions represent the dose deposited by the pencil beam normalised to some parameter such as incident energy fluence. In homogeneous media, pencil beam dose distributions are equivalent to energy deposition distributions (and so such distributions are often called *energy deposition kernels*; Mackie, 1987; Altschuler *et al.,* 1992).

Figure 3-9a) shows a typical energy deposition kernel (contour plot of relative energy deposition) for a 12 MeV 2 mm wide pencil beam of electrons incident on water, calculated using EGS4 Monte Carlo with the usercode RTPCYL (see §2.2.3.1). Figure 3-9b) shows some of the electron tracks which led to this kernel. Note how electron scattering in the water leads to increased spreading of the electron fluence distribution with distance from the point of incidence.

a)

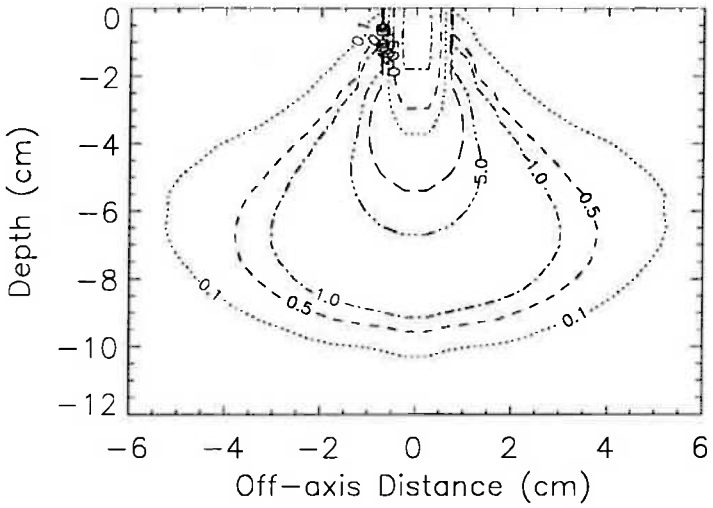

b)

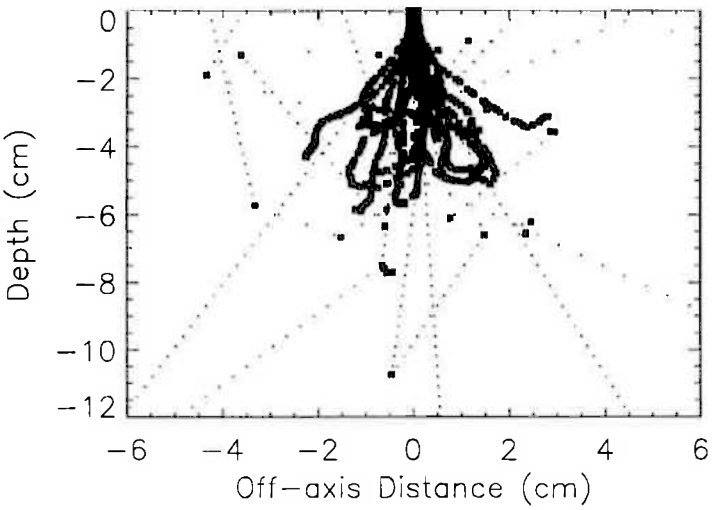

Figure 3-9: a) 12 MeV pencil beam (2mm wide) dose distribution in water, and b) plot of electron (squares) and photon (dots) tracks recorded in generating such a kernel.

3.2.2. Current Clinical Application

With the range of possible radiation treatments available now for cancer treatment, a variety of dose deposition characteristics are available for exploitation. Electron beams are more suitable for some treatment situations than are other modalities. This is due to the particular dose deposition characteristics and ease of production of electron beams. Examples of situations where electron beams are currently used, and the properties of these beams that are optimised for such treatments, are examined below.

3.2.2.1. Clinical Applications of Electron Beams

As shown above, electron beams have a rapid dose fall-off region past d_{max}. The dose distribution due to a megavoltage photon beam however has a relatively gradual fall-off region. This difference can be exploited in treatment by using electron beams to treat tumours at shallow depth, with the biological effectiveness of electrons being equal to that of megavoltage photons (Williams and Hendry, 1978). Megavoltage photon beams are the modality of choice for deep-seated tumours.

The rapid dose fall-off for electron beams allows administration of a high dose to a region of tissue near to the surface, whilst sparing normal tissues which underly the target region. This attribute, combined with the ability to collimate beams to specific shapes at the surface, means that electrons are used for treating many superficial and shallow (<5cm deep) lesions (du V. Tapley, 1980; Brahme, 1982; Klevenhagen, 1985; Shiu *et al.,* 1992). Electron beams have an advantage over superficial photon beams (energies < 300keV) in that photons in this energy range have a high cross section for photoelectric absorption in bone, resulting in high bone doses near to the irradiated surface and increased chances of complication. The absorption of electrons is dominantly controlled by electron density which is similar for bone and other tissues so that the bone-dose enhancement isn't seen for electron treatments (Klevenhagen, 1985).

These properties of electron beams recommend them for use in treatment of most surface and shallow tumours, cancers of the head and neck, salivary glands and upper respiratory tract (Fletcher, 1980; Bomford *et al.,* 1993). Electron treatments are often combined with photon treatments to take advantage of the dose distributions of both, providing *boost* dose to the target region (Fletcher, 1980; M^{c}Naney *et al.,* 1983; Karlsson and Zackrisson, 1993). Electron beams are often used in this capacity for breast or general chest treatments, including post-mastectomy chest wall irradiation (Bomford *et al.,* 1993). The surface dose enhancement of electron beams means they are often used in treatment of mycosis fungoides (Bomford *et al.,* 1993), possibly in total skin irradiation at extended SSD (source to surface distance). The lateral extension of a superficial or subcutaneous lesion can be followed around a curved surface using an arced electron field technique (Leavitt *et al.,* 1985; Hogstrom *et al.,* 1989).

A major deficiency with electron beams is, if a subcutaneous lesion to be treated below healthy tissue (ie., skin), then the deposition of energy from the surface leads to undesired dose deposition within skin layers, surface doses increasing with beam energy (Boone *et al.,* 1965; du V Tapley., 1980). This effect can result in skin reactions such as erythema. Another drawback is the perturbations to the dose distribution which occur whenever tissue inhomogeneities are encountered, particularly air cavities. This is of significant concern for chest irradiations due to the location of the lungs (Boone *et al.,* 1965, 1967; Almond *et al.,* 1967; du V. Tapley, 1980; Klevenhagen, 1985). For accurate prediction of electron dose distributions in the presence of tissue heterogeneities, dose calculation algorithms must be used which can account for the effect of such heterogeneities on electron transport and resulting dose distributions (see §3.3).

3.2.2.2. Optimal Characteristics for Current Applications

Marbach and Almond (1981) have examined in detail the optimal characteristics of static electron beams for therapy purposes. They discuss how beam characteristics such as energy and angle affect the shape of the depth dose curve and flatness of an electron beam. Such characteristics are affected by the general arrangement of the treatment head of the treatment machine including the scattering foil and collimation systems (ICRU, 1984;

Klevenhagen, 1985). These effects were discussed previously in §3.1. Whereas Marbach and Almond (1981) discuss the benefits of having a normally-incident monoenergetic beam due to the maximum steepness in the depth dose fall-off obtained, this does not necessarily lead to the best dose distribution for all electron beam applications.

Alasti and Galbraith (1995) examine the situation where a uniform dose is required from the patient surface to some defined depth. If a monoenergetic beam with a narrow angular spread is used, then the high-dose uniform region of the dose distribution covers a narrow useable region of the dose distribution in the depth direction (Alasti and Galbraith, 1995). They have thus examined techniques for achieving dose uniformity from the surface, as have many other investigations including those aiming at achieving a desired dose distribution over a specified depth region (eg., Brahme and Svensson, 1979; Galbraith and Rawlinson, 1984; Lambert *et al.,* 1985; Leavitt *et al.,* 1990; Alasti and Galbraith, 1991) including the use of *bolus* material (White, 1978; Archimbeau *et al.,* 1981; Haselow *et al.,* 1982; Johns and Cunningham, 1983; Galbraith and Rawlinson, 1984; Moyer *et al.,* 1986; Low *et al.,* 1992, 1995; Antolak *et al.,* 1996).

Beam modification can be used to create a low-energy oblique component for boosting surface doses. Alasti and Galbraith (1995) used a high-atomic number wire mesh above the patient's surface to generate low-energy oblique electrons. They developed a method for optimising the parameters (thickness, grid dimensions etc) of the mesh for obtaining a desired distribution. Examples of the modifications to depth dose curves they obtained are shown in Figure 3-10.

Energy modulation of electron beams, as well as combining low-energy photons with electron beams (Lambert *et al.,* 1985), allows partial modulation of the depth of penetration of the high-energy dose region (Leavitt *et al.,* 1990). If combined with spatial intensity-modulation of the beam, a high degree of dose *conformity* can be achieved, as investigated theoretically by Lief *et al.* (1996) and Hyödynmaa *et al.* (1996) and discussed in §5.2.1. A treatment is considered to be conformal when the high dose region spatially matches the target volume, with a low doses existing elsewhere. The concept of conformal techniques is covered in greater detail in Chapter 5.

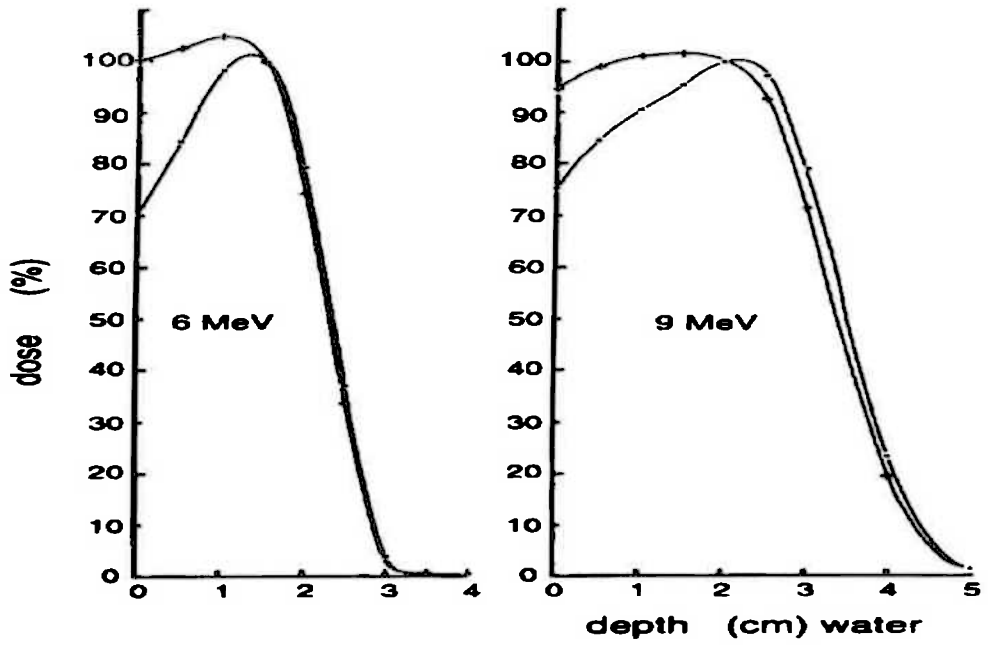

Figure 3-10: Central axis depth dose curves for a 10x10 cm^2 Clinac 2100C electron beam in water, with (ticks) and without (dots) a wire mesh bolus present. The obliquity and lower energy of mesh-scattered electrons raises the dose at shallow depth. Figure from Alasti and Galbraith (1995).

3.2.3. Potential Application

In the discussion in §3.2.2.2 above, it was assumed that restriction in dose delivery is to beams from accelerators with specific energy and angular characteristics which can only be modified using external modifiers, which has been the situation for several decades. With the advent of treatment machines with greater numbers of degrees of freedom such as scanning beam machines (see §3.1.2), as well as computing techniques for efficiently optimising the degrees of freedom available in treatment delivery, the possibilities are arising for tailoring dose distributions to the desired distributions, or the to biological characteristics of patient tissues. With currently available techniques, the potential of electron beams for radiotherapy are optimised when consideration is made of

- electron energy and energy (including spatial and angular) distribution
- the orientation, size, shape, and relative intensity of beams
- combinations with other beam modalities

- the biological response of patient tissues
- the application of external beam modifiers, collimation, bolus, and their various parameters
- potential variance in all applicable parameters.

Chapter 5 of this thesis examines the situation where there is no restriction on the energy and angular distribution of an electron beam for tailoring an electron beam dose distribution to a specified desired dose distribution. The process of using a desired dose distribution or some constrained effect (such as optimising the probability of complication-free tumour control) as the basis for controlling treatment parameters has been termed *inverse treatment planning* by many authors (eg., Censor *et al.*, 1988a,b; Brahme *et al.*, 1990; Barth, 1990; Lind 1990), and shall be discussed in detail in Chapter 5.

3.3. Electron Beam Dose Calculation

The utility of electron beams for therapy is increased when dose distributions due to specific treatment arrangements can be calculated. This allows prediction of treatment response, and accurate dose prescription.

3.3.1. Dose Calculation Algorithms

With recent advances in computer capabilities, the development of accurate electron beam dose calculation techniques has been rapid. Whereas detailed descriptions of the large range of available algorithms shall not be given here, reviews can be found in Keall and Hoban (1996a) and Keall (1996). Of relevance to the investigations presented in this thesis are those techniques that can take advantage of detailed knowledge of the treatment beam. Such methods allow greater accuracy to be achieved by using realistic beam descriptions, and these techniques shall now be briefly discussed.

3.3.1.1. Pencil Beam Methods

Pencil beam methods use scattering theory results to model the energy deposition due to finite-sized pencil beams, and to superpose the distributions due to multiple pencil beams to simulate the broad beam. Many models have centred on the Gaussian approximation for the variation in the pencil beam off-axis dose profile with depth (Kawachi, 1975; Hogstrom *et al.,* 1981; Werner *et al.,* 1982; Bruinvis *et al.,* 1983; Hogstrom *et al.,* 1984, 1989). This is a small-angle approximation, and models which account for large-angle scattering using a sum of several Gaussian distributions have been developed (Brahme *et al.,* 1981; Lax and Brahme, 1985).

Basic two-dimensional pencil beam algorithms (eg., Hogstrom *et al.,* 1981) model the beam as *strip beams* (superposed arrays of line sources) and assume infinite lateral extent of tissue inhomogeneities. Three-dimensional models have been developed to overcome this effect (Kooy and Rashid, 1989; Mah *et al.,* 1989; Starkschall *et al.,* 1991), though both two-dimensional and three-dimensional methods have been shown to be prone to inaccuracy in not accounting correctly for the effects of inhomogeneities (Cygler *et al.,* 1987; Mah *et al.,* 1989; Starkschall *et al.,* 1991). The perturbation of pencil beam dose distributions due to inhomogeneities is accounted for by considering the variation in mass scattering power to a calculation point by a single definition of the pencil beam dose distribution. Techniques have been developed which use multiple redefinitions of the pencil beam dose distributions (*pencil beam redefinition* or the *moments method*; Storchi and Huizenga, 1985; Shiu and Hogstrom, 1991; M^{c}Lellan *et al.,* 1992). This allows the full three-dimensional effect of tissue heterogeneities to be accounted for. Similarly, the lateral extensions of heterogeneities have been accounted for in the *multi-ray* model (Perry and Holt, 1980; Yu *et al.,* 1988), which evaluates the most probable path of electrons to the calculation point and recognises the variation in scattering power to that point.

Two-dimensional pencil beam algorithms use a basic description of the electron beam as input (see §4.1.2.1). The mean incidence angle at any point is determined by projection to a virtual source position, and the angular distribution of electrons defined by a specified standard deviation at the applicator face projected to the patient surface (Hogstrom *et al.,*

1981). The variation of electron fluence across the beam is accounted for in a variation of the weighting of strip (2D) or point (3D) beams. Electron spectra and variations in spectra with depth may be accounted for in redefinition models.

3.3.1.2. Superposition

Superposition models for electron beam dose calculation (Mackie, 1987; Bloch, 1988; Altschuler *et al.,* 1992) use elementary energy deposition kernels (see §3.2.1.4) as the basis for forming the dose distribution due to a broad beam. Using the energy and angular spectrum of electrons in a beam, energy deposition kernels can be generated and then summed in a fluence-weighted superposition (a *convolution* if the energy and angular spectra and kernels are invariant) to yield the broad beam distribution. In this way, the energy and angular spectra of a beam can be included in the dose calculation, though they are usually assumed constant across the field.

The superposition technique uses a *rectilinear scaling* approximation (Woo and Cunningham, 1990) for the effect of tissue density changes which will lead to discrepancies due to the actual form of density variations throughout the patient (Woo and Cunningham, 1987, 1988).

3.3.1.3. Phase Space Evolution

It is possible to consider a system (in this case, a patient irradiated by an electron beam) as a time-dependent set of states, each defined by a set of parameters. In *phase space evolution* methods for electron beam dose calculation (Cordaro and Zucker, 1971; Huizenga and Storchi, 1989; Morawska-Kaczynska and Huizenga, 1992; Janssen *et al.,* 1994; Korevaar *et al.,* 1995), positions (P_i), energies (E_j) and directions (Ω_k) of electrons in an irradiated patient are discretised (via i,j,k) throughout the patient via a nodal representation of the electron *phase space* (the position, direction and energy of all electrons in the system). Each node of the phase space (P_i, E_j, Ω_k) is called a *phasel*, and the content of each phasel is the number of electrons in the particular position-energy-

direction node. The method calculates dose by starting with an input beam (defining the state of all phasels at the surface), and considering the progression of states of phasels due to particle transport [redistributing the contents of phasels according to particle transport distribution functions (Huizenga and Storchi, 1989; Morawska-Kaczynska and Huizenga, 1992)], accounting for tissue heterogeneities according to tissues local to each phasel, until all electrons have either stopped in or exited the phantom. The time dependence of the system has been removed by using the total energy of a particular phasel as the importance of transporting electrons from that node, and by assuming the independence of all subsequent phasel redistributions (Janssen *et al.,* 1994).

By explicitly considering the initial state of electrons in the system, the phase space evolution model is able to account for the complex variations in electron energies and angles across the radiation beam (Korevaar *et al.,* 1995). The model has been found to accurately predict patient dose distributions (Janssen *et al.,* 1994).

3.3.1.4. Monte Carlo

Provided that the mathematical foundations of transport methods used are accurate and that the composition of a patient and properties of radiation particles can be efficiently described, Monte Carlo methods (see §2.2) may be used to accurately determine patient dose distributions (Short *et al.,* 1986; Manfredotti *et al.,* 1990; Andreo, 1991; Murray, 1991; Kawrakow *et al.,* 1996; Hartmann-Siantar *et al.,* 1996). The explicit microscopic transport models employed by most Monte Carlo methods imply that such methods should be as accurate as possible within the constraints of statistical accuracy, and for this reason they have been used as the benchmark for many other electron transport approaches (eg., Mackie, 1987; Jette and Walker, 1992; Janssen *et al.,* 1994; Neuenschwander *et al.,* 1995; Jette, 1996). Furthermore, Monte Carlo methods can account for all detailed characteristics of incident particles in the beam and in fact, it is possible to include modelling of treatment head components simultaneously with dose calculation in Monte Carlo based studies (eg., Manfredotti *et al.,* 1990).

Unfortunately, although being accurate, Monte Carlo methods tend to be extremely time consuming due to the relative microscopic nature of their transport calculations and as such, with contemporary computing capabilities, are not suitable for routine clinical use. In order to exploit the accuracy of Monte Carlo methods whilst endeavouring to achieve reasonable computation times, the macroscopic implementations of Monte Carlo methods detailed in the next section have been developed.

3.3.1.5. Macroscopic Monte Carlo Methods

Macroscopic Monte Carlo methods rely on using locally calculated particle transport distributions to determine global dose distributions. Macro Monte Carlo (MMC; Neuenschwander and Born, 1992; Neuenschwander *et al.,* 1995; Svatos *et al.,* 1996) transports individual particles through macroscopic steps within materials using probability distribution functions (PDFs) pre-calculated with EGS4 Monte Carlo. These distributions give the probability of an electron (or photon) exiting a sphere (with some small radius, say between 0.05 and 0.3 cm - called a *kugel*) at some location on its surface relative to the incident direction. Each electron step involves sampling a kugel PDF, and subsequent steps are from kugel to kugel across the patient. Kugel dimensions are such that this method is much faster than conventional Monte Carlo using microscopic electron steps. Varying kugel size with location relative to heterogeneities allows variation in step size, with larger steps occurring away from heterogeneity boundaries allowing more rapid transport. Energy deposition can be approximated via a continuous slowing down approximation within each kugel, and PDFs can also include the probabilities for generation of secondary particles.

Since MMC is basically a Monte Carlo technique, it can employ full characterisation of the incident electron beam as input to dose calculation. Its accuracy is only limited by the finite size of kugels (governing the possible resolution) and the accuracy of PDFs.

3.3.1.6. Superposition Based Monte Carlo Methods

The Super-Monte Carlo algorithm (SMC - superposition using Monte Carlo track kernels) was developed by Keall and Hoban (1996c,d; Keall, 1996) for efficient electron (or photon) beam dose calculation by combining the accuracy of Monte Carlo transport methods with the efficiency of superposition techniques. Instead of using energy deposition kernels as the elementary dose distribution in the superposition (see §3.3.1.2 above), SMC uses kernels composed of the *tracks* of electrons (location and energy deposition characteristics of each interaction) due to a pencil beam incident on a water phantom as calculated by EGS4 Monte Carlo. The SMC method considers all pencil beams composing an incident beam, and transports each particle in each kernel through the irradiated medium by performing the atomic number and mass density scaling (relative to water) of electron track step sizes, scattering angles, energy depositions and radiative potential of all such particles as they traverse the medium, using the pre-calculated tracks. By replicating electron tracks, SMC dismisses the need for electron step calculations, and doesn't require the large amount of random number sampling necessitated by conventional Monte Carlo techniques.

As with energy deposition kernel-based superposition, SMC accounts for the distribution of incident electron energy and angle in the initial kernel generation, and so similarly assumes uniformity in these distributions across the radiation field. Beam intensity distributions can be accounted for by weighting the kernels according to incident beam fluence.

3.3.2. Requirements for Accurate Dose Calculation

In order to make the best use of the calculational abilities of the above algorithms, they have to be implemented in combination with similar accuracy in the characterisation of the treatment situation. In describing the patient, the contours defining the external patient geometry and geometries of internal structures (target region, sensitive tissues, inhomogeneities) need to be well defined. Such definition can be achieved using imaging

modalities such as CT (providing electron density information) and MRI. Similar accuracy is then required in the physical localisation and positioning of the patient at treatment, as well as in the stability and calibration of the treatment machine.

The characteristics of radiation transport within the patient are also governed by the properties of the radiation beam. Thus, as discussed in §3.2.1, dose distributions are dependent on beam properties, and accurate algorithms must be able to account for this if realistic simulation is to be achieved. These properties include the spatial variation in particle type, energy, direction and fluence when incident on the patient. Many of the algorithms discussed above are capable of including this detailed information.

In addition, the properties of particles in a beam can include their origin in the beam formation system (by particle 'tagging'; see Rogers *et al.,* 1995). Having this knowledge of the properties of a beam allows investigation and optimisation of the beam forming device for the purpose of optimising the resulting dose distributions. The problem of determining the detailed characteristics of an electron beam forms the basis of the research presented in Chapter 4.

4. APPLICATOR SCATTER MODELLING - CURRENT BEAM CHARACTERISTICS

4.1. Modelling the Clinical Beam

Knowledge of the characteristics of an electron beam enables the accuracy of dose calculation algorithms to be realised. Such knowledge also provides insight into why specific dose distributions are obtained, since beam properties govern dose distributions (see §3.2.1). The natural progression is then that we may vary beam formation systems to optimise beam properties and resulting dose distributions (eg., Kassae *et al.*, 1994). Knowledge of beam characteristics also assists in other areas such as dosimetry, where stopping-power ratios may be more accurately determined given energy and angular spectra in electron beams (ICRU 1970; Andreo *et al.*, 1989; Ding *et al.*, 1995). Difficulties arise in beam measurement due to the inadequacy of the various dosimeters in specific measurement situations, due to the effects of response characteristics and physical size (Dawson *et al.*, 1984; Kubsad *et al.*, 1990; Sibata *et al.*, 1991; Ting *et al.*, 1994; Beddar *et al.*, 1994; Deasy *et al.*, 1996). Modelling is thus required for determining unmeasurable beam properties (Heydarian *et al.*, 1996).

4.1.1. Accelerator Design & Effects on Clinical Beam

In the process of electron beam formation, as described in §3.1, a beam is generated with a set of properties which explicitly depend on the detailed characteristics of the accelerator and treatment head design. The beam from the waveguide interacts with the materials of the treatment head and air before reaching the patient, and will thus have undergone scattering and energy loss events, including radiative interactions leading to a photon

contamination component. This leads to a beam which will vary in intensity over space, angle, energy, and radiation type (assuming no macroscopic temporal variation), with these characteristics varying with filter and collimation design.

4.1.1.1. General Effects of Filters & Collimation

Beam characteristics of concern are those which

- affect dose distributions
- describe the effects of beam formation systems
- allow more accurate dosimetry
- cannot readily be measured or are more easily calculated than measured.

These criteria lead to a list of electron beam characteristics, about which information is desired. The list, together with references which deal with the characteristics and their consequences, is given in Table 4-I. These characteristics may be summarised to the sources, energies, angular and spatial distribution, and types of particles in a beam.

Table 4-I: Electron beam characteristics of relevance, together with references concerned with such characteristics.

Beam Characteristic	*Reference*	
Electron beam energy spectrum including spatial and angular variations	Andreo *et al.* (1989) Brahme & Svensson (1976) Deasy *et al.* (1994) Ding and Rogers (1995) Ding *et al.* (1994) Hogstrom *et al.* (1981) Hugtenburg *et al.* (1995) Karlsson *et al.* (1992)	Kassace *et al.* (1994) Keall and Hoban (1994) Korevaar *et al.* (1995) Manfredotti *et al.* (1990) Neuenschwander *et al.* (1995) Rogers *et al.* (1995) Shiu and Hogstrom (1991) Udale-Smith (1992)
Electron beam fluence distribution	Baggarley *et al.* (1994) Biggs *et al.* (1979) Bjärngard *et al.* (1976) Bruinvis *et al.* (1983) Bruinvis and Mathol (1988) Choi *et al.* 1979) Karlsson *et al.* (1992) Kassaee *et al.* (1994)	Korevaar *et al.* (1995) Lax and Brahme (1980) Manfredotti *et al.* (1990) Neuenschwander *et al.* (1995) Shiu and Hogstrom (1991) Udale-Smith (1992) van de Geijn *et al.* (1987) van der Laarse *et al.* (1978)
Electron beam angular distribution	Andreo *et al.* (1989) Ding and Rogers (1995) Hogstrom *et al.* (1981) Keall and Hoban (1994) Korevaar *et al.* (1995) Manfredotti *et al.* (1990)	Mohan *et al.* (1988) Neuenschwander *et al.* (1995) Rogers *et al.* (1995) Sandison and Huda (1988) Udale-Smith (1992)
Photon contamination in electron beams	Klevenhagen (1994) Rogers *et al.* (1995)	Rustgi and Rodgers (1987) Shiu and Hogstrom (1991)

The electron beam immediately after passing through the scattering foil(s) will have undergone scattering and energy loss processes resulting in energy straggling (McLellan *et al.,* 1994) and an angular distribution (Hogstrom *et al.,* 1981; Grussell *et al.,* 1994; Keall and Hoban, 1994). The resulting energy and angular spectra will depend on the detailed geometry of the filters (as described in §3.1.1.2), may not be spatially uniform or symmetric (Grussell *et al.,* 1994), and may lack energy/angle correlation (Andreo and Fransson, 1989). Henceforth, this component of the beam shall be referred to as the *primary* component. The primary component undergoes further interaction with air on its path to the patient, increasing the angular spread of electrons (Keall and Hoban, 1995).

Some particles in the primary component of the beam will interact with the collimation systems being employed, resulting in a *collimator scattered* component of the beam. The relationship between the particles in the primary component of the beam and those in the collimator scattered component depends on the nature of the interactions within the collimators, and the location of the collimators relative to the scattering foils. The latter is of concern since any radiation source at an extended distance from the patient will appear to have a similar angular distribution to the primary beam (similar effective source). At a given off-axis distance, angular spread due to scattering in the sources' (foil's) materials reduces significantly with distance (Keall and Hoban, 1996c). By the time the beam reaches the patient surface, most of the angular spread is due to multiple Coulomb scattering in air (Hogstrom *et al.*, 1981). Thus, secondary collimators (jaws) which are usually much closer to the scattering foils than the patient generate a beam component (by scattering primary beam particles back into the beam) with similar directional characteristics to the primary beam at the patient plane.

Tertiary collimation systems however (eg., applicators or cones) are usually located much closer to the patient plane to ensure accurate beam definition, and scatter from these devices may have widely varying angular characteristics to those of the primary beam, generally providing a more oblique beam component. Electrons and photons scattered from collimation systems to outside the treatment field, or those particles not adequately

collimated, represent leakage radiation from the collimation system (Das *et al.,* 1990; Kassaee *et al.,* 1994; Klein *et al.,* 1995).

The resulting beam (primary and scattered components) will display an energy spectrum which is degraded from the original near-monoenergetic beam from the waveguide, with some spatial intensity distribution, and a spatially varying angular distribution. The major influence of the energy spectrum is to increase the surface dose relative to that from a monoenergetic beam and to broaden the dose fall-off at depths greater then the dose maximum (see §3.2.1.1). The angular variation in the beam will also increase the resulting beam's surface dose due to increased obliquity and a preferential energy deposition at shallower depths relative to normally incident electrons (Bjärngard *et al.,* 1976, van der Laarse *et al.,* 1978; Choi *et al.,* 1979; Marbach and Almond, 1981), as well as provide an SSD dependence of depth dose characteristics (Svensson, 1971; Kassaee *et al.,* 1994; §3.2.1.1). The angular distribution will also influence penumbral definition (as will applicator scattered electrons and contaminant photons), whereas spatial intensity variations will influence beam flatness (Kassaee *et al.,* 1994; see §3.2 for a thorough discussion). Any effects of energy and angular spectral variations due to collimation systems on dose distributions must be considered in light of the general effects of beam shape on machine output, and the influence of the extended source represented by the scattering foils (Bjärngard *et al.,* 1976; Choi *et al.,* 1979; Biggs *et al.,* 1979; Nair *et al.,* 1983).

Two extensive general investigations of the effects of electron beam collimation have been by van der Laarse *et al.* (1978) and Lax and Brahme (1980). van der Laarse *et al.* (1978) measured beam profiles defined by parallel-walled applicators, and showed how electrons scattered off such walls lead to peaks in dose profiles near field edges which can be utilised for achieving beam flatness.

Lax and Brahme (1980) measured the characteristics of collimator scattering in terms of absorbed dose distributions due to scatter from materials of differing composition (density / atomic number) and examined how the lateral motion of electrons in collimators and the irradiated medium affect dose distributions. Their theoretical treatment considered the

dependence of scatter yields on the material characteristics, and found that $\overline{D}_e$, the mean absorbed dose to a phantom below the collimator edge due to electrons scattered from the edge relative to the absorbed dose due to the open field, is approximated by

$$\overline{D}_e \propto \frac{E_p^{3/2} X_0^{1/2} \varrho^{-1}}{E_p^2 + E_p X_0 S_{col} + E_s^2} \tag{4.1}$$

where E_p is the most probable electron energy, X_0 is the radiation length according to Rossi (1952), ϱ the density of and S_{col} the linear collisional stopping power of the collimator material, and $E_s = 21.2$ MeV (Lax and Brahme, 1980). This expression indicates that the resulting scatter dose will be inversely proportional to the density of collimator material (ignoring bremsstrahlung contributions). The expression also implies a weak dependence on incident electron energy. Lax and Brahme (1980) also deduced an approximate expression for the mean energy of scattered electrons, $\overline{\overline{E}}$, with initial mean energy $\overline{E}_0$:

$$\overline{\overline{E}} \approx 0.4\overline{E}_0 \left[1 + \frac{1}{4} \left(\frac{\overline{\theta_0^2}}{TR_p} \right)^2 \right]. \tag{4.2}$$

Here, T is the linear scattering power of the collimator material, R_p the practical electron range, and $\overline{\theta_0^2}$ is the mean square angle of the incident beam. As Lax and Brahme point out, this expression indicates that, when the initial electron angular spread is small, the mean energy of laterally scattered electrons is approximately 40% that of the mean energy of incident electrons, independent of the actual collimator material.

The photon contamination component of an electron beam will appear in dose distributions as a dose *tail* beneath the maximum range of depth of the highest energy electrons, and in increasing dose throughout the irradiated medium by a few percent. This photon component has been found by Rustgi and Rodgers (1987) to dominate photon generation in the (water equivalent) medium being irradiated and to depend on beam quality. The relatively high atomic numbers of treatment head and collimation materials makes them efficient bremsstrahlung generators, though optimisation of clinical electron beams requires minimisation of photon generation with acceptable levels of electron fluence control (Purdy *et al.*, 1980; Rustgi and Rodgers, 1987; Klein *et al.*, 1995).

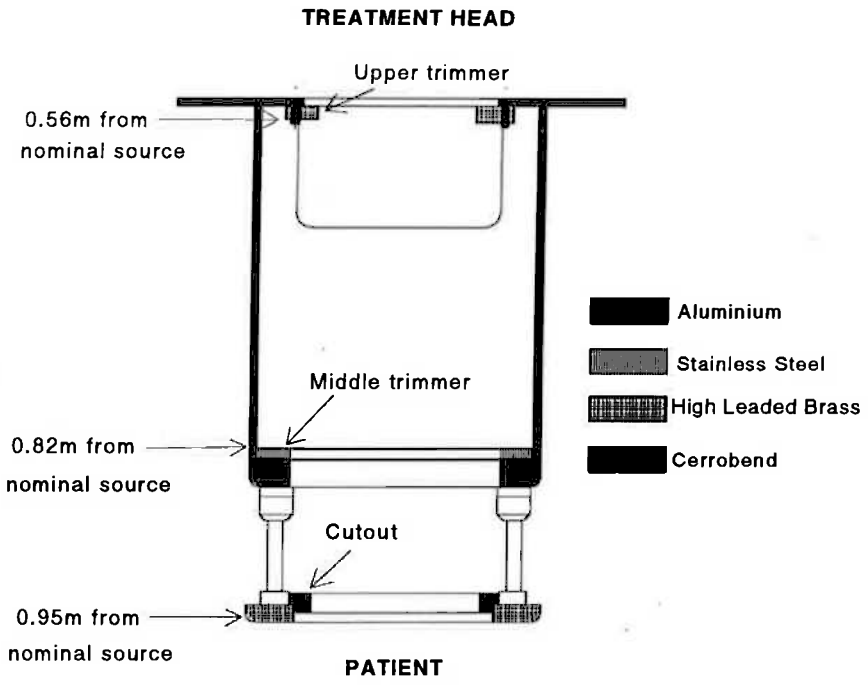

Figure 4-1: Design of the KD2 electron applicators showing trimmer locations and materials. Construction details courtesy of Siemens Corp.

4.1.1.2. KD2 Specific Design and Observed Effects of Applicator Scatter

The accelerator modelled in the investigation presented in §§4.2 - 4.4 is a Mevatron KD2 dual modality device manufactured by the Siemens Corporation (Siemens Medical Systems, Concord, California USA). It is capable of delivering electron beams with nominal energies of 6, 9, 12, 15, 18 and 21 MeV. A dual scattering foil system is used for electron beam formation from the pencil beam from the waveguide. Foil materials and thicknesses[‡] are shown in Table 4-II, with foils approximated as slabs[§]. Two orthogonal

---

[‡] Foil materials and thicknesses are selected to give similar lateral electron spread at isocentre (1 m from the second foil).

[§] The second scattering foil is actually tiered, though was approximated as a slab with the same total thickness.

pairs of secondary collimators (photon jaws) are positioned at large field sizes when the accelerator is in electron mode to reduce contamination.

Table 4-II: Scattering foil materials and thicknesses for KD2 accelerator

Nominal Beam Energy (MeV)	*Material, 1st Foil*[†]	*Thickness, 1st Foil (mm)*
6	None	-
9	Stainless Steel	0.13
12	Gold	0.05
15	Gold	0.15
18	Gold	0.20
21	Gold	0.20

[†]*Second foil 0.81mm of aluminium for all energies.*

The applicators used to achieve beam definition with the Siemens KD2 are constructed as shown in Figure 4-1. Three principal trimming plates composed of aluminium (ϱ = 7 gcm^{-3}), stainless steel (Fe, 72%; Cr, 17%; Mn, 6.5%; Ni, 4.5%; ϱ = 7.81 gcm^{-3}) and high-leaded brass (Cu, 62%; Zn, 35.5%; Pb, 2.5%; ϱ = 8.5 gcm^{-3}) are arranged to intercept particles at field edges, joined by aluminium side panels. Three principle rectangular applicators (as employed in this study) are used for obtaining field sizes at isocentre of 10x10, 15x15, and 20x20 cm^2. Cutouts of a low melting point alloy (LMPA), *cerrobend* (Bi, 52.5%; Sn, 15.5%; Pb, 32%; $\varrho \approx$ 10.8 gcm^{-3}), are placed on the lower trimmer. These are patient-specific apertures, manufactured to provide a field shape which conforms (in two dimensions) to the target area, and shields sensitive regions. Irradiation is usually performed with the patient surface at isocentre, approximately 1 m from the first scattering foil and 50 mm from the front face of the applicator. The small distance from the applicator to the patient reduces the effects of particles scattered from the applicator materials, and minimises patient discomfort (Choi *et al.*, 1979). The trimmer thicknesses are; upper trimmer, 9.5 mm; middle trimmer, 33 mm (6.5 mm stainless steel over 26.5 mm aluminium); cutouts (lower trimmer), 12 mm.

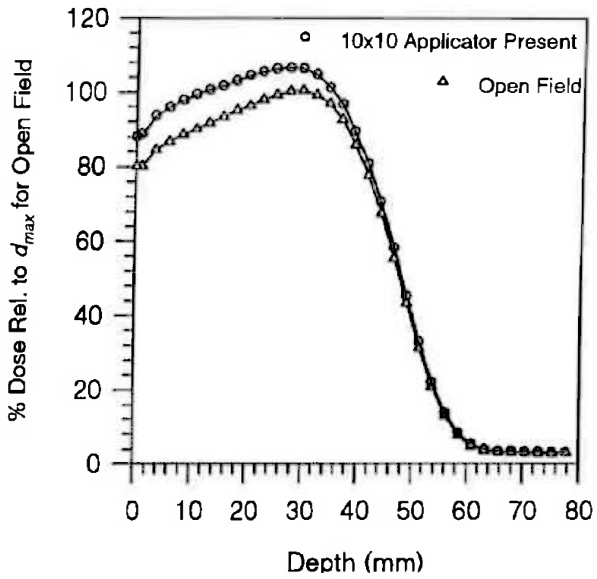

Figure 4-2: Comparison of depth dose curves measured on the Siemens KD2 accelerator with and without an applicator present. The beam energy is 12 MeV. Particles scattered from the applicator assembly increase the machine output relative to the open field, and move d_{max} closer to the surface.

Particles in the primary beam for this machine may interact with these applicators to generate another beam component which shall be called *applicator scatter*. Direct evidence for such scatter can be seen in variations of machine output and dose distributions when an applicator is used compared to the open beam situation. Figure 4-2 compares central-axis depth dose curves measured with and without an applicator present for a 12 MeV beam using the same normalisation for the detector (Scanditronix p-type silicon diode). The added component to the depth dose curve from applicator scatter is obtained when the difference between these two curves is obtained. Such a result is shown in Figure 4-3 for a 12 MeV beam, and several different sized rectangular cutouts. The consistent increase in surface dose due to the applicator indicates the presence of particles which are lower in energy and more obliquely incident then primary beam particles. The apparent negative contribution seen in the 4x4 cm^2 case is due to electronic disequilibrium at central axis of the 12 MeV primary and scattered beam particles.

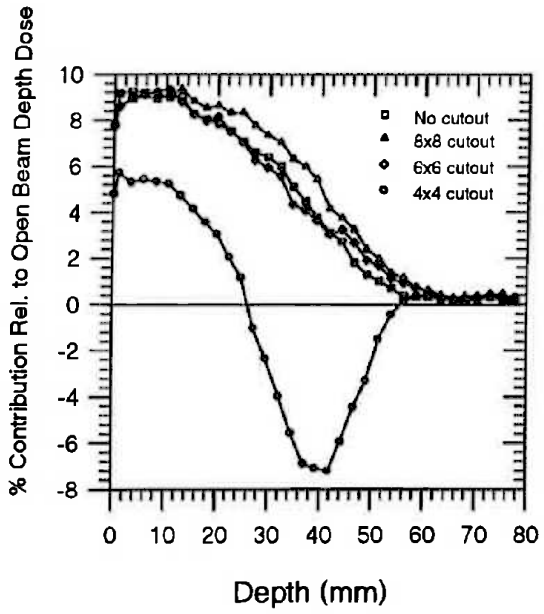

Figure 4-3: Central axis depth dose contributions due to applicator scattered particles (relative to open beam surface dose) as measured for a 12 MeV Siemens KD2 accelerator with a series of cutouts in a 10x10 cm^2 applicator. The negative component in the 4x4 cm^2 case is due to lateral electronic disequilibrium at central-axis.

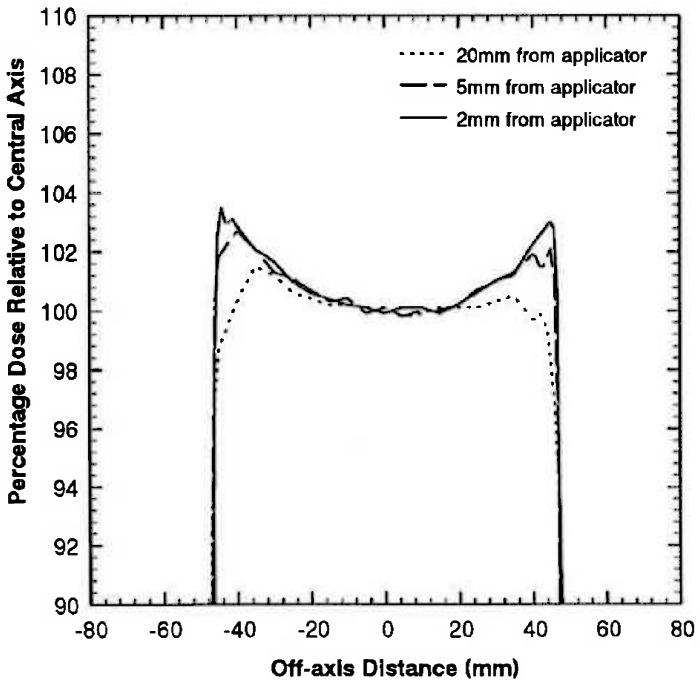

Figure 4-4: Variation of dose profile with distance from the face of a 10x10 cm^2 applicator on the KD2 accelerator with no insert present. Beam energy is 12 MeV.

Figure 4-4 shows a series of profiles measured in a 10x10 cm^2 12 MeV field (no cutout present), at the surface of a water phantom which is at three different distances from the lower trimming plate. The decrease in relative size of field edge 'horns' indicates that the lower trimmer acts as a source of particles which rapidly spread out from the trimmer's edge.

The interaction of the middle and lower trimming plates with primary beam particles is evident in the curve of Figure 4-5. In this figure, the ionisation present in a diode detector scanned vertically down through the applicator during irradiation has been measured. The perturbations seen on top of the approximate inverse-square falloff occur at the locations of the middle and lower trimmers due to particles scattered back into the primary beam from these plates.

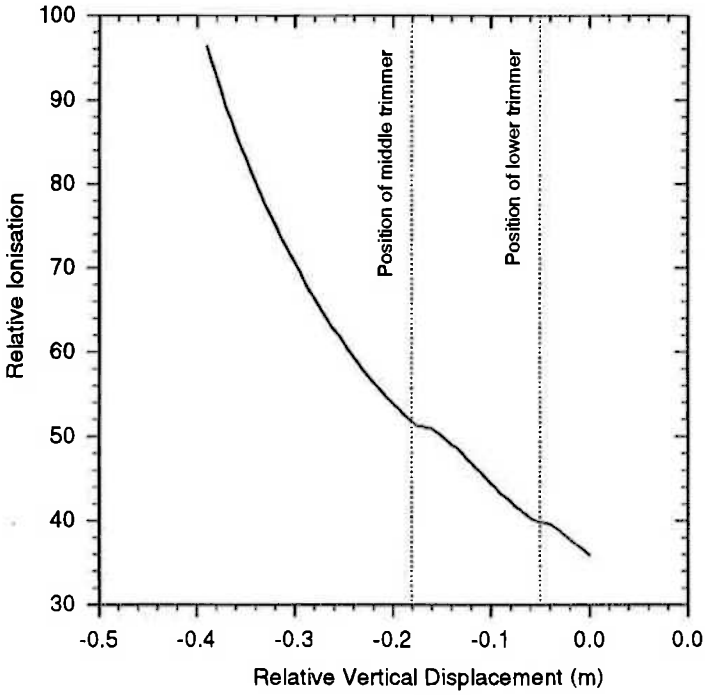

Figure 4-5: Scan in air with a diode detector vertically down through the centre of a 10x10 cm^2 applicator on the KD2 accelerator. The perturbations at each trimmer location are due to scattered electrons reaching the centre of the field.

The properties of the radiation scatter displayed in the above effects will be a result of the complex interactions occurring; from primary beam scattering (in the scattering foils) to subsequent interactions with applicator components. These properties will display complexities in energy and angular spectra, and spatial variation in intensity - complexities which will vary with the applicator used, the patient-specific cutout employed, and the beam energy being used. To determine the properties of applicator scatter for the treatment machine considered, a beam model had to be developed which would be comprehensive enough to yield detailed information of the characteristics of electron beam particles, yet efficient enough to be applied quickly for practical clinical use. In order to place the developed model in the perspective of previous and contemporary beam models, other electron beam simulation techniques shall first be reviewed.

4.1.2. Electron Beam Modelling

4.1.2.1. Analytical / Empirical Models

Analytical descriptions of electron beams are limited since (as discussed in §2.1.2.4) electrons undergo multiple scattering when interacting with media, and the resulting electron transport is much more difficult to calculate than photon transport. Secondary particle production in electron beams (including bremsstrahlung production) is also very difficult to describe analytically, and, whereas secondary filters and collimators have little effect in photon beams (Ahnesjö, 1995), they act as significant sources of scatter in electron beams.

The most convenient analytical approach is to use the multiple scattering small angle approximations of Fermi and Eyges (Eyges, 1948; see Jette *et al.*, 1983 and Zheng-Ming and Brahme, 1993 for good descriptions of this theory), resulting in a Gaussian description of electron spread as discussed in §2.1.2.4. Inclusion of large angle scattering is being considered (Jette, 1995), and may yet be included in analytical electron beam models. Several approaches have been made using the Gaussian approximation for calculating

electron beam dose distributions (Hogstrom, 1981; Bruinvis *et al.,* 1983; Bruinvis and Mathol, 1988; Shiu and Hogstrom, 1991). The beam properties required for such models are the effective (virtual) source distance [or the mean angular divergence $(\bar{\theta}_x, \bar{\theta}_y)$ at some position], angular standard deviation at the patient surface or applicator face $(\sigma_{\theta_x}, \sigma_{\theta_y})$, and the most probable electron energy $(E_{p,0})$ prior to incidence of the beam on the patient. The angular quantities are illustrated in Figure 4-6. [The models of Bruinvis *et al.* (1983; Bruinvis and Mathol, 1988) also require quantification of applicator scatter contributions as described below]. Such characteristics may be obtained from measurements of dose distributions, provided several assumptions are overcome such as uniformity of angular spread and energy spectrum across the full field.

Empirical descriptions of electron beams are routinely used in conjunction with pencil beam calculation methods (Hogstrom, 1995). Further redefinition of electron spread within the patient is based on these initial beam properties, which may be assumed spatially invariant for simplicity (a reasonable approximation in most cases) with uniform beam intensity (Hogstrom *et al.,* 1981). The most probable electron energy can be approximated from measured depth dose data (ICRU, 1984; Hogstrom *et al.,* 1989; Shiu and Hogstrom, 1991; Khan *et al.*, 1991). The angular divergence is calculable using results from Fermi-Eyges theory as previously discussed (see §2.1.2.4), and can be used to obtain approximations for the virtual source position. Several methods for determining the virtual source position are available allowing inverse-square approximation of electron fluence variation with distance (Hogstrom *et al.,* 1981, 1983; Meyer *et al.,* 1984; Khan *et al.,* 1991; Baggarley *et al.*, 1994). The angular standard deviation can also be determined using Fermi-Eyges theory as previously discussed (see §2.1.2.4), and is determinable from measured beam profiles (Mohan *et al.,* 1988). The value of σ_{θ_x} (arbitrarily preferring the x direction) is primarily due to multiple scattering in air (Hogstrom, 1995; Keall and Hoban, 1996c) and, ignoring additional collimation scatter, has been shown (Hogstrom *et al.,* 1981; Keall, 1994) to be given by

$$\sigma_{\theta_x} \approx 0.391 \cdot slope_{10}^{90}(L) \tag{4.3}$$

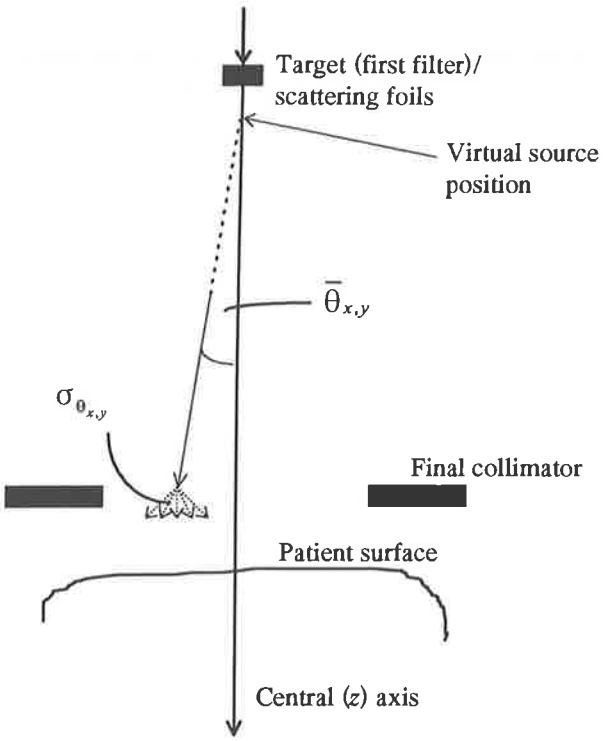

Figure 4-6: Illustration of the angular quantities in an empirical electron beam model.

where $slope_{10}^{90}$ is the slope of the curve produced when the 90% - 10% distance in the measured penumbra is plotted against distance below the final collimator (L).

In terms of the effects of electron beam field shaping devices, including applicators, empirical models must be able to account for the effects on machine output of the change in field size (due to effects on electronic equilibrium) and of scatter from the field defining frames. Field size effects often enter empirical calculations as multiplicative output factors, which are unnecessary in numerical dose calculation algorithms due to explicit calculation of electron transport.

Mills *et al.* (1982) justified a method for obtaining output factors for rectangular fields from the square of the product of the output factors for square fields with edge lengths corresponding to those of the rectangular field. However, contributions due to scatter off collimators was only accounted for in measurements of factors for the square fields and may not have been accurately accounted for. A similar method was examined by Kurup *et al.* (1995) for irregularly shaped fields.

McParland (1989) presented a model for obtaining output factors for irregularly shaped fields which involved multiplying a discrete pencil-beam-calculated weighting factor by a reference output factor for a combination of equivalent regular fields. A multiplicative constant was then applied to account for collimation scatter though, in McParland's investigation, this factor was found to be approximately unity for the accelerator employed. Neither of these investigations evaluated the complex variations across the fields of interest due to the (in general) asymmetric nature of collimator scattering or its influence on dose distributions.

Bruinvis *et al.* (1983; Bruinvis and Mathol, 1988) obtained a linear description of measured central axis depth dose contributions due to applicator scatter for a series of circular fields and then used a sector integration to determine contributions for arbitrary field shapes, combined with a pencil beam algorithm to determine output factor variations due to disequilibrium effects. They reported clinically reasonable results over a broad energy range for depth dose curves though did not discuss predictions for profile variations.

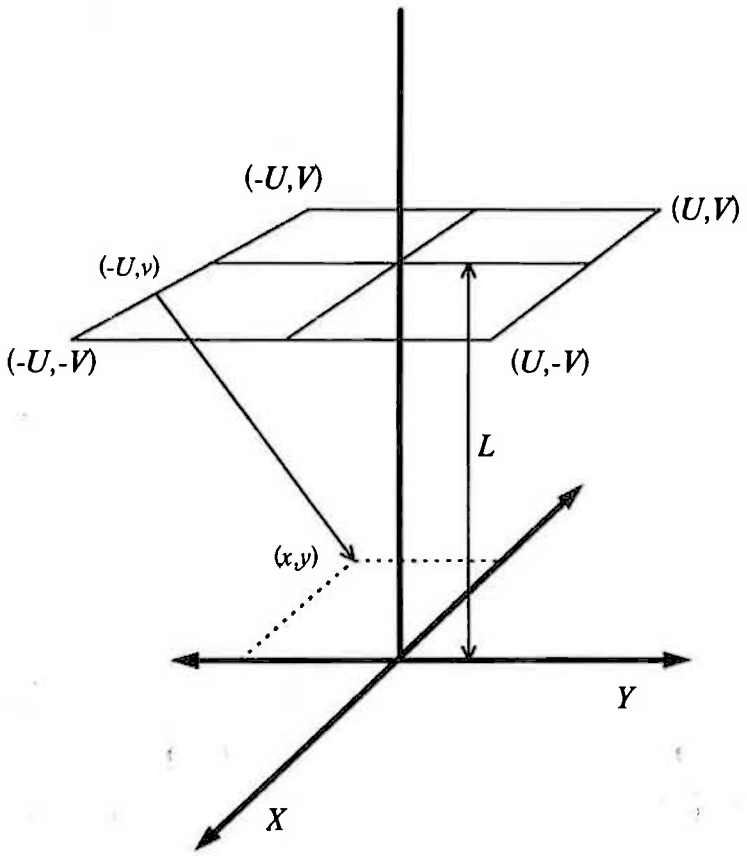

Figure 4-7: Calculating regular scatter from a square rim (adapted from van de Geijn *et al.*, 1987).

van de Geijn *et al.* (1987) modelled applicator rims by considering them as uniform isotropically emitting extended sources. A regular (square) applicator as shown diagrammatically in Figure 4-7, consists of four line sources with electron scatter fluence falling with the inverse of the square of the distance to the rim. As in Figure 4-7, consider an element dv of the edge between $(-U,-V)$ and $(-U,V)$ at $(-U,v)$. The contribution at (x,y) in a plane a distance L below the rim is

$$dI_v(x,y) = I_0 \frac{dv}{L^2 + (v-y)^2 + (U+x)^2}, \tag{4.4}$$

with I_0 a reference rim scatter intensity which must be fitted to match experimentally observed profile data. Integrating along the whole edge yields

$$I_{L,U,V}(x,y) = \frac{I_0}{\alpha}\left[\tan^{-1}\left(\frac{V-y}{\alpha}\right) + \tan^{-1}\left(\frac{V+y}{\alpha}\right)\right], \tag{4.5}$$

with $\alpha^2 = L^2 + (U+x)^2$. Similar expressions are found for the other edges and superposition can be used to determine the scatter contribution to all points (x,y) to determine the profile shape. However, this relies on a generality of edge scattering (ie., assuming isotropic scattering) and not accurate descriptions of scatter distributions, and doesn't consider factors which may influence scattering characteristics.

Few attempts have been made at explicit analytical descriptions of electron transport through treatment head components including intervening air columns. Keall and Hoban (1994, 1996c) have made an approximate description of this transport by considering the series of media that an electron beam from the guide must traverse (ie., first and second foils, air gaps) as a series of infinitely wide slabs with separate scattering characteristics.

A monoenergetic pencil beam is considered, normally incident on the slab representing the first scattering foil. The transport to the patient surface is made by considering the variation in the angular spread of electrons as the electron beam traverses through the scattering foils and air gaps, described by the moments (A_0, A_1, A_2) comprising Eyges' solution to Fermi's transport equation (Eyges, 1948; Hogstrom, 1981; §2.1.2.4, equations 2.8 - 2.10). Using this iterative procedure, Keall and Hoban were able to predict the angular standard deviation of electrons at the patient plane, and to examine the effects of the scattering foils and air individually on producing an angular spread (Keall and Hoban, 1996c) as displayed

in Figure 4-8. The influence of collimation systems on angular characteristics was not considered. Keall and Hoban also found that Monte Carlo simulations of simply the scattering foils and air yielded reasonable primary beam dose distributions. This shall be discussed further in §4.2.2. Values obtained using equation 2.12 can also be used to approximate the virtual source position.

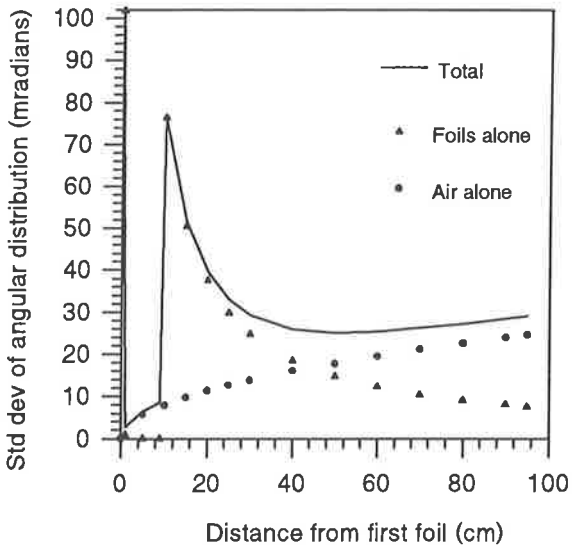

Figure 4-8: Variation in electron angular standard deviation with distance from scattering foils (adapted from Keall and Hoban, 1996c).

Whereas the approximations made by Keall and Hoban yielded satisfactory results, Grusell *et al.* (1994) have suggested that the infinite slab approximation will strongly influence off-axis determinations of angular deviation. In order to determine the required shape of the second foil for optimal beam flattening, Grusell *et al.* (1994) combined a Fermi-Eyges approach with Nigam-Sundaresan-Wu multiple scattering theory (Marion and Zimmerman, 1967) to model dual scatterers in air. In their approach, Fermi-Eyges theory is used to describe electron transport of a pencil beam, with some initial angular spread, through the first foil. Every point in the non-uniform second scatterer then acts as a source of scattered particles, adding to the mean square angular spread of electrons in the beam. Requiring the fluence in the plane of interest to be constant with off-axis distance leads to an integral equation which must be solved inversely to obtain the functional form of the second foil thickness. This approach is useful in describing the effects of non-uniform foils, and may be used to describe the fluence profile of electrons in a plane of interest. The effects of applicators and other beam shaping components were not considered in this work.

Analytical modelling of the influences of collimation systems for electron beams is very involved, and accurate representation of scatter from collimators and the complex variations in scatter with the particular configuration and beam quality is best made with Monte Carlo techniques as will be discussed in the next section. Collimator scatter in electron beams displays intricacies in sources, angular variations and energy spectra. Lax and Brahme (1980) used the Gaussian approximation for electron scattering as formulated by Brahme (1975) to provide a broad description of electron interactions with collimators. This investigation (discussed in §4.1.1.1) highlighted some of the characteristics of the scattering distributions and their ramifications for collimator design, though did not consider explicit characteristics of the scattered particles.

4.1.2.2. Numerical / Monte Carlo Approaches

The holistic approach of the Monte Carlo method suggests that, provided the theoretical basis for Monte Carlo transport is legitimate, that the cross-sectional data used is correct and that sufficient statistical accuracy can be attained, then authentic beam characteristics will be predicted. All that is required is a means of describing the geometry of the treatment head, a set of input particle characteristics, and a bit of spare time. Since, for models employing Monte Carlo codes for mixed photon/electron transport, there is little difference between the setup requirements for electron and photon beam simulation, the evolution of Monte Carlo methods for accelerator simulation shall be considered as a whole.

Initial Monte Carlo studies of accelerator treatment heads (eg., Petti *et al.,* 1983a,b; Mohan *et al.,* 1985) concentrated on transporting particles through the entire head configuration, with simplifications implemented such as cylindrical symmetry. The philosophy of such modelling has altered slightly in recent years, and the compartmental-like design of treatment heads has led to a similar design for Monte Carlo codes designed specifically for treatment head simulation (Udale-Smith, 1990, 1992; Rogers *et al.,* 1995; Lovelock *et al.,* 1995), where detailed consideration is made of all head components. Such comprehensive approaches have been made possible through increases in computing efficiency.

The Monte Carlo prediction of particle scattering in heavy metal targets has provided a benchmark for many Monte Carlo codes, such as ETRAN (Seltzer, 1987), ITS (Halbleib and Mehlhorn, 1986) and EGS (Ford and Nelson, 1978; Nelson *et al.,* 1985; Sixel and Faddegon, 1995; see §2.2). Monte Carlo methods have also been employed in the simulation of radioisotope teletherapy (Co^{60}) units, where geometrical characteristics (particularly of the source and collimators) are most significant (ICRU, 1970; Rogers *et al.,* 1985; Han *et al.,* 1987; Mohan, 1988; Rogers *et al.,* 1988; Rogers *et al.,* 1995).

A multitude of detailed Monte Carlo studies of accelerator beams have been performed in the last couple of decades (Patau *et al.*, 1975; Abou-Mandour and Harder, 1978, as cited in Andreo, 1991; McCall *et al.,* 1978; Nilsson and Brahme, 1981; Petti *et al.,* 1983a,b; Mohan *et al.,* 1985; Luxton and Astrahan, 1988; Udale, 1988; Udale-Smith, 1992, Cullip *et al.,* 1993; Chaney *et al.,* 1994; Ding *et al.,* 1994; Zefkili *et al.,* 1994; Ding and Rogers, 1995; Rogers *et al.,* 1995; Lovelock *et al.,* 1995). Treatment head modelling has also supplemented other related investigations (eg., Manfredotti *et al.,* 1990; Andreo *et al.,* 1989; Kubsad *et al.,* 1990; Keall and Hoban, 1994; Desobry and Boyer, 1994; Lovelock *et al.,* 1994; Ahnesjö, 1995; Ding *et al.,* 1995; Heydarian *et al.,* 1995, Papanikolaou and Paliwal, 1995; Sixel and Faddegon, 1995). Although all modelling investigations will not be examined here, several will be examined in more detail.

The statistical accuracy (or simulation execution time) of treatment head simulations can be reduced by assuming cylindrical symmetry for all components. Geometries for the simulation can then be described via coaxial cylindrical sections, and particle characteristics can be scored in a set of discrete annular scoring regions perpendicular to the beam central axis at some distance from the treatment head, as shown in Figure 4-9.

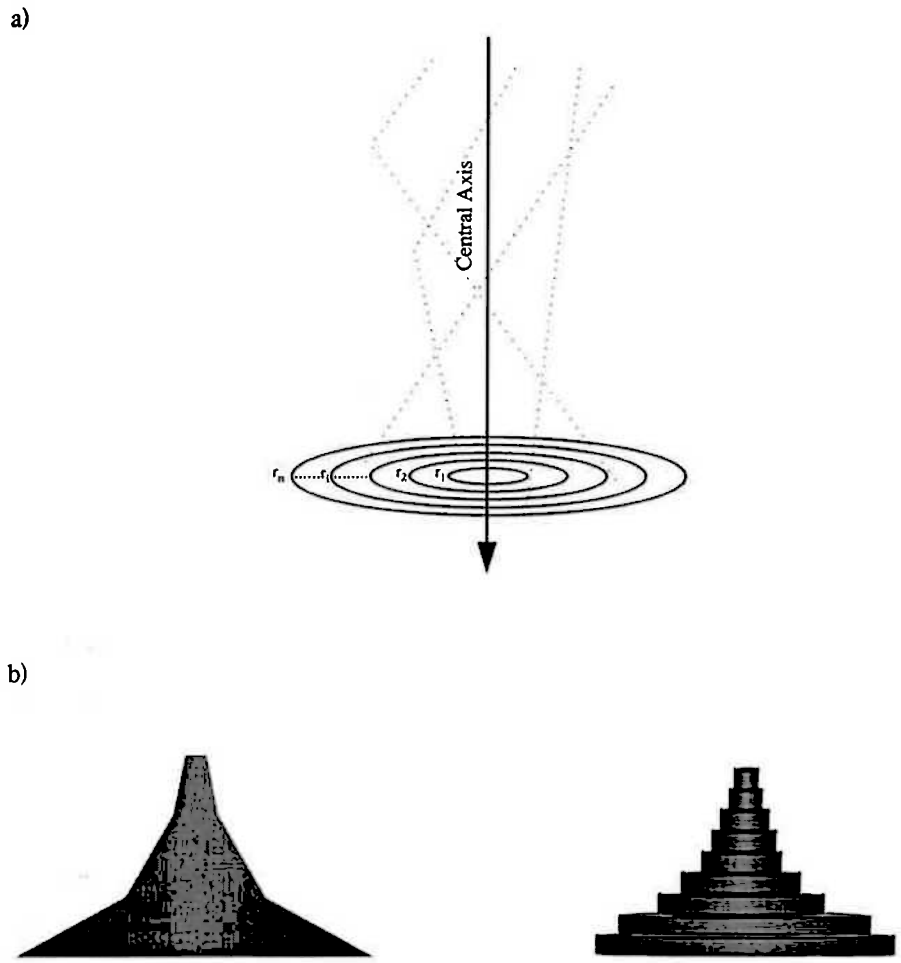

Figure 4-9: Cylindrical approximations in Monte Carlo simulations. a) Scoring particle characteristics in radial sections. b) Approximating the shape of a target/scattering foil as a series of coaxial cylinders.

In a landmark investigation, Mohan *et al.* (1985; Mohan, 1988) employed such a cylindrical geometry in the simulation of accelerators in photon mode. During each simulation, electrons and photons were transported down through the treatment head materials with EGS Monte Carlo until they reached the scoring plane, which was arranged as in Figure 4-9a. As a particle intercepted an annulus of the scoring region, the energy bin in that annulus corresponding to the energy of the particle was incremented. Another characteristic considered was the direction of particles as they were scored. In this way, using the treatment head characteristics of Varian Clinac accelerators, Mohan *et al.* (1985) were able to determine the energy and angular distribution of photons, and to examine the variation in these characteristics with radius. Typical energy spectrum results are shown in

Figure 4-10. Using 'tagging' of photons, which involves labelling scattered photons with the treatment head element that scattered them, Mohan *et al.* were able to determine the relative contributions to scattering of the various head components. This model has since been extended as discussed below.

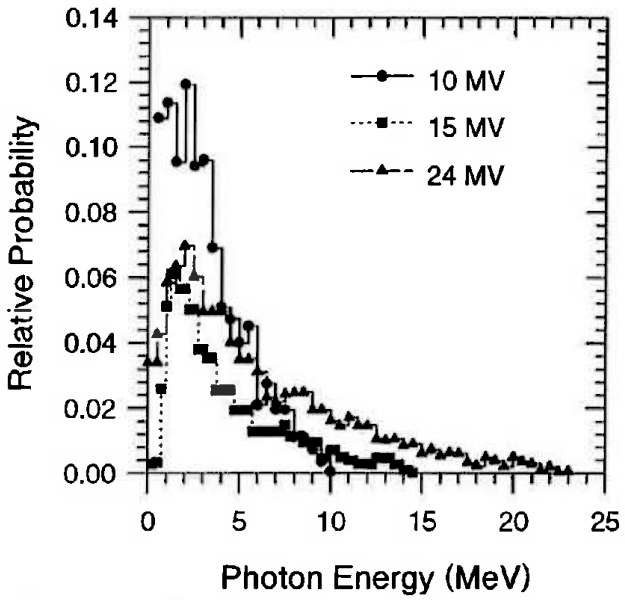

Figure 4-10: Photon energy spectra obtained by Mohan *et al.* for several nominal photon beam energies. Data taken from sample spectra data distributed with the EGS4 Monte Carlo code.

A similar investigation had previously been carried out by Petti *et al.* (1983a,b) using cylindrical geometry packages designed for use with EGS, combined with explicit scoring of electron characteristics for a Varian Clinac-35. Petti *et al.* (1983a) explicitly state that these characteristics were used to create energy and angular *distributions* at the scoring plane, which were *sampled* as input to another Monte Carlo simulation of the beam incident on a water phantom in order to compare results with experiment. This two-step Monte Carlo procedure (Andreo, 1991), where energy and angle are scored independently, is potentially invalid as energy and angular independence cannot be assumed (Andreo and Fransson, 1989). Thus, a more useful scoring procedure is the storage of the individual characteristics of scored particles, which can then be used in subsequent simulations (Rogers *et al.*, 1995; Lovelock *et al.*, 1995).

The full potential of Monte Carlo for treatment head simulation would be realised if many of the features of the above mentioned modelling attempts were combined, and their assumptions reduced. The full characteristics of correlation between particle type, energy and angular spectra, and spatial distribution requires authentic geometric characterisation of treatment head components, and the scoring of individual particle characteristics. Such a simulation would require extensive amounts of computer time and storage, though these requirements can be minimised using reliable variance reduction techniques, and data compression.

Udale (1988; Udale-Smith, 1992) performed extensive EGS4 modelling of Philips accelerators in electron mode, without any restriction to cylindrical geometries. She considered the modular arrangement of a treatment head as a sequential series of separate components as shown in Figure 4-11. Starting with a broad planer beam simulation, components were added in successive simulations in order to observe their separate contributions to characteristics at the scoring plane, though particle 'tagging' was not implemented. Component geometries were explicitly coded using the EGS4 coding system so that surface boundaries could be appropriately identified by the EGS4 HOWFAR routine (Nelson and Rogers, 1988; §2.2.2.2). Using these simulations, Udale was able to determine the energy and angular characteristics of all electrons and photons in the electron beams, their spatial variations and the contributions of head components to scattering. Udale-Smith (1992) highlights the point that a shortcoming of such simulation is still lack of knowledge of the characteristics of electrons from the waveguide, and that energies providing depth doses with similar practical ranges to experimental curves were used in the simulations. Udale also used a two-step simulation, with particle characteristics for phantom simulations sampled from the obtained distributions, and stated that the resulting dose distributions will be independent of any particle spatial-energy-angle correlation (Udale, 1988), apart from the separate simulation of primary and secondary electrons (Udale-Smith, 1992).

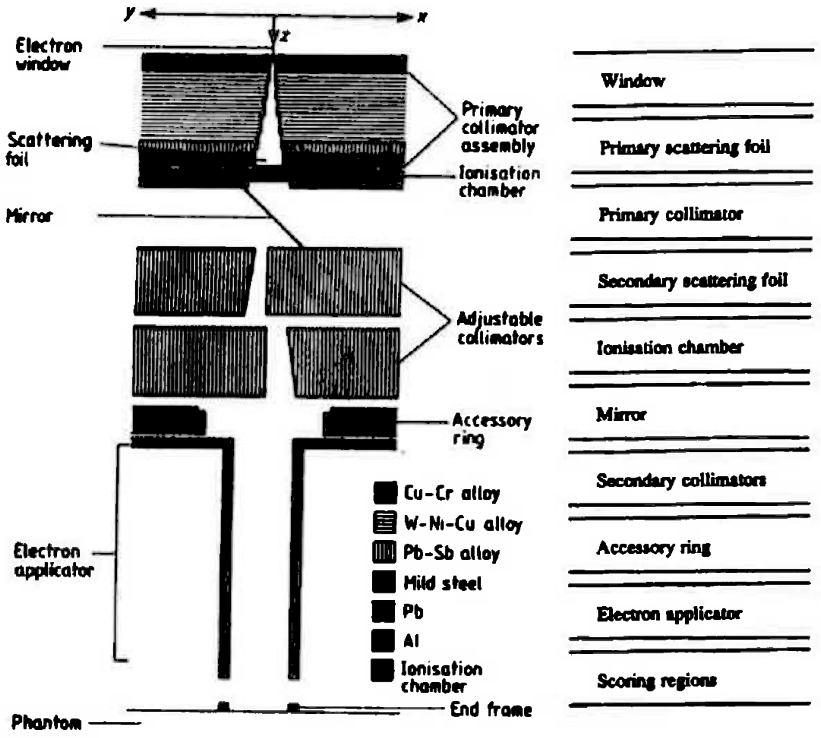

Figure 4-11: Compartmental approach to treatment head simulation employed by Udale (1988, Udale-Smith, 1992).

The dedicated EGS4 user code, BEAM (Rogers *et al.,* 1995), has been specifically designed for treatment head simulation by the OMEGA group (Mackie *et al.,* 1990) , using the compartmental approach of Udale. The aim in design of the user code was to provide a generic simulation system, for all types of accelerators, teletherapy machines, and low energy (superficial/orthovoltage) units. Since EGS4 can reliably simulate the transport of particles, the emphasis was on defining the geometries of head components. A series of *component modules* defining specific geometric forms perpendicular to the beam axis emulate the modular arrangement of head components. The user-code controls transport of particles independently between these modules, so that particle characteristics can be obtained at any plane perpendicular to central axis. Similarly, this arrangement allows particle characteristics to be used as input to any stage of the simulation (ie., to any component module). This is particularly useful for example, when several different applicator designs are to be used, since all components prior to the applicator can be simulated initially, and the resulting scored particles used as input with different

applicators (Rogers *et al.,* 1995), though does not allow for the influence of subsequent downstream component modules on the original phase space data. This has transformed the usual two-step simulation approach into a multi-step one.

Spectral correlation is handled in the approach of Rogers *et al.* (1995) by scoring particle characteristics via a *phase space* description of the beam. The type, position, energy, direction and history (locations of interactions) of each particle reaching a scoring plane are recorded, and these may then be used as input to subsequent component module or phantom simulations. Better understanding of the phase space concept can be gained through Figure 4-12. This phase space approach, or a modified version of it, will most likely become the standard one for beam models and in the input to dose calculation algorithms (Neuenschwander *et al.,* 1995). Problems associated with the excessively large data files generated are being addressed (Ma *et al.,* 1995).

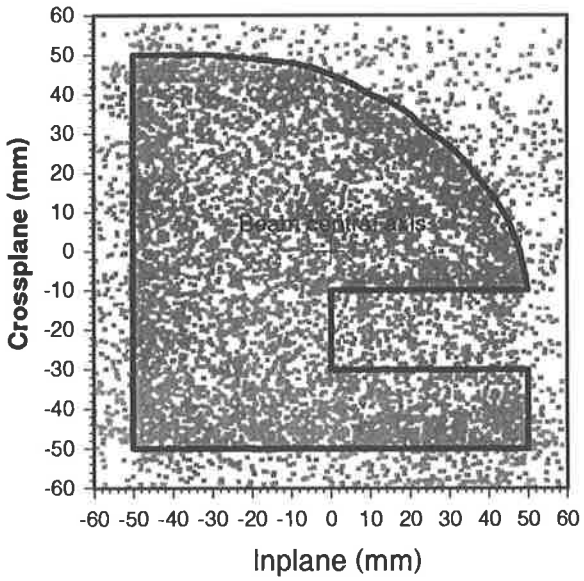

Figure 4-12: Electron phase space - the locations of 10^4 electrons scattered from a cutout (shape as shown by the dark line) incident at the patient plane in a 12 MeV beam for a Siemens KD2 accelerator. Other particle characteristics stored in a phase space file are particle type, energy and direction.

Rogers *et al.* (1995) also acknowledge the inability to exactly characterise the electron beam exiting the wave guide on a linear accelerator. They account for this by again,

adjusting input parameters until consistency with experimental depth doses is achieved. Flexibility in the characteristics of this component is built into the BEAM code, and a variety of source characteristics can be used.

Included in the BEAM code (and potentially useful in *any* Monte Carlo simulation) is a comprehensive set of variance reduction tools, which can be implemented at any stage within the full simulation (Rogers *et al.,* 1995). These include range rejection (especially useful when not concerned with energy deposition in high density materials by particles stopping in the materials), bremsstrahlung splitting (to improve statistical accuracy in user-selected regions) and forced interactions (to eliminate the consideration of particles which do not interact in the geometry). These techniques are detailed in Rogers *et al.* (1995).

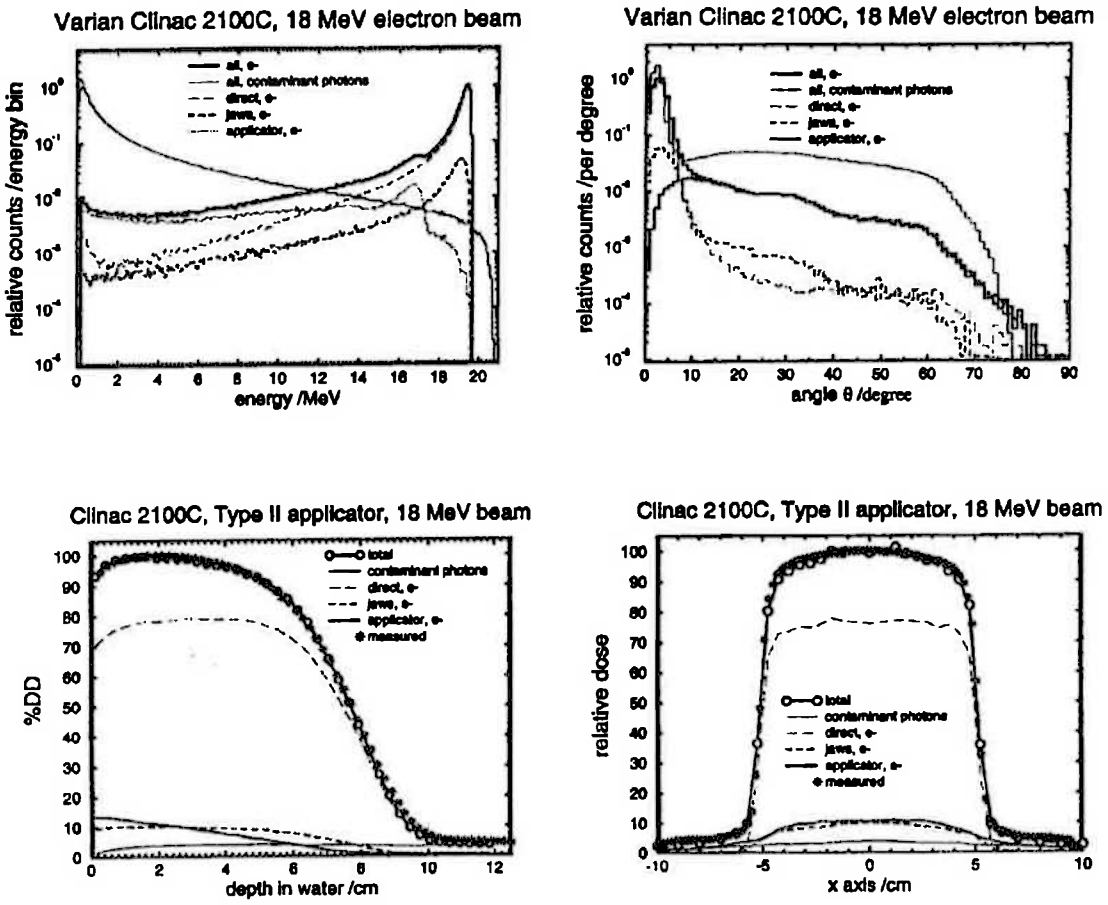

Figure 4-13: Electron beam energy and angular spectra for a Varian 2100C accelerator as calculated by Ding and Rogers (1995).

Since electron beam characteristics display the greatest dependence on variation in treatment head construction, the BEAM code has mainly been used to examine electron beam characteristics (Rogers *et al.,* 1995; Ding *et al.,* 1995; Ding and Rogers, 1995). Examples of results for a Varian 2100C accelerator are shown in Figure 4-13, which include comparison of results from subsequent Monte Carlo simulations using obtained phase space data as input for dose profiles and depth-dose curves, and measured curves.

A similar design philosophy to the BEAM code was used by Lovelock *et al.* (1995) in the design of a photon-beam-specific EGS4 Monte Carlo code, McRad. A similar compartmental design approach is used, with individual particle characteristics (including head component interaction flags) scored at any plane, though several simplifications are made which restrict the McRad code relative to the BEAM code. A major simplification in the model is the restriction to cylindrical symmetry in the geometrical description of head components. This allows greater statistical accuracy to be achieved, but provides data which are a function of radial position only. The main motivation for this restriction was the fact that the data from the model were to be used in dose calculation algorithms which assume radial symmetry (Mohan *et al.*, 1985). A uniform cylindrical spot beam of electrons is incident on the target, with initial electron energy sampled from a Gaussian distribution with a limited maximum. Parameters for the initial energy distribution are obtained by tuning according to resulting depth doses *as well* as resulting profiles. Lovelock *et al.* (1995) found that beam penumbra are more sensitive to initial electron energies than are depth doses for photon beams, due to the effects on electron range of photon energy.

In verification of the McRad code, Lovelock *et al.* (1995) extended the cylindrical symmetry simplification with the use of the differential pencil beam dose calculation algorithm. This algorithm was implemented assuming a common point source for all beam particles, which neglects the effects of scatter within the treatment head, and will potentially affect resulting dose distributions. Nevertheless, reasonably accurate predictions of actual dose distributions were obtained by Lovelock *et al.* (1995) using the McRad model, and extension of the geometrical description of head components to include non-cylindrical symmetry would, whilst increasing the complexity of the calculation, provide greater accuracy in describing non-radially symmetric beam characteristics.

A specific Monte Carlo study of the effects of electron applicators was performed by Kassaee *et al.* (1994), using the Monte Carlo code ITS (Seltzer, 1987) in examination of Varian 2100C applicator design. They performed simulations of the various components of the accelerator head in stages - 1) scattering foil only, 2) scattering foil and main photon jaws, 3) scattering foil, main photon jaws, with a modified applicator, 4) scattering foil, main photon jaws, with a standard 2100C applicator. Using their simulations, they were able to examine how scattered electrons from applicator components contribute to the properties of dose distributions, and evaluate the relative merits of particular applicator designs.

4.2. Characteristics of Applicator Scattering

4.2.1. Introduction

As described above, the applicator or collimation scatter component of the clinical beam represents a perturbation of the primary beam. The set of resulting beam characteristics will depend on the way in which the applicator is applied, including the detailed geometry of patient-specific cutouts. The aim of the current investigation was to examine in detail the effects of electron beam applicators on particles in the primary beam. This was in order to identify the major interactions that occur, and to determine what factors have the greatest influence in eventually affecting absorbed dose in a patient or phantom. With this knowledge, a model for applicator scatter could be developed which would explicitly account for the most important factors determining the properties of the scatter.

In order to account for primary dose deposition, and to allow accurate simulation of primary beam/applicator interactions, the characteristics of the primary beam had to be known.

4.2.2. Primary Beam Modelling

Keall and Hoban (Keall, 1994; Keall and Hoban, 1994; Keall and Hoban, 1996c) have shown that primary beam dose distributions can be reproduced using electron particle data obtained by simple Monte Carlo simulations of the scattering foils of the accelerator under investigation and air to the patient / phantom surface. Using this principle, primary beam information was obtained using the modified version of the EGS4 cylindrical geometry usercode, RTPCYL as described in §2.2.3.1 with parameters AE=ECUT=0.521 MeV, and AP=PCUT=0.01 MeV. A pencil beam of electrons was simulated incident on the scattering foils of the Siemens KD2 accelerator (approximated as infinite slabs of the foil materials) as described in Table 4-II. The electrons and scatter products must pass through the column of air to the effective phantom surface at isocentre. This simulation is displayed graphically in Figure 4-14. From this particular simulation, primary beam electron and photon energy spectra could be obtained.

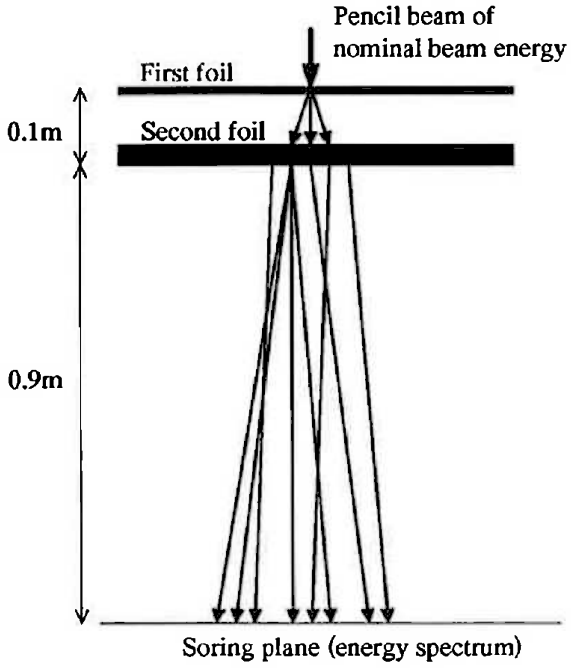

Figure 4-14: Illustration of Monte Carlo primary beam model.

The validity of the resulting spectra was tested by using the obtained spectra in a further Monte Carlo simulation of broad beams incident on water phantoms, and compared with similar experimental measurements. Maintaining consistency in practical range usually required an adjustment of the nominal energy of the pencil beam incident on the first foil to

match the actual energy of electrons from the waveguide in the clinical accelerator (Fernandes, 1985; Udale, 1988; Udale-Smith, 1992; Rogers *et al.,* 1995). Table 4-III compares the nominal electron beam energies with the final ones chosen to represent the clinical beam for the energies considered (6, 12 and 18 MeV). A comparison of a measured depth dose curve with a calculated one is shown in Figure 4-15. Also shown is a depth dose curve calculated using a monoenergetic 12 MeV broad beam. The presence of an electron energy spectrum in contrast to a purely monoenergetic electron beam moves the depth of dose maximum to shallower depths, and decreases the gradient of the fall-off region past d_{max} and to increase the surface dose (Marbach and Almond 1981; Deasy *et al.,* 1994; §3.2.1.1).

Table 4-III: Final chosen pencil beam energies.

Nominal Beam Energy (MeV)	*Pencil Beam Energy (MeV)*
6	5.85
12	12.00
18	18.20

Electrons scattered from the primary and secondary collimation systems and other minor components (monitors, mirrors) are either negligible or have similar energy and angular characteristics to the primary beam (Udale-Smith, 1992; Kassaee *et al.,* 1994) and may thus be included in calculations of primary beam dose distributions without serious inaccuracy. Alternatively, more extensive Monte Carlo simulations (Udale-Smith, 1992; Rogers *et al.,* 1995) may be employed to establish a permanent primary beam phase space irrespective of the field defining applicator employed. For the purposes of modelling applicator scatter, it was thought that such detailed consideration of other treatment head components would over-complicate the proposed model.

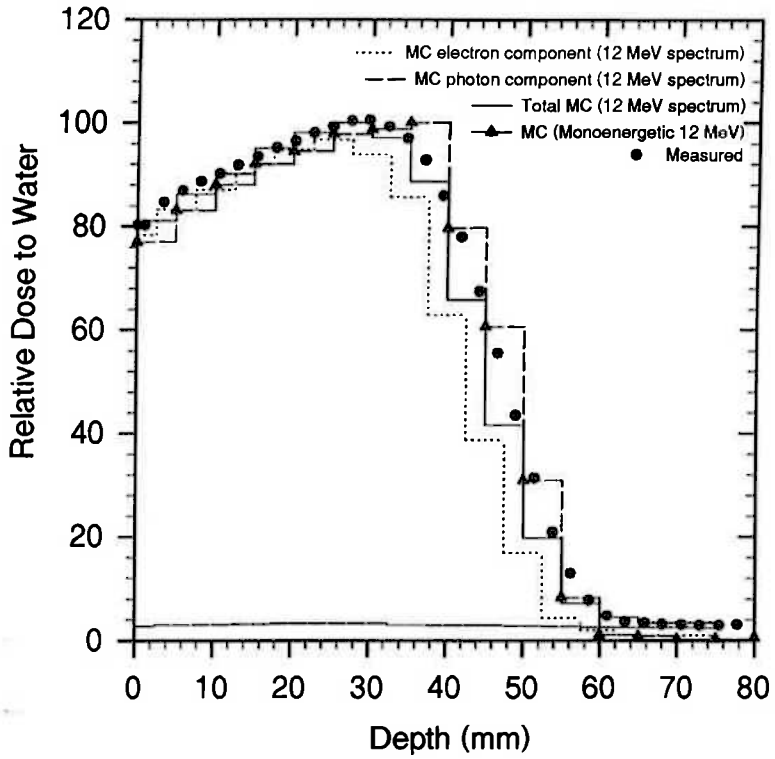

Figure 4-15: Comparison of measured and Monte Carlo generated electron depth dose curves. Monte Carlo curves shown (as in legend) are those for the photon and electron components calculated using realistic beam spectra, and the total of these components; and that for a monoenergetic 12 MeV beam with no photon component.

Table 4-IV: KD2 Electron beam angular standard deviations at the applicator face

Beam energy (MeV)	σ_{θ_x} *(radians)*
6	0.068
9	0.050
12	0.038
15	0.032
18	0.027
21	0.023

When calculating primary beam dose distributions in water phantoms using Monte Carlo methods, the angular distribution of the primary beam electrons needs to be considered, particularly for accurate modelling of penumbral dose. For this purpose, the standard deviation in electron angular spread at the applicator face was taken from results obtained by Keall (1994) who used electron transport calculations in the scattering foils of the KD2 accelerator, and in the air column to the patient surface as described in §4.1.2.1. The values for σ_{θ_x} obtained by Keall (1994) for the relevant energies are shown in Table 4-IV. These values were obtained using equations 2.8 to 2.10 and equation 2.13, and the average of two calculations using scattering powers taken from Jackson (1975) and Rossi (1952).

4.2.3. Method - Edge Simulations

A common configuration for electron beam applicators (or just generally tertiary collimation systems) is as a series of trimming plates or apertures perpendicular to the central axis of the beam (eg., Biggs *et al.,* 1979; ICRU, 1984; Muller-Runkel *et al.*, 1985; Pennington *et al.,* 1988; Das *et al.,* 1990). In order to investigate the characteristics of particles scattered from such plates, elemental sections of a primary beam were simulated incident on a small section of a plate's edge. In this way, the resulting *scatter kernel* (the characteristics of particles scattered from the edge) for applicator scattered particles could be obtained and examined.

A typical simulation geometry is shown in Figure 4.17, where primary beam electrons or photons are incident at an appropriate angle of incidence to a semi-infinite edge of applicator material in air. The beam (using energy spectra obtained above and assuming scatter to be independent of primary beam angular spread) is emergent from the nominal source position and is restricted to the limit of the edge (in the positive z-direction - this is displayed in Figure 4-17), the maximum lateral range of electrons in the material of interest (in the negative x-direction), and to a width of 5 mm (in the y-direction). For the primary beam photon component, similar beam limits are used. The EGS4 Cartesian user-code used was RTPCART_XYZ which is described in §2.2.3.2. Cutoffs used for all simulations were set to AE=ECUT=0.521 MeV for electron transport, and AP=PCUT=0.01 MeV for photon

transport. Low cutoffs were used in order to ensure authentic simulation of low energy particle production and transport. The PRESTA algorithm (Bielajew and Rogers, 1987) was used in all simulations.

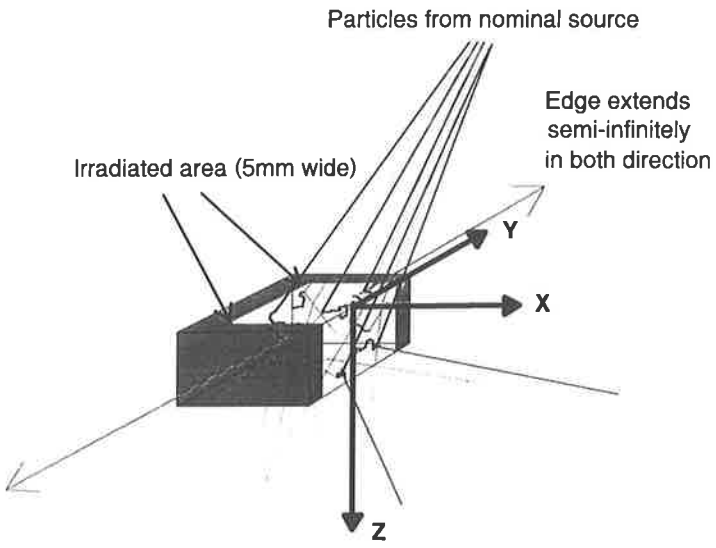

Figure 4-16: Illustration of EGS4 edge scatter simulation.

The number of particles simulated in each case was chosen to minimise simulation errors and yet provide realistic simulation times. This usually meant the simulation of order 10^5-10^6 incident electrons or 10^6-10^7 incident photons. Resulting variances were less than 5% in the regions of highest scored particle fluence, though could be extremely large (> 50%) in regions where only single particles (or a relatively negligible number) were scored for an entire simulation. Variance reduction was achieved in simulations by restricting the beam limit in the negative x-direction, and by exploiting symmetry about the x-axis. The relative numbers of photons and electrons in the primary beam were determined from the measured bremsstrahlung dose along with the calculated dose per electron or photon.

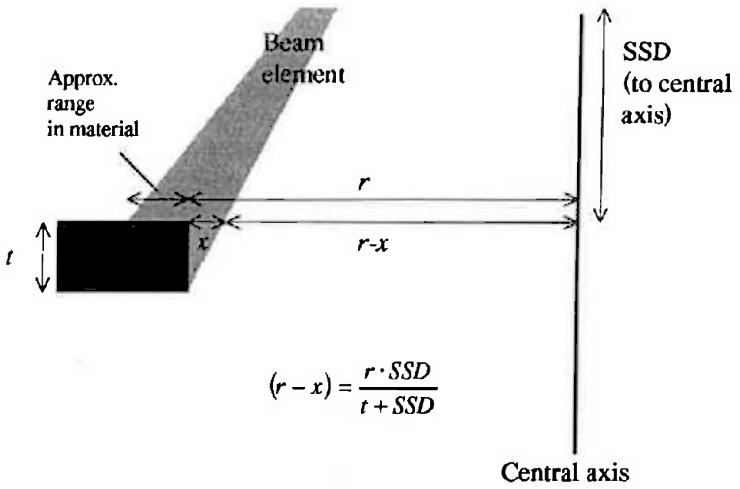

Figure 4-17: Geometry of edge scattering simulations.

Simulations were performed for a variety of beam energies, incident beam angles (each corresponding to a certain field size), and edge materials (corresponding to materials used in KD2 applicator construction). Primary beam energies of 6 MeV, 12 MeV and 18 MeV were considered. The dependence of particle scattering on angle of incidence was considered in terms of the magnitude and spatial distribution of scattered particles. The energy characteristics of scattered particles were also considered.

4.2.4. Results and Discussion

Figure 4-18 and Figure 4-19 show EGS4 simulations of particles scattering off an edge of cerrobend for electron and photon components respectively. The particle paths shown are their positions during transport (three dimensional simulation collapsed into a plane) recorded at each call to the AUSGAB routine (see §2.2.2.2).

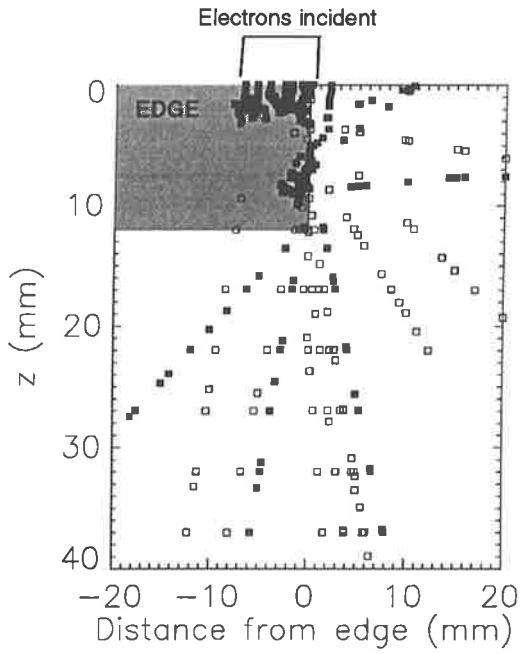

Figure 4-18: Particle tracks recorded in simulation of 10 electrons from a 12 MeV electron beam incident at 1.83° to a cerrobend edge. Particles shown are electrons (filled squares) and photons (open squares).

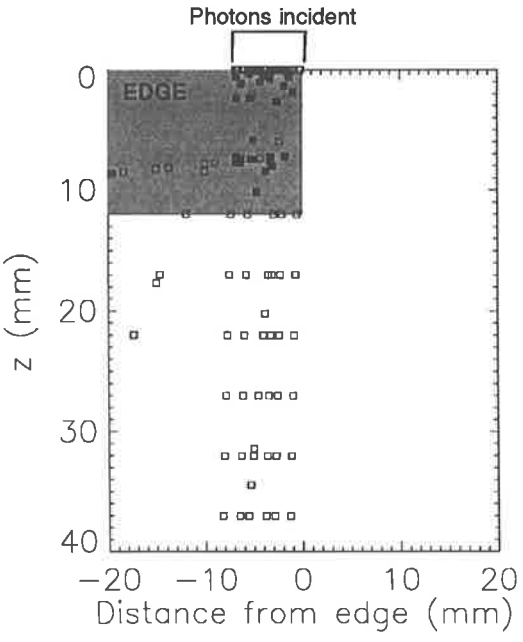

Figure 4-19: Particle tracks recorded in the simulation of 10 photons from a 12 MeV electron beam incident at 1.83° to a cerrobend edge. Particles shown are electrons (filled squares), and photons (empty squares).

In clinical application at the centre where this research was undertaken, cerrobend cutouts of thickness 12 mm are used. For the primary electron component, transmission through a solid block of cerrobend with the same thickness as an edge was found by Monte Carlo simulation to be less then 1% for all energies considered. For the photon component however, the transmission is greater than 30% (considered across the entire bremsstrahlung spectrum in each case). Electrons which emerge from the edge mainly correspond to primary electrons incident on the vertical face of the edge (as the strong dependence on incidence angle indicates - see Figure 4-23a). Modelling an incident electron beam to the maximum possible range in the edge materials may be unnecessary for the accurate simulation of scattered electrons since very few electrons will emerge after entering the edge. However, using this extent of the beam does more effectively model the extensive bremsstrahlung production that occurs in the material and subsequent Compton electron and lower energy photoelectron production (another source of scattered particles).

Figure 4-20 shows the relative contributions of dose to water with its surface 50 mm below a cerrobend edge due to the dominant emerging particles (scattered primary beam electrons, the primary beam photon component, and photons generated in the edge by primary beam electrons). Electrons set in motion by primary photons were found to be mainly absorbed in the cerrobend and contributed negligibly to scatter dose. For the primary photon component, a simple but appropriate approach would be to consider the photon fluence beneath the edge as an attenuation of the primary beam. This indication of photon component transmission implies that electron applicators do not act to effectively absorb bremsstrahlung from the accelerator head. For the electron component, the influence of applicator scatter represents a perturbation of the characteristics of the beam incident on the patient, and this scattering must be considered if an accurate description of the primary beam is to be obtained. The component of dose due to photons generated within the edge is relatively small, though is a consequence of electron interactions in the applicator materials and will be considered.

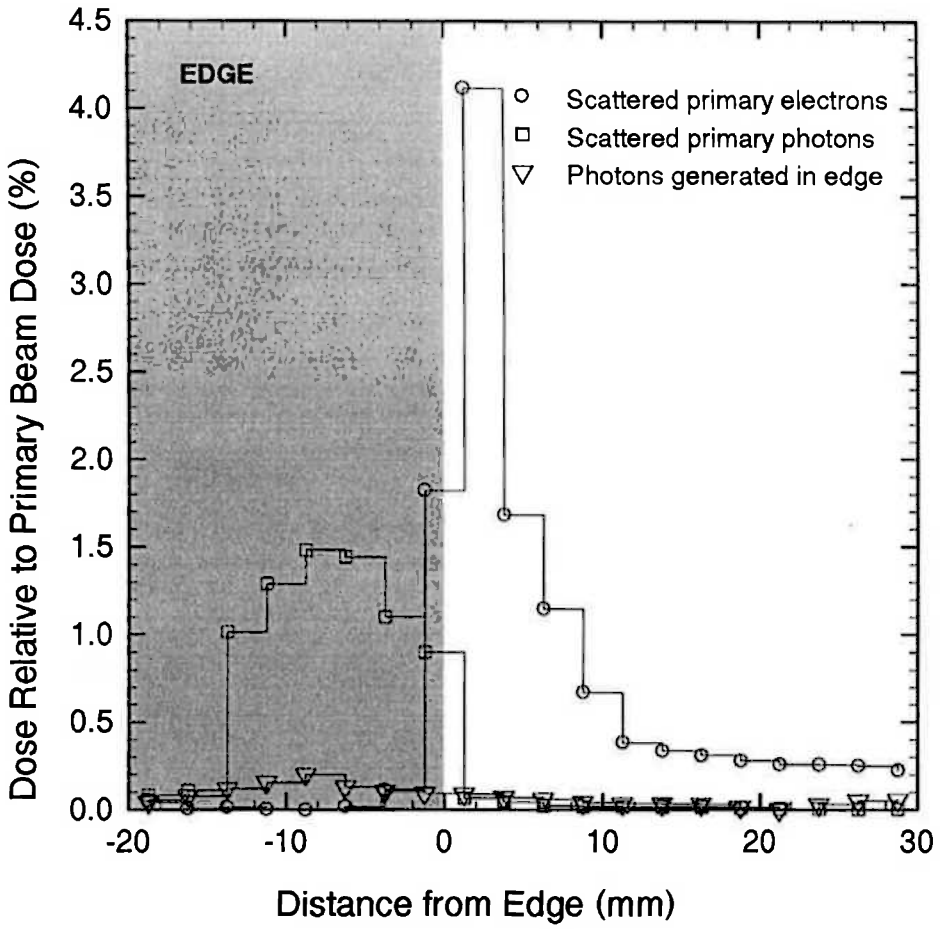

Figure 4-20: Profiles of dose to water due to the three considered components (primary beam scattered electrons, primary beam photons, photons generated in the edge by primary beam electrons) for a 12 MeV beam incident at 1.83° to the edge. The edge is 50 mm above the water surface and profiles are taken at the depth of maximum buildup for each component, parallel to the line from the beam central axis to the edge. Normalisation is to dose due to the primary open beam.

Scattered electron fluence distributions in the *XY* plane are displayed in the contour plots of Figure 4-21 and Figure 4-22 for scattered electrons and edge-generated photons respectively. These distributions were obtained in the *XY* plane 50 mm below the cerrobend edge, with electrons characteristic of a 12 MeV beam incident at 1.83° to the edge. For electrons, the scattering is dominantly forward directed as can be seen, which results in the sharp field edge horns for profiles close to the applicator edge. Superposed contributions from all such elements around an aperture would yield a complete scatter fluence distribution in the patient plane. For photons, Koch and Motz bremsstrahlung angular

sampling (Koch and Motz, 1959; Bielajew *et al.,* 1989) combined with significant electron scattering in the edge materials (and hence a large distribution of initial photon directions) leads to a more isotropic distribution of scattered photons as Figure 4-22 indicates.

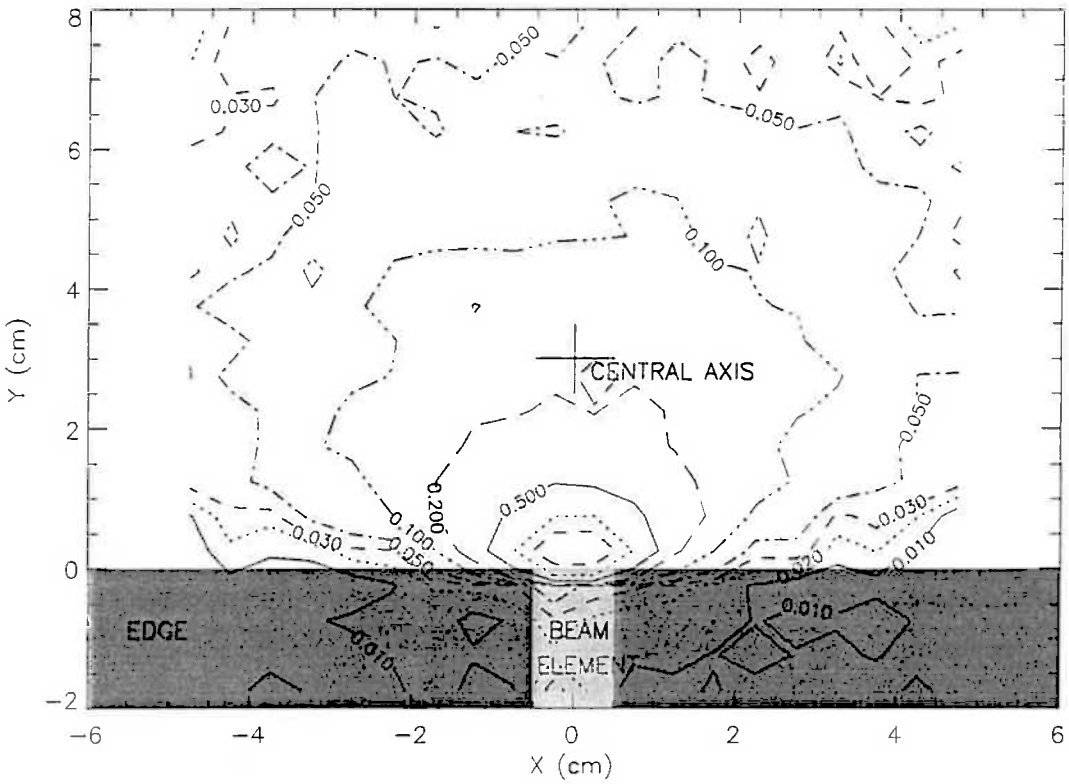

Figure 4-21: Contour plot of scattered electron fluence distribution in the *XY* plane 50 mm below the cerrobend edge. Percentage normalisation is to the incident 12 MeV beam fluence and the angle of incidence was 1.83°.

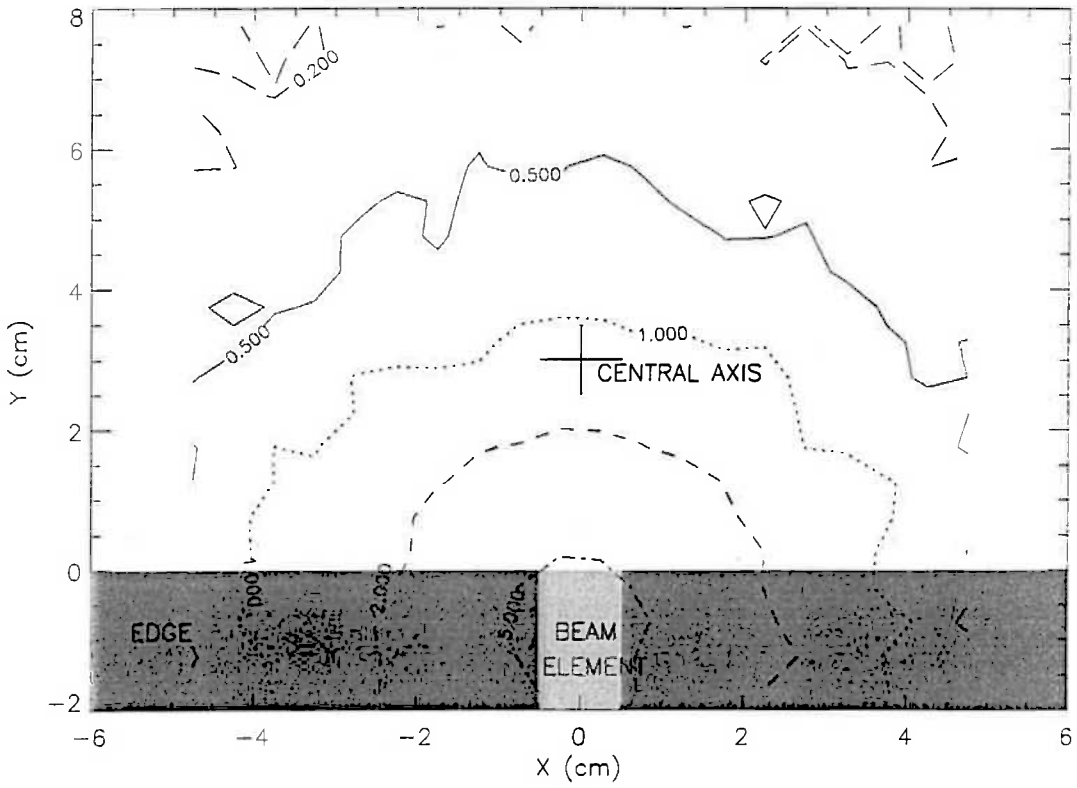

Figure 4-22: Contour plot of edge-generated photon fluence distribution in the *XY* plane 50 mm below the cerrobend edge. Percentage normalisation is to the incident 12 MeV beam fluence and the angle of incidence was 1.83°.

The variation in scattered electron and edge-generated photon fluence with incidence angle of the primary beam on a cerrobend block is shown in the profiles of Figure 4-23 for a 12 MeV beam. Here profiles are shown normalised to incident primary beam fluence, and display variation in the number and distribution of scattered electrons and photons.

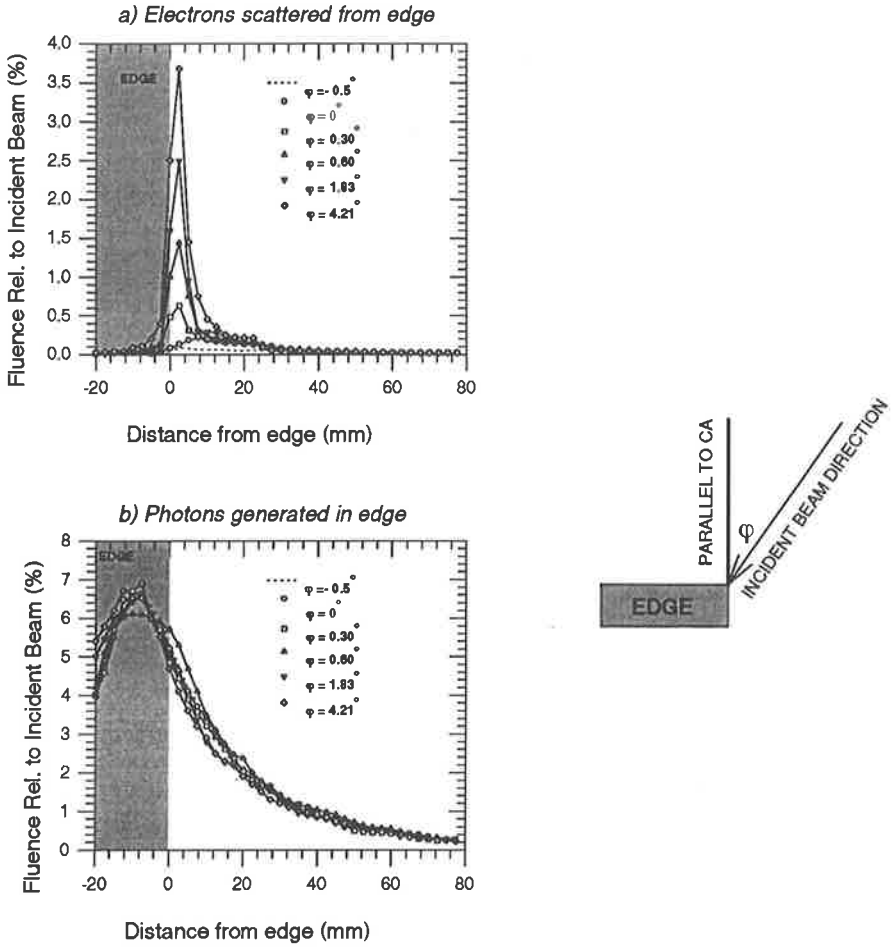

Figure 4-23: Fluence profiles for a) scattered electrons and b) edge-generated photons for a variation in incident angle of primary beam to edge, percentage normalised to the incident beam fluence. A reduction in incidence angle corresponds to a reduction in the size of the applicator aperture. All profiles are scored 20 mm below the cerrobend edge and for a 12 MeV incident electron beam. Only one negative incidence angle (edge overlapping beam central axis) has been shown since electron scatter yields for these angles were minimal. Note that photon production is not as adversely affected by incidence angle.

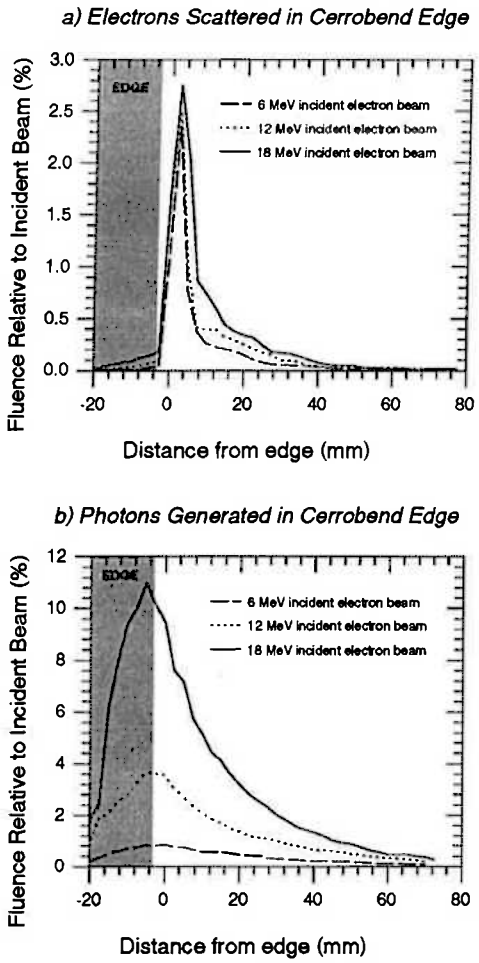

Figure 4-24: a) Scattered electron and b) edge-generated photon fluence profiles for a variation in incident primary beam energy, percentage normalised to the incident beam fluence. All profiles for a beam incident at 1.83° to the primary beam central axis direction and scored 20 mm below the edge.

Figure 4-24 compares these scatter fluence variations for incident primary beam energies of 6 MeV, 12 MeV, and 18 MeV, for an incidence angle of 1.83°. Figure 4-25 shows similar distributions for a 12 MeV beam and variation in aperture material. For Figure 4-25, trimmer materials have been simulated as they are arranged as applicator apertures, though at identical SSDs and radii from central axis. Thus, edge thicknesses (for Figure 4-25) are 12 mm for the cerrobend edge, 9.5 mm for the brass edge and 6.5 mm of stainless steel over 26.5 mm of aluminium for the steel / aluminium edge. The resulting plot indicates the relative numbers of particles scattered from each edge. The curves for the photon component were quite sensitive to the lateral extent of the primary beam (in the $-y$ direction) in the negative portion of the x-axis.

It is apparent from Figure 4-23 that scattered electron and edge-generated photon fluence is significantly influenced by the area of exposed vertical face of the edge. This implies that scatter yields from larger applicators (larger field sizes) will be greater due to beam divergence and the increasing obliquity of beam particles with off-axis distance, which may have some influence on field flatness at larger field sizes and produce a field-size dependence of flatness. At the centre where this work was undertaken, cerrobend cutouts are made with vertical edges, just as the edges were simulated. Figure 4-23a) implies that cutouts with diverging edges would improve field flatness, though this is dependent on how such cutouts, together with other applicator trimmers, are required by the manufacturer to contribute to a beam's profile.

Variations in scatter with primary energy (Figure 4-24) are consistent with scattering and energy loss processes; lower energy incident electrons are scattered through larger angles and stop more rapidly than those of higher energies (linear collisional stopping power being virtually independent of energy at the energies considered - see §2.1.2.1) and so are less likely to be transmitted through the lower parts of the edge. This consequently effects the magnitude of scattered electron fluences, with scatter yield relative to the incident beam fluence increasing with energy. However, the variation in scatter yield does not vary with energy variation as significantly as for angle of incidence variation, consistent with the predictions of Lax and Brahme (1980; see §4.1.1.1). This is because of the balance between electron scattering and stopping within edge materials, as commented on by Lax and Brahme (1980). Lower energy electrons scatter more though will only scatter out of the edge if incident nearer to the edge then higher energy electrons.

The variations in electron scattering with material (trimmer) type (see Figure 4-25) also shows how larger areas of exposed edge face lead to larger scatter yields, since the middle trimmer (stainless steel/aluminium) has a face approximately three times as large as for the other two trimmers. The variations shown are also dependent on the materials themselves. A prediction of Lax and Brahme (1980) was that scatter yield (or dose due to scatter) is inversely proportional to material density. This would greatly increase the scatter from the

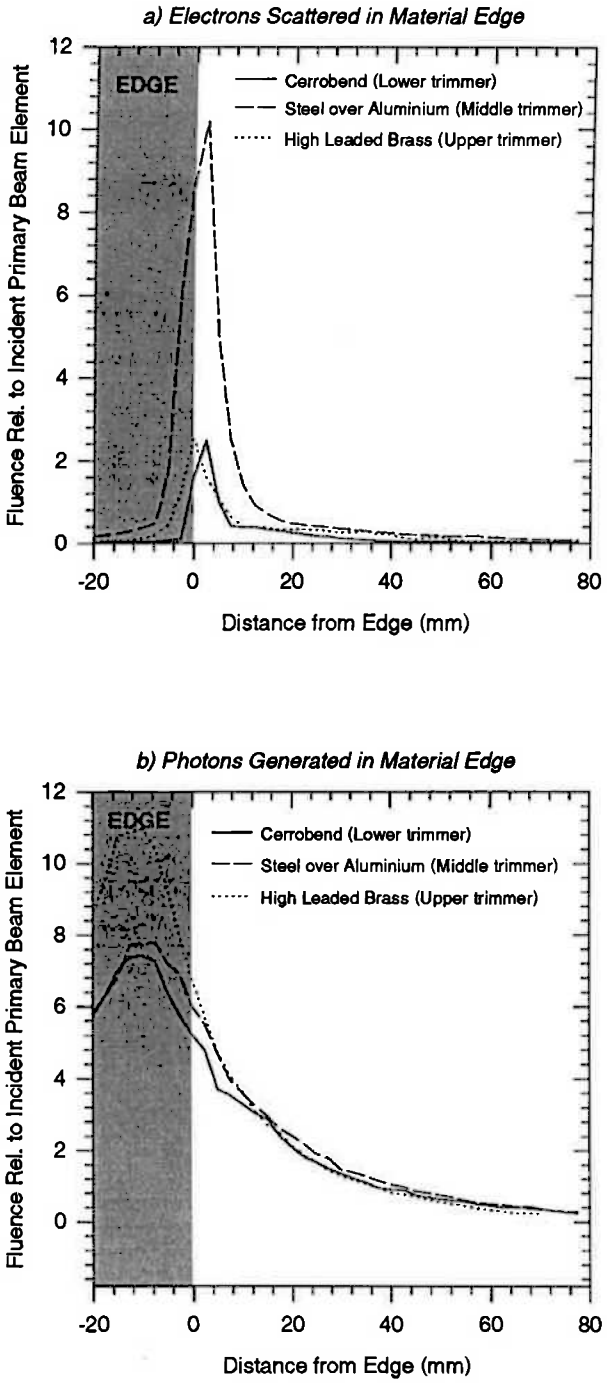

Figure 4-25: a) Scattered electron and b) edge generated photon fluence profiles for a variation in trimmer type (material), percentage normalised to the incident beam fluence. All profiles for a beam incident at 1.83° to the primary beam central axis direction and scored 20 mm below the edge.

aluminium relative to other materials (aluminium having the lowest density of all materials used), and help enhance the level of scatter from the middle trimmer. Also note that, although the brass edge has only approximately 80% of the height of the cerrobend edge, scatter yields are approximately equal, consistent with the predictions of Lax and Brahme (1980) since the brass used has a density approximately 80% that of cerrobend.

Variations in photon scatter yields with incident electron beam angle (Figure 4-23) do not show the variations that electron scatter does since photon generation will not be sensitive to slight changes in the angle of electron incidence. This is since the effect due to incidence angle is overshadowed by electron scattering in the high-density materials. Consequently, the main effect is a slight shift in the photon peak below the edge with variation in incidence angle. Variations with incident electron beam energy (Figure 4-24) can be explained by the variation in energy fluence with energy, and the variation in the ratio of radiative to collisional stopping power (see §2.1.2.3) with energy. As energy increases, the energy fluence increases similarly, and greater amounts of energy are available for release in the edge materials. The ratio S_{rad} / S_{col} is also approximately proportional to electron energy, thus increasing the preference for radiative energy loss with increasing energy.

Variations in photon yields with trimmer type (Figure 4-25) reflect more complex differences in the materials present, and their geometries including the thicknesses of edges. S_{rad} / S_{col} is expected to increase with the atomic number of components of the metals in trimmer apertures, and this would increase photon yields in brass and cerrobend relative to the steel/aluminium combination. The density of materials will also affect such yields since more electrons will be scattered out of lower density materials (Lax and Brahme, 1980), providing fewer electrons to stop by radiative collision in the edges themselves. Photon yields will also be influenced by the thickness of edges due to photon absorption. These factors yield the distributions shown in Figure 4-25.

Figure 4-26 shows the variation in kinetic energy spectrum for electrons scattered from the edge at two different locations, for incident beam energies 6, 12 and 18 MeV. The primary beam spectra for these energies are also shown. The variation in mean energy with distance from the applicator edge (along a horizontal line 50 mm below the edge) for scattered

electrons and edge-generated photons for incident 6, 12 and 18 MeV beams is shown in Figure 4-27. The spectra for small angle (forward directed) scattered electrons (position A of Figure 4-26) are very similar to the incident spectrum indicating that these electrons have travelled little distance through the high density cerrobend. The spectra corresponding to larger angle scattering (position B of Figure 4-26) bear little resemblance to the incident beam spectra, with no obvious peak except for a minor low energy dominance. These electrons have been scattered widely and thus are likely to have travelled a greater distance through the cerrobend. The variations that occur in electron energy spectra imply that it will be necessary to include the variation in spectra with angle of scatter in a model for this component.

In Figure 4-27, it is seen that some beam hardening occurs for electrons that are scattered at highly oblique angles from the edge. Those scattered at larger angles have undergone more scattering in (have traversed larger paths in) the cerrobend and will thus have suffered greater energy loss as mentioned above, leading to lower mean electron energies. A similar pattern is seen for photons generated in the edge.

Figure 4-28 shows, for the photon component of a 12 MeV electron beam, how mean energies of transmitted and scattered primary beam photons vary beneath the edge. Filtering of low energy components of the incident bremsstrahlung spectrum leads to hardening of the transmitted component.

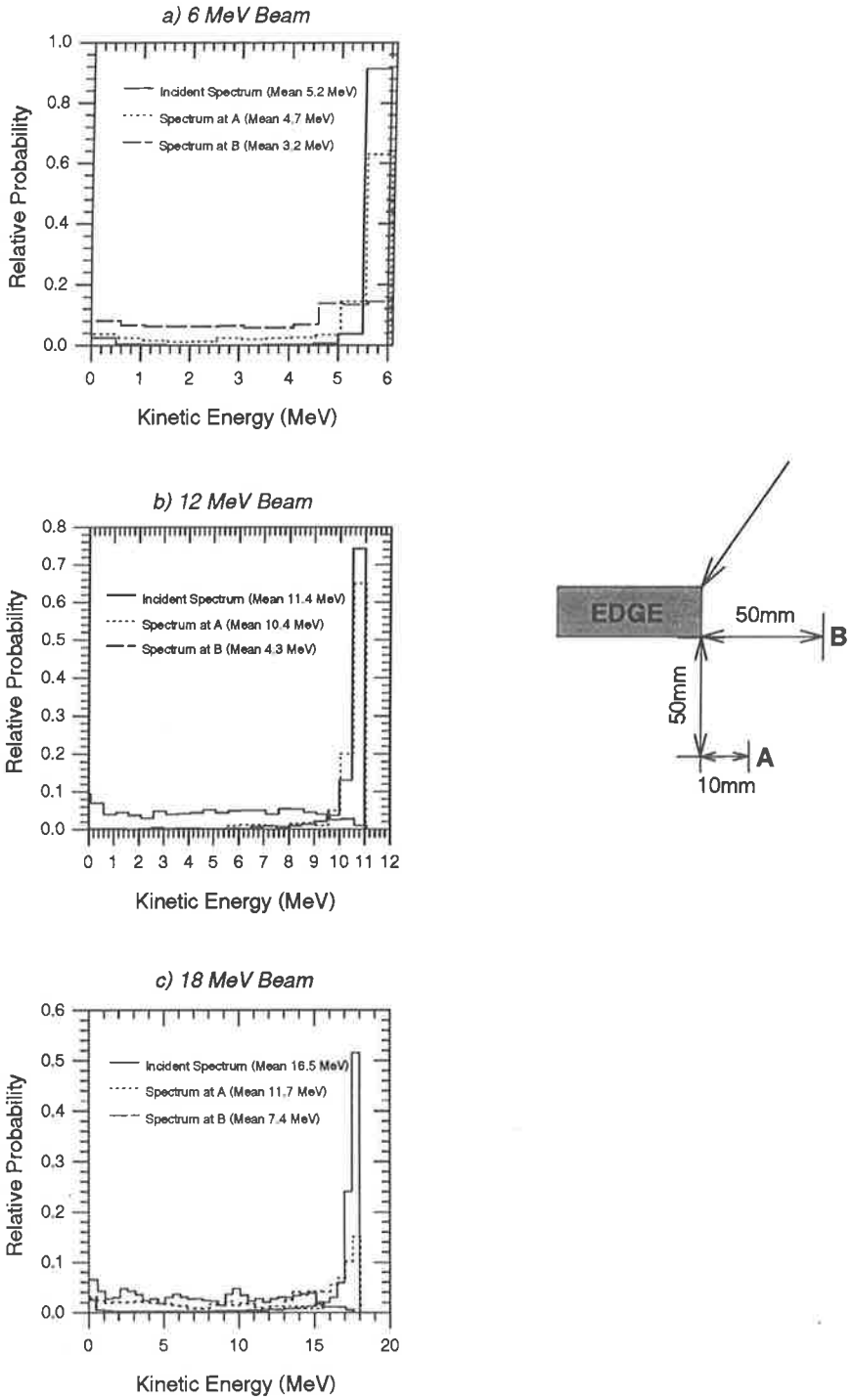

Figure 4-26: Kinetic energy spectra of scattered electrons and incident spectrum, electrons incident at 1.83° to a cerrobend edge for beam energies a) 6 MeV, b) 12 MeV and c) 18 MeV. The scattered spectra have been determined at two locations in the *XZ* plane normal to the edge element as shown.

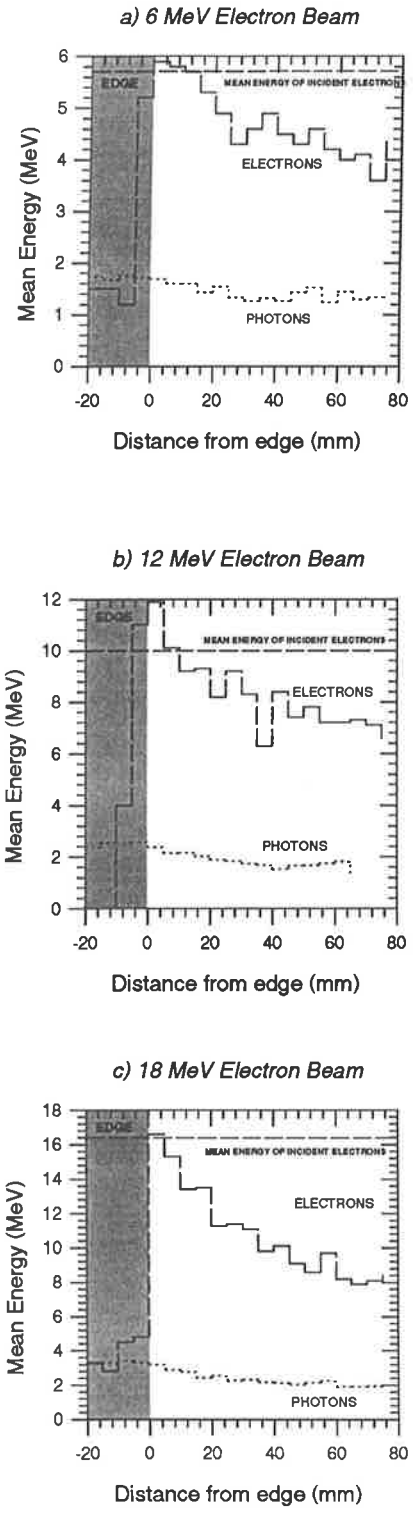

Figure 4-27: Variation in mean energy of scattered primary beam electrons, and edge generated photons, with distance from the edge location. Incident primary beam energies are a) 6 MeV, b) 12 MeV and c) 18 MeV, and the mean energy profiles have been scored 50 mm below the edge.

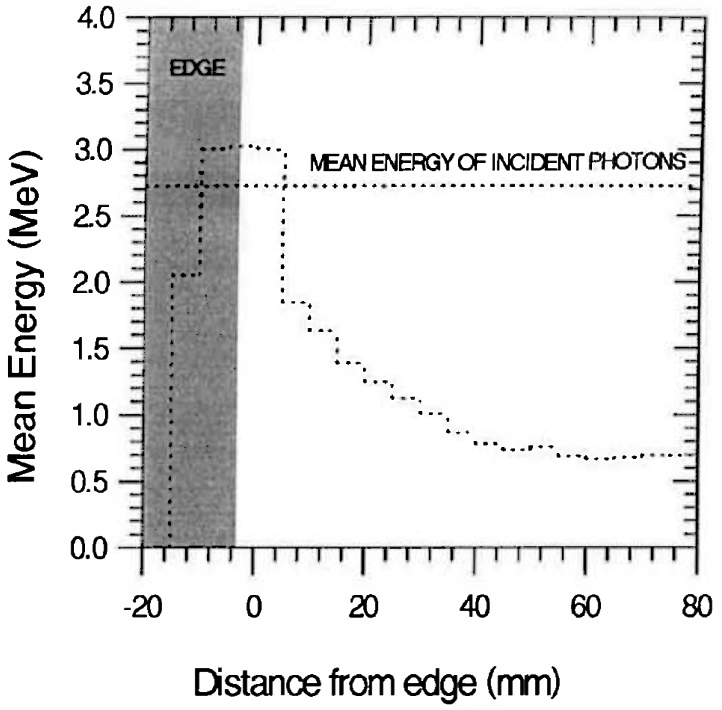

Figure 4-28: Variation in mean energy of scattered primary beam photons with distance from the edge location. Incident primary beam energy is 12 MeV and the mean energy profiles have been scored 50 mm below the edge.

4.2.5. Conclusions

The above investigation of particle scattering from electron beam applicators has provided a basic knowledge of the principle components leading to applicator scatter dose and of their scattering characteristics. It was seen that the major perturbation in the incident beam characteristics caused by an applicator is from scattered electrons. The effect of the applicator trimmers on the photon component of the primary beam may be approximated by a simple attenuation. Variation of scatter characteristics with primary beam energy and angle of incidence (trimming aperture size) indicate that these variables need to be considered when establishing a full model for apertures of irregular shape. This result also

has ramifications for the construction of applicators, since energy-specific applicators may be designed (by considering the edge geometry) in a way to manipulate scatter characteristics in order to achieve desired applicator scatter contributions. The dependence of the spectrum of scattered particles on scattering angle also requires that energy characteristics be considered in order for applicator scatter to be faithfully represented.

4.3. Superposition Model

4.3.1. Introduction

To the author's knowledge, no models have been presented for obtaining extensive knowledge of the effect of shaping devices on the beam phase space short of full Monte Carlo treatment head simulations (Udale, 1988; Udale-Smith, 1992; Rogers *et al.,* 1995). To obtain such information, a model is required which can account for the major factors influencing applicator scatter characteristics and generate phase space data for such scattered particles. Also, considering the possible variation that can occur in cutout geometry and beam energy combinations, the model should be able to simulate arbitrary cutout design with an efficiency acceptable in clinical practice.

To this purpose then, the Monte Carlo based algorithm described below was developed to account for particles scattered from arbitrarily configured tertiary beam shaping collimators. This model takes into consideration the effects of scattering from all trimming plates composing an applicator and the characteristics of this scattering in terms of particle yields (relative to the primary beam), directions, and energies. The estimation of output variations due to scatter from an applicator (though not due to disequilibrium as a result of field size) is thus an inherent feature of the model. Advances in computer hardware speed and storage capabilities are making computationally intensive techniques more viable, and the current model takes advantage of this whilst still retaining a reasonably simplistic and intuitive approach.

4.3.2. Model Description

In order to utilise the accuracy of Monte Carlo, the simulations described in §4.2 were used as the basis for obtaining applicator scatter properties. Characteristics of scattered particles for beams incident on edge elements (beam confined to a small section of a semi-infinitely long edge) are stored in *scatter kernels* - a 2D Cartesian array of voxels representing the fluence of scattered particles beneath the edge relative to incident primary beam fluence, and a scored energy distribution in each voxel. Distributions for different particle types are stored in separate kernels. The edge to scoring plane distance, the voxel resolution, and the energy spectra resolution are chosen in order to optimise resolution in the areas of highest fluence differential, and yet still ensure manageable kernel file sizes as well as scoring of significant fluences at large scattering angles. The influence of the aluminium walls of the applicator (Figure 4-1) on beam characteristics was neglected. Since edge scatter is dependent on edge geometry, material, and beam energy, kernels were generated for each beam energy considered, for each trimming plate SSD and material, and at a set of discrete edge radii relative to the primary beam's central axis. A library of such kernels must be stored so that different energies, field sizes and applicator cutouts can be accounted for.

In order to build up a phase space of particles below the applicator, the established kernels must be sampled. For this purpose, each applicator aperture (each trimmer) is considered in turn, and broken up into elements of the size modelled. In the current method, the number of particles required in the phase space is first specified, and then this number is broken up into contributions from each aperture making up the applicator, and then each element in each aperture.

The final phase space distribution can be considered as a summation of contributions from each kernel applicable to each edge element of each aperture. The set of applicator apertures (trimmers), a_α, (α=1,..,$N^{apertures}$), are broken up into elements a_α^e, (e=1,...,$N_\alpha^{elements}$), where $N_\alpha^{elements}$ is the number of such elements for aperture α, and $N^{apertures}$ the number of apertures. We then have a scatter kernel appropriate for that element, $R_\alpha^e\left(\varphi,\psi,\boldsymbol{r}_\alpha^e\right)\cdot\Omega_\alpha^E\left(i,j,\boldsymbol{r}_{eff}^e\right)$. The factor $\Omega_\alpha^E\left(i,j,\boldsymbol{r}_{eff}^e\right)$ corresponds to the relative fluence value of the i,j voxel of the scatter kernel for aperture type α at position $\boldsymbol{r}$, for an

incident electron beam energy E. r_{eff}^{e} is the effective radius of the edge element and is described in Appendix D. $R_{\alpha}^{e}\left(\varphi,\psi,r_{\alpha}^{e}\right)$ is an operator accounting for the source to aperture distance of the current aperture through the element's position, r_{α}^{e}. It also accounts for the fact that , whereas scatter kernels in the library are generated with edge elements placed symmetrically with respect to the primary beam central axis, real edge elements may not necessarily be so. Such effects may be accounted for with the angle of obliquity , ψ, and the angle of incidence, φ. These angles and appropriate corrections are also described and derived in Appendix D.

The primary beam fluence may be described by

$$\Phi^{p}(r)=\Phi_{s}^{p}(r)\Phi_{CA}^{p} \tag{4.6}$$

where $\Phi_{s}^{p}(r)$ is a function describing the shape of the primary beam fluence profile normalised to the central axis value, and Φ_{CA}^{p} is the central axis primary beam fluence at the phase space SSD. The sampled distribution is then the summation of kernels around all apertures operated on appropriately, and weighted according to $\Phi_{s}^{p}\left(r_{\alpha}^{e}\right)$. So as a function of position (x,y) in the plane of the final phase space, we have a normalised fluence distribution

$$\frac{\Phi\left(x,y,z_{scoring}\right)}{\Phi_{CA}^{p}}=\sum_{\alpha}^{N^{apertures}}\sum_{e}^{N_{k}^{elements}}\sum_{i,j}^{kernel\,size}\Phi_{s}^{p}\left(r_{\alpha}^{e}\right)\cdot R_{\alpha}^{e}\left(\varphi,\psi,r_{\alpha}^{e}\right)\cdot\Omega_{\alpha}^{E}\left(i,j,r_{eff}^{e}\right) \tag{4.7}$$

which the sampled phase space should approximate. The normalisation to Φ_{CA}^{p} is implicit in the establishment of scatter kernels. The general algorithm developed proceeds as described in Appendix E.

The masking effects of lower apertures is carried out using the polygon clipping routine described by Steidley et. al. (1994) (see Appendix C). No attempt is made to account for scattered particles scattering again off lower apertures since it was assumed that such a component would be negligible. In determining a particle's direction, it is assumed that all emerge from a common point at the centre of the face of the edge element. Once a phase space file has been established, it can then be used as input into an advanced treatment

planning algorithm, or further Monte Carlo simulation. This is a two-step simulation (see §4.1.2.2), though energy/angle/position correlation information is retained.

Appendix E provides a flow diagram of the C program written to execute this algorithm, together with examples of input and output files. Scatter kernels generated using EGS4 are ASCII data files which contain a header providing information regarding the kernel (ie., beam energy, trimmer, voxel numbers and sizes, scoring plane location, energy resolution). These files have coded file names for referencing from the superposition program. A typical kernel file name would be **AtB_eC_rD.dat** with

A = 'E' for electron kernels, 'P' for photon kernels;

B = '1' for upper trimmer, '2' for middle trimmer, '3' for lower trimmer / cutout;

C = nominal primary beam energy (eg., '12' for 12 MeV primary beam);

D = edge radius (eg., '3.5' for edge 3.5 cm from central axis).

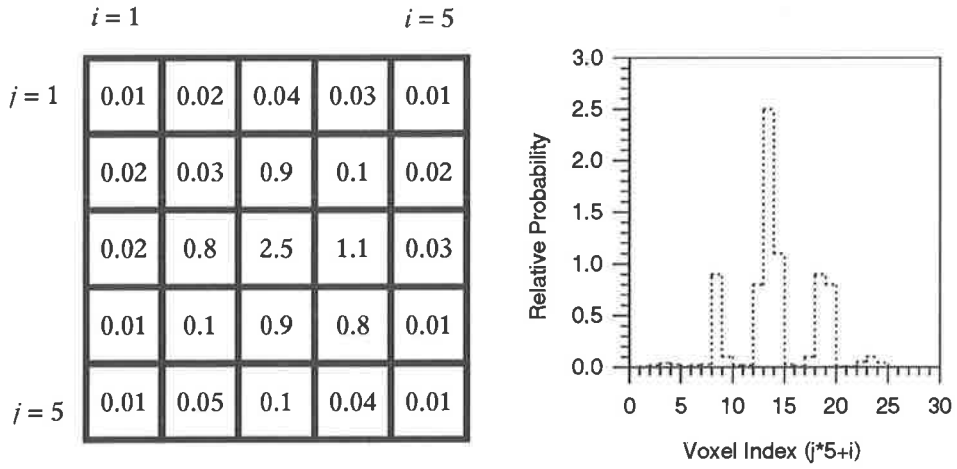

Figure 4-29: Description of scatter probability distribution. The grid on the left represents a scatter kernel beneath an edge element. Voxel values indicate the relative probability of particles scattering to them. The probability distribution represented by this is shown on the right hand side.

Random number generation was achieved using the default ANSI C random number generator with a span of approximately 2^{31} on the DEC 5000/120 workstation used. With the relatively small number of random numbers to be generated per simulation ($< 10^5$) it was felt that the default generator would be sufficient. Probability distributions (spatial

variation of fluence in scatter kernels as well as energy distributions in each voxel of a kernel) were sampled by forming cumulative distributions in each case. A simple example shall be given. Consider the matrix of values in the grid shown on the left of Figure 4-29. This is a simplification of a scatter kernel in a plane below an edge, which shows the relative probability of electrons being scattered to each voxel in the scoring plane. The relative probability with voxel index is shown on the right hand side. To sample from this distribution, we form the cumulative probability distribution as shown in Figure 4-30, with the probability total accumulating with voxel index to a maximum of unity. We form the cumulative distribution

$$P(i,j) = \frac{\sum_{i',j'=1}^{i,j} \Theta(i',j')}{\sum_{i',j'=1}^{I,J} \Theta(i',j')} \tag{4.8}$$

where $\Theta(i,j)$ is the relative probability for the voxel with index $(j*5+i)$. The resulting cumulative probability distribution is shown on the right hand side of Figure 4-30. To sample a kernel voxel, a random number is selected on the interval [0,1]. The selected voxel index then corresponds with the random number as its relative probability [eg., if the number selected is 0.4, then voxel index 13 corresponds (j=2, i=3 in the above example)].

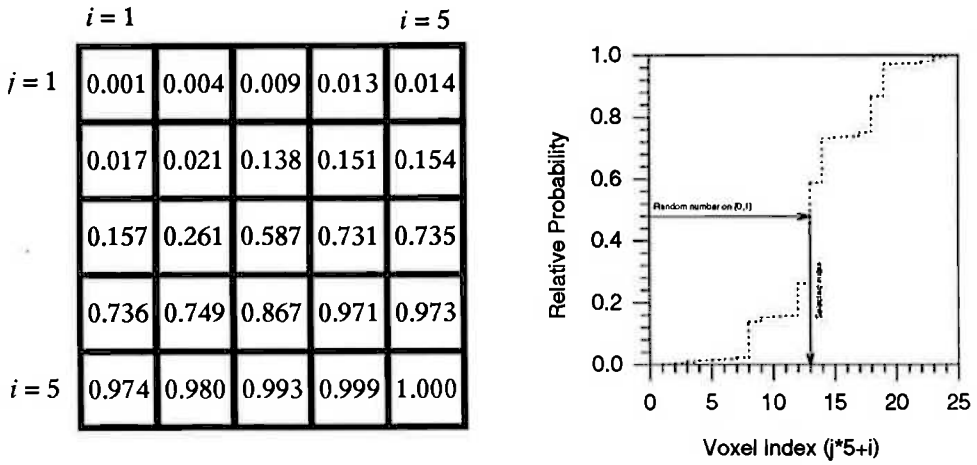

Figure 4-30: The probability distribution of Figure 4-29 transformed into a cumulative distribution for sampling purposes. Sampling the distribution involves obtaining a random number on the interval [0,1], and projecting from the relative probability axis to the probability histogram to determine which voxel index corresponds.

The final phase space file contains the characteristics of each sampled particle. These are the x and y position in the scoring plane (normal to beam axis), the particle charge, particle energy, x,y and z direction cosines, and weighting. The weighting is the probability of each scattered particle resulting from unit incident fluence of the primary beam, and is scaled according to the SSD of the scoring plane and relative location of trimmers. The totalled weighting of all scored particles gives the expected number of particles reaching the scoring plane per unit incident primary beam fluence.

4.3.3. Evaluation Method

The model for applicator scatter was evaluated using measured dose distributions from a Siemens Mevatron KD2 linear accelerator with associated applicators and cerrobend cutouts. Measurement were made with a Scanditronix RFA7 dosimetry system and p-Si electron diode. The applicators of concern have three distinct apertures which shall be referred to as the upper, middle, and lower trimmers as shown in Figure 4-1. Cerrobend LMPA cutouts with non-diverging edges are placed within the lowest aperture. Cross section data for the materials associated with each aperture plate (as shown in Figure 4-1) was generated using the EGS4 preprocessor PEGS4 (Bielajew and Rogers, 1987), and scatter kernels were generated using EGS4 (ECUT=AE=0.521 MeV, PCUT=AP=0.01 MeV) as described above in §4.2.3 for 5 mm wide edge segments at appropriate edge radii to a resolution of 5mm. Kernels were scored in a 20x20 voxel plane with voxel edge sizes varying from 5 mm to 15 mm depending on the resolution required (as described in §4.3.2), with energy spectra scored in 1 MeV bins at each voxel position. Three specific cases were examined:

Case I. A 6x6 cm^2 cerrobend cutout placed on the lowest aperture of a 10x10 cm^2 applicator, for 6 MeV, 12 MeV, and 18 MeV electron beams;

Case II. A 13x13 cm^2 cerrobend cutout placed on the lowest aperture of a 15x15 cm^2 applicator, for a 12 MeV electron beam, and

Case III. An irregular cerrobend cutout (see Figure 4-31) placed on the lowest aperture of a 15x15 cm^2 applicator, for a 12 MeV electron beam.

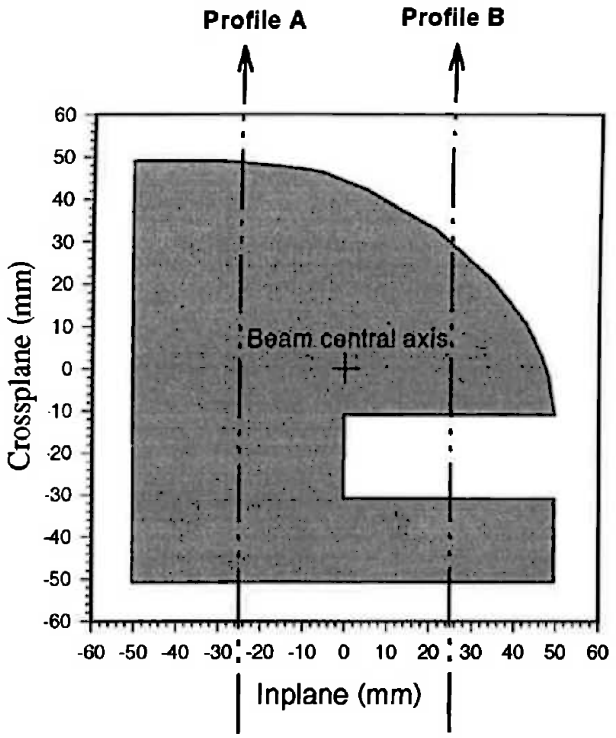

Figure 4-31: The irregular cutout employed with a 15x15 cm^2 applicator in case III showing the two profiles considered.

Nominal field size specifications are at 1m SSD. Phase space data (of between 1x10^5 - 4x10^5 particles per trimmer) for these situations was generated using the developed procedure assuming $\Phi_s^p\left(r_\alpha^e\right)$ to be unity over the full field (this was found experimentally to be accurate for the primary electron beam to within ±5% for the field sizes employed), and used as input to an EGS4 Monte Carlo simulation (ECUT = AE = 0.521 MeV; PCUT = AP = 0.01 MeV) with the user code RTPCART_XYZ (see §2.2.3.2) employing a Cartesian coordinate system. The input option of individual particle characteristics was used in this user code. The same user code was used to simulate primary beam distributions, using either the option for independent collimators for specific field sizes or the polygon clipping option for arbitrary field shape (see §2.2.3.2 and Appendix C) and using angular standard deviation values as shown in Table 4-IV. Normalisation to Φ_{CA}^p for distributions for all

scatter component fluences allowed a simple addition to obtain complete dose distributions normalised to dose due to the primary beam. The primary beam was also simulated using this code, with the angular standard deviation of primary beam electrons determined from beam penumbral measurements (see §4.2.2). The shape of the primary beam fluence profile ($\Phi_s^p(r_\alpha^e)$) was determined from open beam profile measurements and was taken into consideration in the simulation of this component.

For all cases, central axis depth dose distributions to a water phantom beneath the applicator calculated with the superposition method were compared with measured applicator scatter central axis depth dose contributions. The experimental curves were obtained by subtracting an open field depth dose curve (normalised to 100% at the surface) from that measured with the applicator present and the detector normalisation maintained. This is a straight forward procedure when the field employed allows lateral electronic equilibrium to exist at central axis, since in this case the central axis dose is the same as for a collimated primary beam - an increase in field size not affecting the depth dose curve or machine output factor. When this is not the case (as for the 18 MeV beam of 6x6 cm^2 field size and the 12 MeV irregular field), simulations of applicator scatter must be combined with simulations of open beams as well as collimated primary beams (without any applicator scatter) in order to correctly predict the experimental result. The measurement subtraction procedure will magnify measurement errors to values of possibly 5% of primary beam measurements.

Profiles of dose to the water phantom in each case at 5mm depth were measured and calculated for confirmation of the algorithm's ability to predict spatial variations in scatter fluence. These profiles were obtained with the water surface at two different SSD's in each case in order to investigate the validity of the angular characteristics of the modelled scatter. For all regular fields, crossplane profiles passing through central axis were considered. The location of profiles considered for the irregular cutout is displayed in Figure 4-31.

In generating the scatter kernels, the horizontal overlap of the primary beam with the edge elements is large enough so that only those electrons which enter the edge and are capable

of subsequently emerging from the vertical face (due to their maximum range in the material considered) are examined. This is a simple implementation of range rejection variance reduction. A conservative (large) estimate of the electron range was made to determine this overlap distance. As was shown in §4.2.4, dose due to primary beam photons scattered off the applicator may be neglected within the main irradiation field. This component was thus also ignored in calculation of depth dose curves though dose due to photons generated in the applicator by primary beam electrons was considered. For the profiles, the restriction to surface measurements reduced the influence of primary beam photons, though discrepancies due to the influence of low energy or highly oblique photons can still be expected.

4.3.4. Results

Case I

The predicted applicator scatter component of central axis depth dose, together with an experimentally measured curve for the 6x6 cm^2 cerrobend cutout for the three beam energies considered, is shown in Figure 4-32. Dose contributions due to each trimmer are shown in terms of scattered primary beam electrons, and photons generated in each by primary beam electrons. Phase space sizes provided less than 5% uncertainty in surface doses in each depth voxel for the electron depth dose components (for all depth doses considered in this investigation) and 20% for the photon components. This led to less than 7% error in the total depth dose value at the surface since the photon component is minimal in all cases.

Note that the measured scattered component for the 18 MeV beam [Figure 4-32c)] appears to have a negative region because of the open field (uncollimated) depth dose values being larger than the collimated primary plus scatter dose for which there is lateral electronic disequilibrium. This was accounted for in broad and collimated beam simulations as described in the §4.3.3, with the difference between depth dose curves calculated for broad and collimated beams subtracted from the calculated applicator scatter depth dose curve The result of this procedure is shown in Figure 4-33.

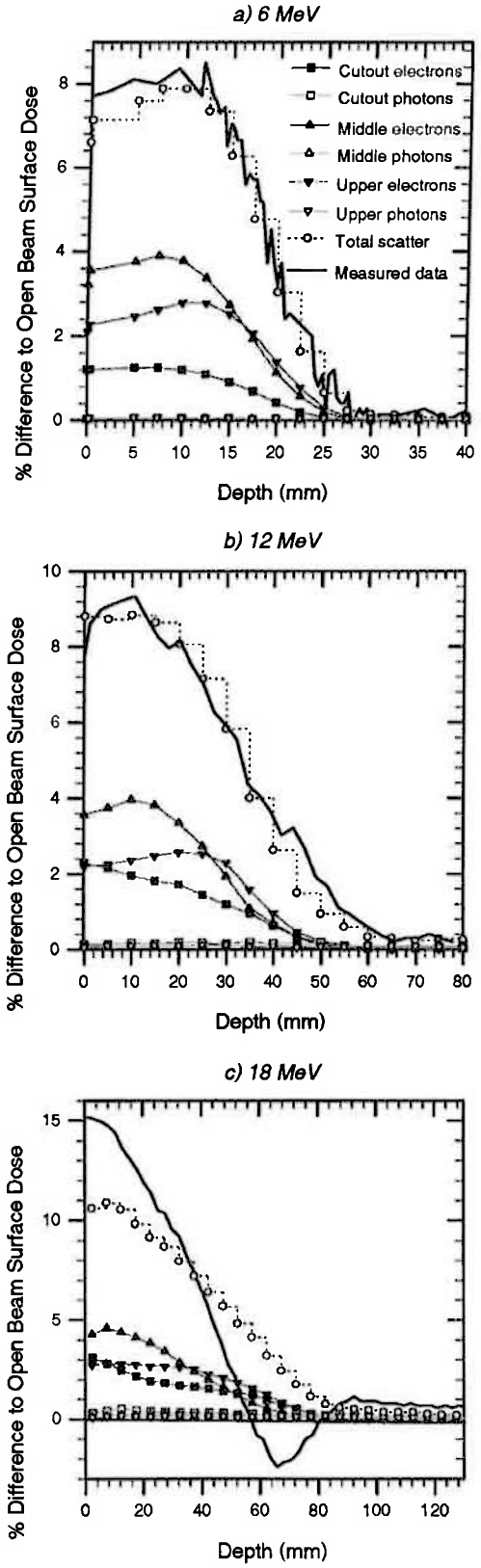

Figure 4-32: Calculated and measured central axis applicator scatter depth dose distributions for a 6x6 cm^2 cutout in a 10x10 cm^2 applicator for electron beam energies of a) 6, b) 12 and c) 18 MeV. Contributions due to electrons scattered from each trimmer as well as photons generated in each are shown. The legend for all depth dose curves is shown in a).

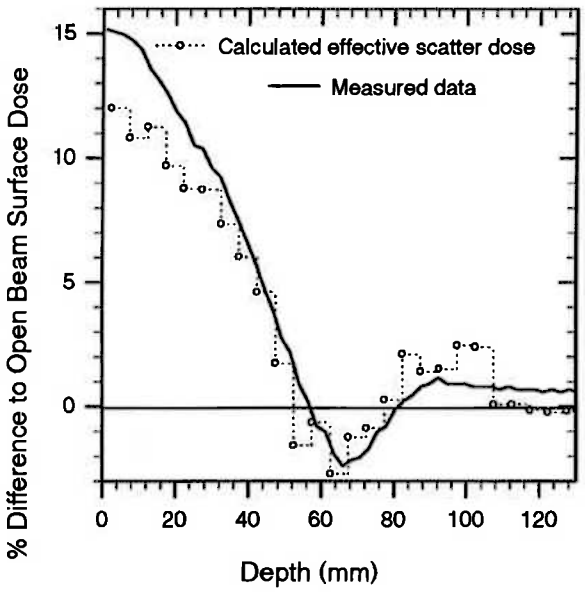

Figure 4-33: Effective applicator scatter depth dose for the 18 MeV electron beam with a 6x6 cm^2 cutout in a 10x10 cm^2 applicator, compared with the measured curve. The calculated curve has been adjusted from the total scatter curve shown in Figure 4-32 by subtracting the difference in depth dose for simulated broad and collimated (6x6 cm^2) beams. This procedure accounts for the lack of electronic equilibrium for the collimated beam and replicates the measurement situation.

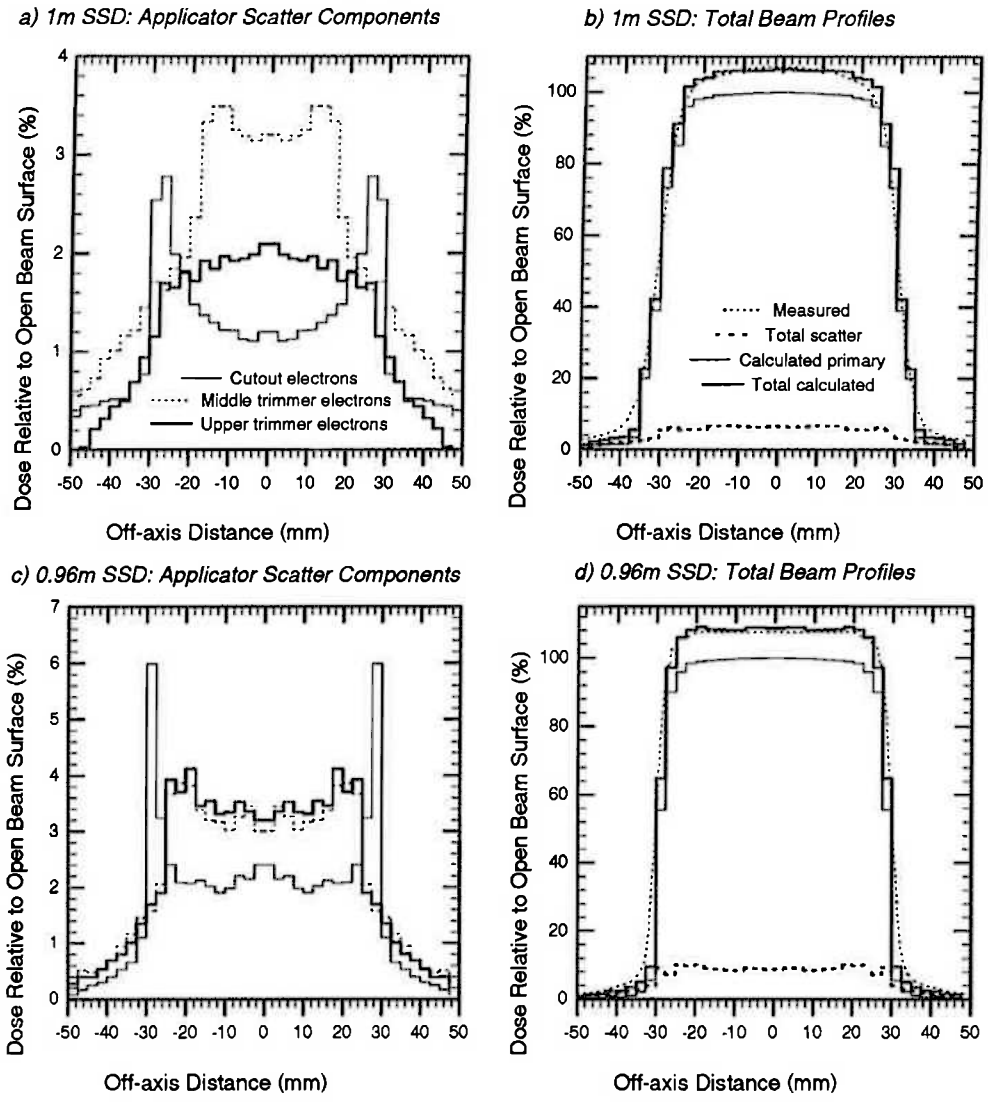

Figure 4-34: Electron beam dose profiles at a depth of 5 mm in a water phantom beneath a 6x6 cm^2 cutout in a 10x10 cm^2 applicator for a 6 MeV electron beam. a) Water surface at 1 m SSD, applicator scatter components only; b) 1 m SSD, total profiles with measured; c) 0.96 m SSD, applicator scatter components only; d) 0.96 m SSD, total profiles with measured.

Profiles for Case I for the 6 MeV electron beam are shown in Figure 4-34. These figures show profiles of dose due to electrons scattered from the three trimming plates of the applicator separately, as well as the resulting total profiles compared with measured results. All profiles are normalised to the surface dose at central axis for the open beam, so that

open beam measured and calculated profiles have 100% at central axis (dose at 5mm depth approximating a surface dose value). The statistical accuracy in individual profile curves is dependent on the voxel resolution employed in sampling scatter kernels as well as the usual Monte Carlo variance. For the profiles considered in this investigation, dose values across most of the principal profile may be assumed to be accurate to within 10% in each voxel. This figure would increase dramatically in low dose areas such as beneath a cutout edge since the phase space data in these areas would consist of numbers of electrons of order 1 to 5 per Monte Carlo simulation voxel. A moderately high uncertainty is not of concern however, as the scattered dose component constitutes a small proportion of the total beam dose. For profiles taken with regular cutouts, symmetry has been used to reduce statistical inaccuracy. Figure 4-35 and Figure 4-36 show similar results for the 12 and 18 MeV beams respectively.

Note the large peaks at field edges for electron scatter from the cutout in each case, corresponding to the dominantly forward-directed scatter from aperture edges (compare Figure 4-21), and the increase in the relative size of the peaks as the distance to the cutout edge decreases.

Case II

Central axis depth dose distributions for case II are shown in Figure 4-37. Calculated and measured profiles for Case II are shown in Figure 4-38, again normalised to central axis open beam surface dose.

Case III

Figure 4-12 shows a scatter plot of $2x10^4$ electron points derived by the superposition algorithm in the scoring plane employed in the 1m SSD case, for electrons scattered from the irregular cerrobend insert (Figure 4-31) for the 12 MeV beam. Note the absence of any distinct scatter aggregation adjacent to the edge along Y = -30mm (-30mm crossplane), which is due to the negative angle of incidence of the beam to this edge, and resulting minimal scatter yield as could be predicted by examination of the variation in scatter with incidence angle [Figure 4-23a)].

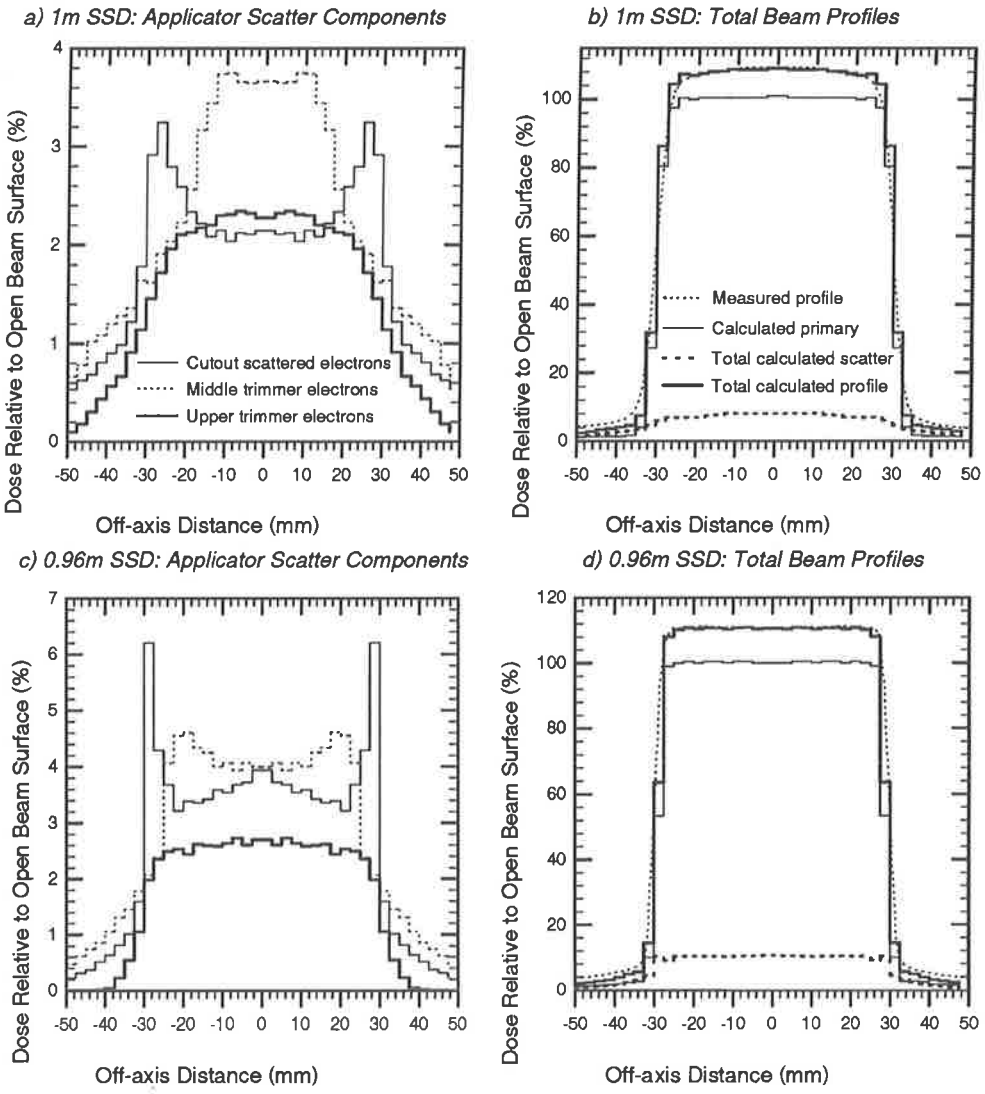

Figure 4-35: Electron beam dose profiles at a depth of 5 mm in a water phantom beneath a 6x6 cm^2 cutout in a 10x10 cm^2 applicator for a 12 MeV electron beam. a) Water surface at 1 m SSD, applicator scatter components only; b) 1 m SSD, total profiles with measured; c) 0.96 m SSD, applicator scatter components only; d) 0.96 m SSD, total profiles with measured.

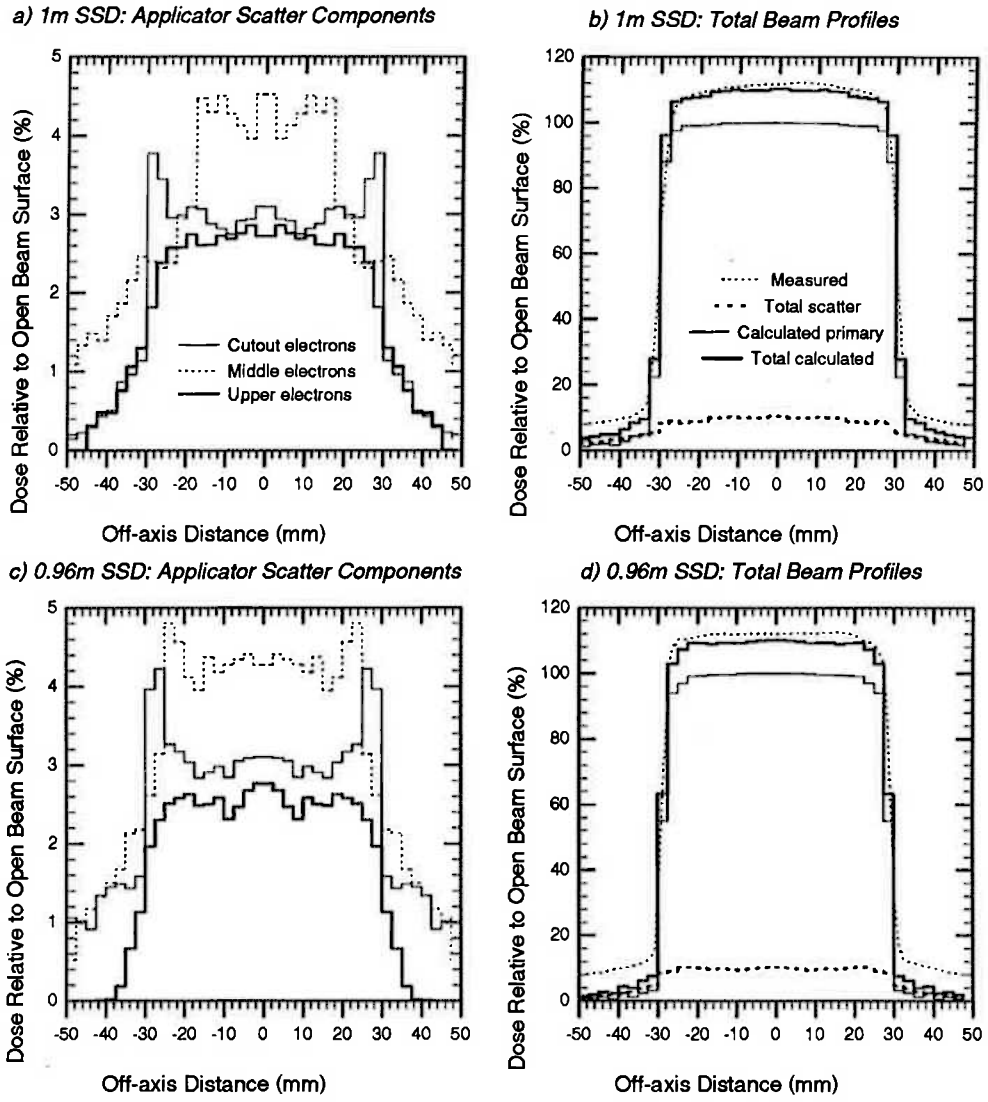

Figure 4-36: Electron beam dose profiles at a depth of 5 mm in a water phantom beneath a 6x6 cm2 cutout in a 10x10 cm2 applicator for a 18 MeV electron beam. a) Water surface at 1 m SSD, applicator scatter components only; b) 1 m SSD, total profiles with measured; c) 0.96 m SSD, applicator scatter components only; d) 0.96 m SSD, total profiles with measured.

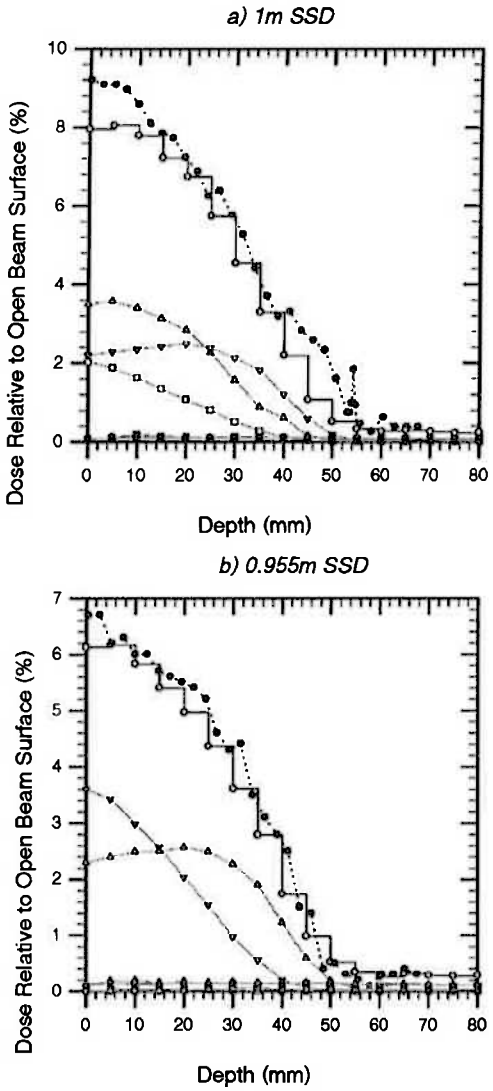

Figure 4-37: Calculated and measured central axis applicator scatter depth dose distributions for a 13x13 cm^2 cutout in a 15x15 cm^2 applicator for an electron beam energy of 12 MeV and water surface at a) 1 m and b) 0.955 m SSD. Contributions due to electrons scattered from each trimmer as well as photons generated in each are shown. The legend for all depth dose curves is shown in Figure 4-32a).

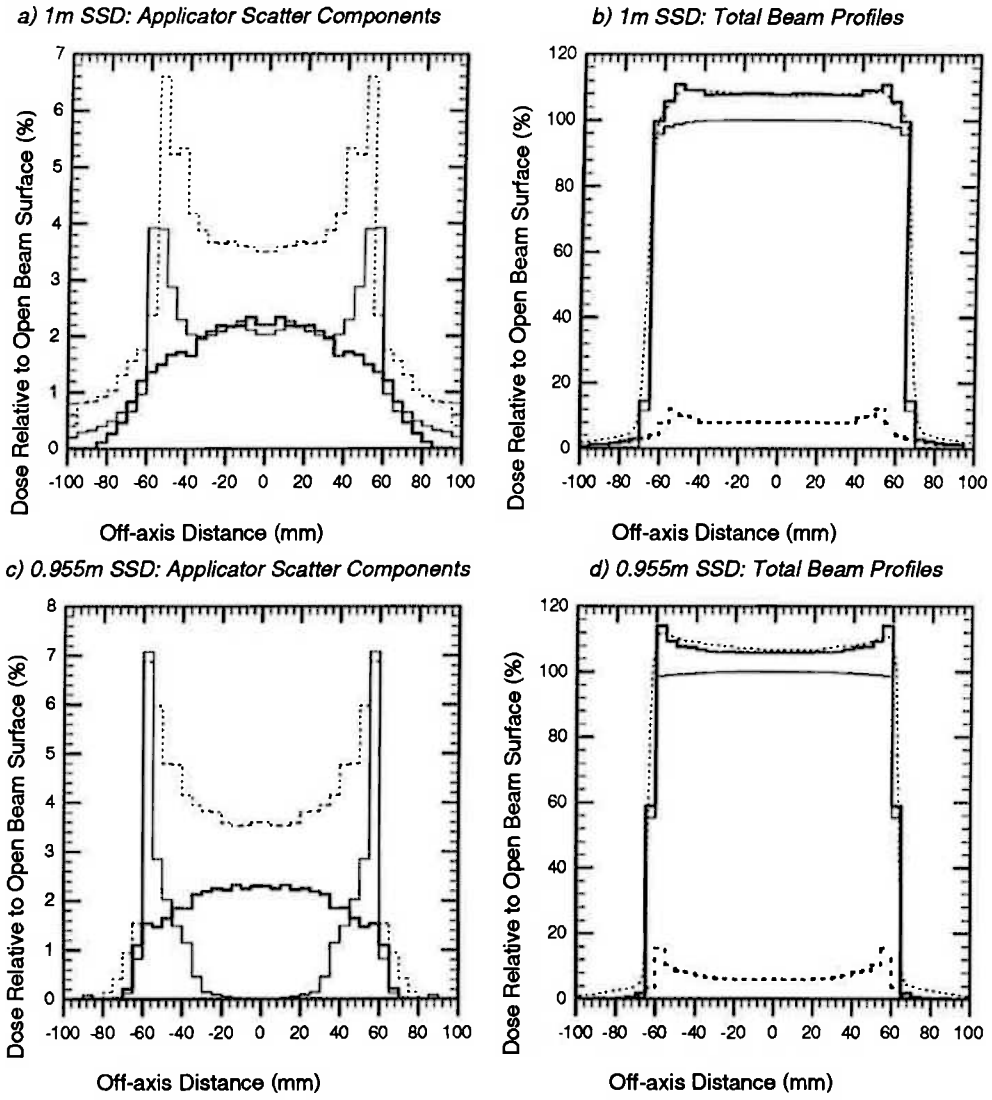

Figure 4-38: Electron beam dose profiles at a depth of 5 mm in a water phantom beneath a 13x13 cm^2 cutout in a 15x15 cm^2 applicator for a 12 MeV electron beam. a) Water surface at 1 m SSD, applicator scatter components only; b) 1 m SSD, total profiles with measured; c) 0.96 m SSD, applicator scatter components only; d) 0.96 m SSD, total profiles with measured. See Figure 4-34 for legend information.

Figure 4-39 displays depth dose curves at central axis for the irregular cutout in a 12 MeV beam. For this figure, the total experimental curve shown was obtained by finding the difference in depth dose between a Monte Carlo simulated open beam, and one simulated by Monte Carlo with a routine applied to simulate the masking of the irregular cutout (in the usercode `RTPCART_XYZ` described in §2.2.3.2), and subtracting this from the total depth dose curve due to the applicator trimmers. This results in the negative contribution

which is seen in these curves [as for Figure 4-32c)]. Figure 4-40 shows the measured and calculated profile A for the irregular cutout, at the two SSDs examined. Profiles for profile B for the irregular cutout are shown in Figure 4-41.

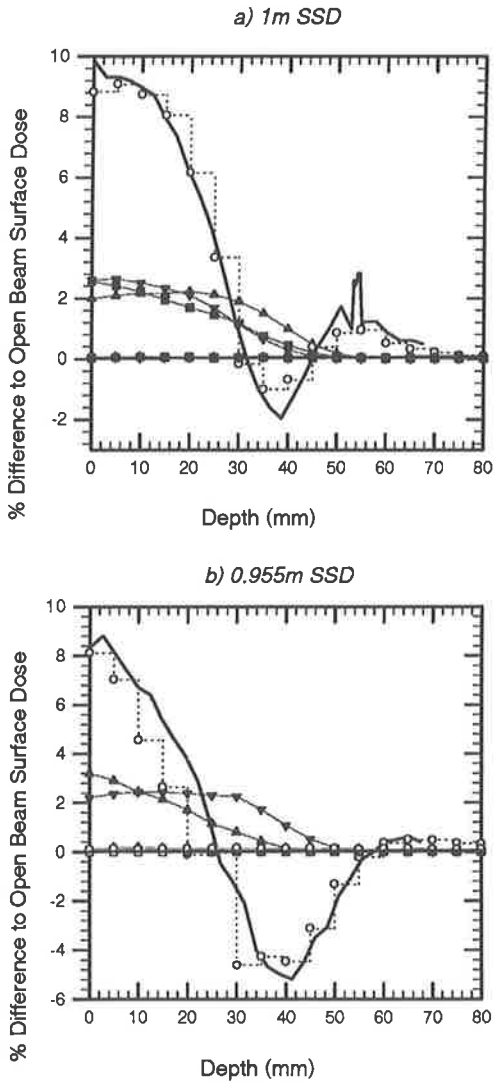

Figure 4-39: Calculated and measured central axis applicator scatter depth dose distributions for the irregular cutout of Figure 4-31 in a 15x15 cm^2 applicator for an electron beam energy of 12 MeV with water phantom surface at a) 1 m and b) 0.955 m SSD. Contributions due to electrons scattered from each trimmer as well as photons generated in each are shown. Correction for lateral electronic disequilibrium has been made to the total calculated curve, which thus represents the effective scatter dose (ie., collimated primary beam + applicator scatter - open primary beam as for Figure 4-33). See Figure 4-32a) for legend information.

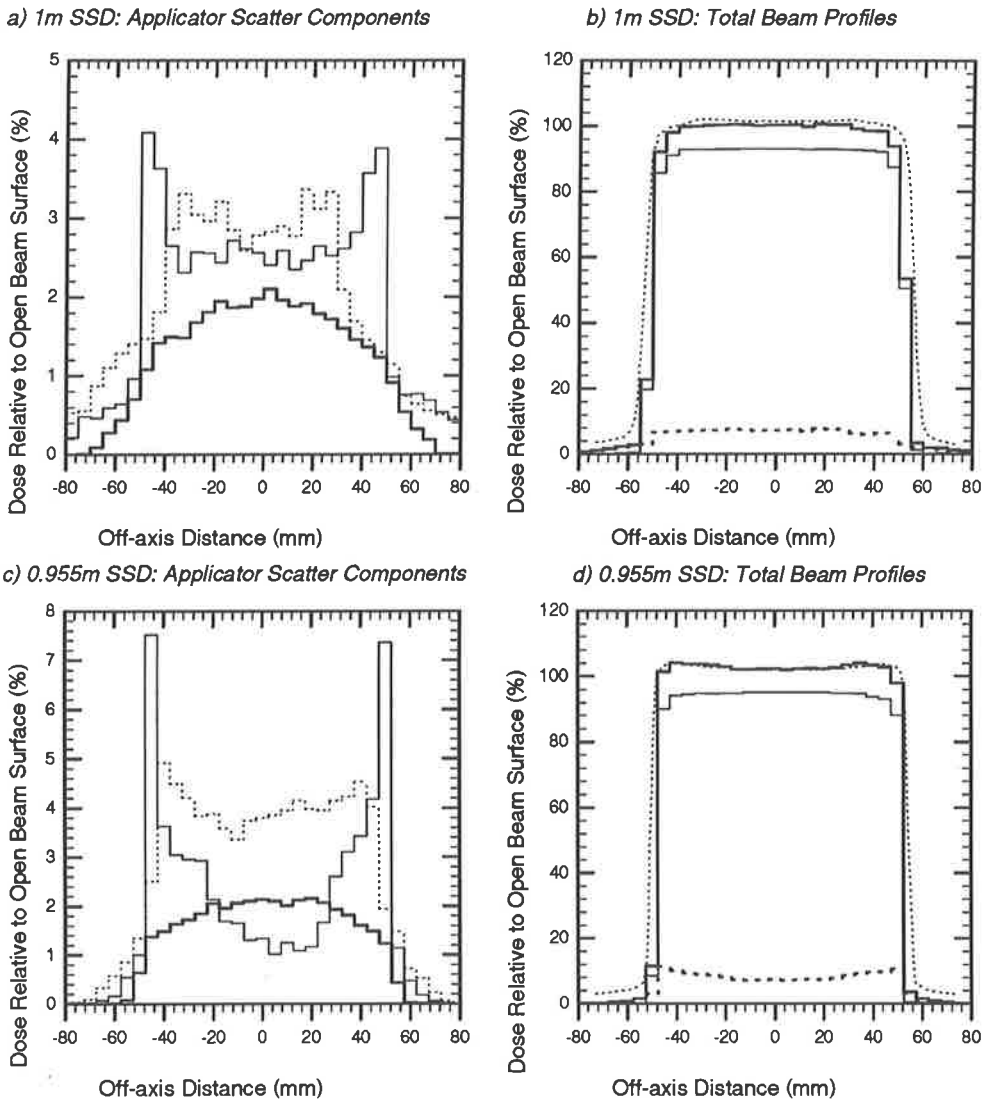

Figure 4-40: Electron beam profile A at a depth of 5 mm in a water phantom for the irregular cutout of Figure 4-31 in a 15x15 cm^2 applicator for a 12 MeV electron beam. a) Water surface at 1 m SSD, applicator scatter components only; b) 1 m SSD, total profiles with measured; c) 0.96 m SSD, applicator scatter components only; d) 0.96 m SSD, total profiles with measured. See Figure 4-34 for legend information.

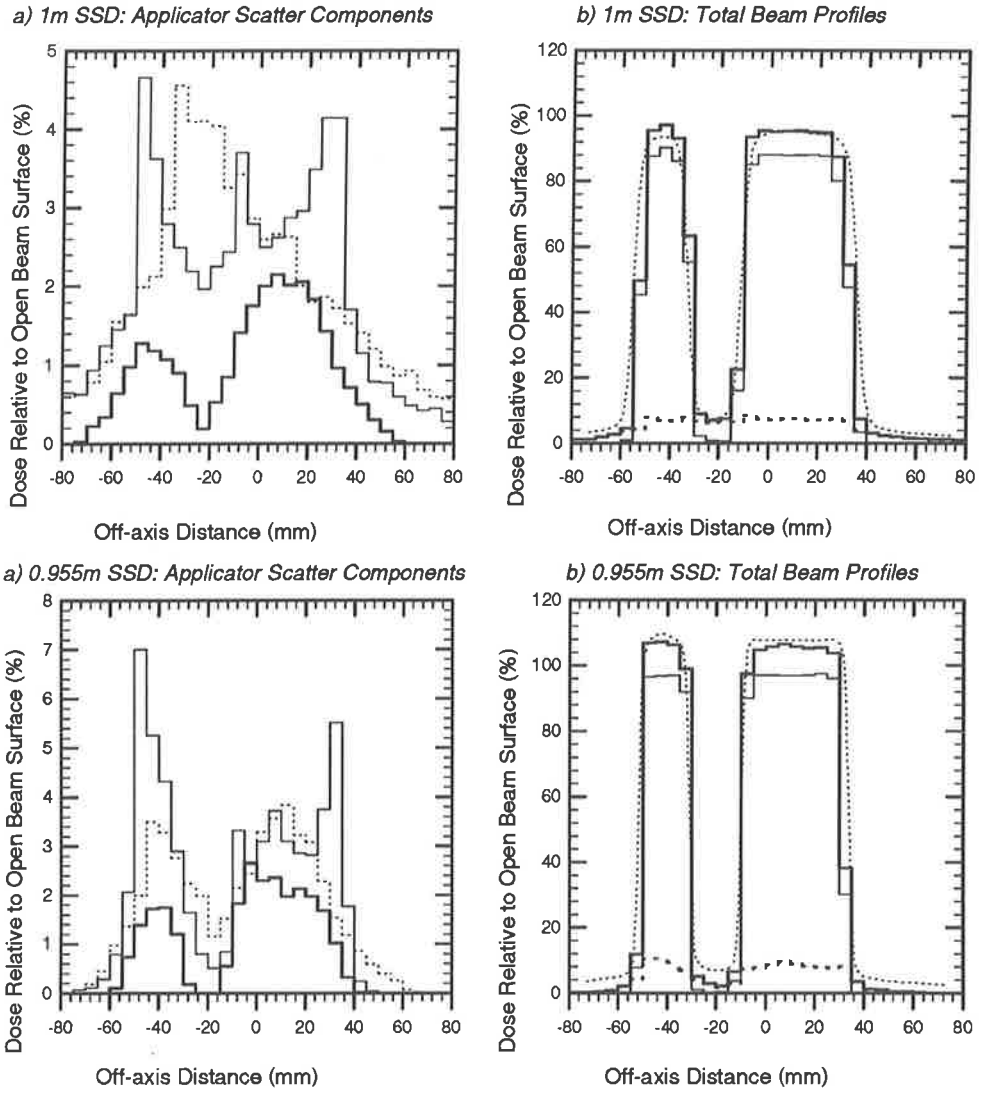

Figure 4-41: Electron beam profile B at a depth of 5 mm in a water phantom for the irregular cutout of Figure 4-31 in a 15x15 cm^2 applicator for a 12 MeV electron beam. a) Water surface at 1 m SSD, applicator scatter components only; b) 1 m SSD, total profiles with measured; c) 0.96 m SSD, applicator scatter components only; d) 0.96 m SSD, total profiles with measured. See Figure 4-34 for legend information.

4.3.5. Discussion

The consistency of calculated and experimental results in this investigation has provided validation of the developed model in several ways. The depth dose curves considered are consistent with measured curves both in terms of curve shape, as well as absolute magnitude. The correct prediction of the effect on output of the applicators stems from the accuracy and correct normalisation of the Monte Carlo simulations employed for obtaining scatter kernels. This is combined with the superposition algorithm's ability to provide each particle in the phase space with an accurate weighting.

One consistent discrepancy between the model and measurement is in the build-up region for the depth dose curves [particularly prevalent in Figure 4-32a) and b), Figure 4-33, and Figure 4-37a)]. In these cases the model tends to underestimate the surface dose due to scattered electrons, implying a neglect of lower energy particles. This could be due to a combination of:

i) the magnitude of the energy bins used in storing kernel data and an inability to faithfully sample lower energy bins (sampling being performed uniformly across a bin);

ii) a lack of low energy bremsstrahlung and photoelectron production in kernel generation due to the range rejection variance reduction employed;

iii) the neglect of electron production in the applicator materials due to primary beam photons, though this component has previously been found to be quite negligible (see §4.2.4).

The individual depth dose curves for trimmer-scattered electrons and trimmer generated photons display the dominant contribution of scattered electrons (rather than photons) to applicator scattered dose. The photon component is quite negligible, though is necessary for ensuring consistency in the tail region of the depth dose curve, with the upper trimmer producing the largest photon component since it has the highest effective atomic number. The shapes of individual electron component curves reflect the variation in origin of electrons from the three trimming plates. d_{max} for each moves closer to the surface as incident electrons become more oblique, the curves for the cutout contribution showing

little build-up and those for the upper trimmer closely resembling depth dose curves for normally incident beams. The middle trimmer contributes a dominant amount to dose since it has the largest vertical face, and results in the largest relative proportion of applicator scattered particles (see Figure 4-25).

When considering depth dose curves where lateral disequilibrium exists (Figure 4-33 and Figure 4-37), it is important to remember that the curves involve a culmination of errors. These stem from the subtraction of the measured open and collimated curves, the calculation and addition of the individual component curves, and the calculation and subtraction of Monte Carlo simulated open and collimated beams. This could lead to the discrepancies of sometimes 3% of the normalisation value which is seen.

Profile results for individual SSDs are consistent with experiment in the umbral as well as penumbral regions, with some discrepancy occurring at field edges due to the neglect of primary beam photons, as well as leakage radiation (Kassaee *et al.,* 1994) which is not taken into account in the generation of kernels. This effect is most obvious for the 18 MeV irradiation [Figure 4-36c)] since this beam has the highest level of photon contamination of the energies considered. The shapes of individual profiles for applicator scatter components again reflects the origin of the electrons, with curves due to cutout scattered electrons displaying the greatest contribution to field edge horns. The influence of the angle of incidence of the beam on the numbers of electrons scattered off edges (see Figure 4-23) implies that the size of field edge horns could be reduced by producing cutouts with edges which diverge from the beam source.

The angular characteristics of the scattering are seen in the variation in the size of field edge horns with distance from the trimmer edges, particularly obvious in comparison of Figure 4-38b) and d). Profiles for individual applicator scatter components also display this effect with curves for electrons scattered from the cutout edge showing marked increases in horn size as SSD is reduced. The effect is also apparent for scattering from the middle applicator trimmer, particularly for the larger applicator curves in Figure 4-38a) and c) where the cutout used did not effectively shield out forward scatter from the middle trimmer.

An interesting effect is seen in profile B of the irregular cutout as shown in Figure 4-41. With the water surface at 1m SSD (50 mm below the bottom of the applicator), the contribution from the middle trimmer appears to be enhanced below the cutout section which protrudes into the beam. This is because the protruding section of the cutout screens the region of the beam for crossplane > 0 mm (see Figure 4-31) due to the location of the middle trimmer with respect to the cutout. When this is simulated correctly the result is the enhancement of dose beneath the protrusion and the correct prediction of this dose in the total profile [Figure 4-41b)]. For the 0.955m SSD case though, this component is greatly reduced and results in an *underestimate* of dose beneath the protrusion in the total profile [Figure 4-41d)]. The penumbral tails for this figure are also more greatly underestimated than for the 1m SSD case. The most likely reason for this is the approximation used in making the centre of a trimmer edge element the origin of scattered particles, combined with the masking routine that is employed. When the polygon clipping routine is employed for the masking effect of the cutout, the close proximity of the scoring plane to the cutout could cause many highly oblique electrons from the middle trimmer to be discarded. This effect is dependent on what SSD is used in the routine to account for masking by the cutout, which can vary over the thickness of the cutouts used (12 mm).

4.3.6. Conclusions

The comparison of the measured and calculated dose distributions examined have shown the developed superposition model for electron beam applicator scatter to be accurate. This method of obtaining applicator scattered phase space information would be considerably more time and compuationally efficient than full Monte Carlo simulations once scatter kernels have been derived. The most significant benefit is in the establishment of this data for cutouts of irregular shape, customised for individual treatments.

The model could possibly be improved in accuracy if several assumptions were not made. These include the assumption of a uniform and symmetric primary electron fluence in superposition calculations (though not in primary beam dose calculations), a uniform

primary beam spectrum across the field, a point source for primary beam electrons, with no angular deviation in the establishment of scatter kernels, an insignificant contribution from primary beam photons, and a common origin for all particles scattered from a particular edge element. However, considering the inherent statistical inaccuracy of the model and final phase space transport simulation, and the relatively small contribution of applicator scatter to the total dose, the consideration of such effects in the simulation of the applicator scattered component of the beam would have little benefit and would unnecessarily increase the model's complexity.

The predictions of the model with regard to the effects of applicator scatter on dose distributions make it a useful investigative tool. It would be particularly beneficial for an examination of the influence of this beam component on surface doses, as well as in describing the degree of uniformity of the beam in terms of energy, angular and fluence distributions. This is done in §4.4 for a specific field arrangement. The results obtained above have shown that the observation of a flat field at some specified SSD may not necessarily indicate a uniform field in terms of the characteristics of particles within that field.

4.4. Characteristics of Applicator Scattered Particles

4.4.1. Introduction

The phase space data generated using the superposition algorithm developed above contains extensive information regarding scattered particles. For a single applicator arrangement, the data represents kernel information sampled with the restrictions of successive collimation and the geometric arrangement of the applicator and cutout assembly. Such phase space data shall be analysed for a simple applicator arrangement in order to observe the possible variations and distributions resulting from electron beam applicator scatter processes.

4.4.2. Analysing Phase Spaces

Phase space data files were generated for 6, 12 and 18 MeV electron beams from the KD2 accelerator, scattering from a 10x10 cm^2 applicator with a 6x6 cm^2 cutout present (essentially, Case I described in §4.3.3 above). Scattered primary beam electrons and photons generated in applicator materials were considered in a plane 5 cm from the applicator's lower trimmer. At least 10^4 samples were considered for each beam energy, trimmer and particle type. These files were analysed by breaking the scoring plane up into a series of annuli as in Figure 4-9a (for spatially varying quantities), or by considering energies and angles of scattered particles according to discrete energy and angular bins. The stored weighting of individual particles could be used to determine fluence and spectral variations according to incident primary beam fluence.

4.4.3. Results

4.4.3.1. Fluence Distributions

The variation in planar fluence of scattered electrons and photons (Φ_{Scatt}) were considered with radial distance from isocentre, by determining which of the series of annular regions particles were located in at the scoring plane, irrespective of particle direction or energy. Total weightings are divided by the area of each annulus to convert to fluence. The resulting distributions are shown in Figure 4-42 where planar fluences are shown per unit fluence of the incident primary beam at isocentre (Φ^{P}_{CA}). Thus a fluence of $0.006 / \Phi^{P}_{CA}$ at 4 cm radius means that there are 0.006 electrons per cm^{-2} scattered with some energy and direction to the radial bin at 4 cm radius for an incident primary beam fluence of 1 electron per cm^{-2} at isocentre. These distributions provide an alternative way of visualising the scatter distribution (ie., in comparison to the dose profile data presented in §4.3.4).

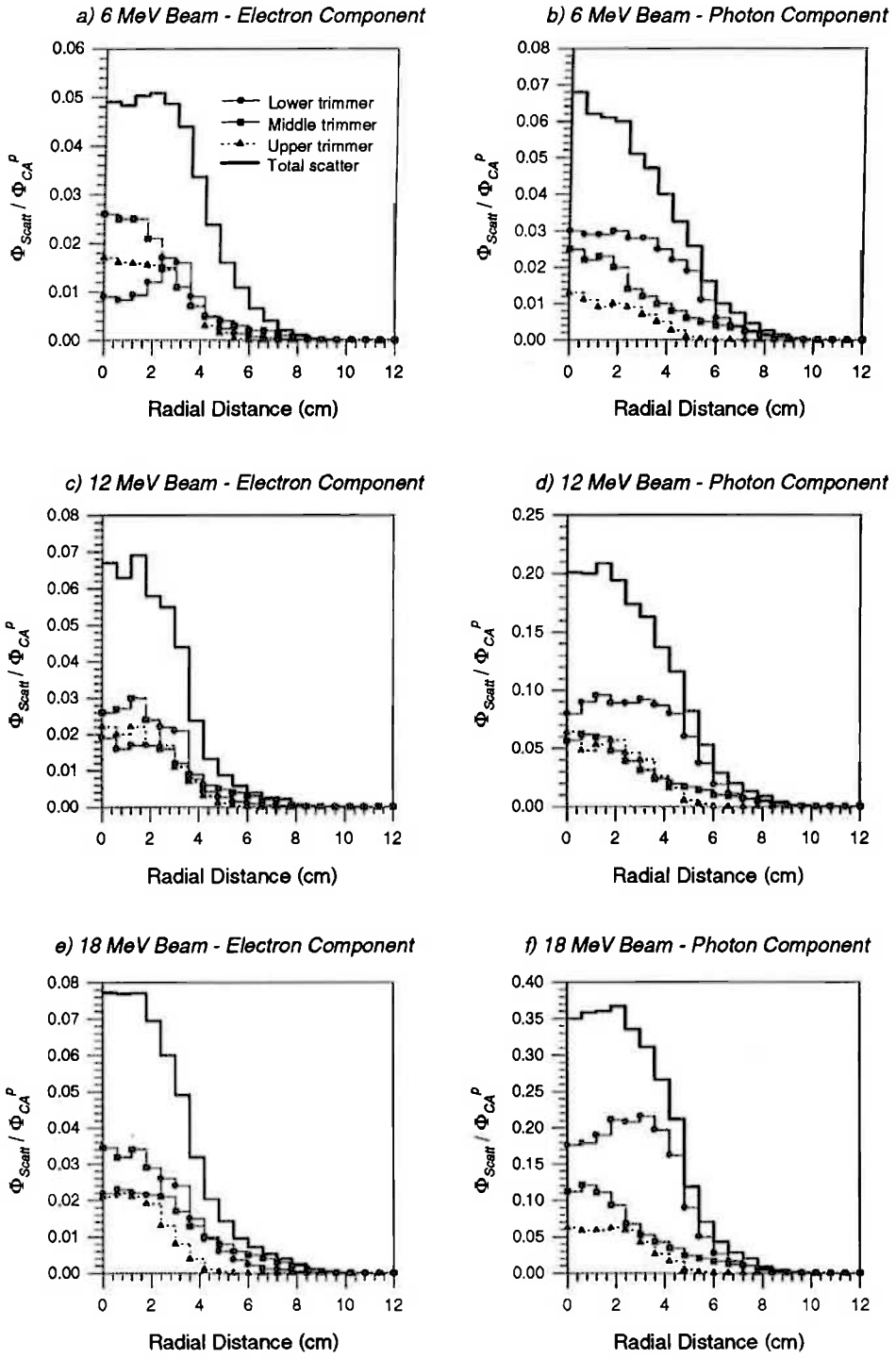

Figure 4-42: Planar fluence distributions with radius at the plane containing isocentre of applicator scattered electrons and photons for a) 6, b) 12 and c) 18 MeV electron beams. Legend shown in a). Fluence is per unit area of the scoring annulus.

4.4.3.2. Energy Spectra

The energies of *all* scored applicator scattered particles were considered across the whole beam and, together with the relative weighting of each particle, were used to form the energy spectra of Figure 4-43. Note that these spectra do not indicate any spatial/spectral correlation. Spectra are shown as numbers of particles expected in each energy bin per unit incident beam fluence at isocentre. Thus 0.2 electrons/Φ^{p}_{CA} at 5.2 MeV means that there are 0.2 electrons scattered with some direction to somewhere in the scoring plane with kinetic energy between 5.2 and 5.4 MeV for an incident primary beam fluence of 1 electron per cm^{-2} at isocentre.

4.4.3.3. Angular Spectra

Similarly, the z direction cosine (the z-axis being the beam's central axis) of all particles was considered to form the polar angular spectra of Figure 4-44.

4.4.3.4. Spatial Variation in Energy

Spatial variations in particle mean energies were examined using annular regions in the scoring plane, and averaging the energies of particles in each annular bin. This gave the radial distribution of mean energy as shown in Figure 4-45. This smears out the effects of scattering off particularly the cutout (lower trimmer) edge, with the region beneath the edge of the square cutout encompassing radii from 2.85 cm to 4.03 cm.

4.4.3.5. Spatial Variation in Angle

The radial distribution in particle z direction cosines were also determined. These distributions are shown in Figure 4-46. When considering Figure 4-45 and Figure 4-46, it should be remembered (according to Figure 4-42), that particle numbers at large radii (> 6 cm) can be very small (often only individual particles in an annulus after the scoring

procedure, though usually none for scatter from the upper trimmer due to the masking effect of the cutout). Consequently, statistical accuracy at these radii will be very low.

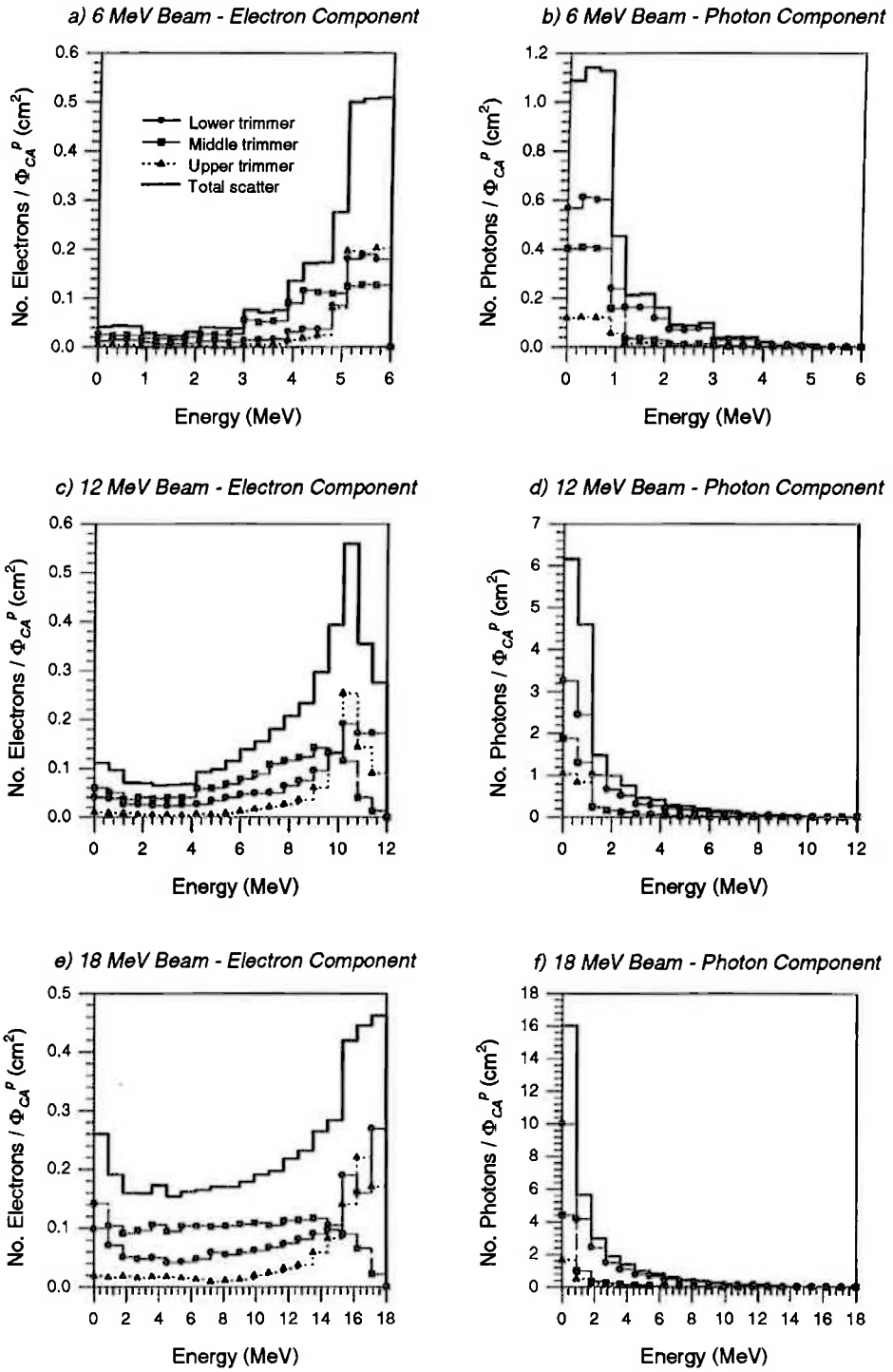

Figure 4-43: Applicator scattered electron and photon beam total energy spectra, obtained by considering particles scored across the entire treatment field using the developed applicator scatter model. Legend shown in a).

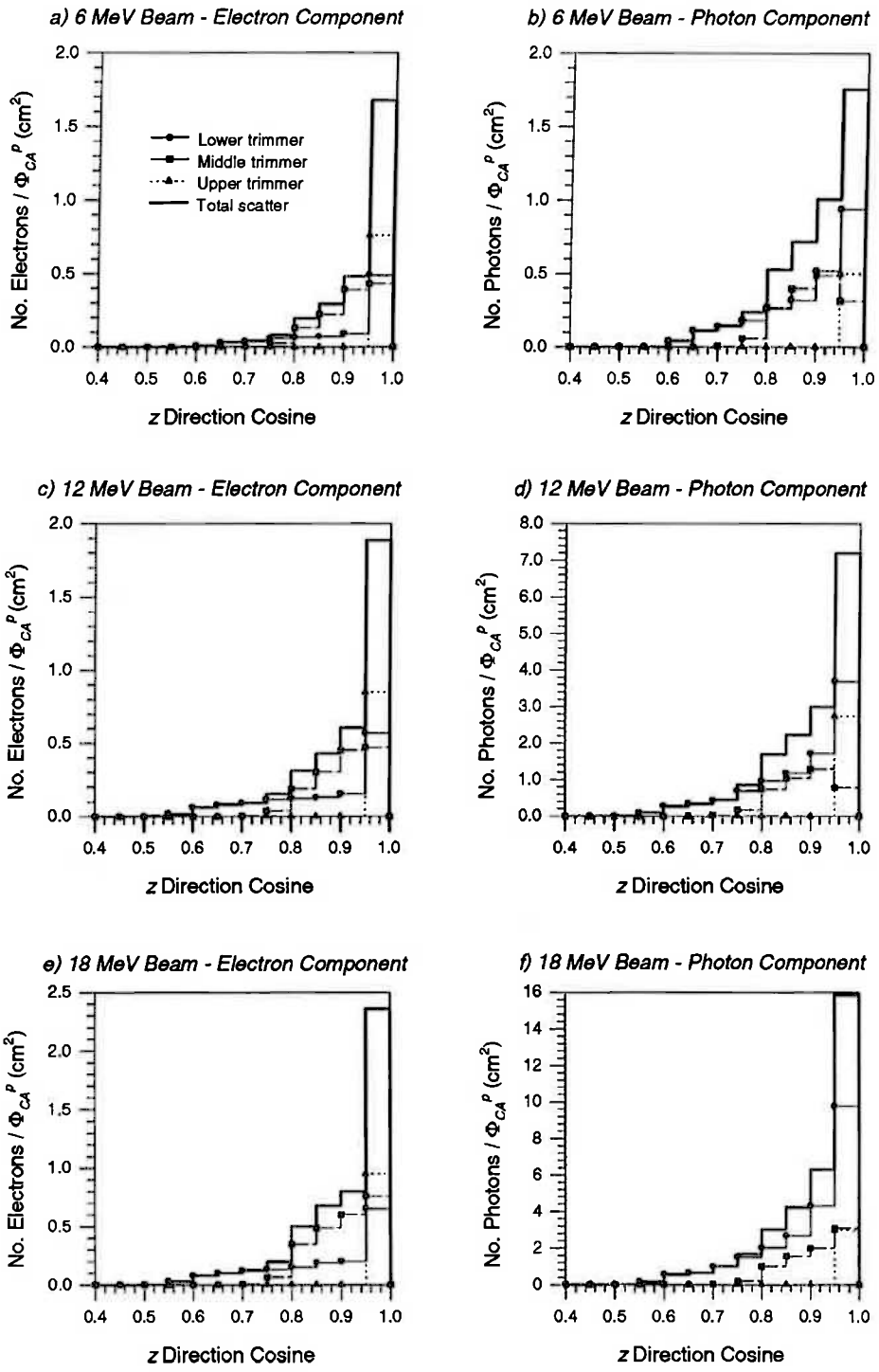

Figure 4-44: Applicator scattered electron and photon beam angular spectra, obtained by considering particles scored across the entire treatment field using the developed applicator scatter model. Legend shown in a).

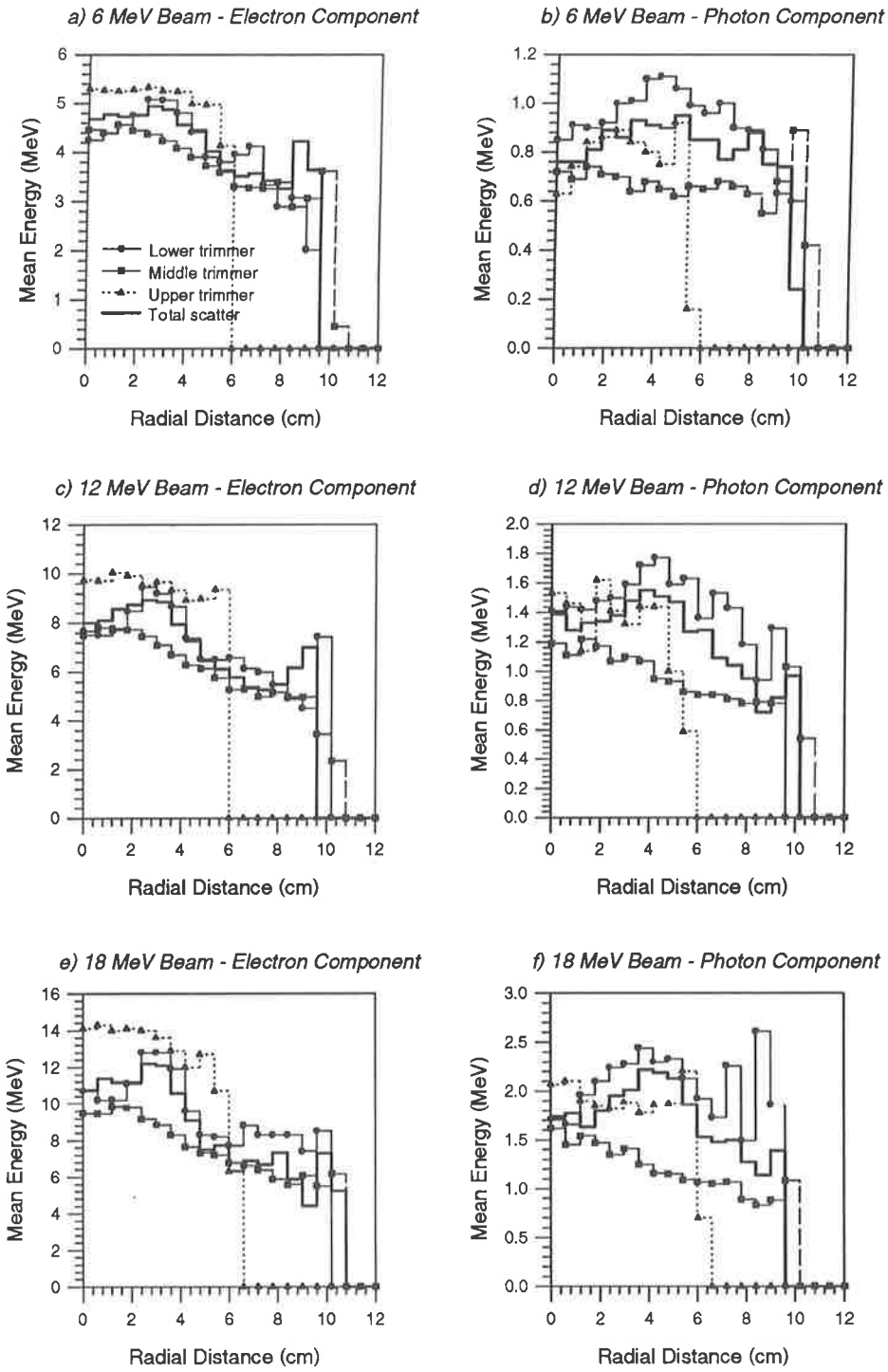

Figure 4-45: Mean energy of applicator scattered electrons and photons with radial distance from isocentre. Legend shown in a).

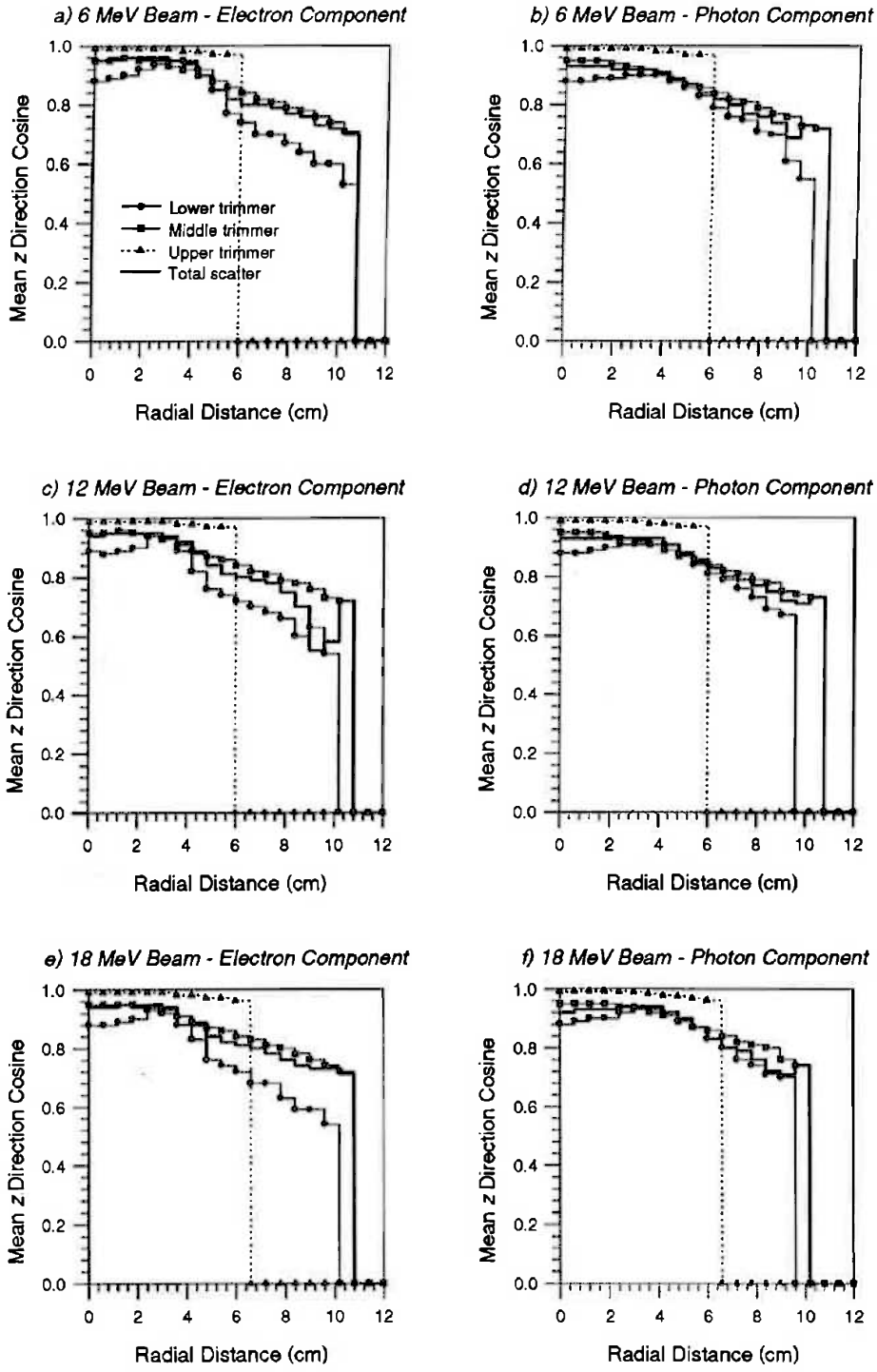

Figure 4-46: Mean angle of applicator scattered electrons and photons with radial distance from isocentre. Legend shown in a).

4.4.3.6. Angular Variation in Energy

In order to investigate any angle/energy correlation, the mean energy distribution with angle was considered. This is shown in Figure 4-47.

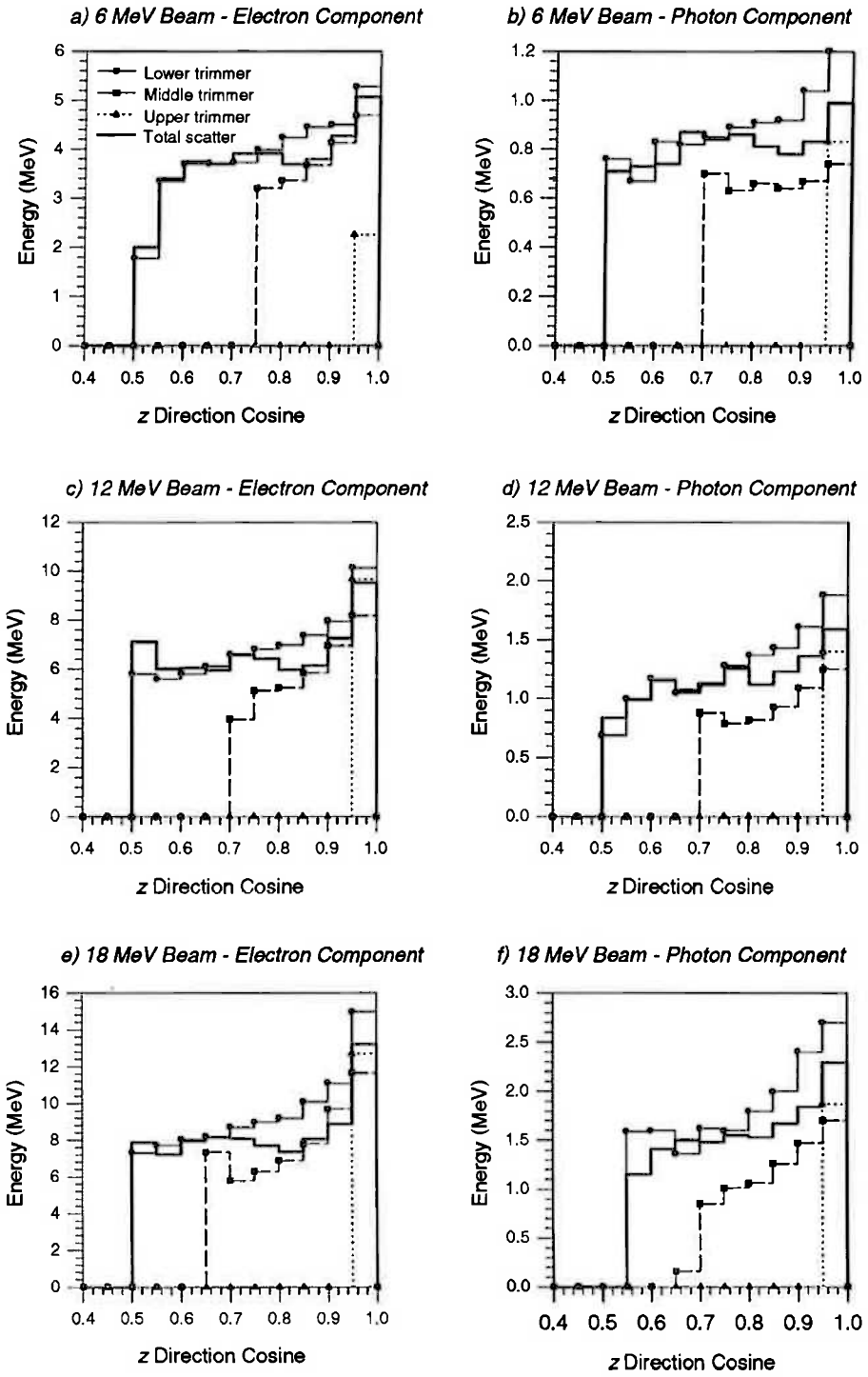

Figure 4-47: Mean energy of applicator scattered electrons and photons with angle. Legend shown in a).

4.4.4. Discussion

The distributions obtained in the above phase space analyses reflect the sources of scattered particles (relative to the scoring plane) in each case, and the properties of scattering as governed by scatter kernel characteristics. Thus, the angular variation of particles about normal incidence (z direction cosine of unity) becomes narrower about unity as we move from the cutout (lower trimmer) to the upper trimmer as seen in Figure 4-44 and Figure 4-46. For particles from the lower trimmer, no masking due to successive apertures occurs and distributions basically represent a resampling of scatter kernels.

The scatter kernels used in calculation of electron characteristics are dominantly forward directed as was shown in §4.2.4 (see for example, Figure 4-21), divergence with distance obscuring the resulting peak. Thus, for the electron distributions in Figure 4-42a) and c), particularly for electrons from the lower trimmer, peaks are present beneath the trimmer edge. The peaks for other trimmers are more complicated due to the masking effects of the lower trimmer. Figure 4-46 clearly demonstrates how the cutout can act as a source of forward directed particles (particularly electrons) with the increase in approach to normal incidence over the region occupied by the cutout edge (approximately 2 to 5 cm). Photons may originate from anywhere within an applicator trimmer material through radiative electron energy loss resulting in photon scatter being more isotropic than electron scatter (see §4.2.4 and Figure 4-22). This results in the more rounded peaks in the fluence distribution for photons compared to electrons as Figure 4-42 indicates. Similar angular spectra for electrons and photons scattered from the middle and upper trimmers (see Figure 4-44) are a reflection of the dominant influence of the position of higher trimmers rather then the scattering occurring within them.

The electrons that have scattered out through applicator trimmers will have suffered some energy degradation due to the paths they must traverse through applicator materials, and so the electron energy spectra of Figure 4-43a) and c) are softer then that of the primary beam (compare Figure 4-26). The middle trimmer is the thickest of the three and electrons scattered from this have the lowest mean energy due to attenuation (see Figure 4-45) and the greatest spread of energies (see Figure 4-43). As shown in §4.2.4, particles scattered

through larger angles are more likely to have experienced greater energy loss due to longer traversal distances and hence more energy loss. This effect is displayed in Figure 4-45 and Figure 4-47 where electron energies decrease away from the region of forward scattering for each trimmer. Similarly, higher energy photons are generated by higher energy primary electrons undergoing radiative energy loss early on in their path through applicator materials, and so they also display a mean energy distribution which decreases with deviation from the forward direction (compare Figure 4-27b). This is particularly well demonstrated in Figure 4-47 where electron and photon mean energies increase towards normal incidence.

As shown in §4.2.4, considerably more photons are generated in the applicator materials then there are electrons emerging (see Figure 4-43 and Figure 4-44). As shown in §4.2 and §4.3 however, due to the much larger local energy deposition in the patient or phantom per electron, the dose due to the electron component of applicator scatter is considerably more significant at relevant depths than that due to the photon component. Note also that, since photon scatter is more isotropic than electron scatter, considerably more upper trimmer photons are collimated before reaching the scoring plane. Consequently, photon numbers due to scatter from the upper trimmer are much smaller (relative to that from the middle or lower trimmer) then photon scatter kernels would suggest.

4.4.5. Conclusions

In the investigation presented above, some of the energy and angular characteristics of scattered particles reaching the patient surface in a clinical electron beam have been revealed. Using the model employed in this investigation for the particular accelerator considered, the characteristics of scattered particles for any arbitrary tertiary collimation configuration could be obtained. The perturbations introduced to dose distributions by scatter in the beam such as examined here should be considered when a beam description is required. The complexity required in the description of such perturbations would have to be evaluated in terms of the application, and in light of the fact that they represent generally a small fraction of the full clinical beam (as §4.3.4 indicated).

The particle characteristics examined in the above investigation represent, by virtue of the sources of the particles, the most widely varying beam component to the primary beam. The distributions obtained thus represent the variations in beam fluence, energy and angular spectra that will occur *for the specific applicator configuration considered.* General variations introduced by other applicator configurations will differ in many aspects due to variation in aperture geometries (thus varying the location of applicator scatter sources across the field as well as scatter yields due to the variation in incidence angle that occurs).

4.5. Conclusions / Summary

This chapter has concentrated on quantifying and subsequently modelling the effects of tertiary collimation systems on a clinical electron beam. Using Monte Carlo methods, the properties of particles scattering off the materials present in an electron beam applicator were examined, their major characteristics identified, and the possible variations in these characteristics investigated. This allowed the establishment of a superposition based model for obtaining the phase space of particles scattered from applicators and patient-specific cutouts on a Siemens KD2 accelerator. This model was found to provide consistency with measured results when the phase space data was used in a dose calculation, again using Monte Carlo methods. The utility of the developed model depends on (other then the limitations of any assumptions made) how specific it is, and in this sense it is limited in several ways:

- The model can only cater for applicators consisting of a series of aperture plates. Although this is a common configuration for such collimators, cylindrical cones and collimators with enclosed sides are also used. Primary beam particles would interact with these other beam components, and such interactions could not be easily described using the above technique. However, patient-specific cutouts are used quite commonly for final beam definition.
- The kernels generated for the superposition technique require knowledge of the energy spectrum of the primary beam, which will vary between accelerators of

different types, as well as between different accelerators of the same type due to local tuning. Thus, primary beam information and scatter kernels would have to be generated for each local site in a clinical application of the model.

The developed model provides detailed information about applicator scatter; far more then has previously been provided by anything other then comprehensive Monte Carlo treatment head simulations, and can be used to evaluate the distributions of scatter properties as shown in §4.4 above. The ability of developing dose calculation algorithms to incorporate such properties into their calculation (see §3.3) will enhance the accuracy obtainable in the dose calculation stage of treatment delivery. Contemporary applications of electron beam models rarely consider more then the effects on machine output of applicator scatter. In fact, in order for dose calculations of the complexity of Monte Carlo (Manfredotti *et al.*, 1987), Phase Space Evolution (Janssen *et al.*, 1994), and Macro Monte Carlo (Neuenschwander *et. al.*, 1995) to generate realistic distributions, they *must* utilise realistic beam characteristics.

5. THE POTENTIAL UTILITY OF ELECTRON BEAMS - OPTIMAL CHARACTERISTICS

5.1. Optimisation in Radiotherapy

Chapter 4 discussed what might be described as the *forward* calculation of the characteristics of a specific electron beam. With the increasing level of technology in radiation delivery, it may be more sensible to determine what the characteristics of an electron beam should be before producing the beam. In this way beam properties would be being *optimised*. Developments in both radiotherapy technology and computing capabilities have seen the rapid development of methods for optimally delivering radiation for therapeutic purposes.

5.1.1. Optimisation Philosophy

Radiotherapy optimisation provides a natural union of the many scientific and engineering fields which contribute to treating tumours. There is no set definition for an optimised treatment - a planning aim is always to deliver the optimal dose distribution using available methods. Optimisation mathematics attempt to account for all factors contributing to treatment and to weight their influence according to the optimal distribution. This can include determining the most efficient way (ultimately economically) to deliver radiation dose to the entire radiation-treatable population, and inclusion of the safety, accuracy, and time requirements of a treatment plan (Brahme, 1994a).

In radiation physics as applied to radiotherapy, optimisation is achieved when a physically realisable dose distribution is delivered, *conforming* to the radiobiological response

characteristics of the patient tissues in order to achieve a desired endpoint*. The concept of conforming a dose distribution to a tumour (combined with the avoidance of healthy tissues) is fundamental to radiotherapy techniques.

The potential degree of conformity attained is dependent on the manipulation of the degrees of freedom available for dose delivery. The techniques of radiation production, collimation and delivery that are currently available provide significant control in terms of energy modulation, radiation type, source location, and the spatial distribution of fluence (eg., Brownwell *et al.,* 1978; Brahme *et al.,* 1989; Smith, 1990; Mackie, *et al.,* 1993; Nahum *et al.,* 1994; Brahme, 1995b). Furthermore, the description of the entire treatment process is rapidly moving from the planar to volumetric, including the implementation of three-dimensional treatment planning (Starkschall, 1996). These advancements, combined with clinical advances (tumour localisation, patient immobilisation, sensitisers, predictive assays etc), are providing the ability to increase tumour control with minimal normal tissue complication, especially when biological response models are incorporated into the manipulation of those degrees of freedom (Leibel *et al.,* 1991; Appendix H).

5.1.2. Degrees of Freedom in Radiation Delivery

When irradiating a patient for the purposes of treatment, certain control over the radiation characteristics which govern the form of resulting dose distributions is available [these being radiation type (Brahme, 1982), energy, source location, direction, fluence, time (including variation in fractionation schedules *throughout the entire patient*)]. These are the degrees of freedom available for the irradiation process. Many radiation characteristics cannot be controlled or must co-exist. These are a result of the radiation delivery device and need to be included in the description of the degree of freedom (eg., an electron irradiation usually has an associated photon contamination component; collimation methods frequently create perturbations as shown in Chapter 4; radionuclides have fixed

---

* Radiotherapy optimisation is a vague concept if no set endpoint is defined. However, endpoints are often quite vague since there are an enormous number of possibilities. Brahme (1995a) has suggested a qualitative goal as making "the quality of life for the patient as high as reasonably achievable from the time of his or her first contact with the medical system". Quantifying such a goal is a challenge of optimisation research.

emission characteristics). The parameters which control or describe degrees of freedom are the variables in the optimisation process. These include such parameters as seed or wire dwell time, number of monitor units per port, mutlileaf collimator leaf positions and beam intensity distributions, beam energies, compensator dimensions etc. They also include the possible variance in each of these parameters due to physical uncertainty in beam alignment, calibration, patient movement, inter- and intra-patient cellular heterogeneity etc (Brahme, 1995a; Appendix H).

It is convenient to form a generic label for the normalised dose (or energy) distribution which results when the degrees of freedom are defined by a complete set of variables, with the normalisation being to some common factor (such as incident energy fluence). Examples include the dose deposition kernel for say, a single electron pencil beam of fixed energy, location of incidence, and angle of incidence per unit energy fluence; or a single seed within a patient per unit time and source activity). If the full set of independent variables controlling radiation delivery spans an N-space (ie., the cumulative product of the number of possible discrete values of each variable is N), then that label could be $\phi_n(r)$ where n refers to one point in the N-space and r to a position within the patient[†]. Whatever $\phi_n(r)$ represents, it is calculable with contemporary algorithms and for clinical purposes, should account for the details of radiation transport (Brahme, 1995a) and the characteristics of the patient (heterogeneities). A dose distribution is defined by weighting the N variables with a discrete distribution, w (which has been called the *kernel density function* or *fluence vector*; Gustafsson *et al.,* 1994, 1995), which may be considered a weighting vector within the N-space. w may be *necessarily* discrete (eg., if a variable is the number of monitor units per port), or may be discrete simply because of computational execution (eg., when weighting a beam profile which *could* be considered continuous, it is broken up into discrete elements at computation).[‡] The dose distribution can be calculated through the superposition of w and the $\phi_n(r)$;

[†] For example, n could represent an incident electron pencil beam of defined energy, direction, and location of incidence. The dimensions of N are then each possible energy, direction, and incidence location.

[‡] Note that, particularly for external beam optimisations, the physical entities arising from a complete statement of all controlling variables have commonly been refereed to as 'bixels' or 'beam elements' for pencil beam calculations (Webb 1993; Gustaffson *et al.,* 1994). The w_i are then the weighting values of each bixel.

$$D(\boldsymbol{r}) = \sum_{n=1}^{N} w_n \phi_n(\boldsymbol{r}) \tag{5.1}$$

(where w_n is a component of $\boldsymbol{w}$) which can be written in matrix notation:

$$\boldsymbol{d} = \boldsymbol{M}\boldsymbol{w} \tag{5.2}$$

(Holmes and Mackie, 1994a; Lefkopoulos *et al.,* 1995a). Here, $\boldsymbol{d}$ is a vector with elements representing the dose to each of the voxels comprising the patient, and the columns of $\boldsymbol{M}$ are vector representations (over all patient voxels) of the N elemental distributions ϕ_n. If the variables in the procedure were continuous rather then discrete, then equation 5.1 would be described by a Fredholm integral of the first kind (Källman *et al.,* 1992; Gustafsson *et al.,* 1994; Webb, 1993);

$$D(\boldsymbol{r}) = \int w(\boldsymbol{p})\phi(\boldsymbol{r},\boldsymbol{p})d\boldsymbol{p} \tag{5.3}$$

where the integral is over the space spanned by all variables.

In the case that the $\phi(\boldsymbol{r})$ are constant with respect to a simple spatial translation (because for example, if the restriction is to monoenergetic, monodirectional single mode beams in homogeneous media) then equation 5.3 becomes the space invariant form of the Fredholm integral of the first kind (Webb, 1993), equivalent to a convolution integral.

Equation 5.1 describes the conventional forward approach to radiotherapy planning. For a simple two-port photon irradiation for example, of fixed energy and collimation, w_1, w_2 are the number of monitor units per port, ϕ_1, ϕ_2 are the dose distributions for each, and the dose distribution is easily calculated once the relative weightings of the two ports has been established. In fact, deciding on values for w_1 and w_2 comprises a simple optimisation procedure, if some straightforward objective is proposed.

The inverse approach is to solve equation 5.1 for the vector w, given the full set of elementary kernels $\phi_n(\boldsymbol{r})$. This of course requires some initial statement of an *objective dose distribution*, $D(\boldsymbol{r})$. However, there are a couple of fundamental problems with this approach. Firstly, an exact solution to this inverse problem will rarely exist within the bounds of physical dose delivery (Popp *et al.,* 1975; Gustafsson *et al.,* 1994; Brahme, 1995a). In particular, the necessary constraint to positive w_n will disallow most solutions. Were the determinant of $\boldsymbol{M}$ in equation 5.2 zero, then the exact solution exists. Problems

will also arise if the number of independent linear equations represented by equation 5.2 is less then the number of points in the dose calculation region, leading to ill-conditioned solutions (Holmes, 1993). Secondly, and as a result of the first problem, it is generally not possible to specify the desired dose distribution prior to the mathematical inversion (Niemierko, 1992). This is because optimisation procedures involve complex dependencies between variables, and the closest physically viable inverse solution to equation 5.1 may not be the optimal physically obtainable one for the current application and objective.

Objectives or cost functions to be minimised for approximating an inverse solution to equation 5.1 can include the simple difference in delivered dose to the desired dose. Alternatively, more complex objectives can be formulated which are a function of the dose to be delivered. (Note that, depending on their particular definition, these objective functions may still require *a priori* knowledge of a desired dose distribution). Iterative techniques can then be used to find the vector w which minimises the cost function, rather then the w which most closely approximates equation 5.1. Iterative techniques score a dose distribution corresponding to an element of the N-space subject to a set of constraints. The set of constraints restrict N-space to the space of feasible solutions to the optimisation problem (Niemierko, 1992). The actual iterative search technique used may be one of a large variety, each with their respective benefits and deficits.

The constraints which govern a particular radiotherapy optimisation problem are many and varied. They may include (Niemierko *et al* 1992)

- Tumour Control Probability (TCP)
- Normal Tissue Complication Probability (NTCP)
- Tissue partial volume doses (dose-volume constraints)
- Treatment complexity
- Dose to dose-limiting organs
- Minimum target dose
- Dose inhomogeneity across the target
- Discrete or continuos values of the beam parameters (such as the restriction to dose per monitor unit)
- General beam delivery constraints (the mechanics of radiation delivery)

- All possible combinations of active constraints

In some cases it may be possible to restrict the N space to a smaller subset of known potential elements, such as specific beam qualities, when all other elements are not clinically viable (such as eliminating the possibility of using low energy electrons to treat deep-seated tumours). Techniques have been developed for automatically scanning the set of possible solutions to an optimisation problem in order to filter out those with the least potential for effect (Söderström and Brahme, 1992; Söderström and Brahme, 1993; Söderstrom *et al.,* 1993; Brahme, 1995a; Gustafsson *et al.,* 1995). As an example, the number of beam portals can be restricted when it is known that increasing the number will not radically increase the potential for the desired outcome. Söderstrom and Brahme (1995) have investigated this problem for several clinical situations and found that the number of coplanar beam portals required for promising outcome can be restricted, provided that beam directions are suitably selected. Similar findings have been reported by Stein *et al.* (1996).

5.1.3. Tests of Conformity: Physical vs Biological Objectives.

5.1.3.1. Physical vs Biological Objectives

As mentioned above in §5.1.2, direct inversion of equations 5.1 to 5.3 requires some statement of the objective energy deposition or dose distribution. Because of the conventional way biological response has been translated into a dose distribution (by assuming for example, that a uniform dose distribution is required over a target volume), objective functions can be numerous and varied. Examples of objectives sometimes used in optimisation techniques are (Niemierko *et al.,* 1992; Holmes and Mackie, 1994a; Brahme, 1995a, Söderström, 1995),

- Closeness to specified integral dose
- Maximum deviation from specified dose
- Mean square deviation from specified dose

- Minimal dose gradient across the target volume
- Matching of isodose lines to target and organ volumes
- Matching specified dose-volume constraints
- Maximum dose homogeneity within the target volume
- TCP
- NTCP
- Maximum value of uncomplicated tumour control probability, UTCP = TCP*(1-NTCP)
- Maximum dose to organs at risk
- Maximum minimum tumour dose
- Combinations of objectives, and temporal and spatial variations in such combinations

All but those objectives explicitly considering functions of biological response make assumptions about optimal dose distributions prior to any optimisation. These are physical objectives, and their usefulness depends on the consequences of the assumptions, and the feasibility of intuitively specifying an objective dose distribution. Objectives of minimal over-dosage (Källman *et al.,* 1988), maximal minimum dose in the target volume (Morrill *et al.,* 1995) and minimal mean square deviation from the prescription (Redpath *et al.,* 1976; Webb, 1989a; Bortfeld *et al.,* 1990; Gustafsson *et al.,* 1994; Morrill *et al.,* 1995; Holmes *et al.,* 1995) have been commonly used (Curran *et al.,* 1996). The choice of physical objective function can also determine various characteristics of the final dose distribution. For example, a least-squares measure may not lead to uniformly high doses in the target volume as will a minimal over dosage approach (Lind, 1990; Söderström *et al.,* 1993; Gustafsson *et al.,* 1994). If characteristics of the *physical dose distribution* are being observed, as in §5.2, then physical objectives are naturally more advantageous.

Biological objectives can only be as reliable as the models used to define them, and when clinical data is insufficient for trust to be put in the biological models (Schultheiss *et al.,* 1996), then physical objectives are generally considered. Relatively complex descriptions of the relative merit of a dose distribution in terms of biological outcome have been presented in terms of the objective of maximum cure probability with minimal complication probability (Ågren *et al.,* 1990; Morrill *et al.,* 1990; Morrill *et al.,* 1991b;

Källman *et al.,* 1992; Morrill *et al.,* 1995; Graham *et al.,* 1996). Due to the lack of confidence placed in radiobiological models, they are seldom used for absolute measure of an irradiation strategy's potential. Instead, they are usually used for ascertaining the relative suitability of rival strategies (where physical objectives have also been used). However, even the suitability of this application of such models has been questioned (Bortfeld *et al.,* 1996; Mohan and Wang, 1996). More doubt arises concerning mathematical response models when potential inter and intra-patient response characteristics are considered (see Appendix H), as well as the cumulative uncertainty in radiotherapy diagnosis, prescription, and dose delivery.

5.1.3.2. Optimal Solutions

The problem of finding the optimal irradiation strategy (according to some predefined objective) within some constrained set is greatly simplified if it is known that there are no local minima. If there are no local minima, then search algorithms can ensure producing the best strategy, and not an inferior solution. In the presence of local minima, an optimisation algorithm must perform a much more extensive search over N space to ensure finding the global maximum.

Niemierko (1996) has investigated this problem for several alternative objective functions, and various constraints on the degrees of freedom. A single global optimum exists if the surface formed by the objective function is mathematically convex (for a maximisation problem) or concave (for a minimisation problem) over the entire N space. This is so if the gradient of the gradient of the objective function (namely, the Hessian matrix introduced in §5.1.5.2.2.1) is either positive definite (for minimisation) or negative definite (for maximisation) over the entire N space. Niemierko (1996) has shown this to be the case for many common objectives (least-squares minimisation, maximisation of the minimum target dose, maximisation of UTCP, maximisation of exponentially weighted UTCP), when the intensity distributions of fixed external beams are being varied. When beam directions are varied though, there are theoretically many local minima over the N space. Also, using more complex objectives (such as TCP maximisation with normal tissue dose-volume constraints) can lead to multiple local maxima or minima (Deasy, 1996).

5.1.4. Dose calculation

In order to compare an irradiation strategy with a desired dose distribution, it is necessary to calculate the dose distribution resulting from that strategy. Since this is a process that may occur many thousands of times in an iterative optimisation procedure, simplified dose calculations are required in order to reduce calculation time. The formalisms represented by equations 5.1 to 5.3 suggest that convolution/superposition techniques would be the most logical approach.

General pencil beam kernels, broad beam distributions, and distributions due to internal point and line sources at multitudes of orientations and energies, all of which may represent the elemental distributions $\phi_n(r)$, may be generated prior to the optimisation routine using analytical approximations (Brahme *et al.,* 1981; Lax and Brahme, 1985; Ahnesjö *et al.,* 1987; Brahme *et al.,* 1989; Eklöf *et al.,* 1990; Holmes *et al.,* 1991; Sloboda, 1992; Zheng-Ming and Brahme, 1993) or numerical (Monte Carlo) calculations (Ahnesjö *et al.,* 1987; Thomason and Higgins, 1989; Andreo, 1990; Eklöf *et al.,* 1990; Simpkin and Mackie, 1990; Webb, 1991a; Gustafsson *et al.,* 1994; Gustafsson *et al.,* 1995).

When the elemental kernels are dose distributions due to full uniform treatment fields or potential source positions, then the number of such fields is generally limited to a small subset of all possible fields, often selected via the experience of a treatment planner (Holmes *et al.,* 1991; Niemierko *et al.,* 1992; Mohan *et al.,* 1992; Mageras and Mohan, 1993) and possibly modified using optimised compensator designs or wedge selections (Brix *et al.,* 1988; Djordjevich *et al.,* 1990; Weeks and Sontag, 1991; Söderström *et al.,* 1993; Brahme, 1995a). In this case, normal treatment planning algorithms can be used to calculate the dose distribution due to each. In the more general case where the kernels are due to pencil beams or point irradiations, then the following assumptions are frequently made;

- Only primary dose is considered with neglect of lateral scatter (eg., Webb, 1989a; Söderström and Brahme, 1993; Chen *et al.,* 1995).
- Tissue heterogeneities are ignored, with no scaling of kernels due to material/density changes. (eg., Bortfeld *et al.,* 1990; Boyer *et al.,* 1991; Webb,

1991a; Sloboda, 1992; Söderström *et al.,* 1993; Holmes and Mackie, 1994b; Webb, 1994; Gustafsson *et al.,* 1994; Gustafsson *et al.,* 1995; Oldham and Webb, 1995). Kernels are often considered spatially invariant (Lind and Brahme, 1987; Brahme, 1988; Källman *et al.,* 1988; Brahme *et al.,* 1989; Lind, 1990; Brahme *et al.,* 1990; Boyer *et al.,* 1991; Holmes *et al.,* 1991; Lind and Brahme, 1992; Källman *et al.,* 1992; Söderström *et al.,* 1993; Holmes and Mackie, 1994a,b).

- 2D dose calculations only (eg., Webb, 1989a; Webb, 1991a; Holmes and Mackie, 1994a; Webb, 1994; - most optimisation approaches).
- Simplified beam divergence and kernel orientation (eg., Söderström *et al.,* 1993; Gustafsson *et al.,* 1995).
- Tissue heterogeneities are included using simple primary dose scaling (eg., Scheib and Pedroni, 1992).

Recent approaches have attempted to overcome simplifications by employing generalised pencil beam kernels (Söderström *et al.,* 1993; Gustafsson *et al.,* 1994, 1995). The consequences of the above assumptions are quite well known for the usual forward planning case. However, in an optimisation routine, such consequences will affect the resulting selection of supposedly optimal treatment strategy. Morrill *et al.* (1994) have emphasised that variations in dose distributions will occur when the usual, particularly heterogeneity, corrections are applied to the strategy recommended by the optimisation - ignoring such corrections can detract from the original objective, resulting in suboptimal dose distributions. Söderström *et al.* (1993) have extensively investigated the consequences of approximations made. They found particularly that neglect of lateral scatter can reduce an optimisation's ability to account for excess dose to critical organs adjacent to the target volume. They point out however, that if such consequences are well understood, then approximations can be made and used effectively in select situations. Similar findings have been obtained by Chen *et al.,* (1995) who recommend full incorporation of scatter calculations into iterative optimisation searches, though such inclusions can greatly increase optimisation execution time (Holmes and Mackie, 1994a). Accurate dose calculations can of course be performed after the optimum beam configuration has been

calculated using simplified transport methods. However, the use of *accurate* calculations during the optimisation routine will lead to a *different* optimal beam configuration.

5.1.5. Mathematical Optimisation Techniques

5.1.5.1. Optimisation Using Mathematical Programming

The constraints placed upon the degrees of freedom in radiotherapy restrict the possible optimisation solution space to a feasible set of radiation delivery strategies (any set from the *N*-space), amongst which is some (possibly unique) optimal feasible strategy. A two dimensional example is shown in Figure 5-1. Furthermore, radiobiological considerations constrain this *N*-space even further due to dose-limiting normal tissues, minimal target doses and dose uniformity etc. Provided there *is* a set of feasible solutions, then amongst the set is at least one optimal solution. The search for an optimal solution in a constrained set is a standard mathematical optimisation problem, and several classes of "mathematical programming" techniques have been developed to solve such problems. These apply equally well to radiotherapy optimisation. Other classes of search algorithm (simulated annealing, RONSC) have been reserved for §5.1.5.3 because of their iterative nature.

5.1.5.1.1. Exhaustive Search

It is possible to examine *every* possible feasible solution within the constrained set, scoring each one according to some measure of the dose distribution which it provides, and then selecting the best one as optimal. This approach has been employed previously (Hope and Orr, 1965; Hope *et al.,* 1967; Hope and Cain, 1972; van der Laarse and Strackee, 1976; Fields *et al.,* 1980). Because of the excessive computational time that could be involved with this approach, it can only be utilised with a small number of kernels (Niemierko, 1992). In such cases however, iterative search techniques are virtually assured of finding a globally optimal solution much more rapidly.

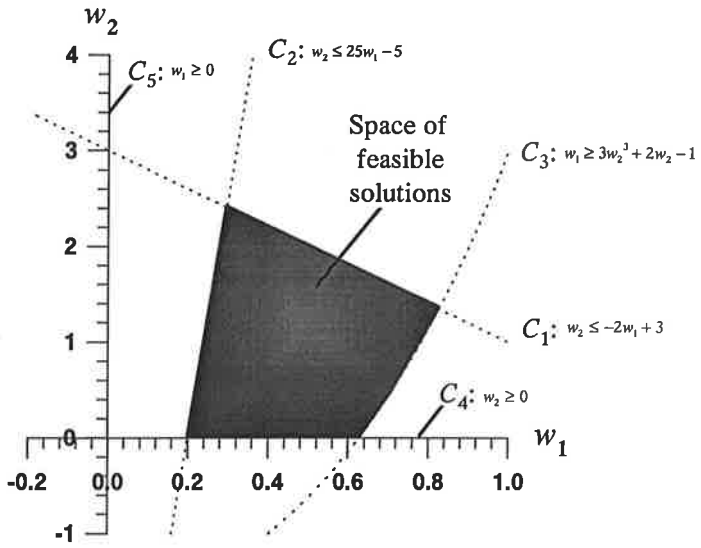

Figure 5-1: A two-dimensional example representing a solution space for two variates, w_1 and w_2, constrained to a feasible set by a series of linear and nonlinear constraints including positivity. The shading of the constrained space could be considered to represent the value of the objective function within the constrained region. Five constraints are represented by the inequalities C_1 - C_5.

5.1.5.1.2 Feasibility Search

An alternative to the exhaustive search approach is to apply a large number of constraints, and to search for *any* solution within the feasible set (Altschuler *et al.,* 1986; Censor *et al.,* 1988a,b; Powlis *et al.,* 1989; Starkschall *et al.,* 1990; Starkschall and Eifel, 1992). An approach in this manner (Starkschall *et al.,* 1990) is to specify minimum and maximum dose limits at specific points or areas within normal tissues and target volumes respectively. The size and uniformity of the resulting feasible solution set then determines the efficiency of the optimisation. If the constraints are too restrictive, a feasible solution space may not exist whereas, if it is too free, then the first feasible solution found could just as easily be the least optimal as the most optimal of the possible solutions. The search techniques in *feasibility* optimisations have been of the *row-action* type (Censor, 1981), and types based on an approximation technique due to Cimmino (1938).

5.1.5.1.3. Linear and Quadratic Programming

Often, the formulation of a radiotherapy optimisation in terms of dose constraints and treatment parameters leads to a solution space bounded by purely linear constraints. If, in addition, the objective can be expressed in terms of a linear function, then linear or integer programming techniques can be used to attempt to solve the problem (Bahr *et al.,* 1968; Hodes, 1974; Mantel *et al.*, 1977; Ebert, 1977; Legras *et al.,* 1982; Sonderman and Abrahamson, 1985; Takai *et al.,* 1987; Langer and Leong, 1987; Langer *et al.*, 1990; Morrill *et al.,* 1991b; Rosen *et al.,* 1991). Linear programming represents an ordered approach to the situation of searching the space of feasible solutions. The linear objective function in N independent variables, x_n (eg., the relative weights of a selection of possible beams), to be minimised can be written

$$f = \boldsymbol{c}\boldsymbol{x} \tag{5.4}$$

where $\boldsymbol{c}$ is a matrix of N coefficients, and $\boldsymbol{x}$ a vector of the N x_n. A common objective in application to radiotherapy optimisation is the minimisation of integral dose to normal tissues, in which case $\boldsymbol{c}$ becomes the dose matrix of equation 5.2 restricted to normal tissues (Rosen *et al.,* 1991). The constraints of the problem are usually dose limits on the tumour and critical structures, and can be written

$$\begin{aligned} \boldsymbol{A}\boldsymbol{x} &\leq \boldsymbol{b} \\ \boldsymbol{x} &\geq 0 \end{aligned} \tag{5.5}$$

where $\boldsymbol{A}$ is a matrix of dose points, and $\boldsymbol{b}$ a vector of dose limits (maximum dose limits can be transformed into minimum limits by negating the appropriate dose value). The theory of linear programming (see for eg., Gass, 1969) says that the set of constraints forms a closed convex set in the $\boldsymbol{x}$ space, with the optimal solution existing at an extreme point of the set.

An iterative and easily computer executable algorithm, the simplex algorithm, examines the extreme points of the closed set in turn, always ensuring that it moves to a point with a lower value of the objective in each case until the minimum is reached. In this way, the algorithm guarantees finding the optimal solution, but at the expense of significant computation when there are a large number of constraints (ie., large number of extreme points). For this reason, the technique is used for relatively small problems (up to 20 variables; Niemierko, 1992). For a thorough review of the application of linear programming to radiotherapy planning optimisation, see Rosen *et al.,* (1990).

Quadratic programming (Redpath *et al.,* 1976; M^{c}Donald and Rubin, 1977; Starkschall, 1984; Djordjevich *et al.,* 1990; Bortfeld *et al.,* 1990) involves specifying a quadratic objective function (such as the sum of squares of the deviations of calculated doses from desired doses). The resulting quadratic problem may be transformed into a series of linear ones for solution by linear programming methods, or be solved by employing matrix transformations to solve the effective least-squares problem (Starkschall, 1984). The major advantage of quadratic programming lies in the slightly increased flexibility in the definition of the objective.

5.1.5.1.4. Singular Value Decomposition Analysis

Solving equation 5.2 for w involves solving the set of linear equations it represents with the restriction of imposed constraints. Approximate solutions for such systems can be obtained using *singular value decomposition* (Press *et al.,* 1992), which relies on an elegant result from fundamental linear algebra which shall not be discussed here. The technique involves obtaining an approximation for the inverse of $\boldsymbol{M}$, ($\boldsymbol{M}^{-1}$), and estimating w by evaluating

$$w_{est} = \boldsymbol{M}^{-1}\boldsymbol{d} \,. \tag{5.6}$$

In application to radiotherapy, this requires *a priori* knowledge of the desired dose distribution since w_{est} is selected according to the solution *residual, r*, defined as

$$r = \left|\boldsymbol{M}w - \boldsymbol{d}\right|. \tag{5.7}$$

Singular value decomposition is also subject to necessary negativity in w.

A feature of singular value decomposition is the ability to examine the effects on the solution of individual components of w through examination of the *singular values* of $\boldsymbol{M}$ (see Campbell and Meyer, 1991; Press *et al.,* 1992). Lefkopoulos *et al.* (1995b) used this facility to examine the effects of varying arc parameters in stereotactic irradiations, and to facilitate their optimisation.

5.1.5.1.5. Expert Systems

Expert knowledge-based systems employing artificial intelligence or neural network techniques offer possibilities for optimisation approaches to radiotherapy planning, though their use has so far been restricted (Zink, 1989; Lennernäs *et al.,* 1995; Willoughby *et al.,*

1996). Optimisation based on learnt treatment techniques incorporating the relative success of each could imitate the combined knowledge of all experts associated with treatment prescription (Niemierko, 1992). Expert systems also include treatment planners (ie., actual clinical staff), who can utilise their experience in estimating optimal treatment strategies.

5.1.5.2. Optimisation Techniques Employing Numerical Inversion

For the reasons covered in §5.1.2, the concept of an *inverse* approach to radiotherapy planning is rather enigmatic. The inverse approach involves, according to equation 5.1, determining how the distribution of radiation fluence leads to some dose distribution, and many optimisation attempts have employed manipulation of various kernels for a distribution-specific aim (eg., Brahme *et al.,* 1982; Brahme, 1988; Cormack, 1995). It is unfortunate if the dose distribution is not physically realisable since the solution does not exist (Brahme *et al.,* 1982; Cormack and Cormack, 1987; Cormack, 1987; Brahme, 1988; Cormack and Quinto, 1989; Barth, 1990; Gustafsson *et al.,* 1994; Brahme, 1995a,b). In this case, the approach to a solution must be controlled by a *constrained inversion*, where the requirement of a physically realisable dose distribution guides the move to a closest solution to the problem. In this way, the so called *inverse problem* becomes an optimisation problem, and it has been approached as such by many researchers (eg., Cormack, 1987; Brahme *et al.,* 1989; Barth, 1990; Kooy and Barth, 1990; Lind and Källman, 1990; Holmes *et al.,* 1991; Mohan *et al.,* 1994). Were an exact solution to equation 5.1 to exist amongst the range of feasible solutions within the given N-space (for some desired dose distribution), then the inverse problem would be solvable.

5.1.5.2.1. Optimisation by Direct Inversion

5.1.5.2.1.1. Solutions for Cylindrically Symmetric Targets

Lax and Brahme (1982) and Brahme *et al.* (1982) considered the special case of full 2π rotations about cylindrically symmetric patients by evaluating an analytical form of the resulting dose deposition kernel. The required dose profiles can be calculated by inverting an appropriate integral form of equation 5.3. This result has been extended to dose distributions without circular symmetry (Cormack, 1987; Cormack and Cormack, 1987;

Barth, 1990). Unfortunately, this method does not yield physically realisable dose distributions (in the general case) due to resulting negative beam weights (Brahme *et al.*, 1982; Cormack, 1987; Cormack and Quinto, 1989; Barth, 1990; Brahme, 1995a). Tulovsky *et al.* (1995) have obtained exact analytical solutions for this optimisation problem for solutions constrained to positivity, and found a physical objective function in this situation yielded unacceptable optimal distributions in real clinical situations.

5.1.5.2.1.2. Direct Inversion by Fourier Deconvolution

In the case that equation 5.3 does become a convolution equation, with the weighting vector being say, fluence at the surface [ie., $w(\boldsymbol{p}) = w(\boldsymbol{r}')$, where $\boldsymbol{r}'$ is a spatial position at the surface], then the dose distribution is given by

$$D(\boldsymbol{r}) = \iint w(\boldsymbol{r}')\phi(\boldsymbol{r}-\boldsymbol{r}')d^2\boldsymbol{r}' . \tag{5.8}$$

Fourier convolution theory then says that solving equation 5.8 for w involves evaluating

$$w(\boldsymbol{r}) = \mathcal{F}^{-1}\left[\frac{\Delta(s)q(s)}{\Gamma(s)}\right], \tag{5.9}$$

where s is the Fourier-conjugate to $\boldsymbol{r}$, and $\Delta(s)$ and $\Gamma(s)$ are the Fourier transforms of $D(\boldsymbol{r})$ and $\phi(\boldsymbol{r})$ respectively. $q(s)$ is a low pass filter which is introduced in order to remove spurious high frequency components from w brought about by zeros in $\Gamma(s)$ (Brahme, 1988).

Brahme (1988) employed this direct Fourier technique in determining beam profiles for multiple fields delivered in a rotation as in §5.1.5.2.1.1 above. In this case, the kernels are *cylindrical convergent point irradiations*, the dose distribution resulting from a continuous rotation of an external photon pencil beam about some convergent point, or from pencil beams convergent on a point from discrete locations about a rotation[§]. In this case, $w(\boldsymbol{r})$ is the *density of point irradiations*, and must be *back-projected* to the radiation source to determine the beam profiles at each discrete location. At angle θ in a rotation, the profile is described by $f_\theta(x,y)$, where x and y are the transverse coordinates of the incident beam.

[§] This approach assumes an equal photon fluence at the centre of convergence from all directions so that the 'convergent point kernels' are symmetric about the rotation.

$f_\theta(x,y)$ can be related to $w(r)$ by a line integral through the patient along the direction of the incident beam:

$$f_\theta(x,y) = \int_{line} w(r) \exp^{\mu z} dz . \tag{5.10}$$

The exponential term accounts for the variation in attenuation with the patient contour and so, in its simplest form, ignores heterogeneity. z is the depth in the target volume along the direction of the line integral. Performing this integral for each profile at each value of θ allows a set of beam profiles to be built up which will provide approximate conformity to the target volume.

The most significant problem with this direct inversion approach is the fact that equation 5.9 will lead to negative values in the density of point irradiations which, as mentioned in §5.1.2, is physically unrealistic. Brahme (1988) approximated the final w by replacing its negative values with zeroes. Imposing the positivity constraint in this way provides a form of constrained inversion, though one which prevents the technique from acting as an optimisation. Holmes *et al.* (1991) developed a filtering operation to account for the effects of zeroing negative beam weights resulting from Fourier deconvolution, and reported no detrimental effects.

5.1.5.2.2. Deterministic Iterative Search Inversion

The similarities between determining beam profiles by back-projection of desired dose distributions and image reconstruction in CT and SPECT through the integral equation 5.10 and the generalised Radon transform has led several authors to form an association between the two, and the development of *filtered backprojection* techniques for estimating required fluence distributions (Lax and Brahme, 1982; Cormack, 1987; Cormack and Cormack, 1987; Brahme, 1988; Cormack and Quinto, 1989; Barth, 1990; Bortfeld *et al.*, 1990; Holmes *et al.*, 1991; Liu *et al.*, 1993; Bortfeld *et al.*, 1994; Mackie *et al.*, 1995; Brahme, 1995a; Bortfeld and Boyer, 1995). The association between image reconstruction and inverse planning is illustrated in Figure 5-2. Since the inverse (or tomographic) problem in radiotherapy cannot be solved exactly (Brahme, 1995a), and because of the positivity constraint, methods of finding the optimal irradiation strategy using iterative forms of inversion or deconvolution which approach an optimal solution have been developed (Schafer *et al.*, 1981).

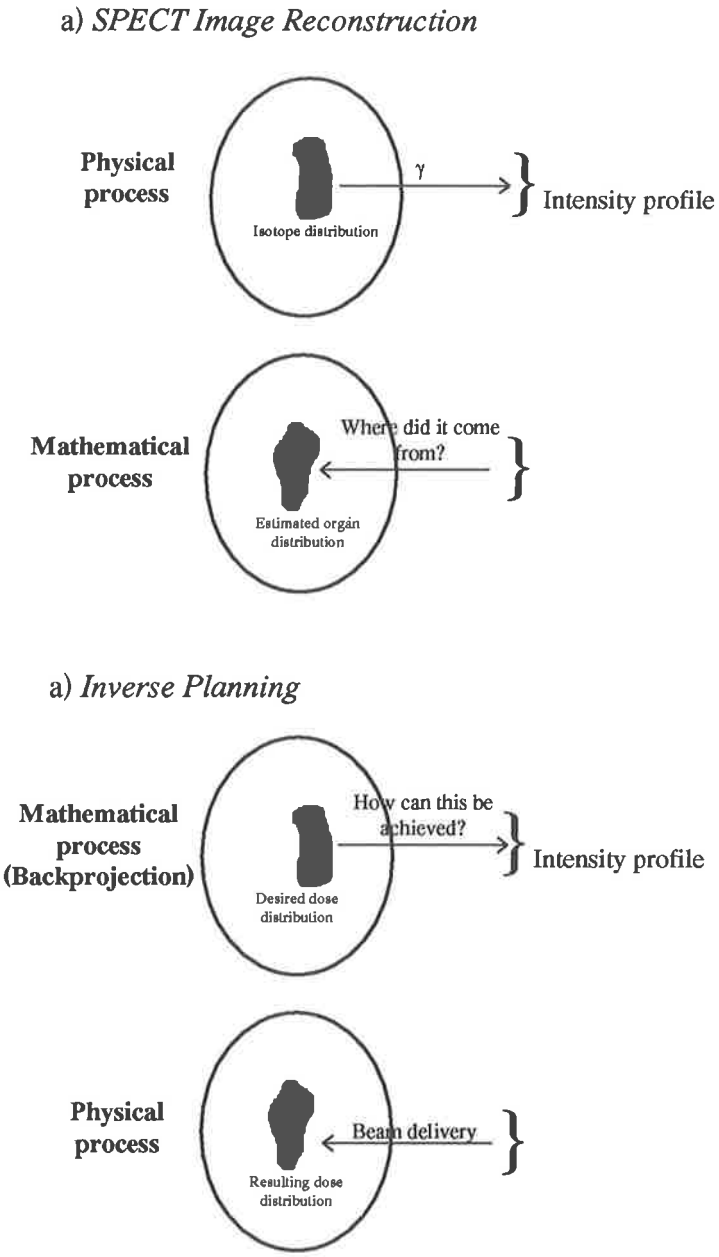

Figure 5-2: Illustration of the analogy between image reconstruction in SPECT and backprojection-inverse planning with external beams. In SPECT, the radiation intensity profile due to emission from an isodose distribution is measured, and mathematically backprojected to determine the organ shape. In inverse planning, the desired dose distribution is mathematically backprojected to obtain a beam intensity profile, which is physically delivered to provide an actual dose distribution.

Many investigations of techniques for such deconvolutions (eg., Cooper, 1978; Lind and Brahme, 1987; Brahme 1988 as in §5.1.5.2.1.2; Brahme *et al.,* 1989; Lind, 1990; Lind and Källman, 1990; Bortfeld *et al.,* 1990; Boyer *et al.,* 1991; Holmes *et al.,* 1991; Lind and

Brahme, 1992; Söderström and Brahme, 1993; Mackie *et al.,* 1995) have concentrated on achieving a desired dose distribution, which may be based on biological response (Källman *et al.,* 1992; Söderström and Brahme, 1992; Wang *et al.,* 1995). Some of these approaches are detailed below. Most of these are based on methods which evaluate the gradient of the objective with respect to changes in variable values, and these shall be considered first. Recently, several researchers (Gustaffson *et al.,* 1994, 1995; Brahme, 1995a; Söderström *et al.,* 1995) have considered a broader view of the optimisation process which globally considers all degrees of freedom via kernel representations of dose due to various irradiations. This approach shall be considered second.

5.1.5.2.2.1. Gradient Methods

The general form of the objective in a radiotherapy optimisation procedure is as some function of the obtained dose distribution, say $f(\boldsymbol{d})$. If, in the space of feasible solutions, the minimum in f occurs at $\boldsymbol{d}_{min}$ when $w=w_{min}$, then the objective function can be expanded by a Taylor series to second order, provided the current approximation $\boldsymbol{d}$ is sufficiently close to $\boldsymbol{d}_{min}$ (Holmes and Mackie, 1994; Brahme, 1995a):

$$f(\boldsymbol{d}) \approx f(\boldsymbol{d}_{min}) - \nabla_d f(\boldsymbol{d}_{min})^T(\boldsymbol{d}-\boldsymbol{d}_{min}) + \frac{1}{2}(\boldsymbol{d}-\boldsymbol{d}_{min})^T \nabla_d{}^2 f(\boldsymbol{d}-\boldsymbol{d}_{min}), \qquad (5.11)$$

where the superscript T refers to matrix transposition. Here, $\nabla_d f(\boldsymbol{d}_{min})$ is the gradient of f at $\boldsymbol{d}_{min}$;

$$\nabla_d f(\boldsymbol{d}_{min})^T = \left[\frac{\partial f}{\partial d_1}, \frac{\partial f}{\partial d_2}, \ldots, \frac{\partial f}{\partial d_N}\right], \qquad (5.12)$$

where it is required (for convergence of the algorithm) that the number of variables, N, be similar to the number of calculation voxels in the target region (Holmes, 1993; Mackie *et al.,* 1995). $\nabla_d{}^2 f(\boldsymbol{d}-\boldsymbol{d}_{min})$ is the *Hessian matrix*

$$\nabla_d{}^2 f(\boldsymbol{d}) = \begin{bmatrix} \frac{\partial^2 f}{\partial^2 d_1} & \frac{\partial^2 f}{\partial d_1 \partial d_2} & \cdots & \frac{\partial^2 f}{\partial d_1 \partial d_N} \\ \frac{\partial^2 f}{\partial d_2 \partial d_1} & \cdots & \cdots & \cdots \\ \cdots & \cdots & \cdots & \cdots \\ \vdots & \cdots & \cdots & \vdots \\ \frac{\partial^2 f}{\partial d_N \partial d_1} & \cdots & \cdots & \frac{\partial^2 f}{\partial^2 d_N} \end{bmatrix}. \qquad (5.13)$$

To determine the minimum in $f(\boldsymbol{d})$ according to equation 5.11, we need to evaluate

$$\nabla_d \, \mathrm{f}(\boldsymbol{d}) = \nabla_d \, \mathrm{f}(\boldsymbol{d}_{\min}) + \nabla_d{}^2 \, \mathrm{f}(\boldsymbol{d} - \boldsymbol{d}_{\min}) = 0 \tag{5.14}$$

whilst considering the necessary constraints (including positivity). This is the basis of Newton's method of iterative minimisation. Imposed constraints tend to make $\nabla_d{}^2 \, \mathrm{f}(\boldsymbol{d} - \boldsymbol{d}_{\min})$ a non-invertible matrix, or a matrix which is extremely difficult to invert because of its size (Brahme, 1995a). As such, an iterative scheme has to be used to successively approximate the solution; at iteration j

$$\boldsymbol{d}_{j+1} = \boldsymbol{d}_j - \left[\nabla_d{}^2 \, \mathrm{f}(\boldsymbol{d}_{j+1} - \boldsymbol{d}_j)\right]^{-1} \nabla_d \, \mathrm{f}(\boldsymbol{d}_j). \tag{5.15}$$

This can be transformed into an expression for $\boldsymbol{w}$ using equation 5.2

$$\boldsymbol{w}_{j+1} = \boldsymbol{w}_j - \boldsymbol{M}^{-1}\left[\nabla_d{}^2 \, \mathrm{f}(\boldsymbol{d}_{j+1} - \boldsymbol{d}_j)\right]^{-1} \nabla_w \, \mathrm{f}(\boldsymbol{d}_j). \tag{5.16}$$

where $\boldsymbol{w}_j$ is the jth approximation of $\boldsymbol{w}$.

Many of the variations in application of this iterative method of deconvolution involve methods of approximating the inverse Hessian matrix (depending on the form of the objective function used; see Holmes and Mackie, 1994), as well as approximating $\boldsymbol{M}^{-1}$. Needless to say there are many variants used, each with their respective merits, though none shall be discussed here in greater detail except for that presented in §5.1.5.2.2.2. Descriptions of the various approximations used are found in the published works (Brahme, 1988; Brahme *et al.,* 1990; Lind, 1990; Bortfeld *et al.,* 1990; Holmes *et al.,* 1991; Källman *et al.,* 1992; Holmes *et al.,* 1993, 1995), and summarised in recent reviews (Holmes and Mackie, 1994; Brahme, 1995a).

Applications of gradient-based iterative deconvolutions in radiotherapy have been very successful, and have facilitated inclusion of biological response into objectives (Källman *et al.,* 1992; Wang *et al.,* 1995). When implemented efficiently, such methods are potentially orders of magnitude faster then stochastic search techniques (§5.1.5.3). With successful approximations of the Hessian matrix and $\boldsymbol{M}^{-1}$, the major time requirement of these techniques is in dose calculation, which can be accelerated using the approximations presented in §5.1.4, or an efficient dose calculation method such as filtered backprojection (Holmes and Mackie, 1994b; Holmes *et al.*, 1995).

Iterative techniques are most efficient when a reasonable approximation is used for the final solution for w when describing w_0, though $w_0 = 0$ is frequently used. Bortfeld *et al.* (1994), in implementing a further modification of an iterative deconvolution, used a method of *projection filtering* of the desired dose distribution. They employed deconvolution in the frequency domain of equation 5-2 to obtain an initial solution estimate, making use of a positivity operator to restrict the dose projection (for further details, see Bortfeld *et al.,* 1990, 1994).

5.1.5.2.2.2. Comprehensive Pencil Beam Optimisation with Biological Objectives

Gustafsson *et al.* (Gustafsson *et al.,* 1994; 1995; Söderström *et al.,* 1995; Brahme, 1995a) have developed an iterative gradient-based deconvolution method for *general* irradiations using pencil beam descriptions of all radiation sources. This allows extensive flexibility in the description of w and incorporation of new technologies with a resolution only limited by that used to describe the pencil beam kernels.

Each pencil beam is described by its modality, m, energy, E, and source position, Ω. The full set of pencil beams depends on the number of modalities, energy bins and allowed source positions, ν_m, ν_E, and ν_Ω respectively, and the number of discrete components describing a fluence profile, ν_ω for a total size of w of $\nu = \nu_m \times \nu_E \times \nu_\Omega \times \nu_\omega$. Gustafsson *et al.* then use an iterative scheme given by (after Lind, 1990; Lind and Brahme, 1992)

$$w_{i+1} = C\left[w_i - aI\nabla \mathrm{f}(d_i)\right] \tag{5.17}$$

for determining the optimal weighting of pencil beams, where C is positivity operator, $\boldsymbol{I}$ is the identity matrix and $a\boldsymbol{I}$ corresponds to the inverse of the Hessian matrix.

In order to incorporate radiobiological response into this scheme, Gustafsson *et al.* have used the probability of cure without severe complication, P_+ (Källman *et al.,* 1992), as the objective, obtaining for the iterative scheme

$$w_{j+1} = C\left[w_j + a\boldsymbol{M}^{\mathrm{T}}\nabla_d P_+(d_j)\right] \tag{5.18}$$

Gustafsson *et al.* have used this scheme for optimising multi-modal treatments in several situations with considerable success.

The ultimate advantage of this developed optimisation technique is the flexibility allowed in selectively including different treatment techniques. This flexibility of the scheme was utilised by Gustafsson *et al.* (1995) in considering multiple approaches using irradiations of widely varying complexity for a single treatment in order to observe the relative benefits of different treatment techniques.

5.1.5.3. Random/Stochastic Iterative Search Inversion

Whereas many of the optimisation techniques described so far rely on systematic or parameter-driven searches of the space of feasible solutions in a radiotherapy optimisation, one class of iterative techniques employs a more stochastic solution-space search. These techniques use random perturbations of the variables defining degrees of freedom at each iteration.

Of the stochastic search methods used in radiotherapy so far, simulated annealing has by far been used the most extensively. It is also the optimisation technique used in the investigation presented in this chapter and so is described in detail. One of the first major introductions of simulated annealing into radiotherapy was by Webb (1989a), who introduced it as a solution to the inverse problem. Other stochastic search techniques which will be discussed are genetic algorithms and RONSC.

5.1.5.3.1. Simulated Annealing

The concept of simulated annealing is founded on an idea attributed to Metropolis *et al.* (1953), in analogy to the notion of the degree of order (total energy) in a cooling solid. If a solid is cooled slowly (annealed), then its atoms can arrange themselves in an order which minimises the total energy of the solid. Whilst cooling, atoms may move to higher energy states (with a probability given by the Boltzmann distribution, dependent on the current temperature of the solid), from which, if given time, they will drop down from as the solid cools. If the solid is cooled quickly however (quenched), then the final arrangement of atoms may be 'trapped' in one where molecules have not fallen from high energy states (ie., in a spatial sense, the molecules form an amorphous rather then crystalline solid). The

well-annealed solid reaches its *global minimum* in the space of possible end-states, whereas the quenched solid has been trapped in a *local minimum*.

If the variables in an optimisation problem are considered to be analogous to the states of molecules in the solid, then the energy (potential) of the system is a function of the variables (via the dose distributions they generate), and the temperature governs the amount by which variables can change as the optimisation proceeds (this amount decreasing with each iteration in the optimisation schedule). The possibility of the system entering a higher energy state is represented by the finite probability of the optimisation moving to a supposedly worse approximation to the optimal solution, with this probability decreasing with decreasing temperature. This prevents the algorithm from becoming trapped in local minima as Figure 5-3 illustrates, guaranteeing the eventual approach to the global minimum. Thus, both variations in variable values (*grain sizes*) as well as probabilities of acceptance can decrease with temperature. This formulation of simulated annealing has been used in many applications in diverse areas including image registration and reconstruction, designing the layout of integrated circuits, economic forecasting, and of course, radiotherapy (Metropolis *et al.*, 1953; Kirkpatrick, 1983; Geman and Geman, 1984; Paxman *et al.*, 1985; Smith *et al.*, 1985; Jeffrey and Rosner, 1986; Press *et al.*, 1986; Willie, 1986; Szu and Hartley, 1987; Johnson, 1988; Corey and Young, 1989; Radcliffe and Wilson, 1990; Press and Teukolsky, 1991; Webb, 1991a,b; Webb, 1992; Sloboda, 1992; Webb, 1994)

The conventional procedure for a simulated annealing algorithm for the problem represented by equation 5.1 proceeds as

1. The vector w is defined for the current problem by associating each component (w_n) with a point in the N space (or with a particular *bixel*). All components of w are given some initial value (perhaps zero).
2. At each iteration, an n is selected (usually randomly) and w_n given some perturbation (has a *grain* added), which may be positive or negative. Grain size may also be constant, or selected from a distribution such as a Cauchy, Lorentzian or Gaussian distribution (see Webb, 1995; Rosen *et al.*, 1995).

Alternatively, perturbations to every element w_n can be considered simultaneously (Rosen *et al.,* 1995).

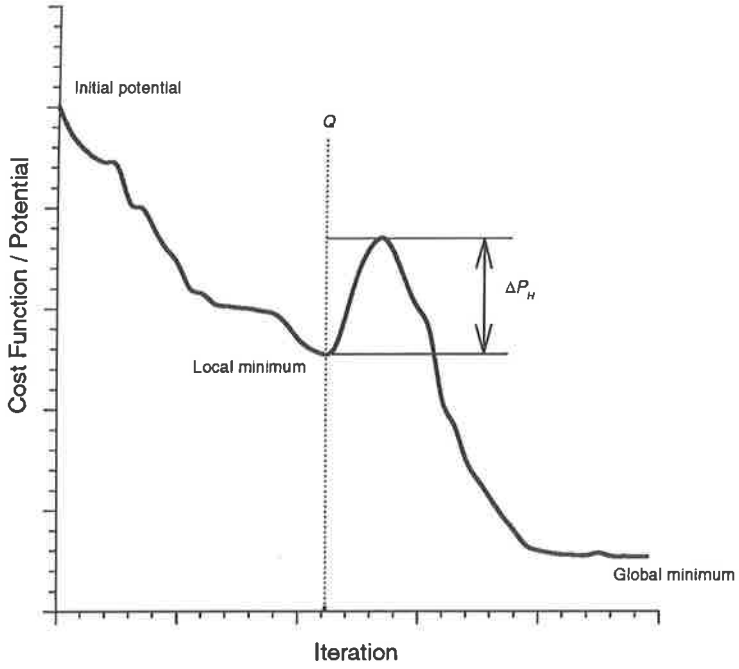

Figure 5-3: Hypothetical variation in a cost function with increasing iterations for an optimisation problem being solved by a simulated annealing technique. At *Q*, the current solution is in a local minimum, and any variations must require positive changes in cost. If successive positive changes in the potential are allowed, then the solution can 'climb' the potential hill (of size ΔP_H in the direction chosen) out of the local minimum, and continue on in its descent towards the global minimum. Provided annealing schedules are cooled sufficiently slowly, they are guaranteed of performing this task.

3. The effect on the dose distribution due to the new w is calculated, and the resulting value of a potential or cost function resulting from the dose distribution evaluated.

4. If the new w is better then the one at the previously accepted iteration, then the change is accepted. Otherwise, it is accepted with a probability governed by the Boltzmann distribution. Thus, if the change in the potential (increase) was ΔP, then the new w is accepted with probability $\exp\left(-\frac{\Delta P}{k_B T}\right)$, where k_B is the Boltzmann constant and T a measure of temperature. In practice, $k_B T$ can be any

numerical value. If T is zero throughout the entire process, then the method is equivalent to a steepest descent approach.

5. This routine proceeds with the size of the perturbations and the probability of acceptance decreasing with time (simulating the cooling down of the annealing solid). The size of the grains and the initial temperature (and the rate at which these decrease) are parameters of the optimisation which themselves have to be optimised, and constitute the annealing *schedule*. The algorithm finishes when some preselected value of the potential is achieved (or the potential is changing sufficiently slowly), or a preselected number of iterations or execution time is reached.

The simplicity of the execution of this routine makes simulated annealing an attractive algorithm for optimisation. In addition, it is extremely flexible in the way in which constraints can be applied. The addition of grains at each iteration can be performed in a controlled way so that values of w_n can never leave some specified range, such as implementing a positivity constraint on all w_n. Constraints can also be placed on dose distributions by not accepting any perturbation which gives an undesired dose distribution, such as exceeding a specified normal tissue tolerance. This capability has been exploited by Morrill *et al.,* (1990). The algorithm also allows extensive flexibility in the definition of the cost function, since it can be evaluated at each iteration by a simple translation from the current dose distribution, to any scalar quantity such as deviation from the desired dose distribution, radiobiological indices etc., as well as multiple combinations of cost functions (Oldham and Webb, 1995).

The dose calculation to be performed during execution of the algorithm can slow the process down extensively, depending on the type of calculation being performed. Webb (1989a), in optimising the intensity modulation of multiple fields, used a simple one-dimensional analytical 'pencil' representation of dose due to beam elements in order to reduce optimisation times. This was subsequently extended to a two-dimensional description to include lateral scatter (Webb, 1991a). In some cases, it is possible to simply 'build up' the dose distribution as the optimisation proceeds. This is done in the next

section of this thesis by adding or subtracting dose kernels from a dose array according to the perturbation of relevant incident pencil beams.

Though simplistic in its approach, and although it can guarantee (after an infinite number of iterations) finding the optimal solution in extremely complex and constrained situations, simulated annealing has the major drawback of being slow (Brahme, 1995a). This does of course depend on the computer platform used to perform the optimisation, though the problem of execution time has led many researchers to investigate methods of speeding up the annealing process whilst still ensuring its accuracy, including combining the procedure with other optimisation techniques (eg., Gibon *et al.,* 1995).

One way of increasing the speed of the algorithm is to use variations in grain size which are as large as possible, and temperatures which decrease as fast as possible. Classical simulated annealing selects grain sizes (Δw_n) according to a Gaussian probability distribution (generator)

$$P_G(\Delta w_n) = \exp\left(\frac{-\Delta w_n^{\,2}}{W_j}\right), \tag{5.19}$$

where W_j controls the latitude of the distribution at iteration j. Temperature, T, and W vary with the inverse log of iteration number

$$T_j, W_j = \frac{T_0, W_0}{\ln\left(\frac{j}{R_{T,W}} + 1\right)}. \tag{5.20}$$

Here, T_0 and W_0 are the starting values of T and W respectively, and R_T and R_W control the rate at which T and W vary. Szu (1987) and Szu and Hartley (1987) proved that it is possible to use a schedule based on a Cauchy generator for grain size;

$$P_G(\Delta w_n) = \frac{W_j}{W_j^2 + \Delta w_n^{\,2}}, \tag{5.21}$$

with T and W varying as the inverse of iteration number

$$T_j, W_j = \frac{T_0, W_0}{\left(\frac{j}{R_{T,W}} + 1\right)}. \tag{5.22}$$

Figure 5-4 compares the Gaussian and Cauchy generators, and shows that the Cauchy distribution has broad tails which can lead to occasional large perturbations in w which allows for tunnelling out of local minima. This increases execution speed and, combined with the more rapid cooling schedule, has given this form of simulated annealing the title, *fast simulated annealing* (Szu, 1987; Szu and Hartley, 1987). Fast simulated annealing has been used successfully in this context in several radiotherapy applications (Mageras and Mohan, 1993; Webb, 1995; Oldham *et al.,* 1995; Oldham and Webb, 1995).

An alternative to using a probability distribution for generating weighting perturbations is to vary perturbation sizes according to the distance of the current estimation of w from the optimal value. In this way, perturbation sizes can start off with large values leading to rapid initial approach to the optimal solution. This technique is known as *variable step size generalised simulated annealing*, and is described in Sutter and Kalivas (1991) and Rosen *et al.* (1995).

Recently, Morrill *et al.* (1995; Rosen *et al.,* 1995) have employed what is known as *very fast simulated reannealing* for the task of treatment plan optimisation. Very fast simulated reannealing was introduced by Ingber (1989; Ingber and Rosen, 1992), and involves several modifications of classical or fast annealing;

- individual variables can have associated with them individual temperatures and grain size generating functions
- cooling is governed by an exponential variation in temperature;

$$T_{n,j} = T_{n,0} \exp\left(c_n j^{\frac{1}{N}} \right) \tag{5.23}$$

  where $T_{n,j}$ is the temperature of variable n at iteration j, c_n a user defined coefficient, and N the size of w
- all variables are restricted to a finite range which may be unique for each variable
- the system is successively *reannealed*, which removes dependence on the choice of initial temperatures and distribution parameters.

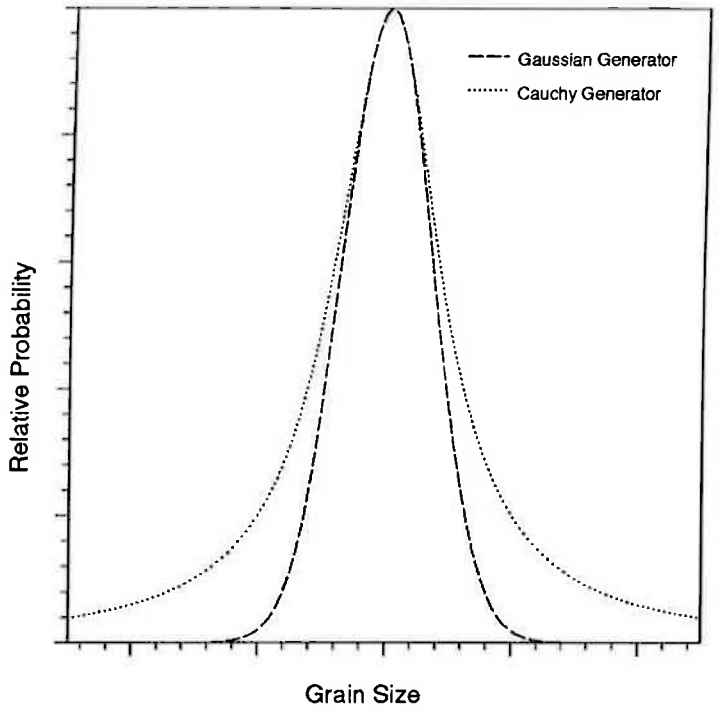

Figure 5-4: Comparison of the variation in grain size for Gaussian (conventional annealing) and Cauchy (fast annealing) generating functions (same temperature and normalisation). The long tails of the Cauchy function provide opportunities for 'tunnelling' out of local minima.

The flexibility provided by very fast simulated reannealing allows individual variables to be evaluated in terms of their effectiveness in altering the potential, and thus tuned to allow the most rapid development of the optimisation. Morrill *et al.* (1995) employed this technique in the optimisation of treatment plans for real clinical situations with clinically reasonable execution times.

5.1.5.3.1.1. Genetic Algorithms

Just as simulated annealing is intended to simulate physical processes involved with the cooling down of a solid, genetic algorithms (Goldberg, 1989; Davis, 1991) simulate the biological processes leading to natural selection and evolution. In the radiotherapy context, individual organisms correspond to specific treatment plans, with a set of feasible (yet undeveloped) plans constituting a population. An objective function (based on arbitrary physical or biological indices) is used to determine the suitability of each plan to the current situation (environment). Treatment plans can combine to spawn new plans (new individuals in the evolutionary process) with a likelihood governed by the suitability

(fitness) of each plan (each parent). The ability to search throughout the set of possible plans is governed by the degree of genetic mutation allowed between successive generations.

Genetic algorithms have been used in radiotherapy for manipulating the weights of potential beams with considerable success (Langer *et al.,* 1994; Ezzell, 1996). Such algorithms can use human-designed plans as the ancestors for successive ones.

As a reasonably fresh approach to optimisation, genetic algorithms need to be refined in order for them to be used most efficiently. Like simulated annealing, genetic algorithms are extremely flexible in definition of constraints and objectives, and are also extremely time consuming. More flexibility is allowed however in the form of search about the space of feasible solutions by variation in the factors affecting mutation at reproduction - these factors may be tuned in order to guide an optimisation around adaptations which are very unlikely to be successful (Ezzell, 1996).

5.1.5.3.1.2. RONSC

Niemierko (1992) has formulated a radiotherapy-specific optimisation algorithm called **R**andom **O**ptimisation with **N**on-linear **S**core functions and **C**onstraints (RONSC). The RONSC algorithm performs a pseudo-random search of the space of feasible solutions formed by the set of applied linear and nonlinear constraints. A point (a set of beam weights) in the total solution set is randomly chosen, and the vector to the point from an arbitrary origin is projected to the edge of a hypersurface defined by the constraints. An objective function is evaluated at this point, and a new point is randomly chosen within a bounded region of the first point, and the projection again made to the edge of the feasible solution space. The objective function is evaluated, and if better then the previous one, retained as the best approximation so far. Otherwise, another point is randomly selected within the region around the first point. The random search is controlled with time by reducing the size of the random moves from successive best estimates.

The RONSC algorithm converges extremely rapidly, and can optimise schedules with 10-20 beams in a matter of minutes on a standard computer platform (in Niemierko's investigation, a MicroVax 3200). Since the RONSC algorithm performs a restricted search

at each iteration, there is a possibility that it could converge to a local minimum in the feasible solution set, a problem which is overcome in the annealing iteration schedule.

5.1.5.4. Searching Universal Phase Space

Due to the restriction in therapy to the treatment machines immediately available, it is natural that most investigations of optimisation in radiotherapy should concentrate on making the best use of the available degrees of freedom. It is possible however, to view the problem as an unconstrained one in which the inversion of a desired dose distribution or the potential for a specified desired biological effect can be used as the basis for determining the actual required characteristics of energetic particles (particle type, energy, location, direction) to most closely match that distribution or effect. The obstacle is, of course, that such radiation tailoring is not possible with contemporary treatment delivery devices. This is the approach taken (for electron beams) in the investigation presented in the next section.

Whereas particle transport normally involves following particles on their forwards path through an irradiated material as they interact and deposit energy, it is possible to track particles backwards along their trajectories by examining the inverse or adjoint transport equation. This is the basis of *inverse Monte Carlo* (Dunn, 1981; Andreo, 1991), which has found application in SPECT imaging (Floyd *et al.,* 1986) and in photon compensating-filter design (Dunn *et al.,* 1987). The practicalities of calculation speed and unrealism of solutions have made detailed inverse transport calculations impractical.

5.2. Current Optimisation Investigation

5.2.1. Introduction - Aims of Investigation

Contemporary developments in radiation treatment delivery are investigating incorporation of as many *useful* degrees of freedom (see §5.1.2) as is practical into the processes of treatment planning and delivery including the manipulation of the treatment beam (Brahme, 1994; Lind and Brahme, 1995). Dose conformity is maximised when the distribution in weighting of the available degrees of freedom is optimised. As technology in dose delivery increases, the degrees of freedom readily available will continue to increase, and it remains to be seen which degrees of freedom are the most important for achieving conformity and ultimately, maximising tumour control with minimal normal tissue complication.

Due to the scattering characteristics of electron beams, tailoring dose distributions with them requires substantial beam manipulation. Such manipulation is already possible (though at significant economic cost), with radiation sources such as microtrons where preferential energy selection is possible, and magnetically scanned pencil beams (eg., Brahme *et al.*, 1989; Lind and Brahme, 1995; Spirou and Chui, 1996; Lief *et al.*, 1996; Zackrisson and Karlsson, 1996; §3.1.2). This investigation looks explicitly at the potential benefits of manipulating electron beams in terms of the electron phase space at a single planar surface of a phantom. It was intended to see how electron manipulation can be employed in order to obtain regular dose distributions with defined dose regions from the smoothly varying dose distributions due to electron pencil beams (see §3.2.1.4). Conversely, it was also intended to see how characteristics of incident electron beams affect dose deposition properties.

In Chapter 3 (§3.2.1) it was seen that the dose distribution characteristics of an electron beam depend upon the energy and angular characteristics of electrons in the beam. It was also seen in that chapter that several studies have been presented for optimising dose

distributions via manipulation of beam characteristics, many concentrating on optimising foil/collimation systems (eg., Marbach and Almond, 1981; Klein *et al.*, 1995). Recent investigations have been performed into the potential for conformal therapy using intensity- and energy/intensity-modulated electron beams (Lief *et al.*, 1995, 1996; Hyödynmaa *et al.*, 1996). Lief *et al.* (1996) considered intensity-modulation of a scanned electron beam for producing desired dose profiles at depth. They considered intensity-modulation via the *amplitude* of elementary electron pencil beams, and the pencil beam spatial *frequency*. Using these methods, illustrated in Figure 5-5, they calculated the surface fluence profiles required for restricting the broadening of electron beam penumbra with depth, limited only by the penumbral sharpness of the elementary pencil beam.

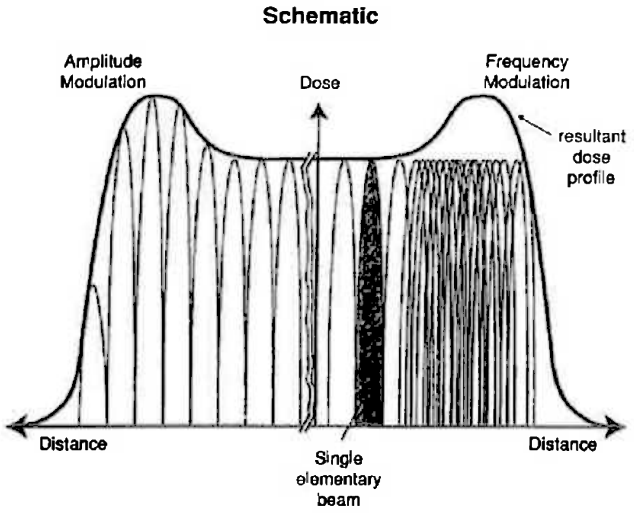

Figure 5-5: Illustration of the amplitude and frequency pencil beam modulation methods used by Lief *et al.* (1996). Pencil beam amplitudes and frequencies were varied in order to optimise dose profile definition at depth in water.

Hyödynmaa *et al.* (1996) combined intensity-modulation with energy-modulation by considering the required intensity distributions for beams of discrete energies which provide the greatest conformity (according to radiobiological indices), to a set of specific desired dose distributions. This degree of manipulation allows greater tailoring of the high-dose region of the resulting dose distribution, providing greater definition of the target region than for single-energy intensity-modulated beams. Hyödynmaa *et al.* (1996) compared this technique to calculations of optimised bolus design made by Low *et al.* (1992), and found moderate improvement on dose homogeneity for similar test cases.

The investigations of Lief *et al.* (1996) and Hyödynmaa *et al.* (1996), exemplify the pursuit of dose conformity using highly manipulated electron beams. The aim of the current investigation was to ascertain the relative benefits of manipulating electron beams in terms of intensity-, energy-, and angular-modulation of the constituent electrons, with a degree of manipulation beyond that available using current technology in electron beam delivery.

The discussion in §5.1 above highlighted the requirements of selecting appropriate objective functions in an optimisation schedule. For the purpose of evaluating electron beam manipulation, it was considered that a physical objective (least-squares minimisation) would provide adequate conformity stringence and thus indication of the potential merits and effects of manipulation of each degree of freedom. It was not the purpose of this investigation to determine the best objective function to use. Also, the actual dose distributions to be conformed to are not important and they are not meant to be *optimal* (though they require a high uniform dose to a target region and low or zero dose to surrounding regions). Only the *beam characteristics* are optimal in that they give the best conformance to the chosen distributions according to the selected objective.

The constraints placed upon the available degrees of freedom, together with dose constraints, define the space of feasible solutions to the optimisation problem. In the current investigation, the radiation type has been restricted to electrons, and the direction of electrons to one side of a plane. This restriction was set in order to evaluate the potential benefits for conformity of manipulation of the energy and angular characteristics in an electron beam, and the degree to which these characteristics influence broad dose distributions.

5.2.2. Method

5.2.2.1. Optimisation Technique

Simulated annealing optimisation (§5.1.5.3.1 above) was used to determine optimal electron phase spaces for specific desired dose distributions. A basic implementation of conventional simulated annealing was used as described by many authors (Corana *et al.*, 1987; Webb, 1989a, 1991a, 1994; Sloboda, 1992; see §5.1.5.3.1), with a Gaussian distribution in grain size selection (see equation 5.19) with standard deviation decreasing with iteration number (see equation 5.20), and an inverse logarithmic cooling schedule (see equation 5.20). The possibility for using a fast annealing schedule was also included in the code written to perform the annealing procedure.

The relative conforming ability of any phase space was evaluated using a least-squares objective. At iteration j, the potential, P_j, is

$$P_j = \sum_{k=1}^{N_k} \sum_{i=1}^{N_i} \alpha_{i,k} \left(D_{i,k} - d_{i,k}^{j} \right)^2 , \tag{5.24}$$

where $D_{i,k}$ is the desired dose (normalised to a user-defined dose value) in voxel (i, k), $d_{i,k}^{j}$ the calculated dose to voxel (i, k) of a two-dimensional phantom at iteration j, and $\alpha_{i,k}$ the predetermined weighting of voxel (i, k) [ie., the relative importance of voxel (i, k) having dose $D_{i,k}$].

The annealing procedure was coded in C and executed on a DEC Alpha platform. The program written to perform the algorithm is summarised and presented in Appendix F, together with sample input and output files. At each iteration, a beam element is selected randomly and has a grain (possibly negative) added. For the Gaussian generator, the perturbation is determined by obtaining two random numbers, ζ_1 and ζ_2 sampled uniformly on the interval [0,1] (with $\zeta_1 > 0$) and evaluating

$$\Delta w_n = W_j \left[-2 \ln(\zeta_1) \right]^{\frac{1}{2}} \cos(2\pi\zeta_2) \tag{5.25}$$

(Press *et al.*, 1992) to obtain the perturbation, Δw_n, of beam element n, where W_j is the standard deviation of the Gaussian spread at iteration j. For the Cauchy generator, the appropriate probability distribution sampling function is

$$\Delta w_n = \pm W_j \tan\left(\frac{\pi\zeta_2}{2}\right) \tag{5.26}$$

with the sign of the perturbation governed by the value of ζ_1.

The perturbation to the dose distribution is calculated as described in §5.2.2.2, and equation 5.24 evaluated to determine the possible change to the potential. If the change decreases the potential, then it is accepted. Otherwise, it is accepted according to the annealing criterion (Boltzmann distribution; Kirkpatrick *et al.*, 1983; §5.1.5.3.1).

A series of random number generators were added to the code which can be individually selected for each annealing schedule. These are based on algorithms described in Knuth (1981) and Press *et al.* (1992). The default C generator was not used due to the large number of random numbers required for an annealing run (often > 10^6).

Multiple constraints may be applied (Morrill *et al.*, 1990) throughout the desired dose distribution, and changes rejected according to minimum and maximum dose tolerances in any region of the phantom. Positivity is always ensured by never allowing a beam element weighting to become negative.

A fast annealing schedule (Szu and Hartley, 1987; Mageras and Mohan, 1993; Webb, 1995) was tested and found difficult to tune, giving irregular solutions (eg., asymmetric fluence profiles for symmetric dose distributions), possibly because of the very large numbers of variables being used. After several executions of a conventional annealing schedule with varying parameters (initial temperature, T_0, temperature variation-rate parameter, R_T, initial Gaussian standard deviation, W_0, standard deviation variation-rate parameter, R_W), suitable values could be decided upon. The variation in temperature and standard deviation with iteration number for various values of R_W and R_T is shown in Figure 5-6. As an example, the values T_0=0.5, W_0=100, R_W=1000 and R_T=10000 were found to provide an efficient annealing schedule for many of the problems examined.

Figure 5-7 shows the variation in potential (according to equation 5.24) with iteration number for the annealing routine for dose distribution B and phase space restriction i) as detailed in §5.2.3.1 below. The early rapidity of convergence shown in Figure 5-7 is fairly typical of all the annealing routines executed, without obvious evidence of the influence of local minima. All schedules were terminated when the potential consistently remained constant to three significant figures.

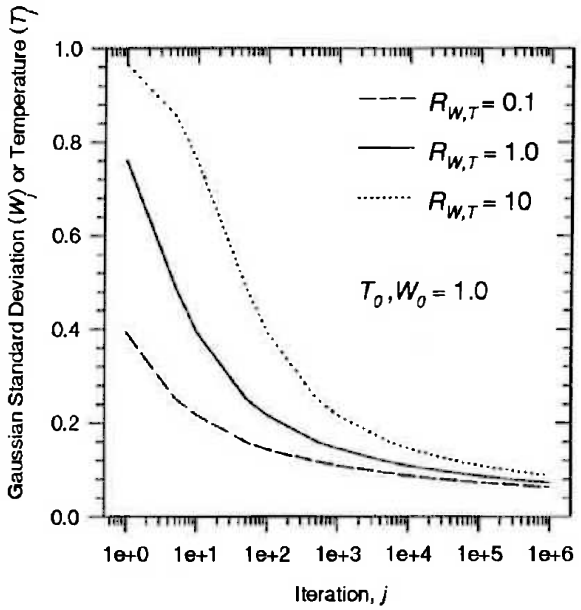

Figure 5-6: Variation in the standard deviation of the Gaussian generating function or temperature with iteration number for different values of the parameters R_W. or R_T. With iteration, j, the variation is $W_j, T_j = \frac{W_0, T_0}{\ln\left(e + \frac{j}{R_{W,T}}\right)}$.

The initial weighting of all beam elements was zero, though the program written to implement the optimisation algorithm had the facility to restart a run at any time should greater resolution be required. This was facilitated by the constant logging of the annealing run during execution, and periodic logging of beam element weightings (phase space files) and resulting dose distributions to text files. This also allowed examination of the development of phase spaces and dose distributions with time.

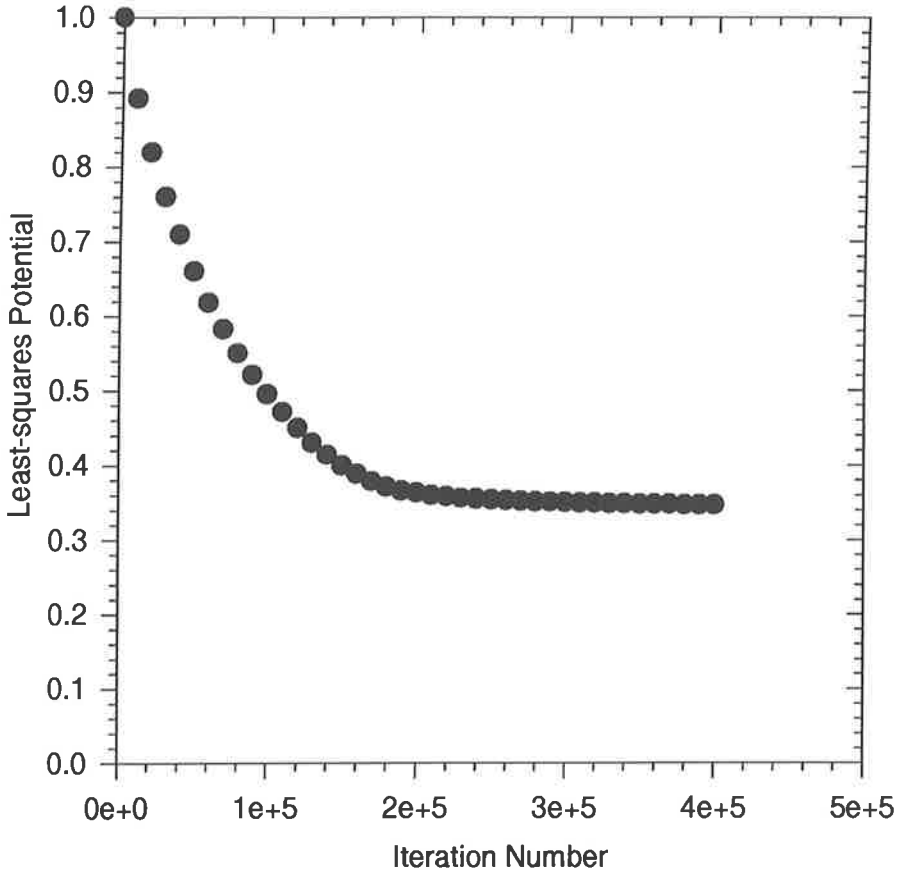

Figure 5-7: Variation in potential with iteration number for dose distribution B and a monoenergetic (12 MeV) normally-incident phase space.

5.2.2.2. Dose Calculation and Kernel Generation

For the implementation of equation 5.2, the matrix $\boldsymbol{M}$ had to be pre-calculated. The columns of $\boldsymbol{M}$ represent the distribution of dose (or energy deposition since only homogeneous water equivalent phantoms were considered) due to incident *pencil beam line sources*, each characterised by a specific angle of incidence and electron energy. Line sources were considered due to the restriction to a one-dimensional beam fluence distribution, and the resulting assumption that the beam is infinitely wide. The elemental pencil beam line sources shall be referred to as *bixels*. Figure 5-8 shows the geometry of

the dose calculation phantom and bixels. The restriction to one dimension in the incident plane was made because of the resulting large size of the fluence weighting vector w (for 50 spatial locations, 17 angles of incidence and 25 energies, w has 21250 elements - there are 21250 bixels).

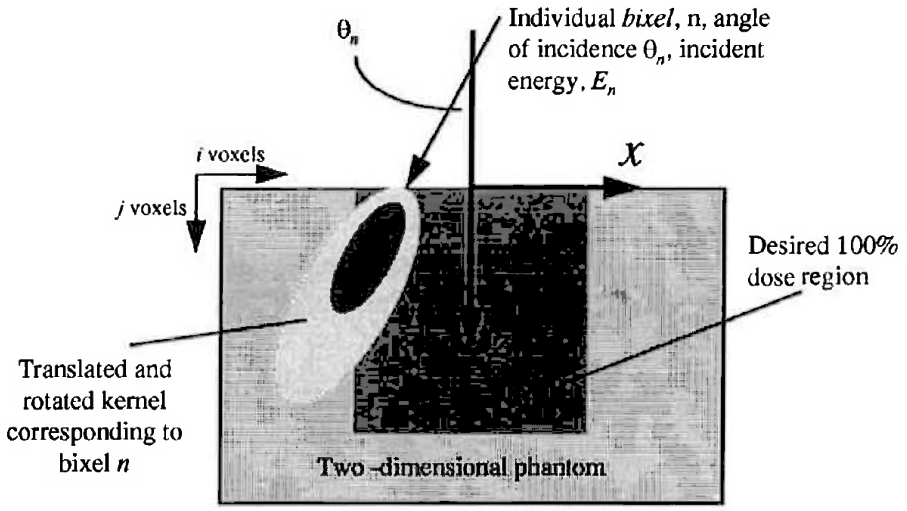

Figure 5-8: Geometry of phantom and kernels for dose calculation.

Dose deposition kernels (normalised to incident fluence) were generated for 2 mm^2 normally incident, monoenergetic electron beams with energies 2 MeV to 50 MeV in 2 MeV increments, using EGS4 Monte Carlo (Nelson *et al.*, 1985) and the usercode RTPCYL (see Appendix A) with energy cutoffs, ECUT=AE=0.512 MeV, PCUT=AP=0.01 MeV. These kernels represent dose (due to all particles, including bremsstrahlung generated in the water) to cylindrical annuli at discrete depths. These kernels were then superposed along a line of such sources (to outside the maximum lateral electron range) to obtain kernels of dose deposition due to infinitely long line sources, and stored in libraries. A typical name for a kernel file in the library is **A**MeV.kernel, where **A** is the energy (in MeV) of the incident electrons (eg., '12.0MeV.kernel' for the 12.0 MeV normal incidence kernel).

Dose kernels for electrons incident at angles other then normal incidence (constituting, with kernels at all off-axis positions, all other columns of M) were not generated. Instead, when a kernel for obliquely incident electrons was required [with doses calculated at

positions $r = (x', y')$], the normally incident kernel of the same energy [with doses calculated at positions $r = (x, y)$], was rotated according to

$$\begin{bmatrix} x' \\ y' \end{bmatrix} = \begin{bmatrix} \cos(\theta_n) & -\sin(\theta_n) \\ \sin(\theta_n) & \cos(\theta_n) \end{bmatrix} \begin{bmatrix} x \\ y \end{bmatrix}. \tag{5.27}$$

The effects on electronic equilibrium at the surface due to kernel rotations were considered minimal and ignored in all calculations. Kernels were thus considered invariant with respect to rotation, even though there will be some effect due to the proximity of the surface for large rotations (due to lack of scatter from missing tissue/extra scatter from additional tissue). Similarly, kernels for bixels incident at off-axis positions were not generated separately, but calculated by translation of the appropriate incidence kernel.

The resulting kernels (after appropriate translations and rotations) are discrete forms of the $\phi_n(r)$ of equation 5.1, where n refers to a complete specification of a bixel's energy, angle of incidence, and location of incidence. The integral equation can then be re-expressed in the form used at calculation for the dose at voxel (i, k) of the phantom;

$$d(i,k) = \sum_{n=1}^{N} w_n \phi_n(i', k'). \tag{5.28}$$

i' and k' are the voxels in the rotated kernel corresponding to voxels i and k of the phantom. The number of incidence locations depends on the specified width of the incident beam [ie., the number of incidence locations = (beam width)/(bixel width)]. The total number of incident bixels (ie., size of N), is thus the product of the number of incidence locations, the number of incidence angles and the number of electron energies.

Kernels and phantoms of varying voxel sizes could be used depending on the resolution required and the resulting calculation sizes. The consequence of this flexibility is that when dose kernels are added to the dose distribution, some aliasing effects occur resulting in artefacts evident in dose distributions and phase spaces.

The dose calculation at each iteration of the annealing procedure represents the largest cost in terms of execution time. With the DEC Alpha platform used to perform the annealing procedure, a mean CPU time of 0.09 sec was recorded per iteration.

5.2.2.3. Dose Distributions Considered

In order to examine the *effects* of electron manipulation, desired dose distributions were considered for which the closeness of fit of the calculated distributions would depend strongly on the degree of electronic disequilibrium, surface dose and practical range (see §3.2.1). For this purpose, three rectangular dose distributions were considered, varying in width, desired depth, and degree of superficiality. These are shown in Figure 5-9. High weightings were applied to the 0% regions of the phantoms in Figure 5-9 in order for the optimisation to place a high value on achieving 0% in these regions. This will be at the expense of flatness in the 100% region. A complex example was also considered as shown in Figure 5-10, comprising multiple complexities including a surface region where dose deposition is to be avoided, and sensitive regions adjacent to the irregular 100% region.

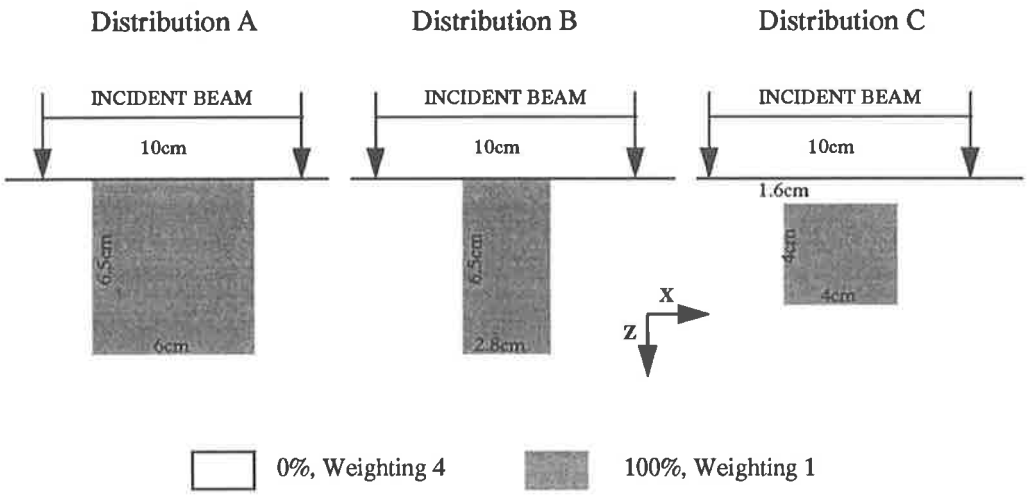

Figure 5-9: The three regular desired dose distributions considered (A, B and C). The desired 100% dose value is an arbitrary value specified in the annealing routine. The weighting applied to each region specifies the values of α in equation 5.24.

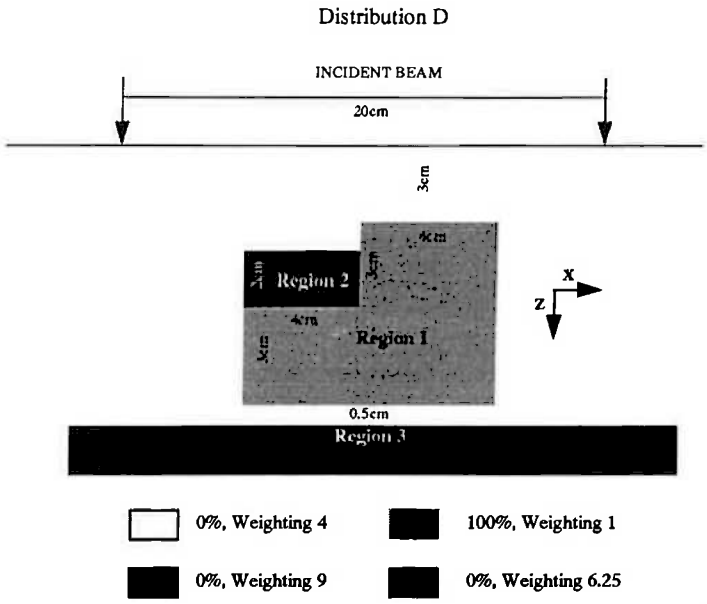

Figure 5-10: The more complex desired dose distribution considered, showing the principle dose regions, their desired dose values, and applied weightings.

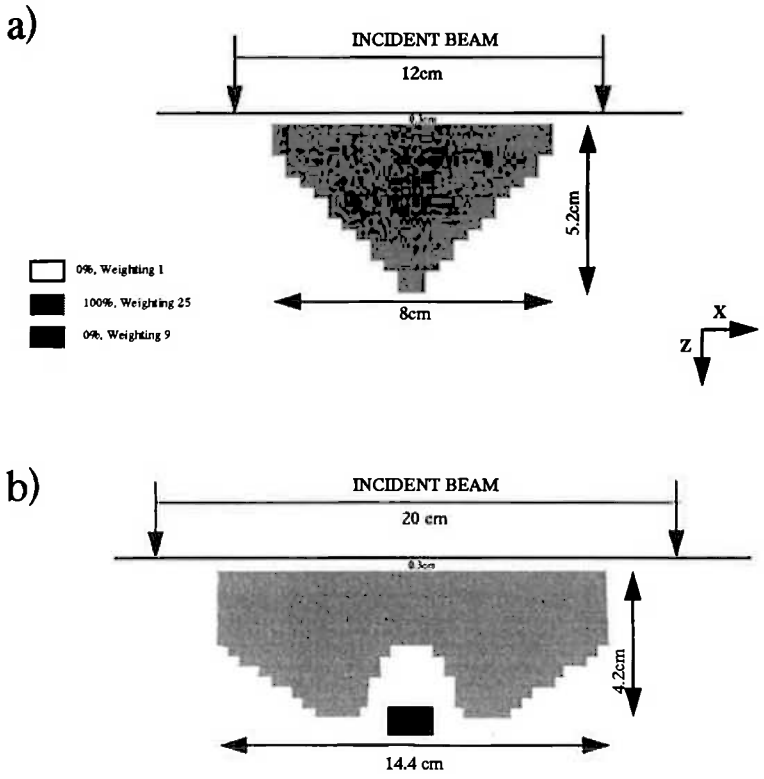

Figure 5-11: Other complex dose distributions examined [also considered by Lief *et al.* (1992, 1995) and Hyödynmaa *et al.* (1996)]. a) A superficial wedge-shaped distribution and, b) simple representation of irradiation of the paraspinal muscle with spinal chord considered an organ at risk.

It was also desired to investigate the potential *benefits* of electron manipulation. For this purpose, two more geometrically complex examples studied by Low *et al.* (1992, 1995) and Hyödynmaa *et al.* (1996) were also considered, these being a wedge-shaped superficial target (Figure 5-11a), and irradiation of the paraspinal muscle, with the spinal chord considered an organ at risk (Figure 5-11b). In these examples, weighting factors are meant to reflect more clinically-relevant objective doses.

5.2.2.4. Phase Space Restrictions

Electron phase spaces of increasing complexity were considered for each desired dose distribution. For the simplest case, where only beam intensity-modulation is considered, w_j, the weighting vector at iteration j, is a weighting vector for only monoenergetic, normally incident bixels evenly spaced along a line at the phantom's surface. If energy modulation is added, then w_j weights bixels of all possible discrete energies (up to 25 energies in this investigation), normally incident at each incidence location. For a monoenergetic phase space with angular modulation, w_j weights bixels at all possible discrete angles of incidence at each incidence location. For angular variations, 17 discrete angles of incidence were used from -80^0 to 80^0 (including normal incidence) distributed linearly in angle. For simulations where greater angular resolution about normal incidence was required, 37 angular bins were distributed in equal cosine increments about normal incidence**. When intensity-, energy- and angular modulation is considered, w_j represents the weighting of bixels which each describes a specific location of incidence, angle of incidence, and electron energy. In such a case, w_j can have approximately 5×10^4 elements, depending on the width of the beam considered, and the selected energy/angular resolution.

Manipulation of spatial, energy, and angular degrees of freedom (using discrete beam elements) were thus considered in the following order:

** Cosine sampling represents bixels incident at angles of $\cos^{-1}(\varsigma)-\frac{\pi}{2}$ (see Figure 5-8), where ς is a random number on [-1,1] rounded to give a resolution equal to that of the desired angular sampling resolution. This type of sampling shall be referred to as 'cosine sampling'.

i) Monoenergetic electrons at select energies with significant peaks in polyenergetic phase spaces, normal incidence[††].

ii) Monoenergetic electrons at energies with significant peaks in polyenergetic phase spaces for the same distribution, variation in angle of incidence.

iii) Polyenergetic electrons, normal incidence.

iv) Polyenergetic electrons, variation in angle of incidence.

5.2.2.5. Sinogram Representation of Intensity Distributions

In order to present the complex variations in beam element intensity with energy, position and incidence angle, a graphical routine was developed to display the relative element intensity using a *sinogram* representation. These are grey scale intensity maps with the grey scale varying either linearly or logarithmically with relative beam element weighting, from black (weighting 0%) to white (weighting 100%). Most phase spaces are presented with logarithmically varying beam weightings since this partially smooths these distributions which were often subject to low-intensity statistical noise.

For fixed angle, polyenergetic beam elements, sinograms show variation in energy spectra with position (*energy sinograms*); for variation in incidence angle with monoenergetic beam elements, they show variation in angular spectra with position (*angular sinograms*). When energy and incidence angle both vary, several sinograms must be generated at different energies or angles to observes variations in either.

[††] For the regular distributions (A and B), the energies chosen for monoenergetic beams were based approximately on R_{50} and R_p. since it was thought that peaks in energy spectra would occur near such energies. It was thought that such selection would be more appropriate for the least-squares potential used than would a more clinically based value, such as R_{80}. For the purpose of the investigation, the actual energy selected is really quite arbitrary as long as the optimal solution is not the trivial one ($w = 0$).

5.2.3. Results

5.2.3.1. Rectangular Distributions (Distributions A-C)

Table 5-I to Table 5-III show the variation in the ratio of the final optimisation potential to the initial value (where all beam element weights are zero), as well as maximum (D_{max}), minimum (D_{min}), mean (D_{mean}) and standard deviation (D_σ) in dose (for each dose region) for the rectangular dose distributions considered (distributions A-C), and for separate phase space restrictions. The dose total (D_{tot}) for the phantom represents the summed dose (%) received by the 0% region (weighing 4) of each phantom. Since this will depend on voxel numbers and sizes used in each calculation, values of D_{tot} can only be compared for the same dose distribution.

Cumulative dose-area histograms for the 100% dose regions for each of the rectangular distributions (distributions A-C) and for the various phase space restrictions are shown in Figure 5-12. Histograms have been separated out into monoenergetic and polyenergetic cases for clarity.

The dose distributions obtained at the completion of the optimisations with the four phase space restrictions for distribution A are shown in Figure 5-13 as dose distribution contour plots. Note that these plots display the effects of aliasing in superposing dose kernels as irregularities in the dose distribution. Similar distributions are shown in Figure 5-14 for distribution B, and Figure 5-15 for distribution C. For distributions A and B, it was found that monoenergetic beams above 16 MeV could not approach the desired 100% dose value in the 100% dose region due to excessive dose deposition in the 0% region distal to the 100% region.

Table 5-I: Collated results for dose distribution A

	P_{final}/P_o †	D_{max} 100% (D_{min} 100%) *D_{mean} 100% (D_o 100%)*	D_{max} 0%‡	D_{tot} 0%‡
Normal incidence, mono-energetic (12 MeV).	0.236	**144.2** **(1.3)** *73.6* *(3.1)*	39.9	781.6
Normal incidence, mono-energetic (16 MeV)	0.204	**114.5** **(32.0)** *80.7* *(2.1)*	38.3	1919.2
Variable angle, mono-energetic (12 MeV)	0.210	**126.3** **(1.2)** *78.4* *(3.0)*	23.5	558.5
Variable angle, mono-energetic (16 MeV)	0.155	**131.6** **(32.2)** *85.8* *(1.9)*	31.2	1521.8
Normal incidence, poly-energetic	0.148	**125.2** **(31.9)** *84.4* *(2.1)*	30.3	1674.4
Variable angle, poly-energetic	0.145	**115.4** **(23.2)** *83.6* *(2.0)*	27.4	1680.9

† Initial potentials calculated with all beam element weights zero, ie., Equation 5.24 with all d_{ik}^{j} zero. Annealing runs finished when potential consistent in two iterations to three significant figures.

‡ 0% dose region.

Table 5-II: Collated results for dose distribution B

	P_{final}/P_o †	D_{max} 100% (D_{min} 100%) *D_{mean} 100% (D_σ 100%)*	D_{max} 0%‡	D_{tot} 0%‡
Normal incidence, mono-energetic (12 MeV)	0.349	**134.0** **(1.0)** *65.7* *(2.6)*	55.2	1989.9
Normal incidence, mono-energetic (16 MeV)	0.298	**119.3** **(27.8)** *71.2* *(1.9)*	41.8	3335.9
Variable angle, mono-energetic (12 MeV)	0.286	**131.7** **(0.8)** *70.6* *(2.7)*	42.6	1690.4
Variable angle, mono-energetic (16 MeV)	0.270	**131.8** **(31.5)** *75.7* *(1.9)*	31.8	3097.1
Normal incidence, poly-energetic	0.271	**122.3** **(22.5)** *69.1* *(2.0)*	27.8	4219.0
Variable angle, poly-energetic	0.263	**121.3** **(19.4)** *(70.8)* *(2.1)*	30.2	4042.6

† Initial potentials calculated with all beam element weights zero, ie., Equation 5.24 with all d^j_{ik} zero. Annealing runs finished when potential consistent in two iterations to three significant figures.

‡ 0% dose region.

Table 5-III: Collated results for dose distribution C

	P_{final}/P_o †	D_{max} 100% (D_{min} 100%) *D_{mean} 100% (D_c 100%)*	D_{max} 0%‡	D_{tot} 0%‡
Normal incidence, mono-energetic.	0.479	**106.1** **(25.5)** *53.2* *(2.3)*	84.5	2139.3
Variable angle, mono-energetic	0.372	**118.7** **(33.1)** *61.9* *(2.2)*	89.3	2131.7
Normal incidence, poly-energetic	0.468	**101.8** **(31.2)** *53.0* *(2.0)*	84.4	2205.8
Variable angle, poly-energetic	0.380	**104.9** **(29.7)** *60.0* *(2.2)*	74.0	2404.3

† Initial potentials calculated with all beam element weights zero, ie., Equation 5.24 with all d_{ik}^{j} zero. Annealing runs finished when potential consistent in two iterations to three significant figures.

‡ 0% dose region.

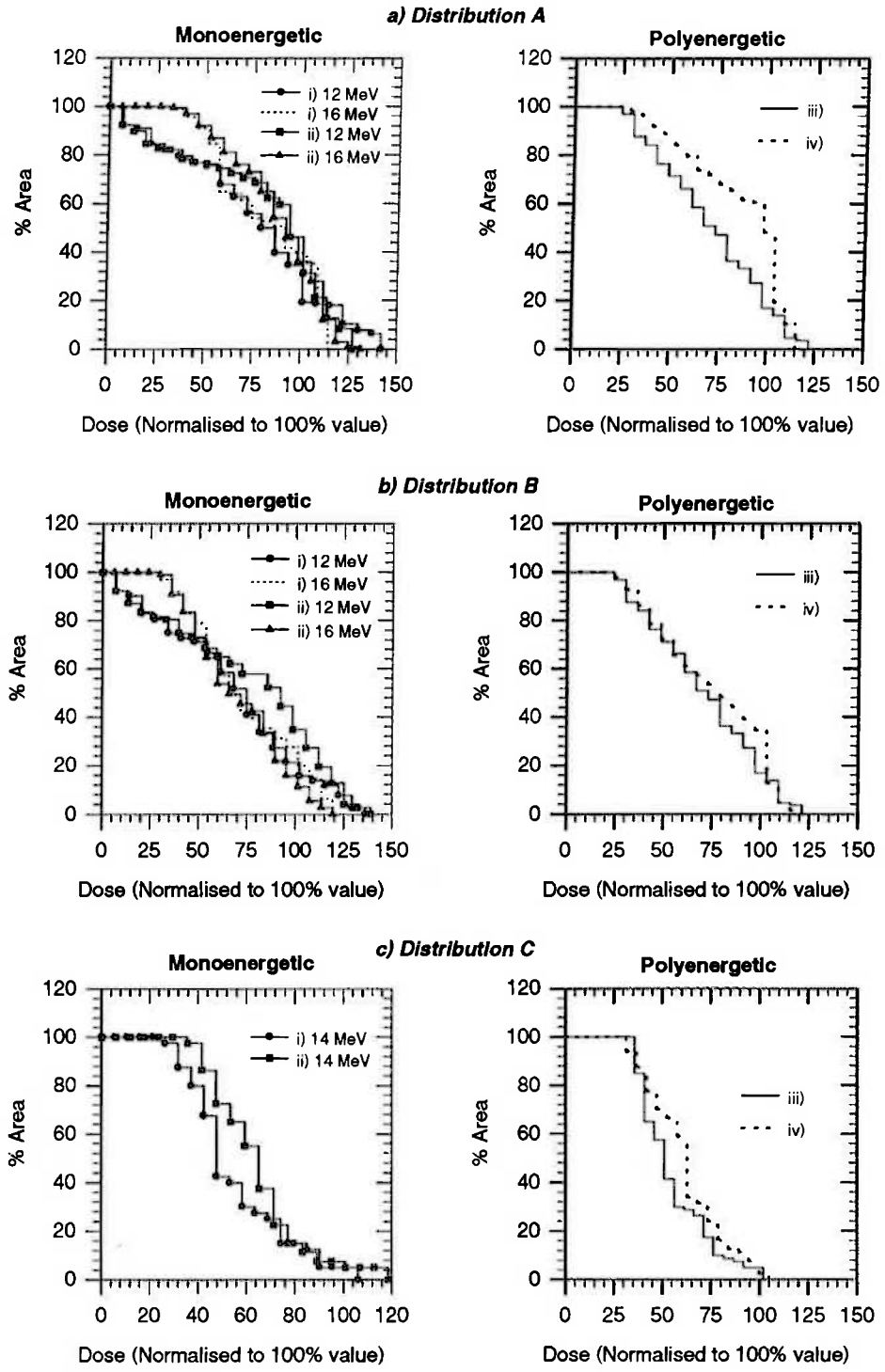

Figure 5-12: Dose-area histograms for resulting closest-approach dose distributions from the annealing procedure for the 100% dose region of a) desired distribution A, b) desired distribution B and c) desired distribution C (Compare Figure 5-9). The phase space restrictions are, for each histogram, incident electrons which are i) monoenergetic [a) 12 MeV and 16 MeV, b) 12 MeV and 16 MeV, c) 14 MeV] and normally incident, ii) monoenergetic and having variable incidence angle, iii) polyenergetic and normally incident, iv) polyenergetic and having variable incidence angle.

a) *12 MeV, normally incident*

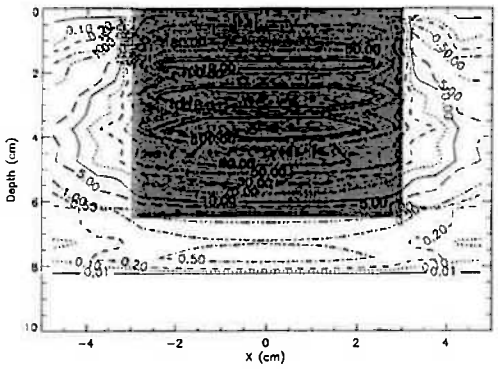

b) *16 MeV, normally incident*

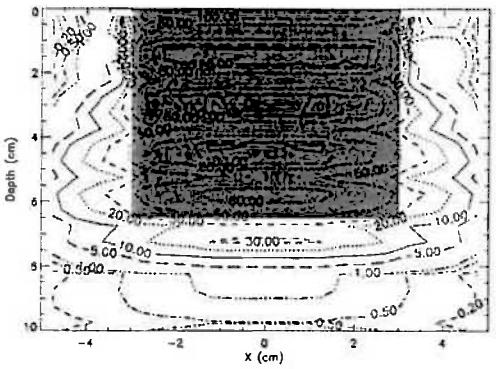

c) *12 MeV, variable incidence angle*

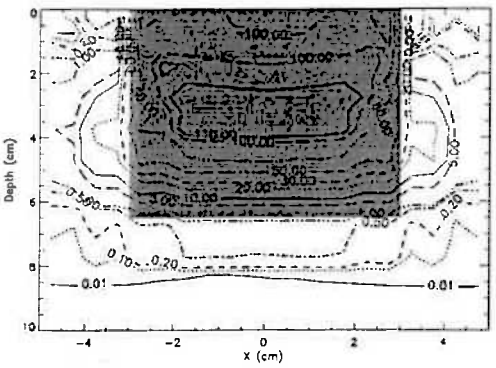

d) *16 MeV, variable incidence angle*

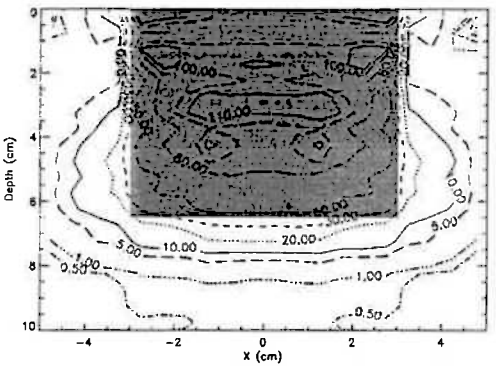

e) *Polyenergetic, normally incident*

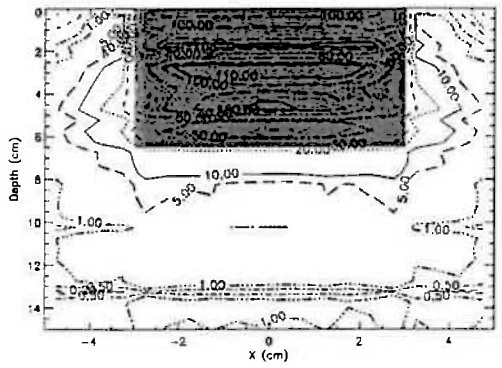

f) *Polyenergetic, variable incidence angle*

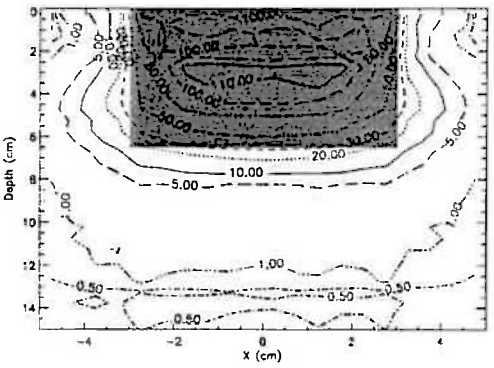

Figure 5-13: Final dose distributions for distribution A for incident electron phase spaces a) 12 MeV monoenergetic normally incident, b) 16 MeV monoenergetic normally incident, c) 12 MeV monoenergetic with variable incidence angle, d) 16 MeV monoenergetic with variable incidence angle, e) polyenergetic, normally incident, and f) polyenergetic, variable incidence angle.

a) *12 MeV, normally incident*

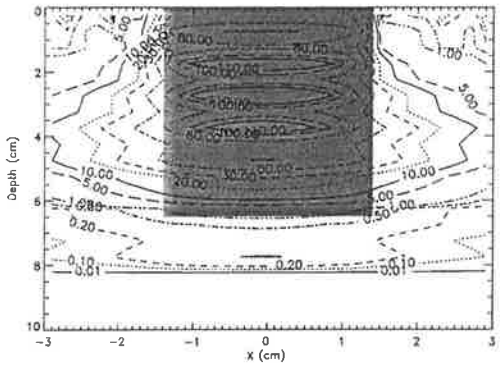

b) *16 MeV, normally incident*

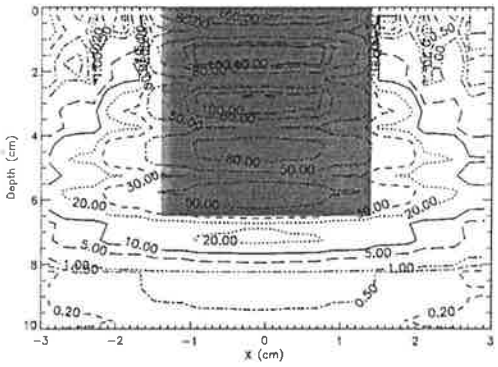

c) *12 MeV, variable incidence angle*

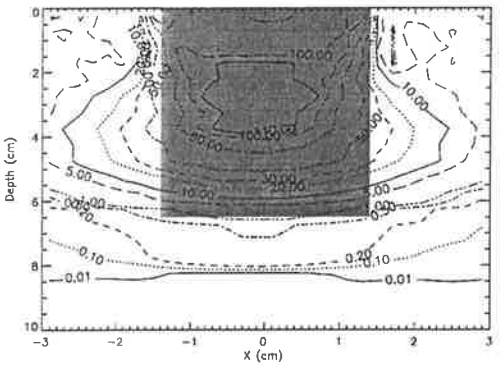

d) *16 MeV, variable incidence angle*

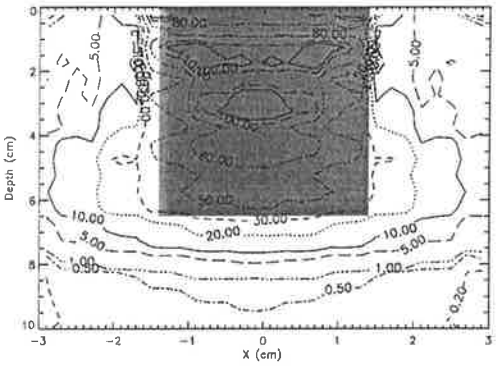

e) *Polyenergetic, normally incident*

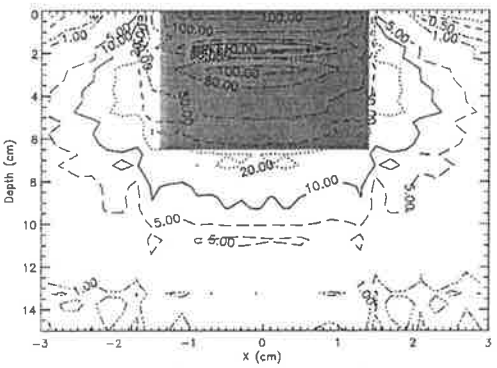

f) *Polyenergetic, variable incidence angle*

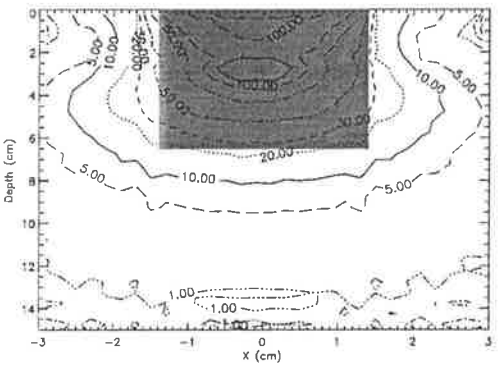

Figure 5-14: Final dose distributions for distribution B for incident electron phase spaces a) 12 MeV monoenergetic normally incident, b) 16 MeV monoenergetic normally incident, c) 12 MeV monoenergetic with variable incidence angle, d) 16 MeV monoenergetic with variable incidence angle, e) polyenergetic, normally incident, and f) polyenergetic, variable incidence angle.

a) *14 MeV, normally incident*

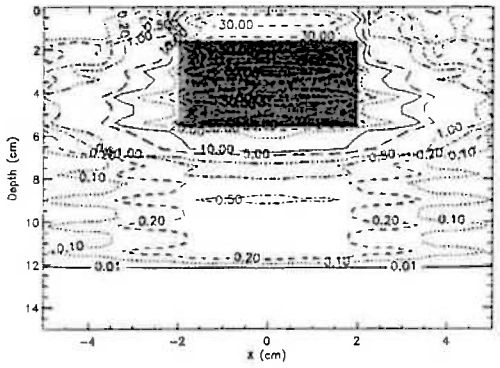

b) *14 MeV, variable incidence angle*

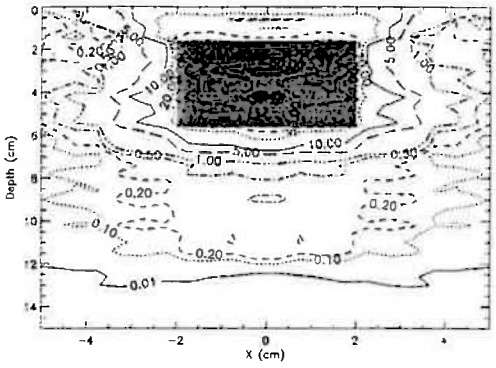

c) *Polyenergetic, normally incident*

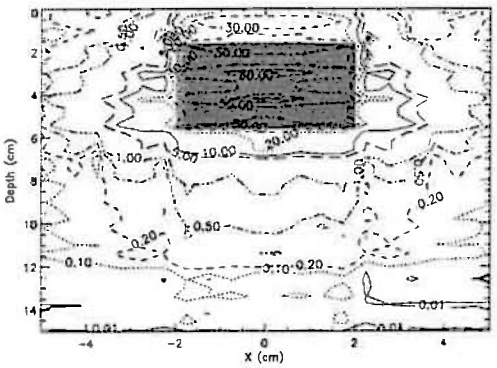

d) *Polyenergetic, variable incidence angle*

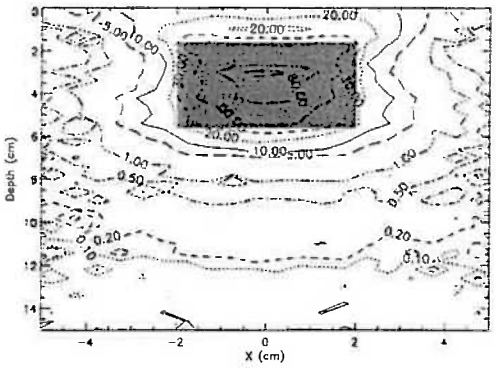

Figure 5-15: Final dose distributions for distribution C for incident electron phase spaces a) 14 MeV monoenergetic normally incident, b) 14 MeV with variable incidence angle, c) polyenergetic, normally incident, and d) polyenergetic, variable incidence angle.

With only normally incident monoenergetic (12 MeV and 16 MeV) electrons incident for distribution A, the fluence profiles shown in Figure 5-16a) were obtained. For distribution B (12 MeV and 16 MeV), these profiles are shown in Figure 5-16b), and for distribution C (14 MeV), Figure 5-16c).

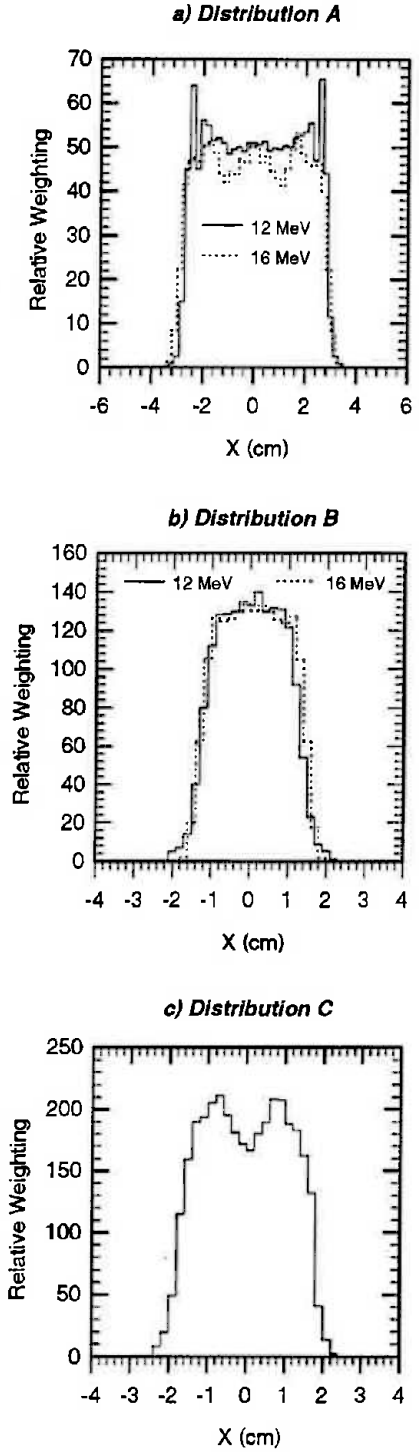

Figure 5-16: Weighting (fluence) profiles obtained when normally incident monoenergetic electrons are used to attempt to conform to a) desired distribution A (12 MeV and 16 MeV); b) desired distribution B (12 MeV and 16 MeV); and c) desired distribution C (14 MeV).

Figure 5-17 shows angular sinograms for the monoenergetic (12 MeV and 16 MeV) phase spaces for distribution A, with incidence angle sampled both linearly and by the cosine about normal incidence. With the difference in resolution between linearly and cosine-sampled angular sinograms, it is expected that slightly different optimal phase spaces will result. This is most obvious in comparison of the 12 MeV sinograms of Figure 5-17a) and Figure 5-17b). Differences in the appearance of these distributions also results from differences in y-axis pixel scaling between the two methods of angular sampling. For normally incident polyenergetic electrons, the phase space shown in the energy sinogram of Figure 5-18 was obtained. The energy sinograms obtained at positive angles of incidence with a fully modulated (angle and energy) incident electron phase space (utilising the symmetry of distribution A) are shown in Figure 5-19.

a) *12 MeV*

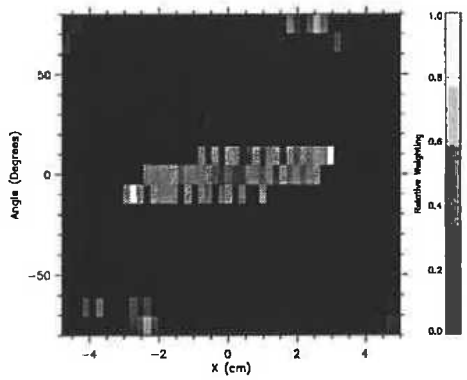

b) *16 MeV*

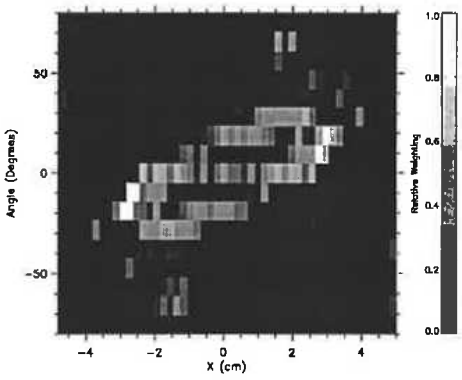

c) *12 MeV, Cosine Sampled*

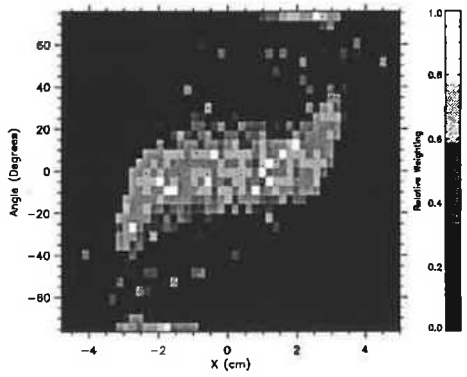

d) *16 MeV, Cosine Sampled*

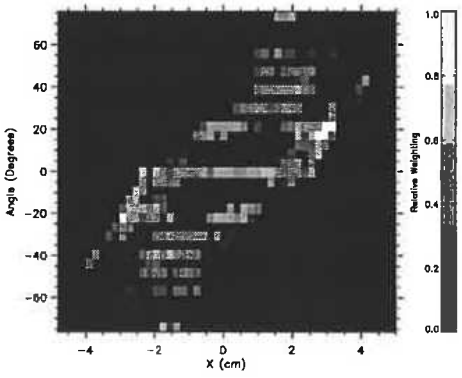

Figure 5-17: Angular sinograms for distribution A, for incident electron phase spaces a) 12 MeV, b) 16 MeV, c) 12 MeV with cosine angular sampling, d) 16 MeV with cosine angular sampling.

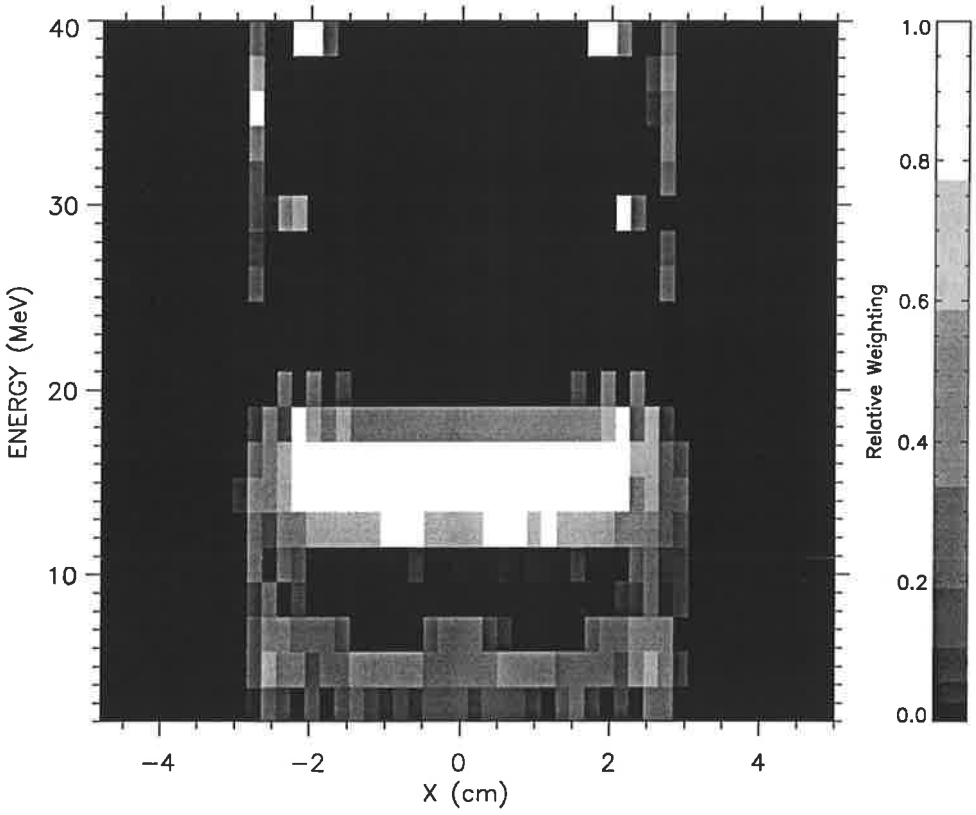

Figure 5-18: Energy sinogram for distribution A, with electrons restricted to normal incidence.

a) *Normal Incidence* b) *+10°* c) *+20°*

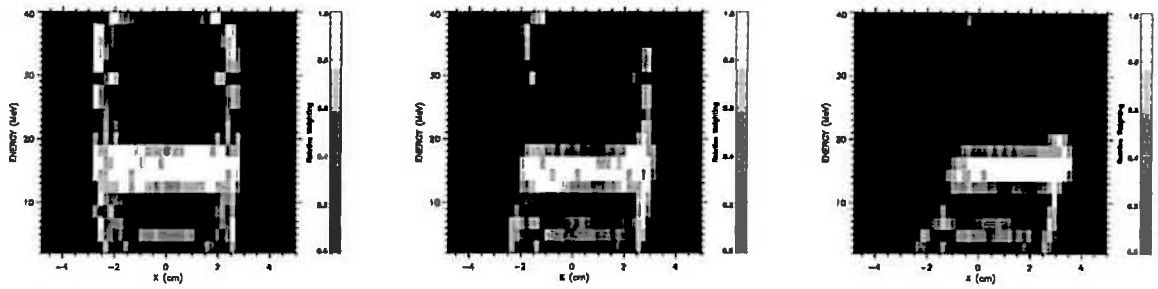

d) *+30°* e) *+40°* f) *+50°*

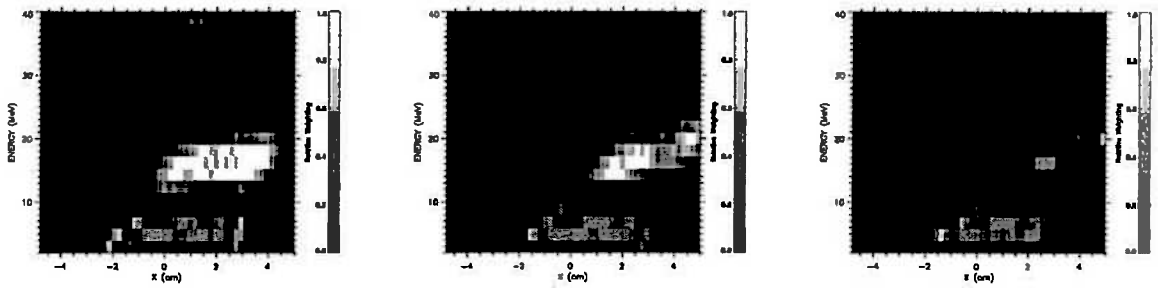

g) *+60°* h) *+70°* i) *+80°*

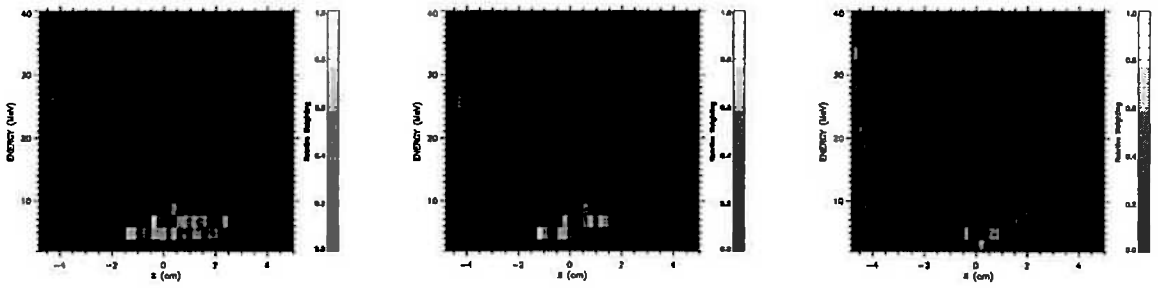

Figure 5-19: Energy sinograms for distribution A for a phase space with full energy and angle of incidence modulation, at discrete positive angles of incidence.

Figure 5-20 shows angular sinograms for the monoenergetic (12 MeV and 16 MeV) phase spaces for distribution B, with incidence angle sampled both linearly and by the cosine about normal incidence. For normally incident polyenergetic electrons, the phase spaces shown in the energy sinograms of Figure 5-21 were obtained. This sinogram has been shown with logarithmic as well as linear intensity scaling due to the lack of detail obtained in the logarithmic case. The energy sinograms obtained at positive angles of incidence with a fully modulated (angle and energy) incident electron phase space (utilising the symmetry of distribution B) are shown in Figure 5-22.

a) *12 MeV*

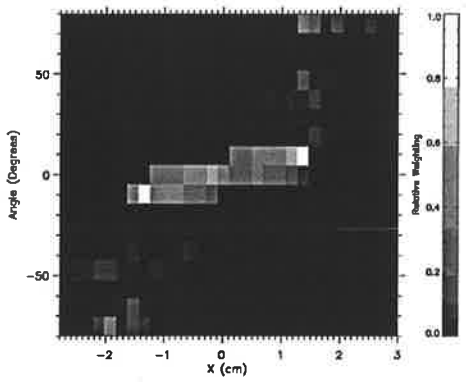

b) *16 MeV*

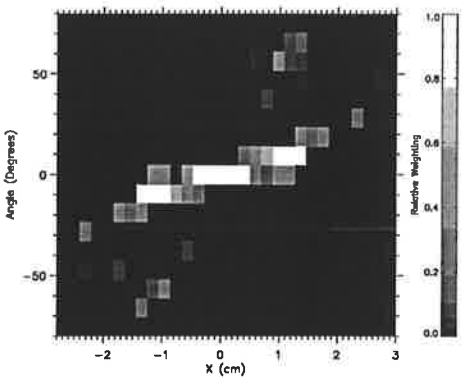

c) *12 MeV, Cosine Sampled*

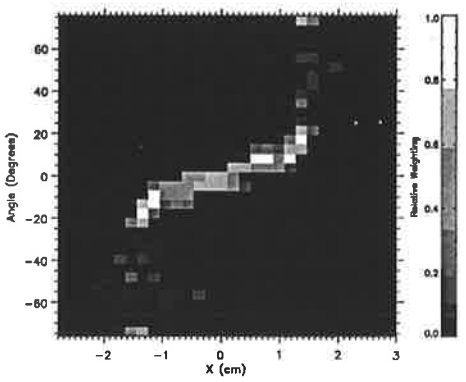

d) *16 MeV, Cosine Sampled*

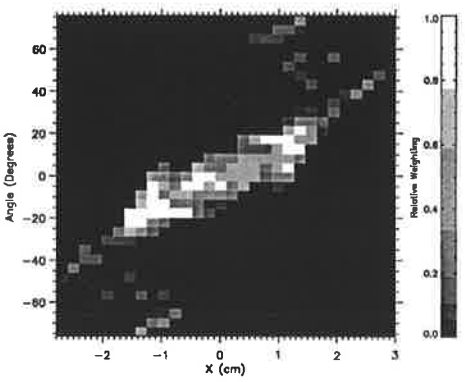

Figure 5-20: Angular sinograms for distribution B, for incident electron phase spaces a) 12 MeV, b) 16 MeV, c) 12 MeV with cosine angular sampling, d) 16 MeV with cosine angular sampling.

a) *Logarithmic Intensity Distribution*

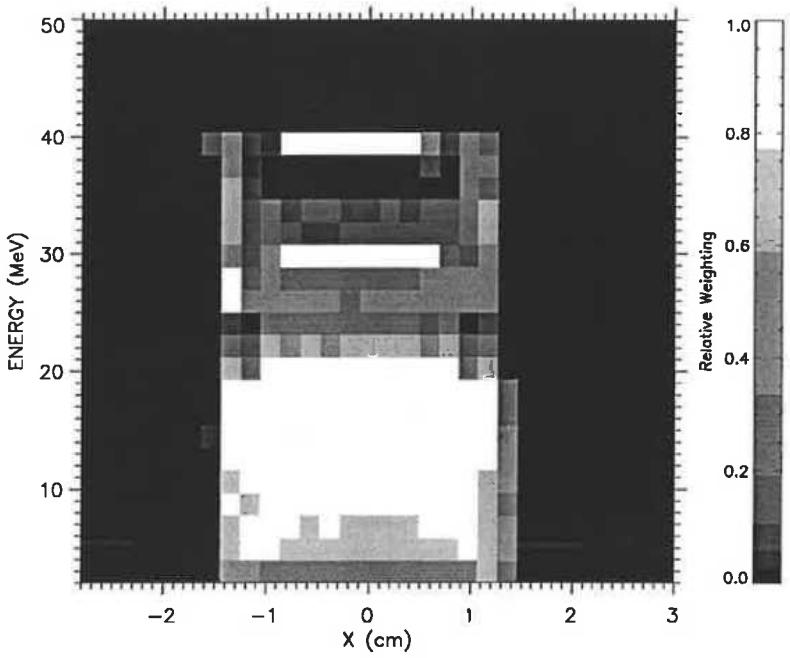

b) *Linear Intensity Distribution*

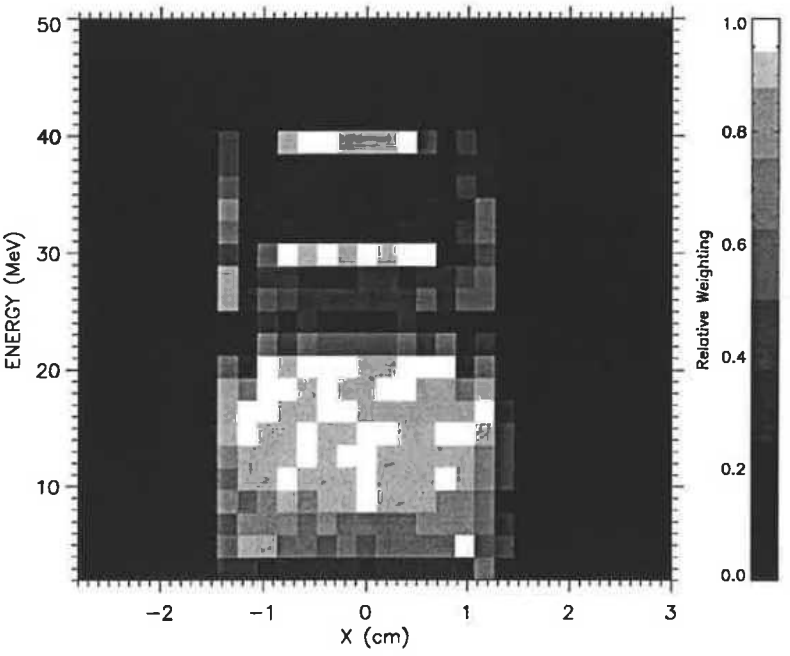

Figure 5-21: Energy sinogram for distribution B, with electrons restricted to normal incidence, and with relative intensity scaled a) logarithmically, and b) linearly.

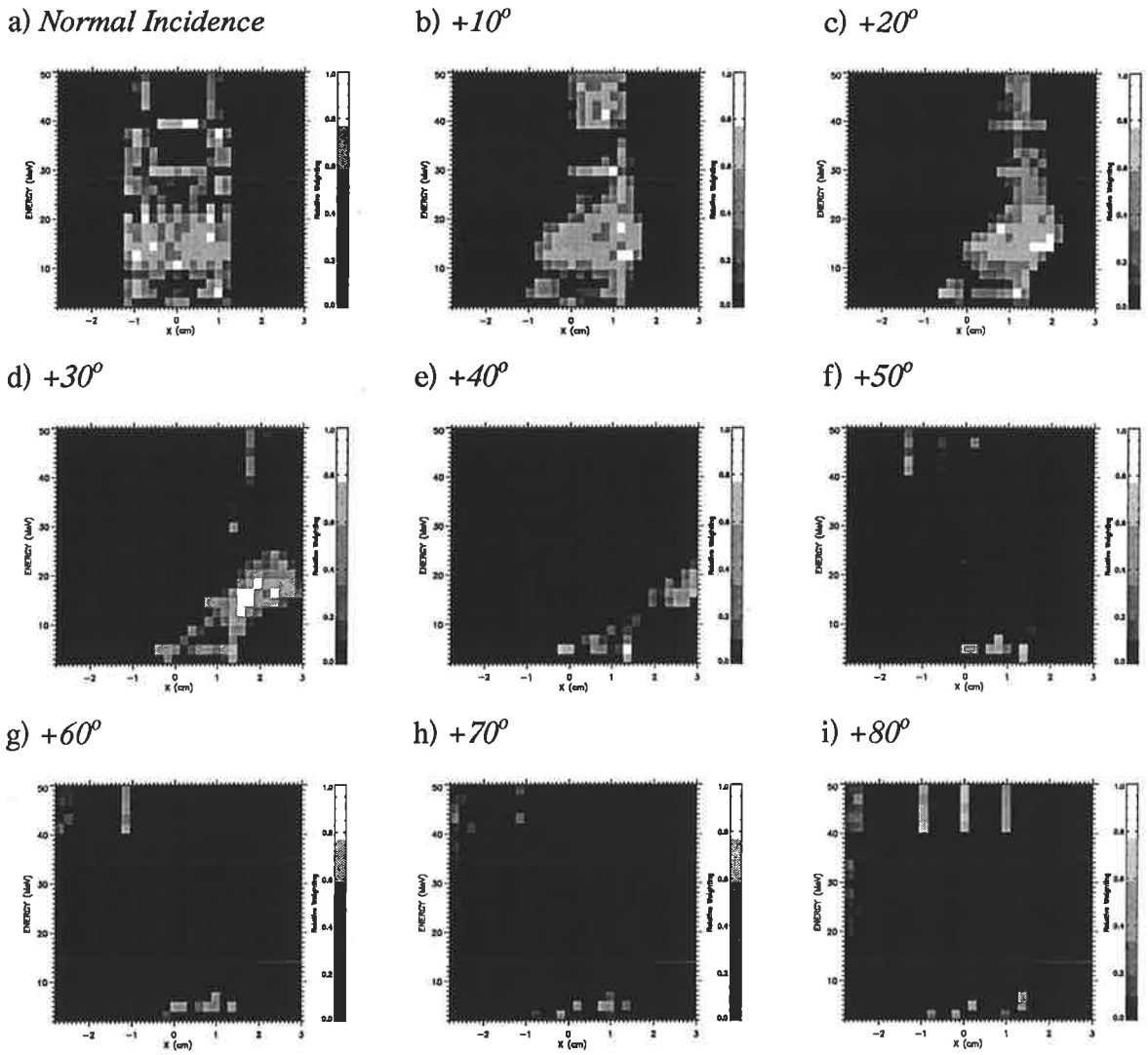

Figure 5-22: Energy sinograms for distribution B for a phase space with full energy and angle of incidence modulation, at discrete positive angles of incidence.

Figure 5-23 shows angular sinograms for the monoenergetic (14 MeV) phase spaces for distribution C, with incidence angle sampled both linearly and by the cosine about normal incidence. For normally incident polyenergetic electrons, the phase space shown in the energy sinogram of Figure 5-24 was obtained. The energy sinograms obtained at positive angles of incidence with a fully modulated (angle and energy) incident electron phase space (utilising the symmetry of distribution C) are shown in Figure 5-25.

a) *14 MeV*

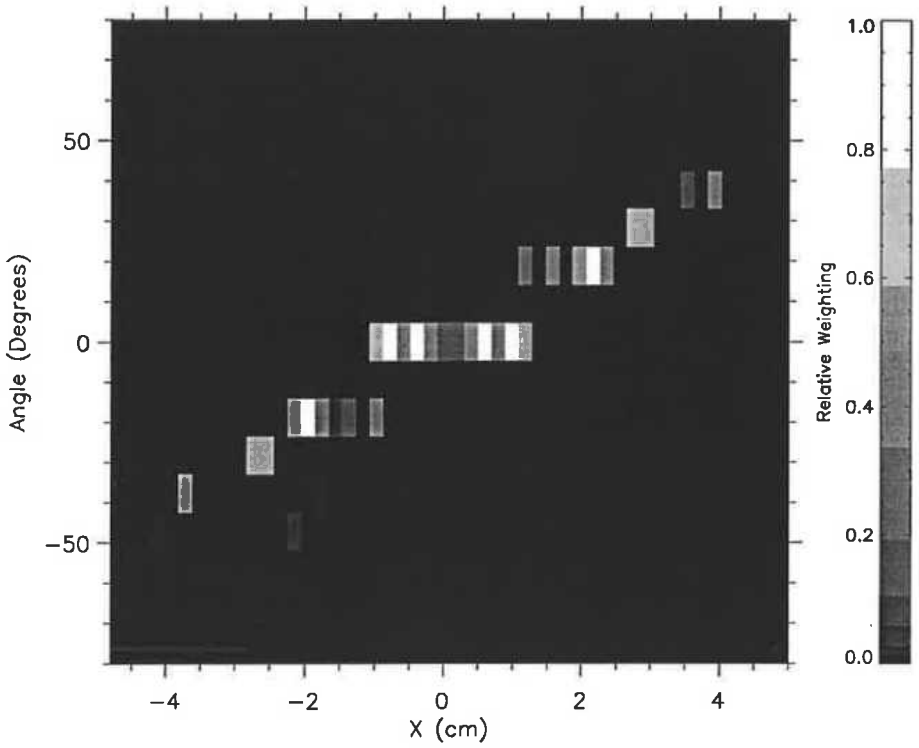

b) *14 MeV, Cosine Sampled*

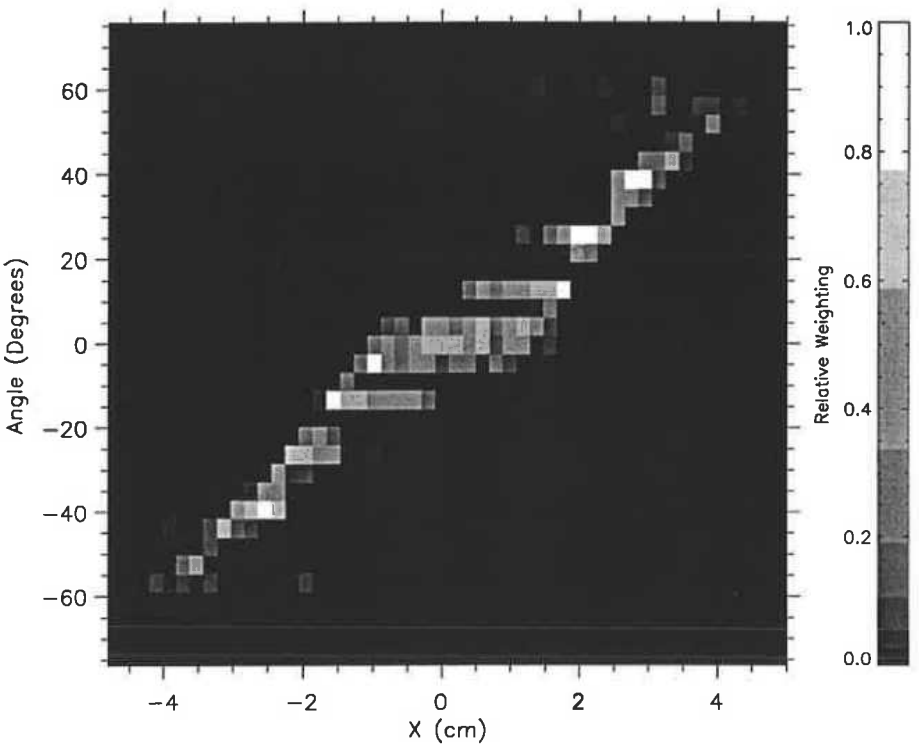

Figure 5-23: Angular sinograms for distribution C, for incident electron phase spaces a) 14 MeV, b) 14 MeV with cosine angular sampling.

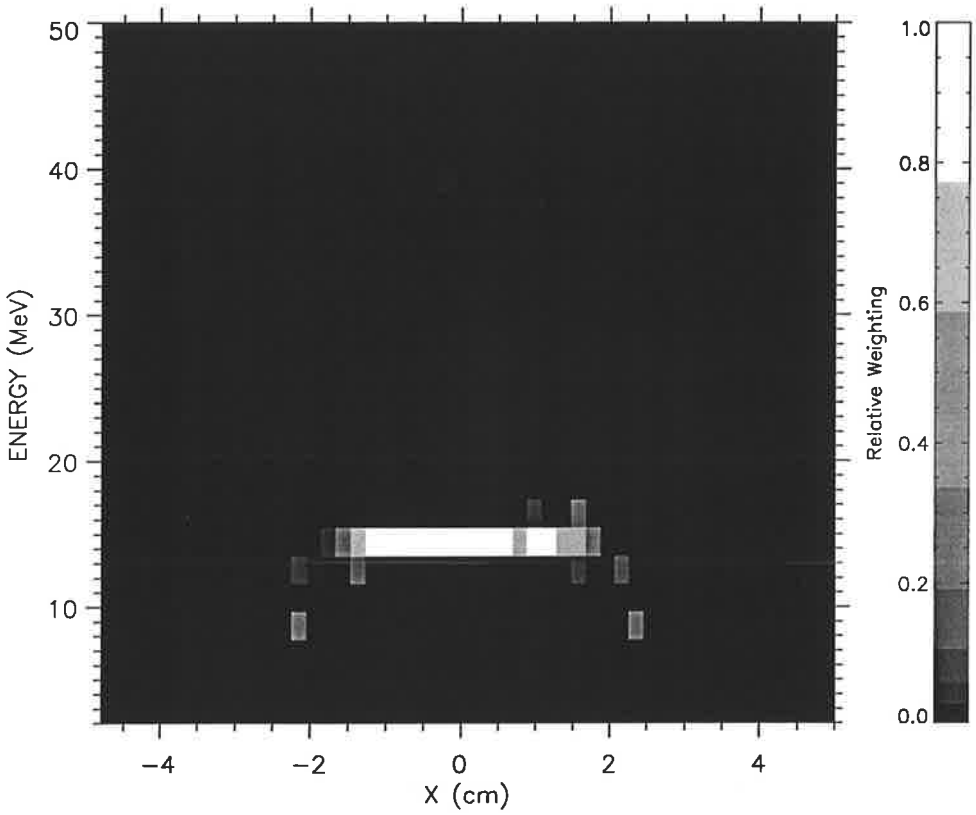

Figure 5-24: Energy sinogram for distribution C, with electrons restricted to normal incidence.

a) *Normal Incidence* b) *+10°* c) *+20°*

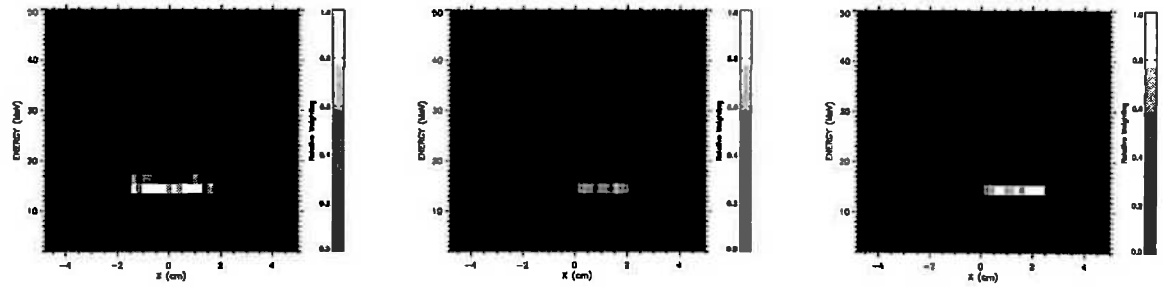

d) *+30°* e) *+40°* f) *+50°*

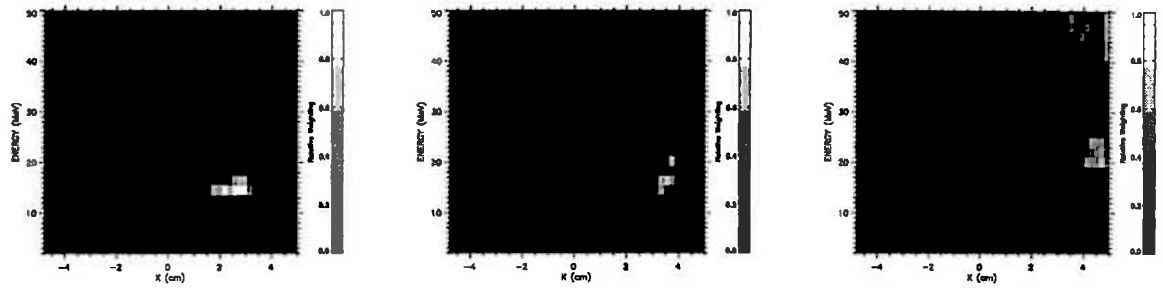

g) *+60°* h) *+70°* i) *+80°*

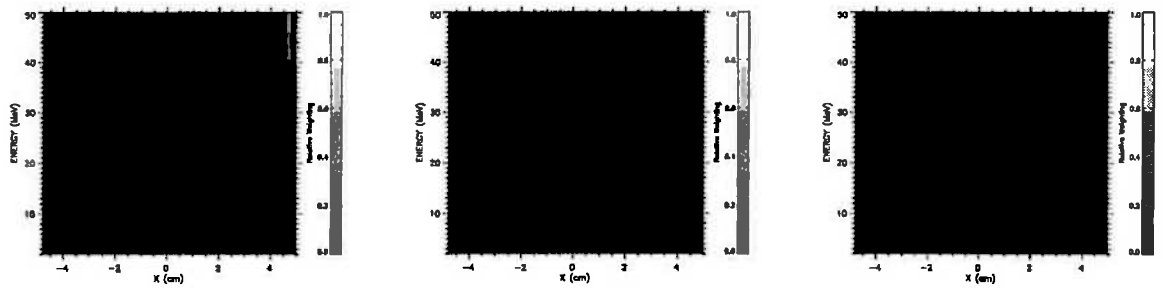

Figure 5-25: Energy sinograms for distribution C for a phase space with full energy and angle of incidence modulation, at discrete positive angles of incidence.

5.2.3.2. Complex Distribution (Distribution D)

Table 5-IV shows the resulting dose results for Distribution D (see Figure 5-10) for each specific dose region, and for each phase space restriction.

Table 5-IV: Collated results for dose distribution D. Region 1 - 100% dose, weighting 1; Region 2, 0% dose, weighting 9; Region 3, 0% dose, weighting 6.25.

	P_{final}/P_o †	D_{max} Region 1 (D_{min} Region 1) *D_{mean} Region 1* *(D_σ Region 1)*	D_{max} Region 2 (D_{min} Region 2) *D_{mean} Region 2* *(D_σ Region 2)*	D_{max} Region 3 (D_{min} Region 3) *D_{mean} Region 3* *(D_σ Region 3)*	D_{max} Phantom‡	D_{tot} Phantom‡
Normal incidence, mono-energetic.	0.729	**77.9** **(3.3)** *26.8* *(2.4)*	**23.2** **(4.4)** *8.2* *(1.4)*	**12.9** **(0.0)** *2.2* *(0.3)*	66.5	2510.7
Variable angle, mono-energetic	0.645	**84.2** **(3.3)** *34.6* *(3.0)*	**21.8** **(3.8)** *8.8* *(1.5)*	**17.1** **(0.0)** *2.1* *(0.3)*	43.4	3335.7
Normal incidence, poly-energetic	0.592	**110.4** **(6.5)** *39.2* *(3.4)*	**40.8** **(3.1)** *11.2* *(2.1)*	**15.8** **(0.0)** *3.0* *(0.4)*	47.2	3102.2
Variable angle, poly-energetic	0.522	**116.4** **(7.5)** *44.3* *(3.8)*	**32.0** **(3.2)** *10.9* *(2.0)*	**15.7** **(0.1)** *3.5* *(0.4)*	32.9	3623.9

† Initial potentials calculated with all beam element weights zero, ie., Equation 1 with all $d_{i,k}^{j}$ zero. Annealing runs finished when potential consistent in two iterations to three significant figures.

‡ The 0 % region surrounding the principal structures.

Dose-area histograms for the three principle dose-restricted regions of distribution D (see Figure 5-10) are shown in Figure 5-26.

Figure 5-27 shows (as contour plots) the final dose distributions obtained for distribution D for the four incident electron phase spaces, with different dose regions shown shaded. Figure 5-28 shows the resulting optimal profile for this distribution for a monoenergetic (24 MeV) normally incident electron phase space.

Figure 5-29 shows, for incident electrons of energy 24 MeV, angular sinograms (including cosine angular sampled) for distribution D. For normally incident polyenergetic electrons for distribution D, Figure 5-30 displays the resulting energy sinogram of the resulting optimal phase space. Energy spectra at all incidence angles for the optimal polyenergetic - variable incidence angle phase space for dose distribution D have been reserved for Appendix G.

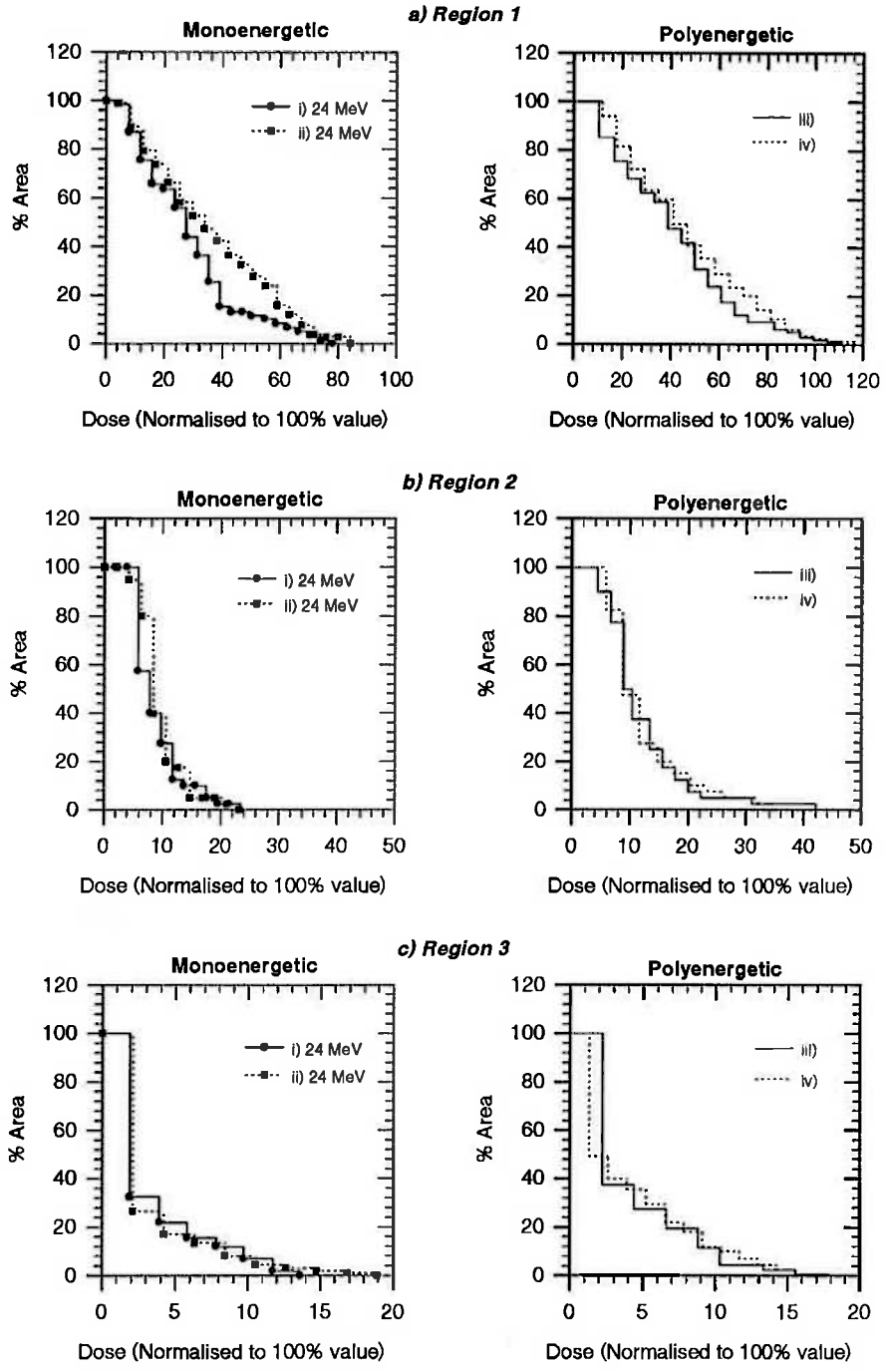

Figure 5-26: Dose-area histograms for resulting closest-approach dose distributions from the annealing procedure for the three dose regions of desired distribution D (Compare Figure 5-10); a) region 1, b) region 2, c) region 3. The phase space restrictions are, for each histogram, incident electrons which are i) monoenergetic (24 MeV) and normally incident, ii) monoenergetic and having variable incidence angle, iii) polyenergetic and normally incident, iv) polyenergetic and having variable incidence angle.

a) *24 MeV, normally incident*

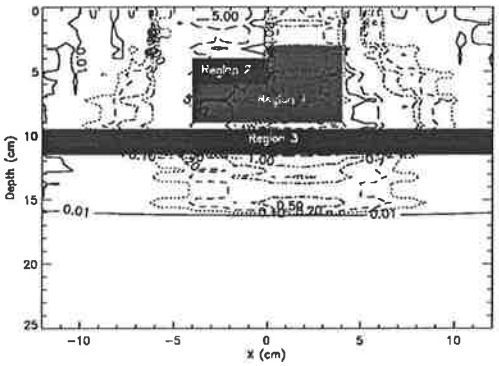

b) *24 MeV, variable incidence angle*

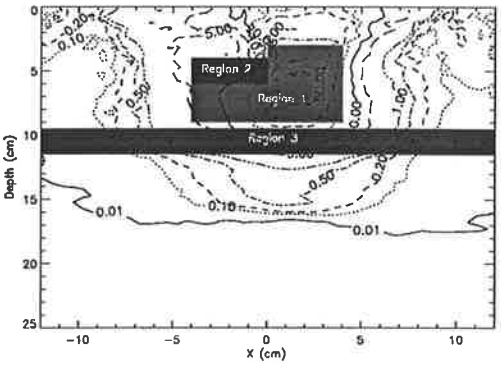

c) *Polyenergetic, normally incident*

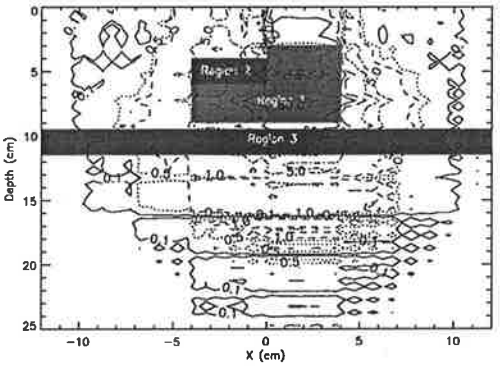

d) *Polyenergetic, variable incidence angle*

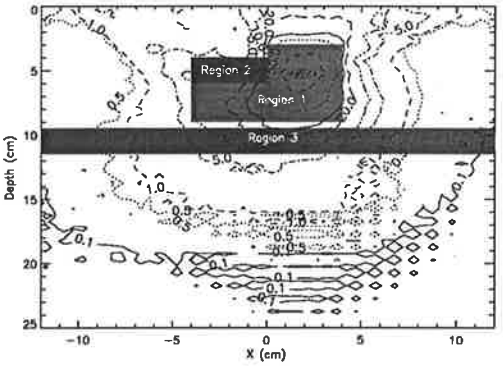

Figure 5-27: Final dose distributions for distribution D for incident electron phase spaces a) 24 MeV monoenergetic normally incident, b) 24 MeV monoenergetic with variable incidence angle c) polyenergetic, normally incident, and d) polyenergetic, variable incidence angle.

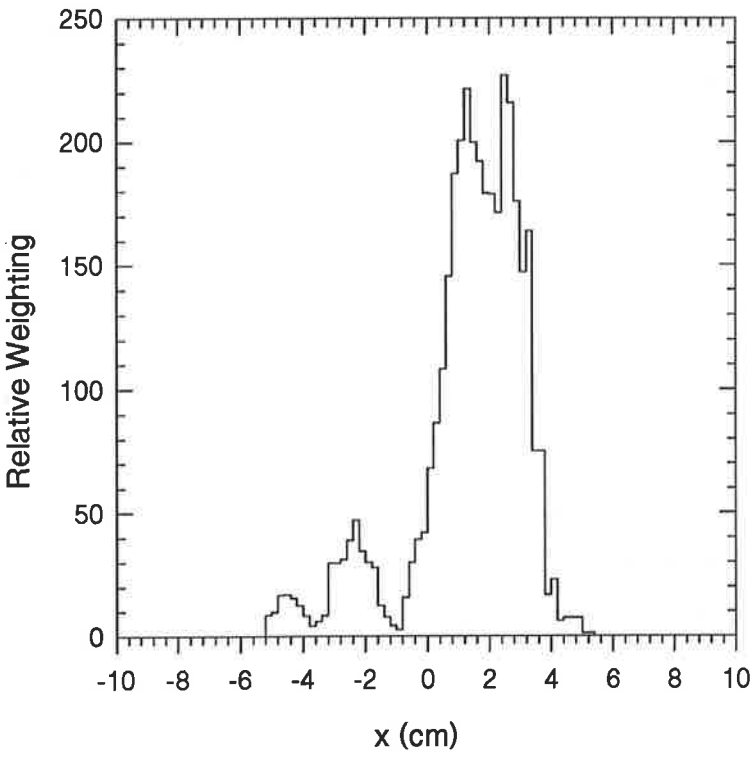

Figure 5-28: Weighting (fluence) profiles obtained when normally incident monoenergetic (24 MeV) electrons were used to attempt to conform to desired distribution D.

a) *24 MeV*

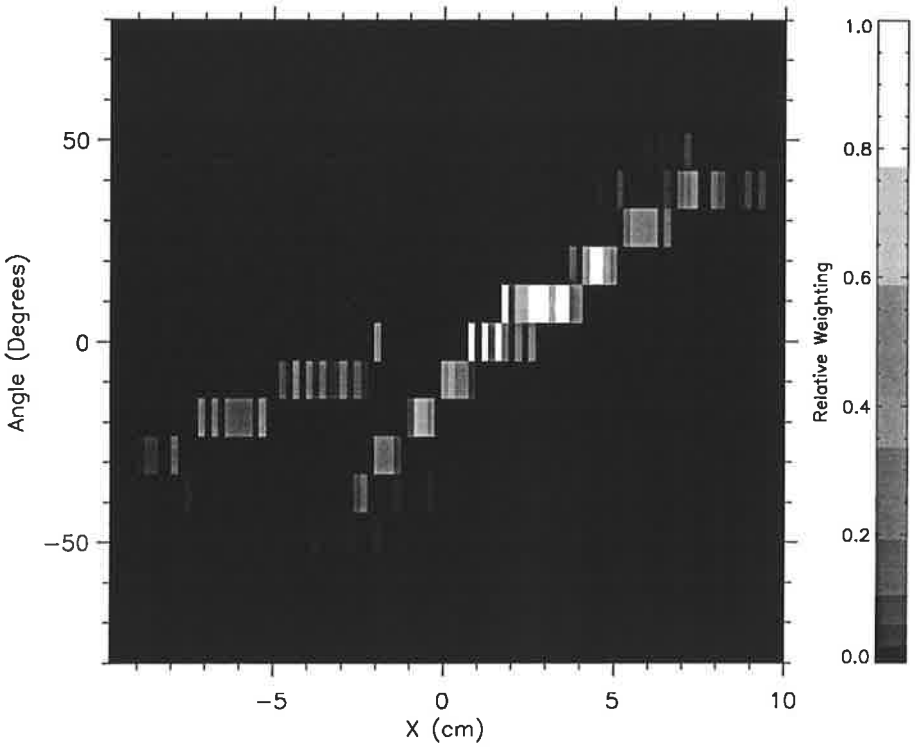

b) *24 MeV, Cosine Sampled*

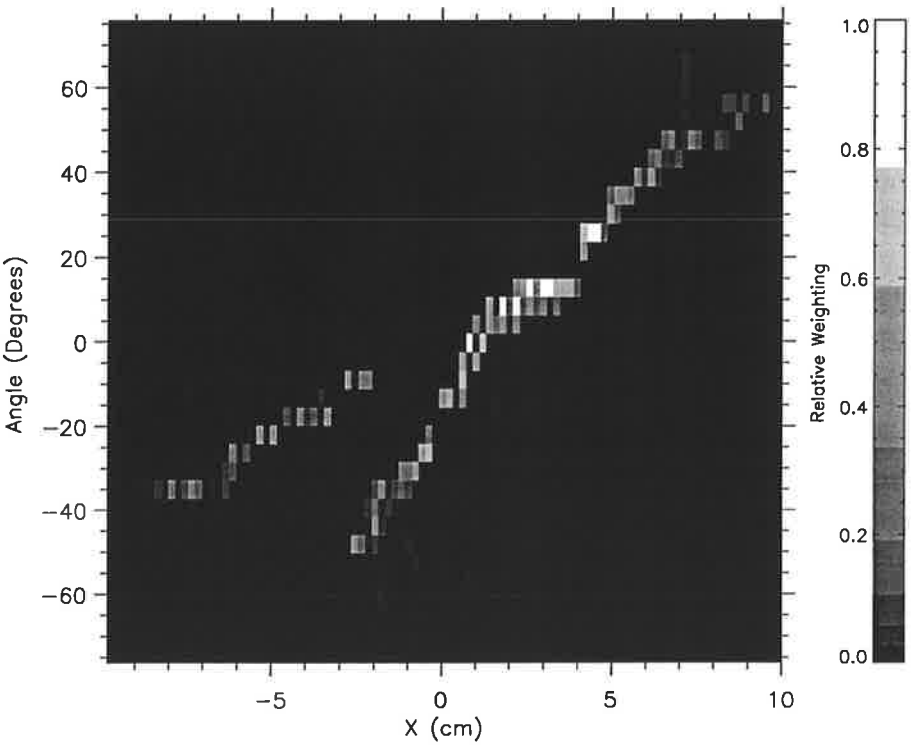

Figure 5-29: Angular sinograms for distribution D, for incident electron phase spaces a) 24 MeV, b) 24 MeV with cosine angular sampling.

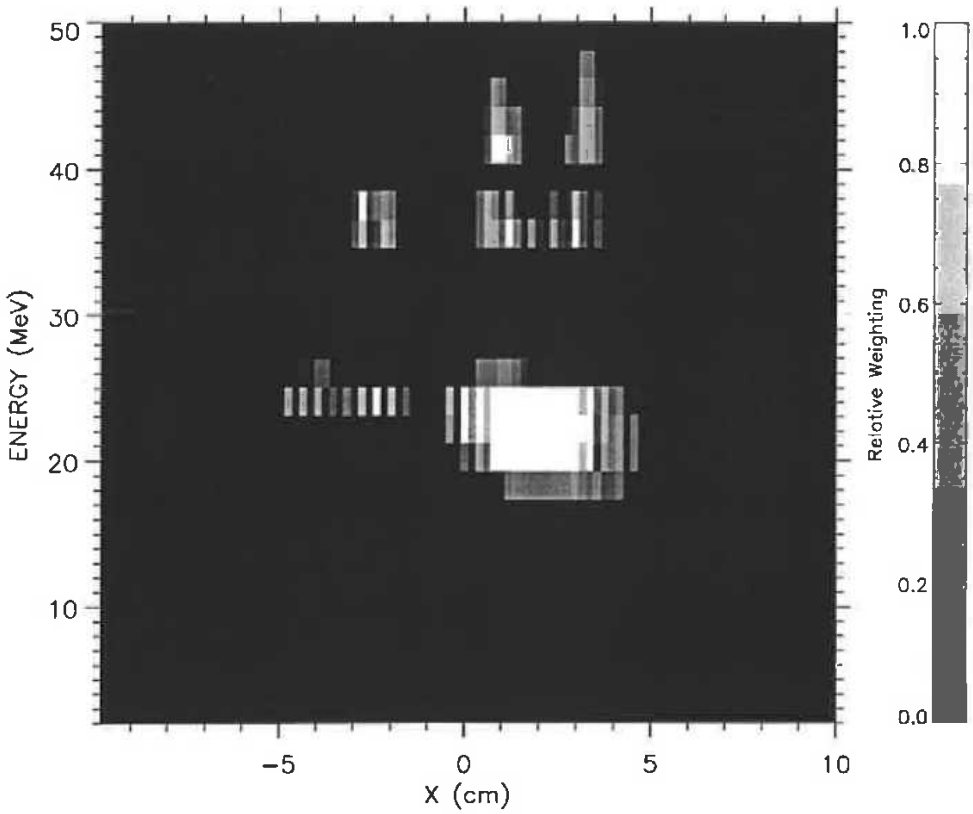

Figure 5-30: Energy sinogram for distribution D, with electrons restricted to normal incidence.

5.2.3.3. Wedge-shaped Distribution

Table 5-V lists the appropriate dose results for the wedge-shaped distribution considered (see Figure 5-11a).

Table 5-V: Summary of final dose results for the wedge-shaped distribution (see Figure 5-11a).

	P_{final}/P_o †	D_{max} 100% (D_{min} 100%) *D_{mean} 100%* *(D_σ 100%)*	D_{max} 0%‡	D_{tot} 0%‡
Normal incidence, mono-energetic (14 MeV)	0.126	**128.9** **(45.3)** *87.4* *(1.8)*	138.5	24894.4
Variable angle, mono-energetic (14 MeV)	0.014	**108.6** **(63.7)** *98.5* *(0.4)*	86.6	12634.2
Normal incidence, poly-energetic	0.029	**113.7** **(72.1)** *97.7* *(0.6)*	90.0	21009.6
Variable angle, poly-energetic	0.009	**104.4** **(87.0)** *99.0* *(0.2)*	72.3	13851.0

† Initial potentials calculated with all beam element weights zero, ie., Equation 5.24 with all $d_{i,k}^{j}$ zero. Annealing runs finished when potential consistent in two iterations to three significant figures.

‡ 0% dose region.

Dose-area histogram results for this distribution, and for the various phase space restrictions, are displayed in Figure 5-31.

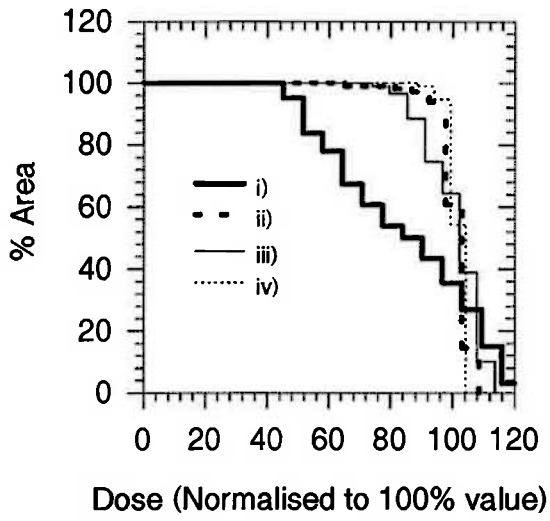

Figure 5-31: Dose-area histograms for resulting closest-approach dose distributions from the annealing procedure for the 100% dose region of the wedge-shaped distribution (see Figure 5-11a). The phase space restrictions are incident electrons which are i) monoenergetic (14 MeV) and normally incident, ii) monoenergetic and having variable incidence angle, iii) polyenergetic and normally incident, and iv) polyenergetic and having variable incidence angle.

The dose distributions obtained at the completion of the optimisations with the four phase space restrictions for the wedge-shaped distribution are shown in Figure 5-32 as dose distribution contour plots. With the weightings (values of α) chosen, the optimisation routine led to an encompassing of the desired 100% region by approximately the 80% isodose line.

a) *14 MeV, normally incident*

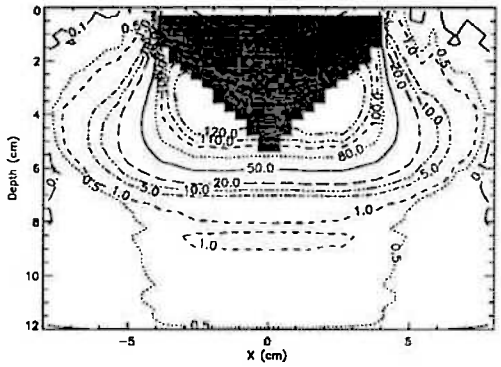

b) *14 MeV, variable incidence angle*

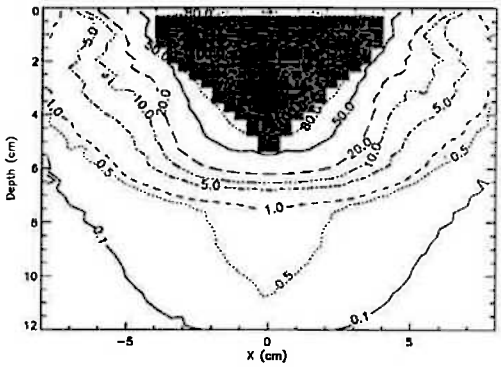

c) *Polyenergetic, normally incident*

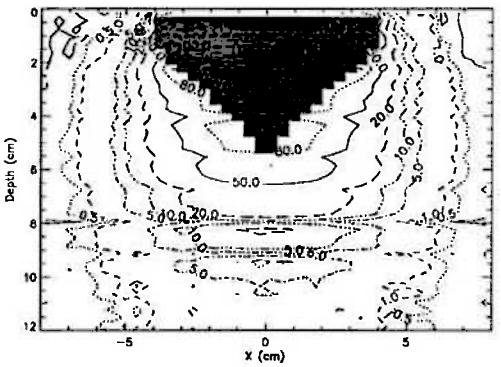

d) *Polyenergetic, variable incidence angle*

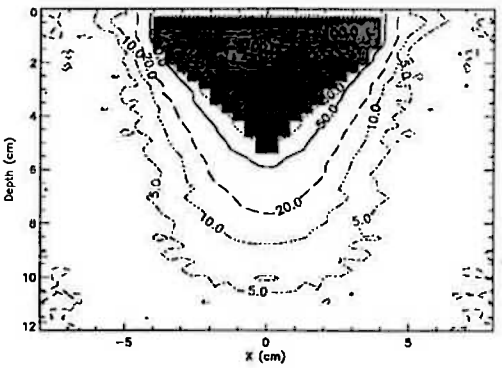

Figure 5-32: Final dose distributions for the wedge-shaped desired distribution. Incident electron phase spaces are a) monoenergetic (14 MeV), normally incident, b) monoenergetic (14 MeV), variable incidence angle, c) polyenergetic, normally incident, and d) polyenergetic, variable incidence angle.

The optimal profile for 14 MeV electrons incident normally on the wedge-shaped distribution is shown in Figure 5-33.

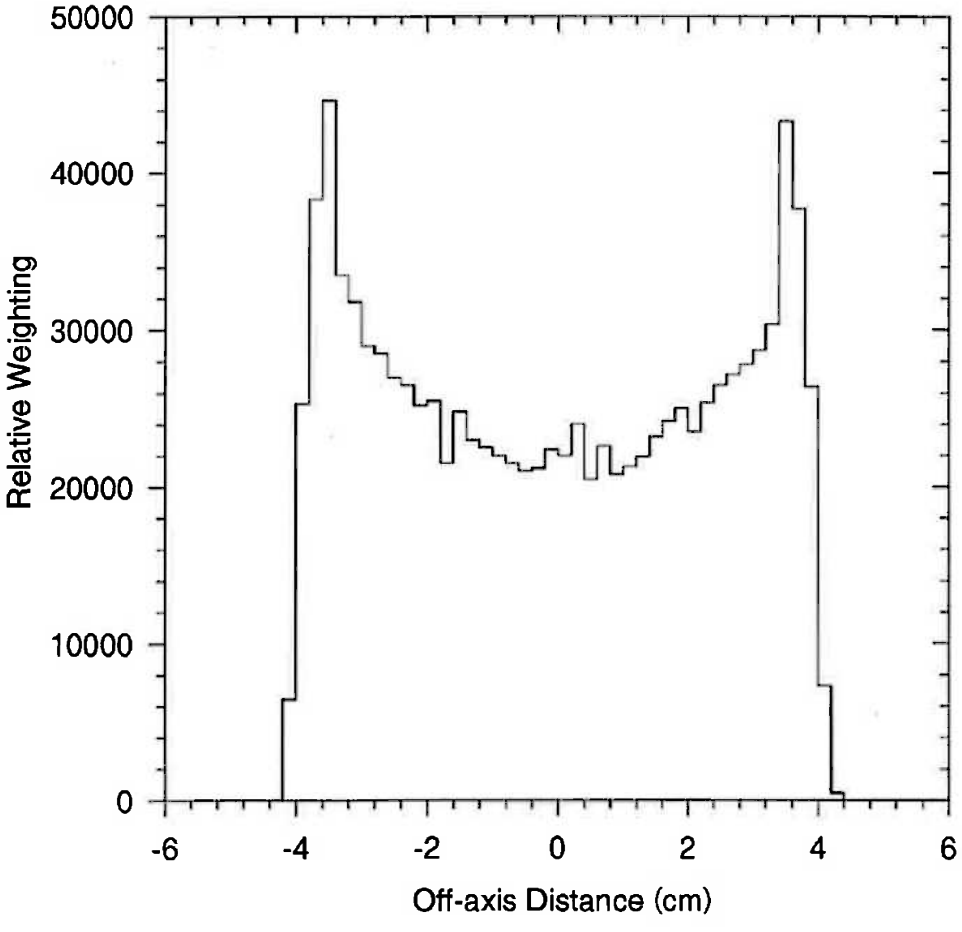

Figure 5-33: Weighting (fluence) profiles obtained when normally incident monoenergetic (14 MeV) electrons are used to attempt to conform dose to the wedge-shaped distribution (Figure 5-11a).

Figure 5-34 shows an angular sinogram for the monoenergetic (14 MeV) phase space for the wedge-shaped distribution. Incidence angle has been sampled linearly about normal incidence. For normally incident, polyenergetic electrons, the phase space of Figure 5-35 was obtained. The energy sinograms obtained at positive angles of incidence (utilising the symmetry of the wedge-shaped distribution) are shown in Figure 5-36.

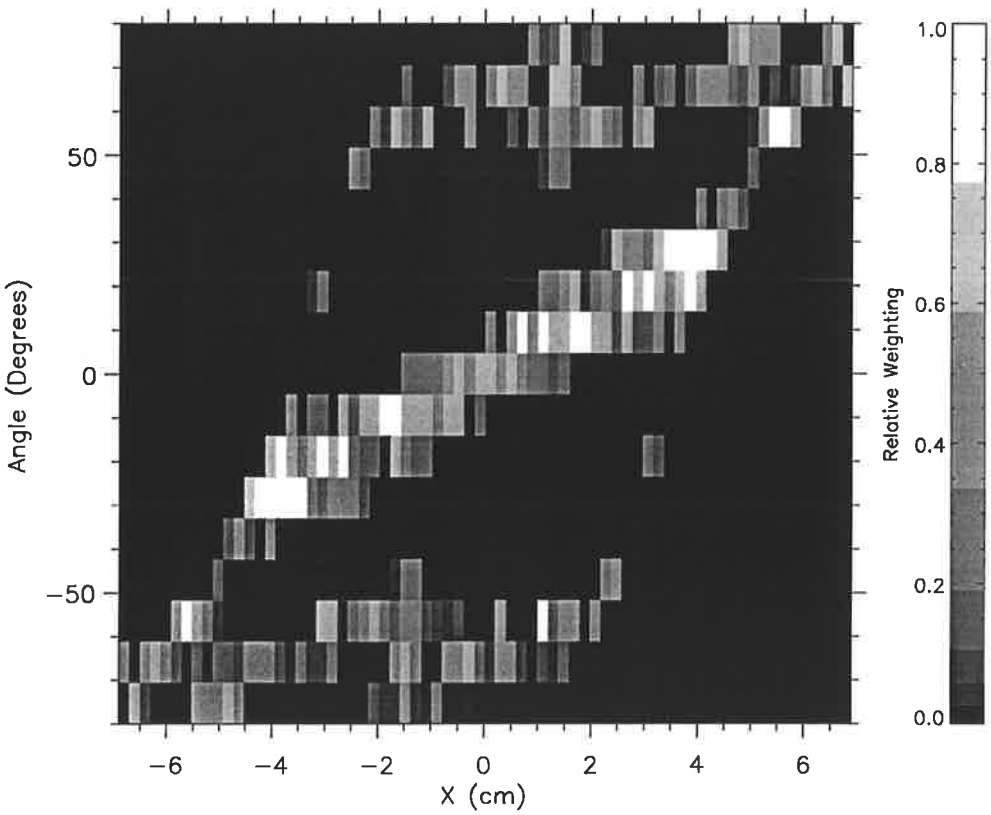

Figure 5-34: Angular sinogram for the wedge-shaped distribution, for monoenergetic (14 MeV) incident electrons.

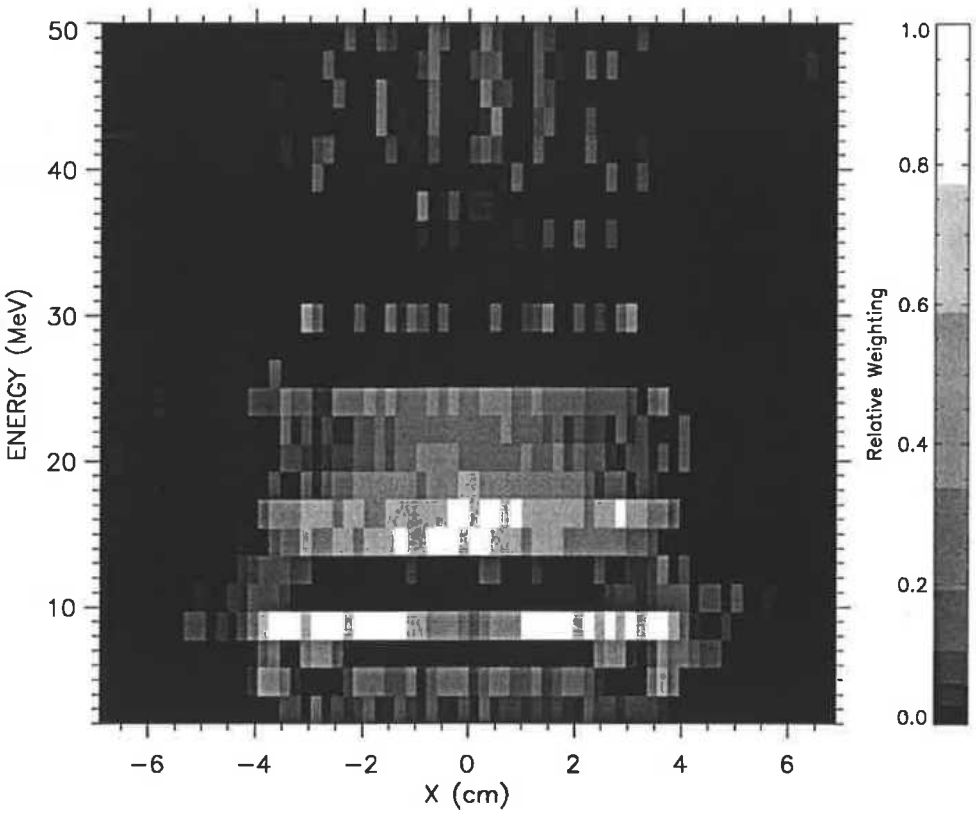

Figure 5-35: Energy sinogram for the wedge-shaped distribution, with electrons restricted to normal incidence.

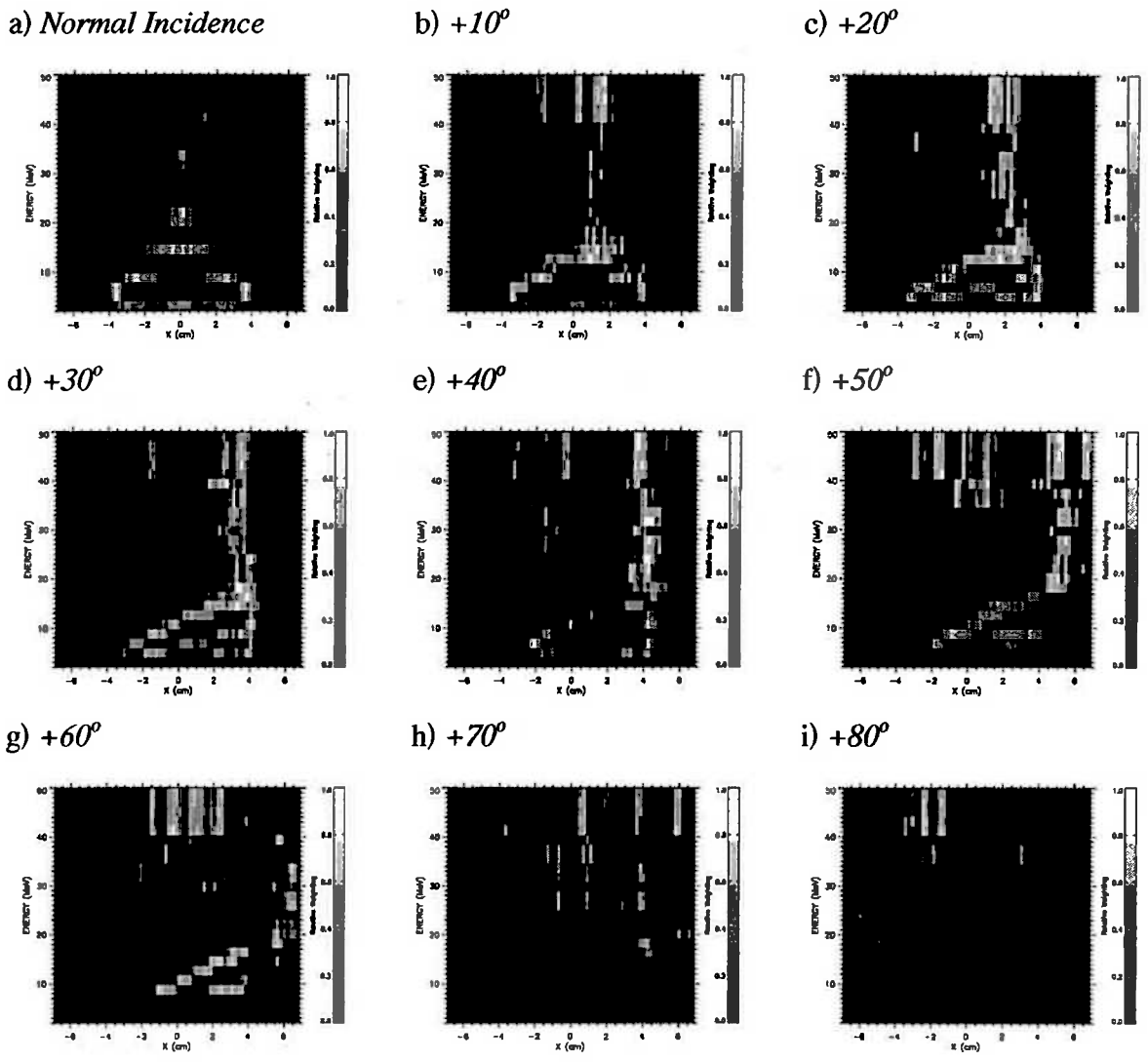

Figure 5-36: Energy sinograms for the wedge-shaped distribution for a phase space with full energy and angle of incidence modulation, at discrete positive angles of incidence.

5.2.3.4. Paraspinal Muscle Irradiation

Table 5-VI lists the appropriate dose results for the paraspinal muscle irradiation (with spinal chord; Figure 5-11b).

Table 5-VI: Summary of final dose results for the paraspinal muscle irradiation (Figure 5-11b).

	P_{final}/P_o†	**D_{max} 100%** **(D_{min} 100%)** *D_{mean} 100%* *(D_σ 100%)*	**D_{max} Chord** **(D_{min} Chord)** *D_{mean} Chord* *(D_σ Chord)*	D_{max} 0%‡	D_{tot} 0%‡
Normal incidence, mono-energetic (16 MeV)	0.041	**100.4** **(84.0)** *95.9* *(0.16)*	**92.0** **(89.8)** *90.9* *(0.22)*	100.0	41603.9
Variable angle, mono-energetic (16 MeV)	0.014	**107.4** **(84.5)** *98.5* *(0.22*	**30.0** **(21.3)** *26.9* *(1.03)*	106.7	22696.0
Normal incidence, poly-energetic	0.023	**112.7** **(67.4)** *97.6* *(0.4)*	**39.7** **(27.4)** *32.4* *(1.3)*	92.7	28381.4
Variable angle, poly-energetic	0.012	**104.7** **(83.9)** *98.8* *(0.2)*	**24.2** **(16.2)** *18.5* *(0.9)*	83.8	26780.8

† Initial potentials calculated with all beam element weights zero, ie., Equation 5.24 with all $d_{i,k}^{j}$ zero. Annealing runs finished when potential consistent in two iterations to three significant figures.

‡ 0%, weighting 9 dose region.

Dose-area histogram results for this distribution, and for the various phase space restrictions, are displayed in Figure 5-37. The dose distributions obtained at the completion of the optimisations with the four phase space restrictions for the paraspinal muscle irradiation are shown in Figure 5-38.

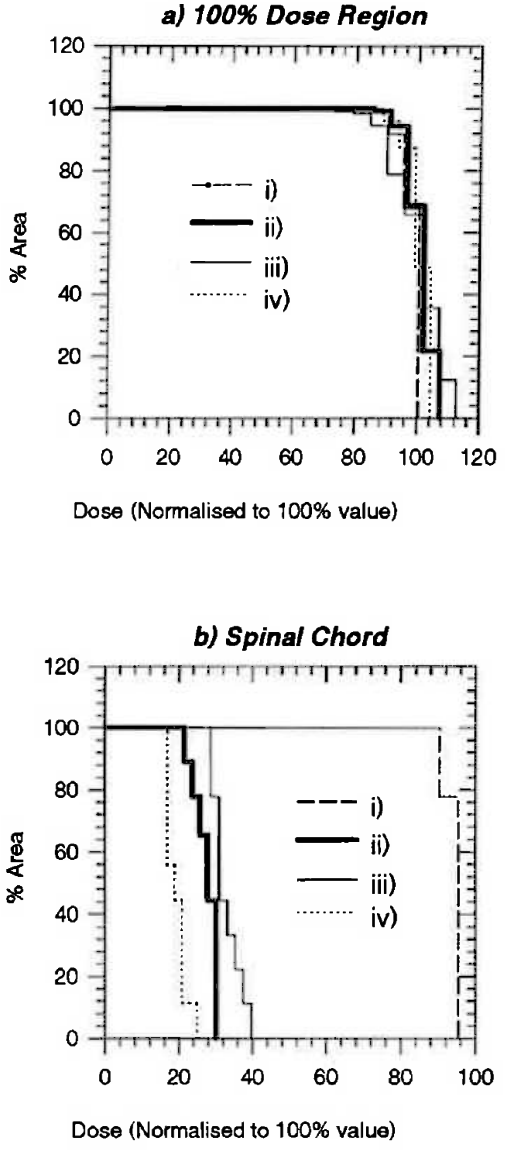

Figure 5-37: Dose-area histograms for resulting closest-approach dose distributions from the annealing procedure for a) the 100% dose region, and b) the spinal chord region of the paraspinal muscle irradiation (Figure 5-11b). The phase space restrictions are, for each histogram, electrons which are i) monoenergetic (16 MeV), normally incident, ii) monoenergetic (16 MeV), having variable incidence angle, iii) polyenergetic, normally incident, and iv) polyenergetic, with variable incidence angle.

a) *16 MeV, normally incident*

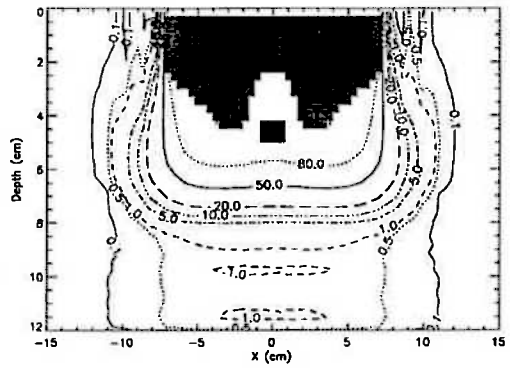

b) *16 MeV, variable incidence angle*

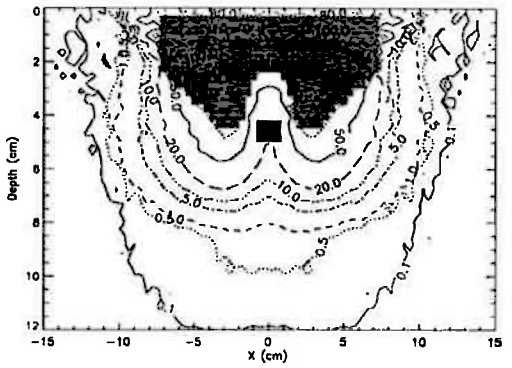

c) *Polyenergetic, normally incident*

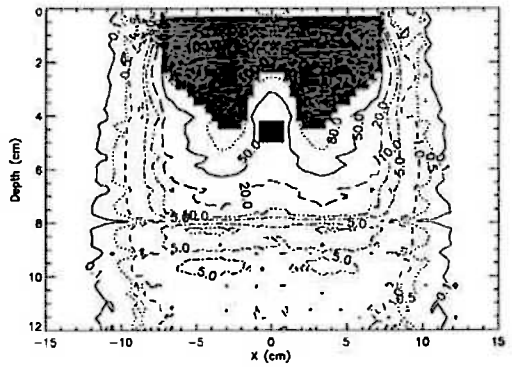

d) *Polyenergetic, variable incidence angle*

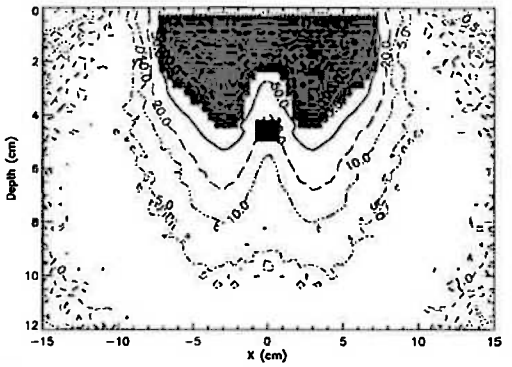

Figure 5-38: Final dose distributions for the paraspinal muscle irradiation. Incident electron phase spaces are a) monoenergetic (16 MeV), normally incident, b) monoenergetic (16 MeV), with variable incidence angle, c) polyenergetic, normally incident, and d) polyenergetic with variable incidence angle.

The optimal profile for 16 MeV electrons incident normally on the paraspinal muscle distribution is shown in Figure 5-39.

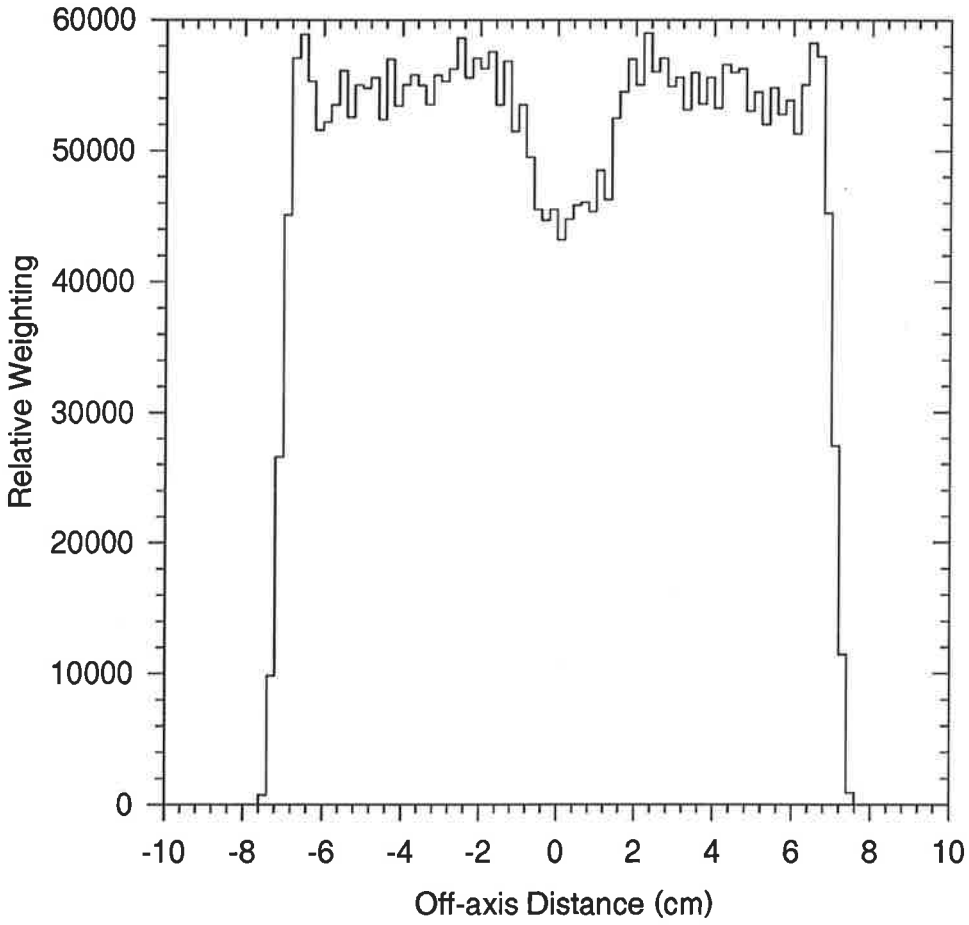

Figure 5-39: Weighting (fluence) profile obtained when normally incident monoenergetic (16 MeV) electrons were used to attempt to conform to the distribution for the paraspinal muscle irradiation.

Figure 5-40 shows, for incident electrons of energy 16 MeV, an angular sinogram for the paraspinal muscle irradiation. For normally incident polyenergetic electrons, Figure 5-41 displays the resulting energy sinogram of the resulting optimal phase space. For a full (energy, angle and intensity-modulated) phase space incident on this distribution, the energy sinograms at discrete positive angles of incidence (utilising the symmetry of this distribution) are shown in Figure 5-42.

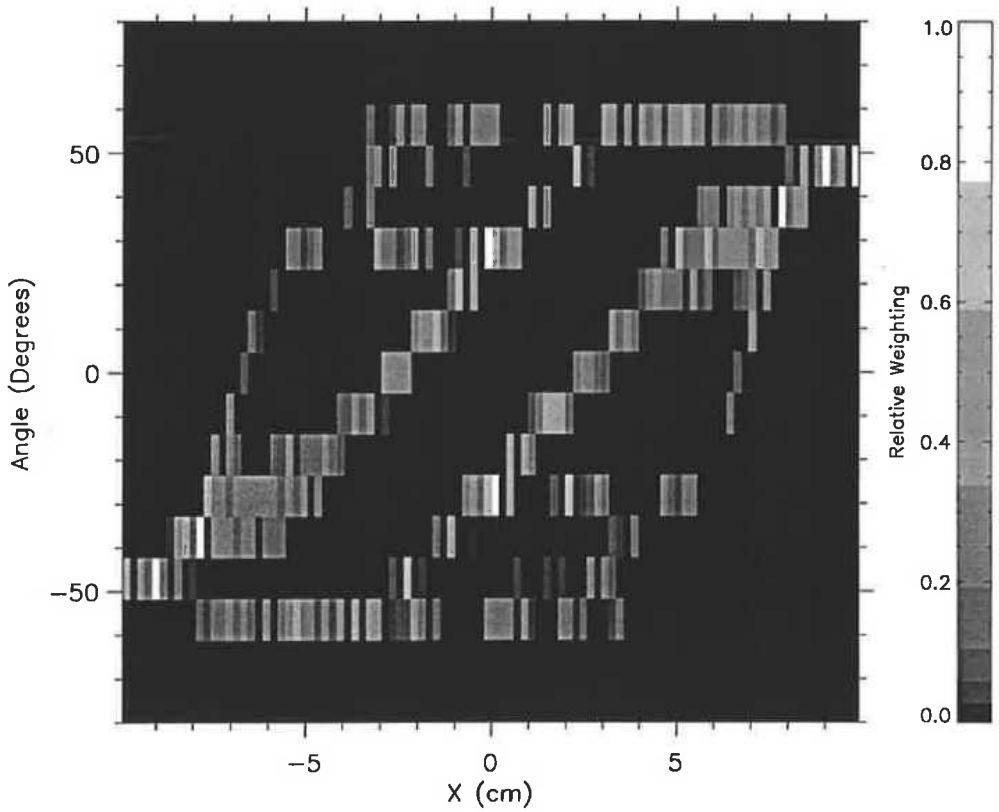

Figure 5-40: Angular sinogram for paraspinal muscle irradiation, for monoenergetic (16 MeV) electrons. Incidence angle sampled linearly about normal incidence.

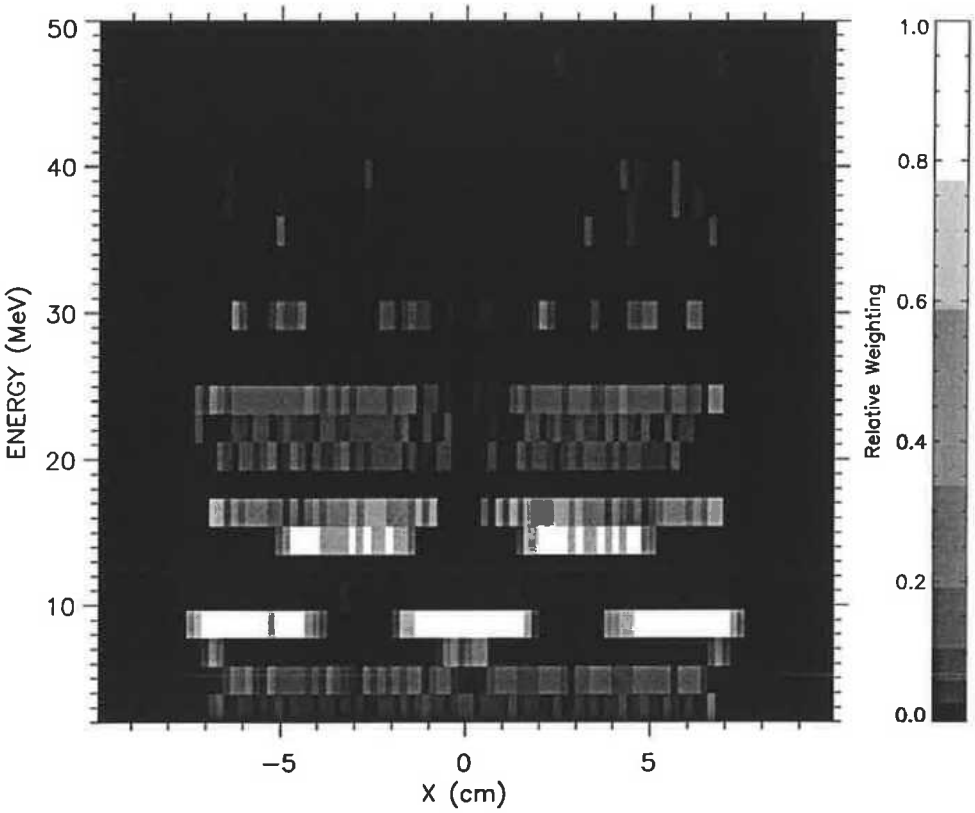

Figure 5-41: Energy sinogram for the paraspinal muscle distribution, with electrons restricted to normal incidence.

a) *Normal Incidence* b) *+10°* c) *+20°*

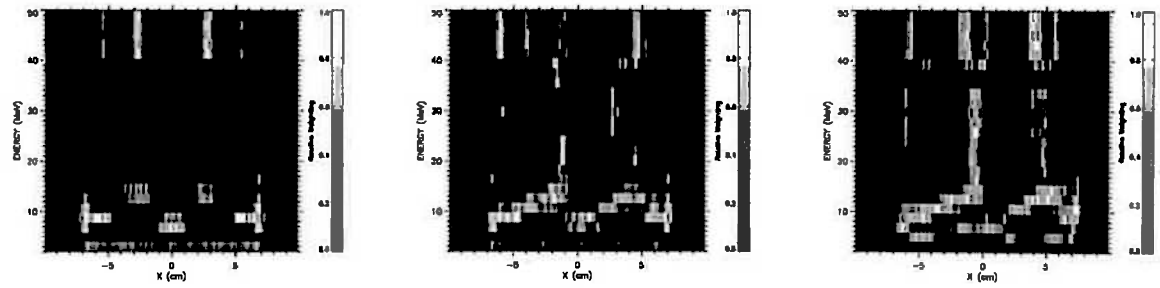

d) *+30°* e) *+40°* f) *+50°*

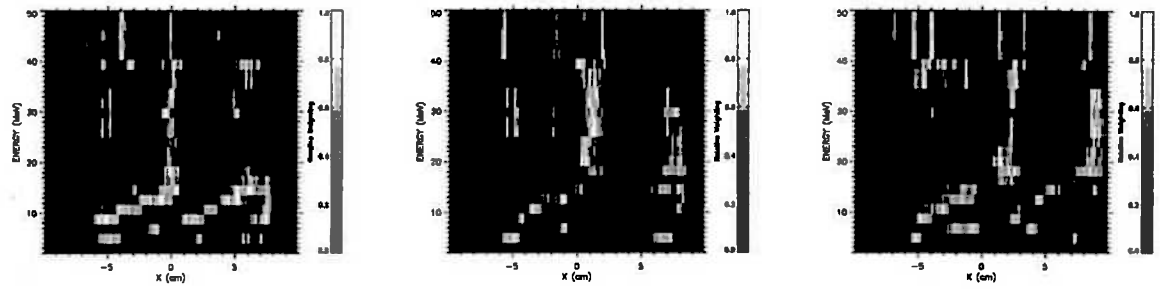

g) *+60°* h) *+70°* i) *+80°*

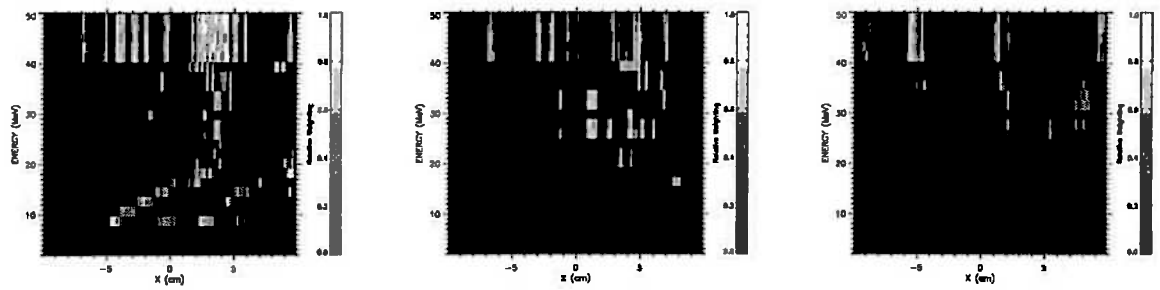

Figure 5-42: Energy sinograms for the paraspinal muscle distribution for a phase space with full energy and angle of incidence modulation, at discrete positive angles of incidence.

5.2.4. Discussion

The results obtained above indicate how manipulation of the characteristics of the treatment beam may be used to optimise all physical properties for a *specific* dose distribution. When considering the implications of the results, it is important to remember that the objective of equation 5.24 was chosen arbitrarily from a large number of possibilities [such as physical objectives requiring tolerance doses and dose uniformity, objectives employing radiobiological objectives (see §5.1.3), and more common clinically

relevant objectives such as an 80-90% contour encompassing the target region (Klevenhagen, 1985)] as were the applied combinations of dose region weightings. Applying different weightings to the target and 0% regions will vary the optimal distribution of dose at the boundaries of such regions, and will affect the resulting uniformity of dose across the target (Webb, 1994). Thus, the results only apply directly for the least-squares criterion, and should not be used as the basis for conclusions regarding the potential of electron beam conformity from a radiobiological perspective. However, the results do demonstrate the relative potential benefits of varying electron energy and incidence angle from a physical perspective which, considering that there is a correspondence between dose and biological affect, will have implications for potential radiobiological benefits. The results also provide insight into the properties of the optimisation routine, objectives chosen and constraints applied.

5.2.4.1. Advantages of Degrees of Freedom

The dose-area histograms shown above in Figure 5-12 for distributions A-C, together with Table 5-I to Table 5-III, provide insight into the relative effects of the differing degrees of freedom in phase space manipulation on resulting dose distributions. Taking dose distribution A as an example, we see from Figure 5-12a) that there is little variation in the dose-area histogram as degrees of freedom are added to the incident phase space. Energy modulation provides some increase in the mean dose (by increasing surface dose and dose at depth at the expense of dose deposition in the 0% region at depth) and angular modulation helps in avoiding dose deposition in the 0% region (reducing the maximum in the third column of Table 5-I, though the potential and dose-area histograms change only slightly. These results, and similar results for dose distribution B, show that minimal and predictable gains are to be made for such desired dose distributions. The effects of energy and angular modulation on dose distributions shall be discussed in detail in §5.2.4.2.

The variation in monoenergetic dose-area histogram with energy used for distributions A and B is a reflection of the relative suitability of each energy for the distributions considered, the objective used, and the weightings applied. For distribution C, preferential surface dose deposition for beam elements of *any* energy meant (using the closely-

approximating 14 MeV kernel) that most gain was to be made in minimising penumbral widths via angular modulation as Table 5-III indicates.

In Table 5-III [for distribution C], the potential actually increased relative to the monoenergetic / variable incidence case when energy modulation was included. Were the optimisation procedure allowed to progress past the finishing condition (consistency in potential between two batches to 3 significant figures) then the potential for the fully-variable phase space would have inevitably fallen below that of the monoenergetic/variable incidence case, though the approach was very slow indicating flatness in the objective about the minimum. This observation could have differed were an alternative optimisation objective used [such as dose flatness, or a combination of objectives (Webb, 1995)]. Additionally, the lack of restriction in the allowable phase space provides a large range of feasible solutions for the optimisation algorithm to search.

For distribution C where surface sparing is required, the least-squares criteria allowed the beam element weightings to build up despite the inevitable deposition of dose at the surface by electrons of any energy. Coincidently, the optimal match to desired distribution C was that of a virtually pure 14 MeV beam (little contribution was made by other beam energies, even when all angles of incidence were considered as in Figure 5-25.

The dose distributions in Figure 5-13, Figure 5-14 and Figure 5-15 allow additional comparison of the benefits of manipulation of the available degrees of freedom, and also indicate characteristics of the optimisation schedule. With the weightings applied (see Figure 5-9), it is seen that, in polyenergetic cases particularly, the 100% dose region is closely encircled by the 30% dose contour. This observation would depend on the relative proportion of 100% area to 0% area, and is a consequence of the least-squares objective combined with the applied weightings.

It can be seen, particularly for distributions B and C, that the narrowness of penumbral regions was sacrificed (relative to monoenergetic cases) for greater uniformity in the 100% region as more degrees of freedom were added to beam manipulation (in particular, energy modulation). Comparing columns three and four in Table 5-II and Table 5-III, it is seen that

the total dose deposition outside of the 100% region increased as multiple degrees of freedom were added, accommodated by the increased uniformity in the 100% region.

The results for distribution D mainly provide insight into the characteristics of the optimisation routine rather then the benefits of electron manipulation. This is because the intricacies of this distribution (though less detailed than that of patient tissues), necessarily lead to a complex optimal phase space as the results indicate. In attempting to conform under the least-squares criterion, the annealing routine was required to deal with several conflicting dose characteristics, such as (i) using sufficiently high energies to cover the desired 100% region whilst protecting region 3 (see Figure 5-10), (ii) exploiting angular modulation whilst avoiding the highly weighted region 2, and (iii) the usual requirement of avoidance of the general 0% region of the phantom.

Given such difficulties, it is obvious from Figure 5-27a)-d) that, even with full electron manipulation, the complexities of the dose distribution allow minimal conformation. In particular, region 2 had a major shielding effect on the area of region 1 distal to the surface leading to a substantial reduction in dose in that area of region 1. This is shown dramatically in Figure 5-26 where high dose levels in region 1 are sustained over only small areas. The required stringence of avoidance of region 2 assured consistently low doses in that region, though the deeper location of region 3, although weighted less, allowed region 3 to receive lower mean doses as shown in comparison of columns 2 and 3 of Table 5-IV.

The inadequacy of the monoenergetic intensity-modulated beam to conform to the wedge-shaped distribution is shown dramatically in Figure 5-32a), where the maximum dose *outside* the target (100%) region reached 138.5% of the desired target value (see Table 5-V). The dose-area histogram for this case (Figure 5-31) also shows how poorly this beam covered the target region in comparison to the other phase spaces considered. The introduction of energy modulation [Figure 5-32b)] allowed the dose distribution to follow the distal edge of the target with approximately the 80% contour. The selected region weightings for this distribution and the paraspinal muscle irradiation led to more clinically acceptable target-region doses than did the weightings selected for distributions A-D.

With angular modulation introduced for a monoenergetic (in this case, 14 MeV) beam incident on the wedge-shaped distribution, it is seen that a judiciously selected energy allows reasonable conformation - the final potential ratio for this phase space was 0.014 compared to 0.029 for the normally incident polyenergetic case. However, energy modulation allowed greater uniformity to be achieved in the 100% region, with a lower maximum and higher mean (see Table 5-V). It is seen that the introduction of angular modulation allowed significant reduction of total dose to the 0% region (in Table 5-V, 4th column, compare 1st/2nd, 3rd/4th rows) by allowing bixels incident at oblique angles at field edges.

For the paraspinal muscle irradiation, it is seen that again, with the selected region weightings, the 100% desired dose region was generally encompassed by approximately the 80% dose contour, except when a monoenergetic normally incident beam was considered (see Figure 5-38). The organ at risk (spinal chord) received excessively high doses in the case of intensity-modulated irradiation with monoenergetic (16 MeV) electrons (see Table 5-VI and the dose-area histogram of Figure 5-37), though in all other cases was maintained below 40%. The dose-area histograms in Figure 5-37a) show that, for the monoenergetic normally incident beam, coverage of the target (100%) region was similar to that for more complex phase spaces. In Figure 5-37b) however, it is seen that the dose to the spinal chord was dramatically reduced when more degrees of freedom were added.

5.2.4.2. Effects of Degrees of Freedom

The rectangular dose distributions considered [distributions A and B] illustrate the ability for electron fluence tailoring to achieve steep penumbral regions. The dominant factors controlling this effect were the spatial variation in fluence near the edges of 100% regions (as illustrated in Figure 5-16) and the ability to provide fluence incident at oblique angles from outside the region incident on the desired high dose-area (as illustrated in eg., Figure 5-17, Figure 5-20, and Figure 5-23) ie., negative angles of incidence from negative off-axis locations moving to dominantly positive angles of incidence from positive off-axis

locations). Both energy and angular effects allow 'filling in' of the surface dose region in distributions A and B due to preferential surface dose deposition. For distribution C, a lack of low energy components (see Figure 5-24) leads to greater surface (skin) sparing compared to distribution B (see Figure 5-21) where surface sparing is to be avoided, and the energy spectrum extends to lower energies. The increase in surface dose due to low-energy oblique electrons has been utilised clinically (see for eg., Alasti and Galbraith, 1995; §3.2.2.2).

A particularly interesting feature displayed by the profiles of Figure 5-16 is the variation in location of 'bumps' at field edges with width of the 100% dose region for similar-energy monoenergetic normally incident phase spaces. The width of the 100% region is greatest in Figure 5-16a), then c), then b). As the dose region narrows, these field edge bumps coalesce. The increase in electron fluence at the edge is a consequence of the approximately Gaussian shape of the lateral electron fluence profile at depth, the resulting electronic disequilibrium at field edges (see §3.2.1.2), and the desire of the optimisation routine to create a significantly steep penumbra (see also, Lief *et al.,* 1996). A single Gaussian distribution has steeper sides than a superposition of Gaussians. This effect is also seen to occur for the wedge-shaped distribution in Figure 5-33.

Intensity peaks are also seen to occur in the energy sinograms for distributions, such as in Figure 5-21b), with high energy peaks (>20 MeV) being present at the field edges. As was shown in §2.1.1.4 (see Figure 2-4), the mass scattering power of electrons in water decreases with increasing energy. Thus, although higher-energy electrons have longer ranges in water relative to lower-energy electrons, their spread at a given depth is lower and so they can contribute to dose at the edges of 100% regions with less influence on penumbral broadening.

Specifying an appropriate energy for monoenergetic beam phase spaces involves evaluating the trade off between adequate coverage of the target region at depth and dose deposition at depths greater then the target region. Thus, for distributions A and B, using higher energy monoenergetic beam elements (16 MeV rather then 12 MeV) led to higher mean doses in the 100% dose region (see column 2 of Table 5-I and Table 5-II), though increased dose

deposition in the 0% region of the phantoms (see column 4 of Table 5-I and Table 5-II). The higher energy beam gave greater conformity in each case because of the similar shapes of the depth dose distributions for each energy, though greater penetration of higher doses for the 16 MeV beam [D_{50} is, according to equation 3.22 of ICRU 35 (1984), approximately 5.2 cm and 6.9 cm for 12 MeV and 16 MeV broad, normally incident beams respectively].

Phase spaces employing full electron manipulation (energy and incidence-angle modulation) display the complex interplay between the advantages of energy and angular modulation for achieving dose conformity. The unique observation to be made using the figures showing energy sinograms at multiple incidence angles (over simple energy or angular sinograms), is the variation in energy with angle and spatial location.

In Figure 5-19, it is seen that, away from normal incidence, the high energy peaks at field edges disappear. However, as incidence angle begins to increase (ie., $>20^{\circ}$), the dominant incident beam elements increase in energy as more use is made of the extended electron range laterally across the 100% dose region. This effect is considerably less pronounced in Figure 5-21 and Figure 5-25 (for distributions B and C respectively) due to the fact that the 100% dose regions were much narrower (in the x direction) for these distributions, and high energy obliquely incident beam elements would provide kernels extending outside of the 100% dose region.

For the complex distribution (D), the relative benefits for conformity of phase space manipulation are more pronounced, though the final degree of conformity is still not high. Again, angular variation allows avoidance of low dose regions; energy modulation allows a more even distribution of energy deposition in the 100% region (governed by the simultaneous deposition elsewhere in the phantom). When combined, a greater degree of conformity is obtained with relative efficiency (compared to optimisation with only one degree of freedom) using the annealing algorithm. Note the almost monodirectional incidence of beam elements when angular modulation is allowed with this complex distribution (see Figure 5-29), governed by the locations of sensitive regions adjacent to the

100 % region. Such a tight angular distribution at each position is not seen with the simple rectangular configurations.

Table 5-IV suggests that, for distribution D, energy modulation most significantly improved the degree of conformity. This is suggested by the decrease in optimum potential when energy modulation was included (column 1 of Table 5-IV) and the significantly higher mean doses in region 1 (column 2 of Table 5-IV) for similar mean doses to the sensitive region 2 (column 3 of Table 5-IV), compared to the monoenergetic (24 MeV) cases. The universality of this result cannot be implied from this particular case. The beam components with energies much greater than 24 MeV at normal and positive angles of incidence (see Figure 5-30 and Appendix G) allow steepening of the penumbra, and hence greater definition of the 100% dose region (region 1, Figure 5-10). Such definition is limited in the monoenergetic case since restriction is to various orientations of a single kernel, and it is very likely that an alternative energy would have provided greater conformity to distribution D when angular modulation was included.

Some of the sinograms presented above will display artefacts which will not be separable from actual physical results due to the method used for kernel generation and dose summation, as discussed in §5.2.2.3. These artefacts include intense energy and angular 'bands' in sinograms (such as at 30 MeV and 40 MeV in Figure 5-22), or energy and angular 'gaps' [such as around normal incidence in Figure 5-17a) and d)]. To say that such characteristics are purely a result of the dose calculation process would be to ignore certain properties of the optimal phase spaces. However, it must be kept in mind that, due to the relatively simple superposition dose calculation performed during the annealing procedure, it is possible that artificial phase space attributes could have been introduced.

The variation in the depth of the distal edge of the target region for the wedge-shaped distribution and the paraspinal muscle distribution led to the employment of energy modulation for obtaining adequate target coverage. The normal incidence sinograms for these distributions (Figure 5-35 and Figure 5-41) show how lower energy components are the most intense at the parts of the distribution with shallower target distal edges, with higher energies utilised more in the deep-target regions. This reasonable intuitive result

was also found by Hyödynmaa *et al.* (1996). The final phase spaces for these distributions shown in Figure 5-36 and Figure 5-42 are significantly noisy indicating again that the solution space is quite flat about the optimal solution for the least-squares objective. However, it can be seen that, as incidence angle increases, the higher energy components become increasingly important, with dominant energies increasing with off-axis distance (x position) as the distal edge of the target becomes deeper from the point of view of each incident location.

It is also apparent from the results for the wedge and paraspinal muscle distributions that, provided an appropriate energy is selected, angular modulation can also provide uniform dose deposition across the target and the tracking of the distal edge of the target with the high-dose region. This is displayed particularly well for the paraspinal muscle distribution in Table 5-VI, where the final potential ratio for the monoenergetic (16 MeV) variable incidence angle phase space (0.014) is extremely close to that for the full phase space (0.012). Major advantage for this result also came from the ability to avoid the sensitive region (spinal chord) through beam angular-modulation. The conforming ability provided by angular modulation is a result of the overlap in the high-dose region of the effective obliquely-incident fields.

5.2.4.3. Practical Implementation

The degree of electron beam modulation considered in this study far exceeds that readily available in current radiation therapy practice. Also, the description of the dose delivery situation was greatly simplified - only homogeneous two-dimensional phantoms with uncontoured surfaces were considered with perfectly characterised incident elemental beams. Whereas the results have shown the effects of beam modulation and indicated some potential benefits, the results would require considerable modification if translated to practical application using contemporary treatment devices.

Beam intensity modulation is currently achievable using variation in the scanning speed of a scanning beam machine (see §3.1.2), or using dynamic collimation (Brahme, 1987; Lief *et al.,* 1994, 1995; Lind and Brahme, 1995; Lief *et al.,* 1996). Energy modulation is

available, though at a much lower resolution than that presented in this study. Electron accelerators are often capable of producing beams at multiple discrete energies, though this will usually only be at between two and five energies over a 20-30 MeV range for an approximate 5 MeV energy resolution. Using appropriate filters, this resolution can be increased (Hyödynmaa *et al.,* 1996). The use of bolus material also allows for the continual spatial variation of electron energy, though account has to be made for the effects on the electron spectrum, and the angular spread and electron intensity due to scattering in bolus materials (Low *et al.,* 1992, 1995). Even greater flexibility would be obtained if intensity-modulation and bolusing techniques were combined.

The elemental beams used were characterised very precisely. In practice, such beams are difficult to produce due to angular spread introduced over the path from the beam's source to the patient's surface (Karlsson *et al.,* 1992). This effect can be minimised by having the patient as close as possible to the beam's source, and by introducing a low atomic number medium (such as helium) into the region between the patient and the source to minimise scattering. The actual form of elemental beams (spatial, angular and energy distribution) would need to be factored into the optimisation calculation in practice.

The angular modulation considered in this study would be achievable provided that there is sufficient flexibility in the relative positioning of the beam source and the patient. The results obtained for the wedge-shaped and paraspinal muscle distributions, where the target is relatively superficial with a varying distal-edge depth, showed that a high degree of conformity is achievable using angular and intensity modulation with a suitably selected beam energy. This suggests that a possible irradiation strategy of benefit (for well localised lesions) would be multiple intensity-modulated electron beams incident at discrete angles of incidence using a single beam energy. It may also be possible to reduce the number of discrete angles (as considered in this study) if a lower resolution does not greatly affect the level of conformity. For the full three-dimensional structure of the lesion to be considered, then the angular modulation should extend out of the single plane as investigated here.

A major problem associated with the degree of modulation investigated above is the time required to achieve even less complicated modulation in practice. Variations in electron

energy can require some time (of the order of minutes). Dynamic bolusing with low-atomic number filters (eg., liquid helium, beryllium) could be pursued provided that the variation in machine output including the variation in the form of the elemental beam could be taken into account. Any implemented modulation techniques must consider the resulting treatment time in the interests of patient comfort and treatment throughput. Another time factor to be considered is that associated with the dosimetry of the treatment [apart from the usual complications of dosimetry for three-dimensional conformal techniques (Ten Haken *et al.,* 1996)]. Output dosemeters must be able to respond to the quickly varying output required of intensity-modulation including output over small periods of time, and be able to be calibrated over a broad energy range.

5.3. Conclusion / Summary - The Merits of Degrees of Freedom

Optimisation in radiotherapy, as discussed in §5.1, involves manipulation of a large number of degrees of freedom for the optimal therapeutic use of radiation. The investigation presented above has allowed evaluation of the optimal characteristics of electron beams - a relatively small subset of the full radiotherapy optimisation problem. Nevertheless, it has allowed an examination of the potential usefulness of manipulating those degrees of freedom considered; electron beam energy, incidence angle, and spatial distribution of intensity.

Within the framework of the objectives, constraints, and desired dose distributions considered, several intuitive aspects of the effects of electron beam characteristics were confirmed. Energy modulation permitted the distribution of dose with depth due to the increased range of electrons with increasing electron energy. However, as expected, surface energy deposition restricted the avoidance of surface dose. Energy modulation also allowed some control over the definition of dose penumbra through the variation in electron scattering and angular spread with energy.

Varying electron incidence angle also permitted some compensation for the effects of the spread of electron pencil beams, as well as a more uniform distribution of dose in desired

regions and the possibility to avoid sensitive regions. This variation in incidence angle represents extremely flexible angular definition at the incident plane. Thus, dose due to electrons incident at a single spatial location and with a single angle of incidence was deposited in a way as to *complement* the dose due to electrons incident at all other locations and angles of incidence. Combined with the potential energy modulation considered, the situations examined represents one of extreme flexibility relative to currently available beam delivery techniques.

In clinical radiation delivery, the degrees of freedom that are available are limited by the physical characteristics of the actual radiation delivery devices. Thus, for most applications of optimisation mathematics to radiation therapy, solution spaces are relatively highly constrained. In this investigation, the constraints have been to a large number of discrete spatial locations, angles and energies of incidence of electrons from one side of a plane, with the resulting solution space representing a level of complexity in electron delivery still not readily available, though which is being approached as the technology for dose delivery increases.

In practical implementation of the above theory, the relative ease of manipulation of various degrees of freedom would be a major factor in their optimal utilisation, including the mechanics of the manipulation and time constraints. Current methods of achieving such flexibility in electron manipulation (ie., scanned and intensity/energy modulated electron pencil beams) would not allow practical execution, even considering the potential benefits. However, it is useful to acknowledge the potential benefits (as investigated above) for the purpose of guiding research and development in radiation delivery systems.

As an optimisation technique, conventional simulated annealing may or may not have been the best one to use in the current application. However, since execution time was not an important factor, and since it is efficient in finding the global minimum to a minimisation problem, simulated annealing adequately provided the results this investigation sought. If the investigation were extended to one involving a more detailed description of the objective and constraints, or to one involving determining the optimal objectives and constraints to use, then a faster method such as very fast simulated reannealing would be

recommended. The implemented technique is only useful when considering homogeneous (water equivalent) media (all kernels being generated for such media), and the results may only be interpreted for such media. Also, no conclusions may be drawn with respect to the effects of variations in electron beam characteristics out of the plane where the desired dose distribution is defined, as a purely two dimensional beam description was used in order to minimise the complexity of the problem.

6. CONCLUSIONS

6.1. Summary of Main Findings

Although this investigation has only concentrated on *electron beam* radiotherapy, a relatively minor treatment modality (though one which is increasing in importance), the concepts covered, namely, accurate characterisation of the treatment situation (applicator scatter modelling) and the optimal delivery of radiation for therapy purposes (optimisation of electron beam properties) comprise significant contemporary issues. Accuracy at all stages of treatment is required for correct dose prescription, and optimisation of radiation delivery ensures efficient use of available methods and technologies.

Electron beam applicator scatter comprises a relatively minor component of a therapeutic electron beam (less then 10% of central-axis surface dose for broad fields and the accelerator examined in this study). However, the variation in this component with field geometry (applicator and cutout used) and energy means that the applicator scatter component will vary between specific irradiations, and accurate beam modelling requires quantification of this variation. In Chapter 4, the variation in scatter from the materials used in applicator construction with energy and irradiation geometry was investigated, and allowed development of a superposition-based model for applicator scatter. The results presented in Chapter 4 for the superposition model developed indicate that the model can efficiently account for this component. This model takes advantage of the accuracy of the detailed particle transport implemented by EGS4 Monte Carlo. The use of Monte Carlo methods in the investigations presented in this thesis provide some indication of the utility of this technique. The developed superposition model allowed an investigation to be made of the characteristics of scatter from an applicator of a Siemens KD2 accelerator.

The investigation presented in Chapter 5 allowed evaluation of the potential for conformity of electron beams through the explicit manipulation of electrons in the beam. Although the conclusions found in this study are useful for characterising the effects of specific degrees of freedom on dose distributions, the difficulties of defining objectives and constraints for the optimisation problem were highlighted. In this way, the investigation into optimal electron beam properties also provided insight into application of optimisation methods in general and, in this case specifically, application of simulated annealing optimisation. This study revealed and highlighted some potential benefits of high degrees of electron beam manipulation, including the advantages for modulating the depth of a high-dose region with electron energy, the possibility of achieving uniformly high doses with judiciously selected beam energies, and the advantages for penumbral sharpening using electron energy and intensity peaks.

6.2. Possible Future Research and Application

The applicator scatter model presented in Chapter 4 could be used clinically in combination with a thorough characterisation of the primary beam. A detailed description of the primary beam could be obtained by modelling the full treatment head with Monte Carlo methods. The contribution due to patient-specific cutouts could be calculated with the superposition model. This would provide a full description of a treatment beam for input to an appropriate electron dose calculation algorithm. This also requires assessment of the techniques dose calculation algorithms use for describing the incident electron beam, and, for non-Monte Carlo based methods, development of techniques to utilise complete beam descriptions.

The effects of applicator scatter presented in Chapter 4 could be reduced by optimising the applicator collimation system. Alternatively, with knowledge of the results presented in Chapter 5, the full treatment head assembly could be modified to provide electron beams with greater conforming potential. Such development would have to be considered in light of competing alternative techniques, such as magnetically scanned electron beams and alternative beam modalities.

Several possible extensions of the research presented in this thesis have become obvious.

- In order for the investigation into applicator scatter be of the most benefit, it will be necessary to analyse exactly how the information revealed by the superposition model could be incorporated into actual treatment planning algorithms.
- The use of multi-leaf collimation in electron therapy may replace the use of patient-specific cutouts in the near future. The developed model could be easily adapted for modelling scatter from leaf ends, particularly useful if the collimator leaves are non-diverging.
- The phase space description of the radiation beam is a complex one. Consequently, the data files describing a beam's phase space tend to be very large. An investigation could be made into methods of extracting a simplified model of the beam from the beam's phase space description. Such a model would have to be able to retain the details of the complex correlation between particle type, energy, position and direction that exists in a beam.
- With regards to the investigation into electron beam optimisation, it would appear that a more thorough exploration of the alternatives available for describing an objective would be of benefit.
- A more involved investigation of optimal beam properties could consider the detailed effects of phantom heterogeneities on optimal solutions. It could also be possible to incorporate a full three-dimensional dose calculation into the optimisation routine. However, if no single plane is to be preferred in this case, then, compared with the two-dimensional case, a full phase space description would require a squaring of the number of spatial locations and angles of incidence for the same resolution - this would create an extremely large solution space (eg., for the paraspinal muscle irradiation, the number of beam elements was approximately 4×10^4 for the two-dimensional case, though would be approximately 7×10^7 for the three-dimensional case).
- An even more unconstrained optimisation investigation could consider the potential for combining other modalities (eg., photons, protons, external and internal sources, beams incident from more then one plane). Because of their

scattering characteristics, there is minimal dose-escalation advantage in using them in abutted or rotation techniques, although such techniques with photons and protons are potentially very successful. It is also possible to sharpen the penumbra of an electron field using photon irradiations at the field edge, so it would seem feasible that some benefits would be achieved by incorporating this modality into the optimisation process. It would also be advantageous to compare all modalities individually in order to ascertain their relative utility.

- An alternative to investigating an *increase* in the degrees of freedom in beam manipulation is to investigate the optimal number of degrees of freedom. Such an investigation could evaluate the relative benefits for dose conformation of increasing the numbers of discrete energies available, or of the resolution used in angular and intensity modulation.
- A thorough analysis of currently available technology in radiation delivery would identify what is available for achieving high degrees of beam manipulation. Alternatively, the results presented in this thesis could be used as the basis for developing treatment technology capable of more complex beam manipulation, or the optimisation of current technology (especially tertiary collimation systems).

APPENDIX A: EXAMPLE INPUT FILE TO RTPCYL

Example of an input file to the RTPCYL usercode. Simulation was of the scattering foils and air column for a 12 MeV beam on a Siemens KD2 accelerator.

SCATTERING FOIL SIMULATION	Simulation title
AIR	Material 1
GOLD	Material 2
ALUMINIUM	Material 3
DUMMY	Material 4 (Not used)
200.0, -4, 1	Phantom thickness (cm), number of cylindrical layer groups (negative since thicknesses input next), number of radial scoring regions
0.01, 1, 2, 19.32, 0.521, 0.01	First layer group (gold foil) thickness (cm), number of layers, material index, density, ECUT, PCUT
10.0, 1, 1, 0.001, 0.521, 0.01	Second layer group (air between foils)
0.081, 1, 3, 2.70, 0.521,.0.01	Third layer group (aluminium foil)
5.0, 20, 1, 0.001, 0.521, 0.01	Fourth layer group (air column to past isocentre)
0.0	Inner radius (cm) for first radial region
10.0	Outer radius (cm) for first radial region
12.0, 0.0, 0.521, 0.01	Kinetic energy of incident particles (MeV), standard deviation in angular spread, global ECUT, global PCUT
0	Indicates parallel beam source on major axis
0.1	Radius (cm) of parallel beam
1000000, -1, 0, 600.0, 0, 12345	Number of particle histories, particle charge (electrons), simulation monitor routine off, CPU time limit (hours), histogram output off, random number seed
200.0, 1.0	Russian roulette depth, and survival probability
0,0,0,0	All PRESTA options on
0,0,0,0,0,0,0,1	All output options off (zeroes) except for electron spectrum scoring at a plane defined in RTPCYL

APPENDIX B: EXAMPLE INPUT FILE TO RTPCART_XYZ

Example of an input file to the RTPCART_XYZ usercode. Simulation was of a beam element collimated to a small edge of cerrobend for a 12 MeV beam on a Siemens KD2 accelerator.

EDGE SCATTERING SIMULATION	Simulation title
AIR	Material 1
CERROBEND	Material 2
DUMMY	Material 3 (Not used)
DUMMY	Material 4 (Not used)
0.5, 0.5	Sizes of rectangular voxels in x and y planes. Voxel numbers stipulated in RTPCART_XYZ
2	Number of different z region boundaries
1.2, 1	First z region (cerrobend edge) thickness (cm), number of layers
0.5, 19	Second z region (air)
1, 0.001	Base phantom material index, density
1	Number of regions of differing material to base phantom
2, 10.80, 1, 4, 1, 20, 1, 1	First region material index, density, x region lower voxel limit, x region upper, y region lower, y region upper, z region lower, z region upper
-12.0, 0.0, 0.521, 0.01	Kinetic energy of incident particles (negative since spectrum input next), standard deviation of angular distribution, global ECUT, global PCUT
0.0	Lower energy of first spectral bin
0.5, 0.2	Upper energy of first spectral bin, relative weighting
1.0, 0.1	Second spectral bin
1.5, 0.2	Third spectral bin
2.0, 0.1	Fourth spectral bin
...	...
10.5, 3.7	Twenty first spectral bin
11.0, 13.0	Twenty second spectral bin
11.5, 74.2	Twenty third spectral bin

0	End of spectrum
3	Indicates rectangular beam with following properties
5.0, 5.0, -4.5, -2.97, -0.5, 0.5, 95.0	Beam origin x coordinate, y coordinate, x beam limit, x beam limit, y beam limit, y beam limit, distance from source to phantom
1000000, -1, 0, 600.0, 0, 12345	Number of particle histories, particle charge (electrons), simulation monitor routine off, CPU time limit (hours), histogram output off, random number seed
200.0, 1.0	Russian roulette depth, and survival probability
0,0,0,0	All PRESTA options on
0,0,0,0,0,1	All output options off (zeroes) except for formation of a scatter kernel for electrons at the z level following
12	z level at which to establish scatter kernel

APPENDIX C: POLYGON CLIPPING ROUTINE FOR PARTICLE INTERCEPTION CHECKING

The aperture represented by each applicator trimmer is characterised by a set K ($K = A_1, A_2, \ldots, A_{N_\alpha^{elements}}$) of $N_\alpha^{elements}$ coordinates specifying the vertices of the aperture (α) in its 2D plane (for the middle and upper trimmers, these are the four corners of the rectangular aperture, whereas for the lower trimmer defined by a cutout, many more vertices are likely to be required). When a particle is sampled from an upper trimmer, it has a specific location and orientation in space given by the vector $v_p = (x_p, y_p, z_p)$ which is determined by the location of the edge segment it scattered from, $r_{\alpha,i}^k = (x_{\alpha,i}^k, y_{\alpha,i}^k, z_{\alpha,i}^k)$, and its location in the scatter kernel after appropriate translations and rotations in space, $r_p^{\ker nel} = (x_p^{\ker nel}, y_p^{\ker nel}, z_p^{\ker nel})$. Thus

$$v_p = r_{\alpha,i}^k + \lambda\left(r_p^{\ker nel} - r_{\alpha,i}^k\right) \tag{C1}$$

where λ is some multiplier. This sampled particle will intercept a lower trimmer (β) plane at the point r_β with z coordinate z_β (the SSD of trimmer β). Solving equation (C1) in this case gives

$$r_\beta = \left[x_{\alpha,i}^k + \lambda_\beta\left(x_p^{\ker nel} - x_{\alpha,i}^k\right), y_{\alpha,i}^k + \lambda_\beta\left(y_p^{\ker nel} - y_{\alpha,i}^k\right), z_\beta\right] = \left(x_\beta, y_\beta, z_\beta\right) \tag{C2}$$

with

$$\lambda_\beta = \frac{z_\beta - z_{\alpha,i}^k}{z_p^{\ker nel} - z_{\alpha,i}^k} \tag{C3}$$

These points may be more clearly understood with reference to Figure C1 which shows a sampled particle intercepting a trimmer with an irregular aperture.

Following the algorithm described by Steidley *et al.* (1994) and Pavlidis (1982), we consider the $N_\alpha^{elements}$ determinants

$$S_i = \det\left[A_i, (0,0,z_\beta), r_\beta\right] = \begin{vmatrix} X_i & 0 & x_\beta \\ Y_i & 0 & y_\beta \\ 1 & 1 & 1 \end{vmatrix}, \qquad i = 1, \ldots, N_\alpha^{elements} \tag{C4}$$

(setting the value of z_β conveniently to 1). The line subtended by $\boldsymbol{r}_\beta$ in the $z=z_\beta$ plane will cross the aperture segment $\overline{A_i, A_{i+1}}$ if S_i is of opposite sign to S_{i+1}. Considering all S_i in this way indicates what edge segments (if any) are intercepted by $\boldsymbol{r}_\beta$ in this plane. Whether the origin is inside or outside the aperture (in Figure C1 it is inside the aperture) then determines whether or not $\boldsymbol{r}_\beta$ is inside or outside the aperture and whether or not the sampled particle is intercepted by the lower trimmer.

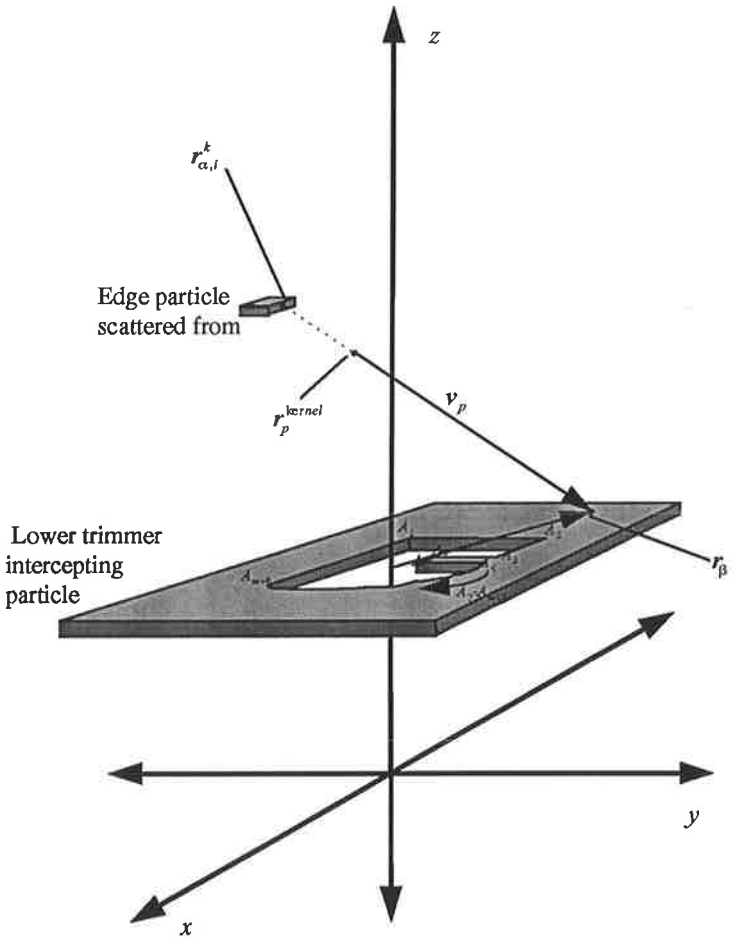

Figure C-1: Example of determination of particle interception using the polygon clipping routine.

In programming this algorithm, it is required that special cases such as S_i being equal to zero ($\boldsymbol{r}_\beta$ being on an extrapolated edge segment), the possible combinations of changes of sign of S_i, and the different possible locations of the origin are accounted for.

APPENDIX D: DERIVATION OF INCIDENCE AND OBLIQUITY ANGLES

The position and orientation of an edge element will determine the area of exposed face (and hence which library kernel is most appropriate in describing scatter from the edge), as well as the obliquity of the beam. The geometry for determining the angles of incidence (φ) and obliquity (ψ) is shown in figure D-1 a) and b).

a) b)

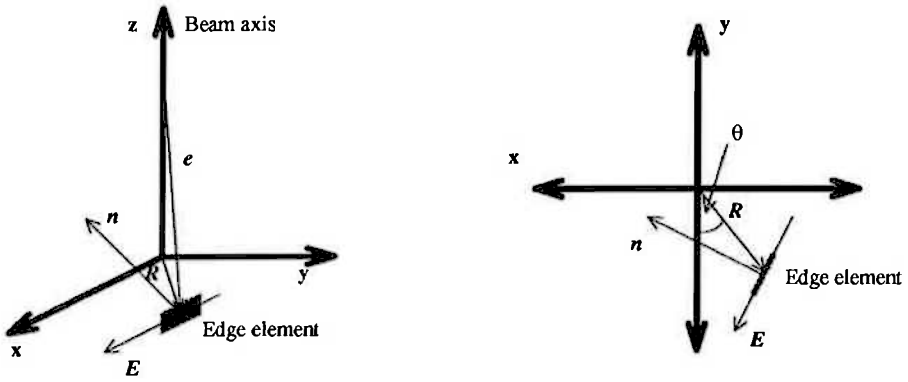

Figure D-1: Geometry for edge element orientation definition in the frame of the aperture being considered.

The vectors shown are,

e - effective source position to centre of edge element;

R - location of centre of edge element in aperture plane;

E - direction of edge element in aperture plane;

n - normal to edge surface in aperture plane;

Angles of interest are,

θ - azimuthal of ***R*** in aperture plane

φ - angle of incidence of beam to edge face, which is angle between ***e*** and ***n***.

ψ - angle of obliquity of beam to edge face, which is angle between ***E*** and ***e***.

In the coordinate system shown and with the above definitions,

$$\varphi = \cos^{-1}(\boldsymbol{e}\cdot\boldsymbol{n}) \tag{D1}$$

$$\varphi = \cos^{-1}(\boldsymbol{E}\cdot\boldsymbol{e}) \tag{D2}$$

Letting the edge element be defined by limits (x_1, y_1), (x_2, y_2) we have

$$\boldsymbol{R} = \left(x_2 - \frac{x_2 - x_1}{2}, y_2 - \frac{y_2 - y_1}{2}, 0 \right) = (R_x, R_y, 0) \,. \tag{D3}$$

A unit normal vector in direction $\boldsymbol{E}$ is

$$\hat{\boldsymbol{E}} = \frac{(x_2 - x_1, y_2 - y_1, 0)}{\left[(x_2 - x_1)^2 + (y_2 - y_1)^2 \right]^{\frac{1}{2}}} \tag{D4}$$

For any rotation by ϕ in a positive sense about the z axis, a coordinate transformation matrix is

$$\mathrm{A}(\phi) = \begin{bmatrix} \cos\phi & \sin\phi & 0 \\ -\sin\phi & \cos\phi & 0 \\ 0 & 0 & 1 \end{bmatrix} \tag{D5}$$

To obtain a unit normal vector in direction $\boldsymbol{n}$:

$$\hat{\boldsymbol{n}} = A\left(\frac{\pi}{2} \right) \hat{\boldsymbol{E}} = \frac{(y_2 - y_1, x_1 - x_2, 0)}{\left[(x_2 - x_1)^2 + (y_2 - y_1)^2 \right]^{\frac{1}{2}}} \tag{D6}$$

A unit normal vector in direction $\boldsymbol{e}$ is

$$\hat{\boldsymbol{e}} = \frac{(R_x, R_y, -s)}{\left(|\boldsymbol{R}|^2 + s^2 \right)^{\frac{1}{2}}} \tag{D7}$$

We then have

$$\varphi = \cos^{-1}\left[\frac{R_x (y_2 - y_1) + R_y (x_1 - x_2)}{\left(|\boldsymbol{R}|^2 + s^2 \right)^{\frac{1}{2}} \left[(x_2 - x_1)^2 + (y_2 - y_1)^2 \right]^{\frac{1}{2}}} \right]$$

$$\psi = \cos^{-1}\left[\frac{R_x (x_2 - x_1) + R_y (y_2 - y_1)}{\left(|\boldsymbol{R}|^2 + s^2 \right)^{\frac{1}{2}} \left[(x_2 - x_1)^2 + (y_2 - y_1)^2 \right]^{\frac{1}{2}}} \right] \tag{D8,9}$$

for the incidence and obliquity angles respectively. We need to evaluate which normal incidence radius (R_{eff}) corresponds to the incidence angle of an oblique edge element. This is given by

$$R_{eff} = \frac{s}{\tan(\varphi)} \,. \tag{D10}$$

APPENDIX E: APPLICATOR SCATTER SUPERPOSITION PROGRAM

Algorithm Pseudocode

for each aperture in the applicator **do** {

determine the number of particles to sample from the current aperture;

break up the current aperture into edge elements of the size modelled;

for each edge element in the current aperture **do** {

determine the number of particles to sample from the current edge element;

calculate the angles of incidence (φ) and obliquity (ψ);

determine the effective edge radius (r_{eff});

load the appropriate scatter kernel;

rotate the kernel for obliquity;

for each required particle **do** {

sample the kernel's 2D fluence distribution;

sample randomly from within the selected voxel;

extrapolate to the required final scoring plane to determine position and direction;

if the current particle will not be masked by lower apertures **then** {

sample the energy distribution of the selected voxel;

weight the particle according to the total number sampled, the expected number per Φ_{CA}^{p}, SSD_{α}, and $\Phi_{s}^{p}\left(r_{\alpha}^{e}\right)$;

write particle's characteristics to phase space file; }}}}

Program Structure

Figure E-1 shows the structure of the C program written to perform the sampling of applicator scatter phase space data.

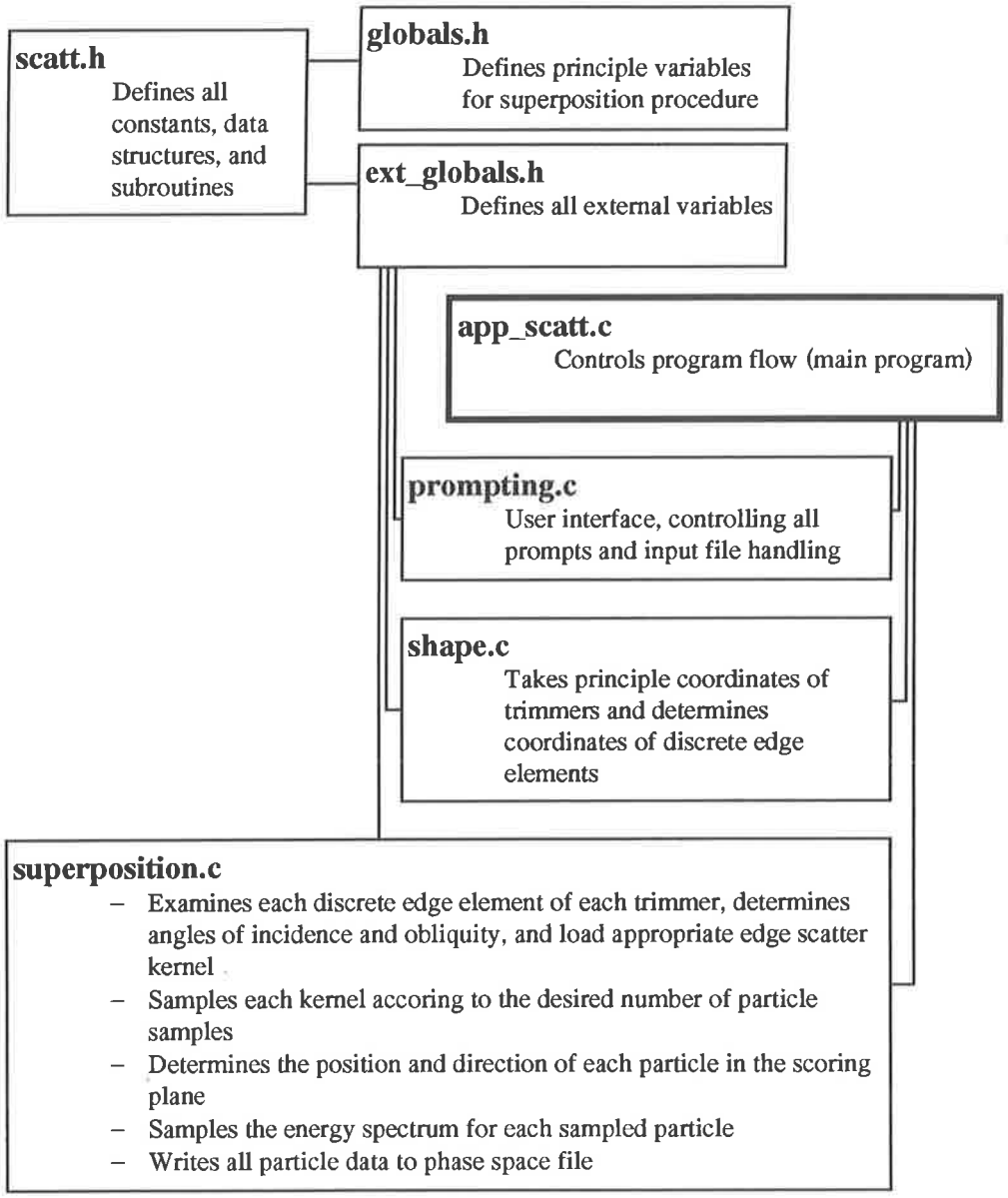

Figure E-1: Basic structure of the code written to perform phase space sampling of applicator-scatter kernels

Sample Input File

15	Applicator size (10-10x10 cm^2; 15-15x15 cm^2; 20-20x20 cm^2)
100	SSD of scoring plane
12.0	Nominal primary beam energy (MeV)
12	Side length of scoring plane region (cm)
50000	Number of applicator scattered particles to sample
E	Particles to sample (E-electrons, P-photons)
25	Number of vertices defining cutout shape
-5.0, 5.0	First pair (x, y) of vertices (cm from central axis)
5.0, 5.0	Second pair of vertices
----------	----------
-3.0, -5.0	Twenty-fourth pair of vertices
-5.0, -5.0	Twenty-fifth pair of vertices

Sample Phase Space File

3.879013e-01,-1.029867e+00	First particle; x position (cm from central-axis), y position
3.869052e-01,-4.968852e-01,-7.767944e-01	First particle; x direction cosine, y direction cosine, z direction cosine
6.173411e+00,1.724744e-02,-1	First particle; kinetic energy (MeV), particle weighting, particle charge
-8.820288e-01,-1.623845e-01	Second particle
2.561509e-01,-4.336510e-01,-8.639060e-01	
7.166318e+00,1.724744e-02,-1	
-2.710558e+00,2.836216e+00	Third particle
-7.288536e-02,-2.591956e-02,-9.970035e-01	
1.718063e+01,1.724744e-02,-1	
2.110541e-01,-2.772016e+00	Fourth particle
2.767799e-01,-6.491438e-01,-7.085232e-01	
1.501739e+01,1.724744e-02,-1	
.	.
.	.

APPENDIX F: SIMULATED ANNEALING PROGRAM

Program Structure

The structure of the C program written to execute the simulated annealing procedure is shown in Figure F-1.

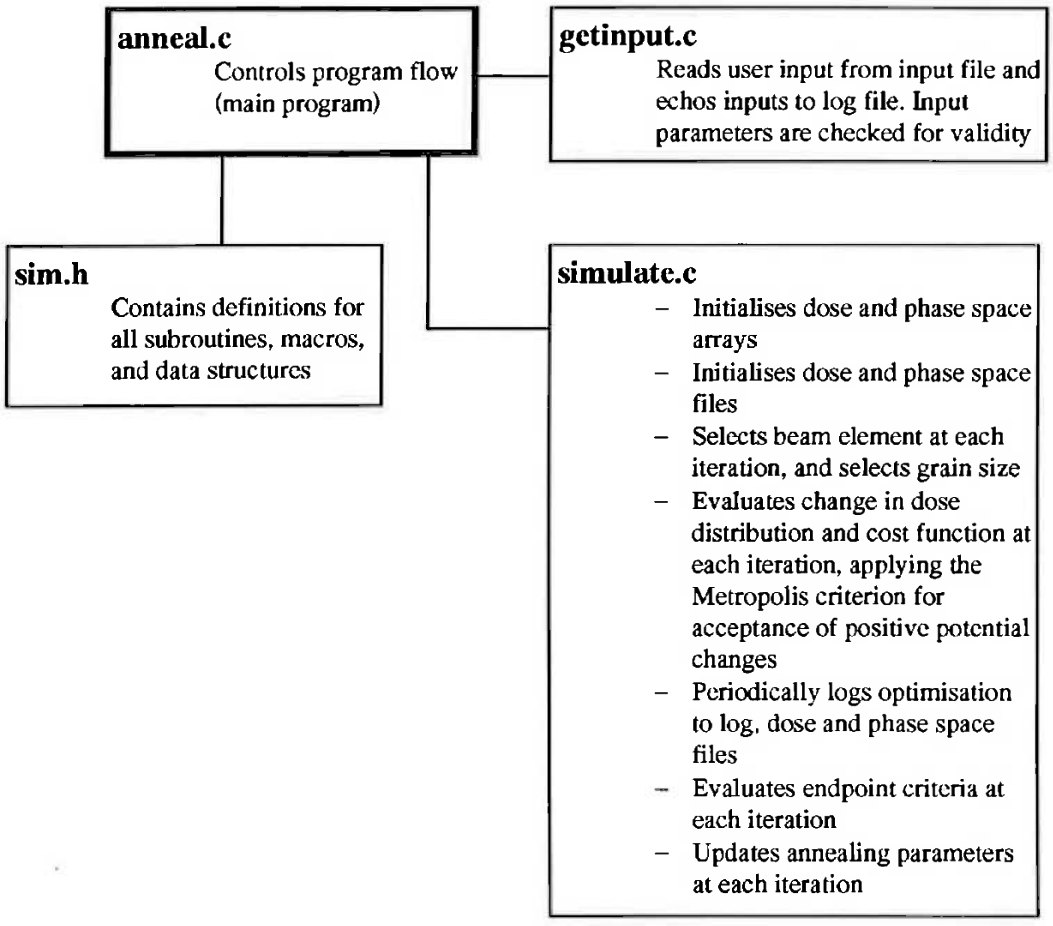

Figure F-1: Basic structure of the simulated annealing code.

Sample Input File

STANDARD DISTRIBUTION	Title
0.5,30	Size of x voxels (cm), number of x voxels
0.0,0	Size of y voxels (cm), number of y voxels; if zero, then problem is two-dimensional
0.4,50	Size of z voxels (cm), number of z voxels
0.0,0,2.0	Base phantom characteristics; desired dose (%), dose flag (0-near as possible, 1-maximum limit, 2 minimum limit), weighting
1	Number of dose regions different from base phantom
12,19,0,0,5,14,100.0,0,1.0	Region characteristics; minimum x voxel, maximum x voxel, minimum y voxel, maximum y voxel, minimum z voxel, maximum z voxel, desired dose (%), dose flag, weighting
7.5,7.5,-5.0,5.0,0.0,0.0	Electron beam dimensions; x centre (cm), y centre (cm) (arbitrary in two-dimensional problems), x minimum (cm), x maximum (cm), y minimum and maximum (arbitrary in two-dimensional problems)
0,25	Phase space characteristics; angle of incidence options (0-normal incidence, 1-variable incidence angle)
2.0	First discrete energy
4.0	Second discrete energy
48.0	Twenty-fourth discrete energy
50.0	Twenty-fifth discrete energy
0	Cost function to use (0-sums of squares, no other options)
0	Annealing schedule to use (0-conventional, 1 fast)
10000000,0.0	Endpoint conditions; maximum number of iterations, desired ratio of potential to original value
20.0,0.1,1000.0,10000	Initial annealing parameter values; W_0, T_0, R_T, R_W
100000,1628122,2	Number of iterations after which to log simulation; random number seed; random number generator (0-3)
1	Finnigan factor - number of pencil beams to split each beam element up into
1	Recover previous data option (0-new data, 1-recover data)

Sample Log File

```
==========================================================
==          Simulated annealing program for optimisation of          ==
==                electron beam characteristics.                     ==
==                                                                   ==
==                M.A.Ebert, R.A.H., 1995                            ==
==========================================================

From file standard.input
Norm val = 1.0000e-05 (corresp. to 100 units)
STANDARD DISTRIBUTION

X voxel characteristics
        xsize= 0.5000, xnum=30
Y voxel characteristics
        ynum=0 - 2D problem
Z voxel characteristics
        zsize= 0.4000, znum=50
Base phantom characteristics
        Base dose= 0.0000 - nearest value  Weighting= 2.0000
1 regions different from base phantom
Region characteristics...
        Region 1, xlow,xhigh,ylow,yhigh,zlow,zhigh, dose, dose flag, weighting
        12, 19, 0, 0, 5, 14, 100.0000, 0, 1.0000
Beam characteristics
        x/ycentre  7.50, 7.50, xmin/max -5.00, 5.00, ymin/max  0.00, 0.00
Angular option off
Energies to be used...
        2.0000 MeV
        4.0000 MeV
        .
        .
        .
        48.0000 MeV
        50.0000 MeV
Potential (cost function) to be employed...
        Least squares minimisation
Annealing schedule to employ...
        Conventional annealing
```

Endpoint conditions

Max no iterations=10000000, Potential tolerance to acheive=0.0000

Initial parameter values...

Wo=20.0000, To= 0.1000, Rt=1000.0000, Rw=10000.0000

Logging frequency, RN seed, RN Gen type (0-3)

Every 100000 iterations; Initial seed = 1628122, Gen = 2

CORRECTING SEED

Finnigan factor

1

RECOVERING PREVIOUS DATA

Making phase space without angular option

Update, at 0th iteration after 0 seconds CPU

POTENTIAL = 4.08480e+05, RATIO TO INITIAL = 1.00000e+00

Tt = 0.10000, Wt = 20.00000

No_REJECTED = 0, No_ACCEPTED = 0, No_through_METROPOLIS = 0

Update, at 100000th iteration after -894 seconds CPU

POTENTIAL = 4.02716e+05, RATIO TO INITIAL = 9.85888e-01

Tt = 0.02159, Wt = 7.86463

No_REJECTED = 95921, No_ACCEPTED = 4079, No_through_METROPOLIS = 816

Update, at 200000th iteration after -1729 seconds CPU

POTENTIAL = 3.99260e+05, RATIO TO INITIAL = 9.77428e-01

Tt = 0.01883, Wt = 6.40376

No_REJECTED = 191681, No_ACCEPTED = 8319, No_through_METROPOLIS = 1660

.

.

.

.

APPENDIX G: ENERGY SINOGRAMS FOR DISTRIBUTION D AT DISCRETE ANGLES OF INCIDENCE

a) *-80°*

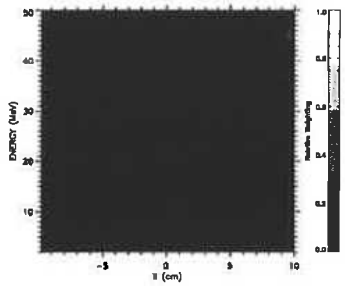

b) *-70°*

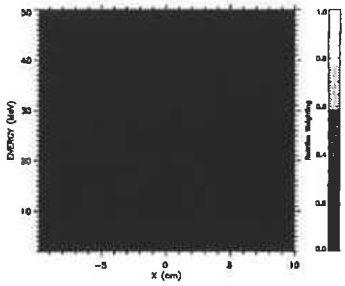

c) *-60°*

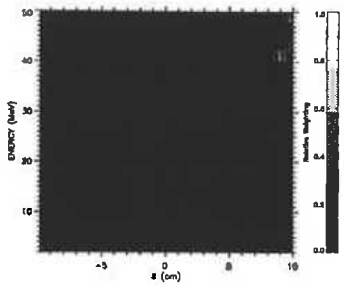

d) *-50°*

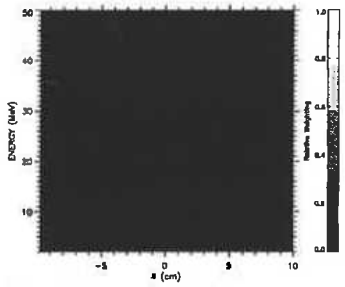

e) *-40°*

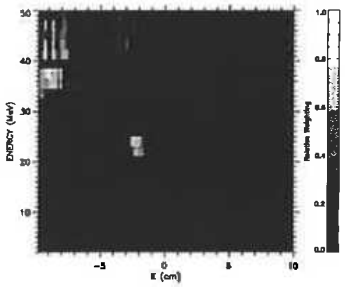

f) *-30°*

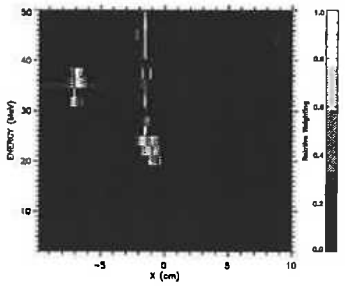

g) *-20°*

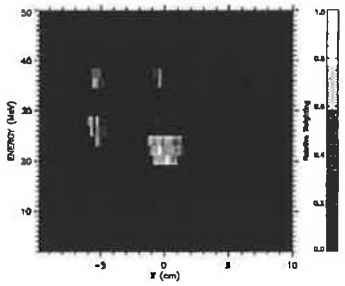

h) *-10°*

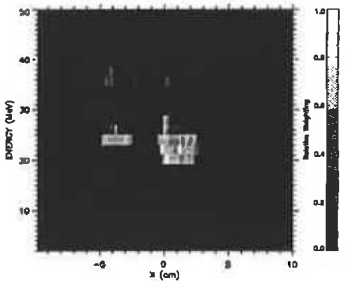

i) *Normal Incidence*

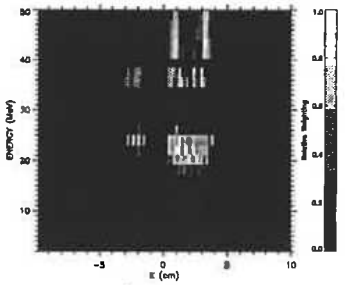

j) *+10°*

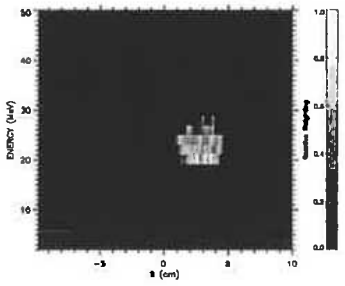

k) *+20°*

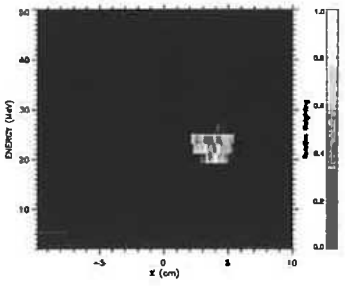

l) *+30°*

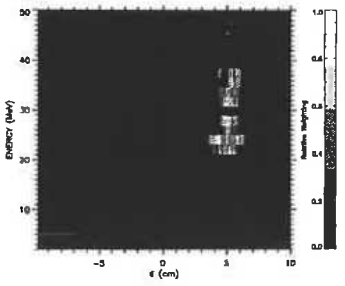

m) *+40°*

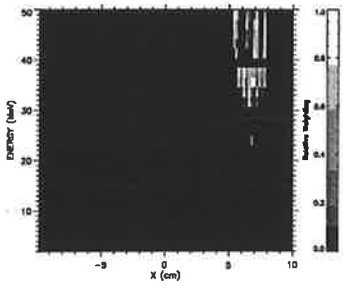

n) *+50°*

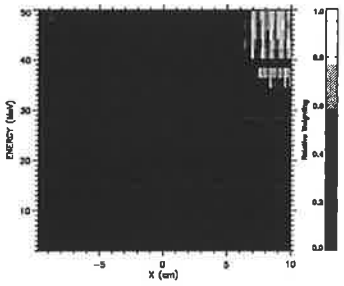

o) *+60°*

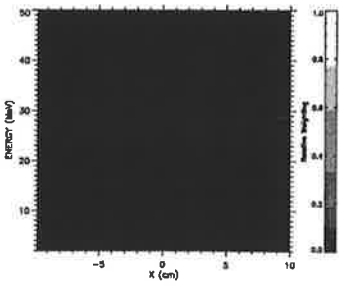

p) *+70°*

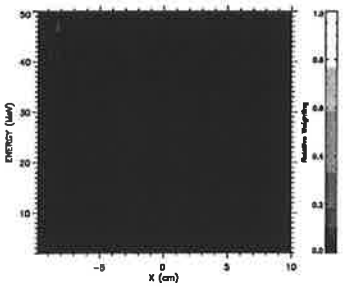

q) *+80°*

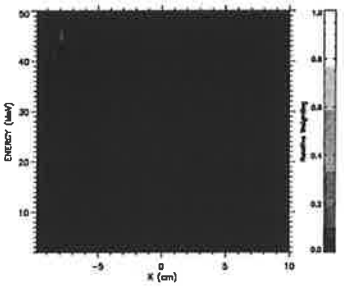

APPENDIX H

COMPANION PAPER – TUMOUR CONTROL PROBABILITY

M.A. Ebert and P.W. Hoban (1996) Some characteristics of tumour control probability for heterogeneous tumours.
Physics in Medicine and Biology, v. 41 (10), pp. 2125-2133, October 1996

REFERENCES

Abou-Mandour, M. and Harder, D. (1978) Systematic optimization of the double-scatter system for electron field flattening, *Strahlenther.*, **154**, 328

Ågren, A., Brahme, A. and Turesson, I. (1990) Optimization of uncomplicated control for head and neck tumors, *Int. J. Radiat. Oncol. Biol. Phys.*, **19**, 1077-1085

Ahnesjö, A. (1995) Collimator scatter in photon therapy beams, *Med. Phys.*, **22**, 267-278

Ahnesjö, A. Andreo, P. and Brahme, A. (1987) Calculation and application of point spread functions for treatment planning with high energy photon beams, *Acta Oncol.*, **26**, 49-56

Alasti, H. and Galbraith, D.M. (1995) Depth dose flattening of electron beams with a wire mesh bolus, *Med. Phys.*, **22**, 1675-1683

Almond, P.R., Wright, A.E. and Boone, M.L. (1967) High energy electron dose perturbations in regions of tissue heterogeneity, II: Physical models of tissue heterogeneities, *Radiol.*, **88**, 1146

Altschuler, M.D., Censor, Y., Powlis, W.D., Smith, A.R. and Wallace, R.E. (1986) Selecting beams and beam weights for 3-D treatment planning, *Med. Phys.*, **13**, 590 (abstract)

Altschuler, M.D., Bloch, P., Buhle, E.L. and Ayyalasomayajula, S. (1992) 3D dose calculations for electron and photon beams, *Phys. Med. Biol.*, **37**, 391-411

Andreo, P. (1990) Depth dose and stopping power data for monoenergetic electron beams, *Nucl. Instr. Meth.*, **B51**, 107-121

Andreo, P. (1991) Monte Carlo techniques in medical radiation physics, *Phys. Med. Biol.*, **36**, 861-920

Andreo, P. and Fransson, A. (1989) Stopping power ratios and their uncertainties for clinical electron beam dosimetry, *Phys. Med. Biol.*, **34**, 1847-1861

Andreo, P., Brahme, A., Nahum, A.E. and Mattsson, Q. (1989) Influence of energy and angular spread on stopping-power ratios for electron beams, *Phys. Med. Biol.*, **34**, 751-768

Antolak, J.A., Hogstrom, K. and Rosen, I.I. (1996) Optimization of bolus design, *Med. Phys.*, **23**, 1101 (abstract)

Archambeau, J.O., Forell, B., Doria, R., Findley, D.O., Jurisch, R. and Jackson, R. (1981) Use of variable thickness bolus to control electron beam penetration in chest wall irradiation, *Int. J. Radiat. Oncol. Biol. Phys.*, **7**, 835-842

Attix, F.H. (1979) The partition of kerma to account for bremsstrahlung, *Health Phys.*, **36**, 347-354

Baggarley, S.P., Mannering, D.M., Hugtenburg, R.P. and Turner, J.R. (1994) Field size dependence of effective source distance and field factors of a 9 MeV electron beam, *Aust. Phys. Eng. Sci. Med.*, **17**, 84-87

Bahr, G.K., Kereiakes, J.G., Horwitz, H., Finney, R., Galvin, J. and Goode, K. (1968) The method of linear programming applied to radiation treatment planning, *Radiol.*, **91**, 686-693

Barth, N.H. (1990) An inverse problem in radiation therapy, *Int. J. Radiat. Oncol. Biol. Phys.*, **18**, 425-431

Beattie, J.W., Tsien, K.C., Ovadia, J. and Laughlin, J.S. (1962) Production and properties of high energy electrons for therapy, *Am. J. Roentgenol.*, **88**, 235

Beddar, A.S., Mason, D.J. and O'Brien, P.F. (1994) Absorbed dose perurbation caused by diodes for small field photon dosimetry, *Med. Phys.*, **21**, 1075-1079

Berger, M.J. and Seltzer, S.M. (1964) Tables of energy losses and ranges of electrons and positrons, *in Studies in Penetration of Chraged Particles in Matter*, National Academy of Science Publication 1133, National Research Council

Berger, M.J. and Seltzer, S.M. (1982) *Stopping Power and Ranges of Electrons and Positrons*, NBSIR 82-2550, National Bureau of Standards, Washington, DC

Berger, M.J. and Wang, R. (1988) Multiple scattering angular deflections and energy-loss straggling, in Jenkins *et. al.* (1988), 21-56

Bethe, H.A. (1930) Zur theorie des durchgangs schneller Korpuskular-strahlen durch materie, *Ann. Phys.*, **5**, 325

Bethe, H.A. (1932) Bremsformel für elektronen relativischer geschwindigkeit, *Z. Phys.*, **76**, 293

Bielajew, A.F. and Rogers, D.W.O. (1987) PRESTA: The Parameter Reduced Electron-Step Algorithm for electron Monte Carlo transport, *Nucl. Instr. Meth.*, **B18**, 165-181

Bielajew, A.F., Mohan, R. and Chui, C.-S. (1989) *Improved Bremsstrahlung Angular Sampling in the EGS4 Code System*, National Research Council of Canada Report PIRS-0203

Bielajew, A.F. and Rogers, D.W.O. (1992) A standard timing benchmark for EGS4 Monte Carlo calculations, *Med. Phys.*, **19**, 303-304

Biggs, P.J., Boyer, A.L. and Dopke, K.P. (1979) Electron dosimetry of irregular fields on the Clinac 18, *Int. J. Radiat. Oncol. Biol. Phys.*, **5**, 433-440

Bjärngard, B.E., Pionteck, R.W. and Svensson, H. (1976) Electron scattering and collimation system for a 12 MeV linear accelerator, *Med. Phys.*, **3**, 152-158

Bjärngard, B.E., Pionteck, R.W. and Svensson, H. (1980) Electron and photon beams from a 50 MeV racetrack microtron, *Acta Radiol. Oncol.*, **19**, 305-319

Bloch, P. (1988) A unified electron/photon dosimetry approach, *Phys. Med. Biol.*, **33**, 373-377

Bomford, C.K., Kunkler, I.H. and Sherriff, S.B. (1993) *Textbook of Radiotherapy*, Endinburgh: Churchill Livingstone

Boone, M.C.M., Crosby, E.H. and Shalek, R.J. (1965) Skin reactions and heterogeneity in electron beam therapy II. In vivo dosimetry, *Radiol.*, **84**, 817

Boone, M.C.M., Almond, P.R. and Wright, A.E. (1967) High energy electron dose perturbations in regions of tissue heterogeneity I. In vivo dosimetry, *Radiol.*, **88**, 1136

Bortfeld, T.R. and Boyer, A.L. (1995) The exponential radon transform and projection filtering in radiotherapy planning, *Int. J. Imag. Syst. Technol.*, **6**, 62-70

Bortfeld, T., Burkelbach, J., Boesecke, R. and Schlegel, W. (1990) Methods of image reconstruction from projections applied to conformation radiotherapy, *Phys. Med. Biol.*, **35**, 1423-1434

Bortfeld, T., Boyer, A.L., Schlegel, W., Kahler, D.L. and Waldron, T.J. (1994) Realization and verification of three-dimensional conformal radiotherapy with modulated fields, *Int. J. Radiat. Oncol. Biol. Phys.*, **30**, 899-908

Bortfeld, T., Schlegel, W., Dykstra, C., Levegrün, S. and Preiser, K. (1996) Physical vs. biological objectives for treatment plan optimization, *Radiotherapy and Oncology*, **40**, 185

Boyer, A.L., Desobry, G.E. and Wells, N.H. (1991) Potential and limitations of invariant kernel conformal therapy, *Med. Phys.*, **18**, 703-712

Bradshaw, A.C. and Maysent, A.M. (1964) Physical aspects of electron therpay using a 15 MeV linear accelerator, *Br. J. Radiol.*, **37**, 219

Brahme, A. (1971) *Multiple Scattering of Relativistic Electrons in Air*, Royal Institute of Technology Report TRITA-EPP 71-72, Stockholm, Sweden

Brahme, A. (1972) *On the Optimal Choice of Scattering Foils for Electron Therapy*, Royal Institute of Technology Report TRITA-EPP 72-17, Stockholm, Sweden

Brahme, A. (1975) *Simple Relation for the Penetration of High Energy Electron Beams in Matter*, SSI:1975-011, Dept. Radiation Physics, Karolinska Institutet, Stockhlom, Sweden

Brahme, A. (1977) Electron transport phenomena and absorbed dose distribution in electron beams, *International Congress of Radiology*, Rio de Janeiro

Brahme, A. (1982) Physical and biologic aspects on the optimum choice of radiation modality, *Acta Radiol. Oncol.*, **21**, 469-479

Brahme, A. (1987) Design principles and clinical possibilities with a new generation of radiation therapy equipment, *Acta Oncol.*, **26**, 403-413

Brahme, A. (1988) Optimization of stationary and moving beam radiation therapy techniques, *Radiotherapy and Oncology*, **12**, 129-140

Brahme, A. (1994a) Optimization of radiation therapy, *Int. J. Radiat. Oncol. Biol. Phys.*, **28**, 785-787

Brahme, A. (1994b) Inverse radiation therapy planning: Principles and possibilties, in Hounsell, A.R., Wilkinson, J.M and Williams, P.C. (eds), *Proceedings of the XIth ICCR*, Manchester, UK

Brahme, A. (1995a) Treatment optimisation using physical and radiobiological objective functions, in Smith, A.R. (Ed.), *Radiation Therapy Physics*, Berlin: Springer, 209-246

Brahme, A. (1995b) Similarities and differences in radiation therapy opimization and tomographic reconstruction, *Int. J. Imag. Syst. Technol.*, **6**, 6-13

Brahme, A. and Svensson, H. (1976) Specification of electron beam quality from the central-axis depth absorbed-dose distribution, *Med. Phys.*, **3**, 95-102

Brahme, A. and Svensson, H. (1979) Radiation beam characteristics of a 22-MeV microtron, *Acta Radiol. Oncol.*, **18**, 244

Brahme, A, Hultén, G. and Svensson, H. (1975) Electron depth absorbed dose distribution for a 10 MeV clinical microtron, *Phys. Med. Biol.*, **20**, 39-46

Brahme, A., Lax, I. and Andreo, P. (1981) Electron beam dose planning using discrete Gaussian beams: Mathematical background, *Acta Radiol. Oncol.*, **20**, 147-158

Brahme, A., Roos, J.E. and Lax, I. (1982) Solution of an integral equation encountered in radiotherapy, *Phys. Med. Biol.*, **27**, 1221-1229

Brahme, A., Källman, P. and Lind, B.K. (1989) Optimization of proton and heavy ion therapy using an adaptive inversion algorithm, *Radiotherapy and Oncology*, **15**, 189-197

Brahme, A., Lind, B. and Källman, P. (1990) Inverse radiation therapy planning as a tool for 3D dose optimization, *Phys. Med.*, **6**, 53-63

Brix, F., Christiansen, R., Hancken, C. and Quirin, A. (1988) The field integrated dose modification (FIDM): three typical clinical applications of a new irradiation technique, *Radiotherapy and Oncology*, **12**, 199-207

Brownwell, G.L., Zamenhof, R.G., Murray, B.W. and Wellum, G.R. (1978) Boron neutron capture therapy, in Spencer, R.P. (ed.), *Therapy in Nuclear Medicine*, New York, NY: Grune & Stratton

Bruinvis, I.A.D. and Mathol, W.A.F. (1988) Calculation of electron beam depth-dose curves and output factors for arbitrary field shapes, *Radiotherapy and Oncology*, **11**, 395-404

Bruinvis, I.A.D., van Amstel, A., Elevelt, A.J. and van der Laarse, R. (1983) Calculation of electron beam dose distributions for arbitrarily shaped fields, *Phys. Med. Biol.*, **28**, 667-683

Campbell, S.L. and Meyer, C.D. (1991) *Generalised Inverses of Linear Transformations*, New York, NY: Dover Publications

Carpender, J.W. *et al.* (1963) Radiation therapy with high energy electrons using pencil beam scanning, *Am. J. Roentgenol.*, **90**, 221-230

Censor, Y. (1981) Row-action methods for huge and sparse systems and their applications, *SIAM Rev.*, **23**, 444-466

Censor, Y., Altschuler, M.D. and Powlis, W.D. (1988a) A comutational solution to the inverse problem in radiation therapy treatment planning, *Appl. Math. Comput.*, **25**, 57-87

Censor, Y., Altschuler, M.D. and Powlis, W.D. (1988b) On the use of Cimmino's simultaneous projections method for computing a solution of the inverse problem in radiation therapy treatment planning, *Inv. Prob.*, **4**, 607-623

Chaney, E.L., Cullip, T.J. and Gabriel, T.A. (1994) A Monte Carlo study of accelerator head scatter, *Med. Phys.*, **21**, 1383-1390

Chen, Z., Wang, X., Bortfeld, T., Mohan, R. and Reinstein, L. (1995) The influence of scatter on the design of optimized intensity modulations, *Med. Phys.*, **22**, 1727-1733

Choi, M.C. and Mohan, R. (1988) Extraction of pencil beam kernels by the deconvolution method, *Med. Phys.*, **15**, 138-144

Choi, M.C., Purdy, J.A., Gerbi, B, Abrath, F.G. and Glasgow, G.P. (1979) Variation in output factor casued by secondary blocking for 7-16 MeV electrons, *Med. Phys.*, **6**, 137

Cimmino, G. (1938) Calculo approssimato per le soluzioni dei sistemi di equazioni lineari, *Ricerca Sci. Roma*, **1938-XVI, ser II, anno IX, I**, 326-333

Cooper, R.E.M. (1978) A gradient method of optimizing externel-beam radiotherapy treatment plans, *Radiol.*, **128**, 235-243

Corana, A., Marchesi, M., Martini, C. and Ridella, S. (1987) Minimising multimodal functions of continuous variables with the 'simulated annealing' algorithm, *ACM Transactions on Mathematical Software*, **13**, 262-280

Corey, E.M. and Young, D.A. (1989) Opimization of physical data tables by simulated annealing, *J. Comput. Phys.*, **3**, 33-37

Cordaro, C. and Zucker, M.S. (1971) A method for solving time-dependent electron transport problems, *Nucl. Eng. Sci.*, **45**, 107-116

Cormack, A.M. (1987) A problem in rotation therapy with x-rays, *Int. J. Radiat. Oncol. Biol. Phys.*, **13**, 623-630

Cormack, A.M (1995) Some early radiotherapy optimization work, *Int. J. Imag. Syst. Technol.*, **6**, 2-5

Cormack, A.M. and Cormack, R.A. (1987) A problem in rotation therapy with X-rays: Dose distributions with an axis of symmetry, *Int. J. Radiat. Oncol. Biol. Phys.*, **13**, 1921-1925

Cormack, A.M. and Quinto, E.T. (1989) On a problem in radiation therapy: Questions of non-negativity, *Int. J. Imag. Syst. Technol.*, **1**, 120-124

Cullip, T.J., Gabriel, T.A. and Chaney, E.L. (1993) A Monte Carlo study of linac head scatter, *Med. Phys.*, **20**, 906 (abstract)

Curran, B.H., Strait, J.P., Hill, R.H. and Carol, M.P. (1996) Development of an optimization technique for radiation therapy treatment planning using cumulative dose volume histograms, Presented at the 1996 Meeting of the AAPM, Philadelphia, PA

Cygler, J., Battista, J.J., Scrimger, J.W., Mah, E. and Antolak, J. (1987) Electron dose distributions in experimental phantoms: A comparison with 2D pencil beam calculations, *Phys. Med. Biol.*, **32**, 1073-1086

Das, K.R., Cramb, J.A., Millar, R.M., Kenny, M.B., Patterson, W.R., Ackerly, T.L., Perkins, A.E. and Chongkitivitya, K. (1990) Levels of leakage radiation from electron collimators of a linear accelerator, *Med. Phys.*, **17**, 1058-1063

Das, I.J., Copeland, J.F. and Bushe, H.S. (1994) Spatial distribution of bremsstrahlung in a dual electron beam used in total skin electron treatments: Errors due to ionization chamber cable irradiation, *Med. Phys.*, **21**, 1733-1738

Davis, L. (1991) *Handbook of Genetic Algorithms*, Van Nostrand, New York, NY

Dawson, D.J., Harper, J.M. and Akiaradewo, A.C. (1984) Analysis of physical parameters associated with the measurement of high energy X-ray penumbra, *Med. Phys.*, **11**, 491-497

Deasy, J.O., Almond, P.R. and M^{c}Ellistrom, M.T. (1994) The spectral dependence of electron central-axis depth dose curves, *Med. Phys.*, **21**, 1369-1376

Deasy, J.O. (1996) General features of multiple local minima in TCP optimization problems with dose-volume constraints, *Med. Phys.*, **23**, 1112 (abstract)

Deasy, J.O., Almond, P.R. and McEllistrem, M.T. (1996) Measured electron energy and angular distributions from clinical accelerators, *Med. Phys.*, **23**, 675-684

Desobry, G.E. and Boyer, A.L. (1994) An analytic calculation of the energy fluence spectrum of a linear accelerator, *Med. Phys.*, **21**, 1943-1952

Ding, G.X. and Rogers, D.W.O. (1995) *Energy Spectra, Angular Spread and Dose Distributions of Electron Beams from Various Accelerators Used in Radiotherapy*, National Research Council of Canada Report PIRS-0439

Ding, G.X., Rogers, D.W.O. and Ma, C.-M. (1994) *Energy Distributions of Electron Beams from Various Accelerators Used in Radiotherapy*, National Research Council of Canada Report PIRS-0439

Ding, G.X., Rogers, D.W.O. and Mackie, T.R. (1995) Calculation of stopping power ratios using realistic clinical electron beams, *Med. Phys.*, **22**, 489-502

Djordjevich, A., Bonham, D.J., Hussein, E.M.A., Andrew, J.W. and Hale, M.E. (1990) Optimal design of radiation compensators, *Med. Phys.*, **17**, 397-404

Dunn, W.L. (1981) Inverse Monte Carlo analysis, *J. Comput. Phys.*, **41**, 154-166

Dunn, W.L., Boffi, V.C. and O'Foghludha, F. (1987) Applications of the inverse Monte Carlo method in photon beam physics, *Nucl. Instr. Meth.*, **A255**, 147-151

du V. Tapley, N. (1980) Electron Beam, in Fletcher, G.H., *Textbook of Radiotherapy*, (3rd edn), Philadelphia, PA: Lea and Febiger

Ebert, U. (1977) Computation of optimal radiation treatment plans. *J. Comp. App. Math.*, **3**, 99-104

Ebert, M.A. and Hoban, P.W. (1996) Some characteristics of tumour control probability for heterogeneous tumours, *Phys. Med. Biol.*, **41**, 2125-2133

Eklöf, A., Ahnesjö, A. and Brahme, A. (1990) Photon beam energy deposition kernels for inverse radiotherapy planning, *Acta Oncol.*, **29**, 447-454

Eyges, L. (1948) Multiple scattering with energy loss, *Phys. Rev.*, **74**, 1534-1535

Ezzell, G.A. (1996) Genetic and geometric optimization of three-dimensional radiation therapy treatment planning, *Med. Phys.*, **23**, 293-305

Fernandes, R.F. (1985) The energy of the intrinsic electron beam before the exit window of an accelerator and the spread of the energy spectrum at a phantom surface, *Phys. Med. Biol.*, **30**, 1343-1347

Fermi, E. (1940) The ionization loss of energy in gasses and in condensed materials, *Phys. Rev.*, **57**, 485

Fields, R.S., Spanos, W.J., Tapley, N.duV., Cundiff, J.H. and Sampiere, V.A. (1980) Computer optimization for combining electron and photon beams, *Int. J. Radiat. Oncol. Biol. Phys.*, **6**, 1444 (abstract)

Fletcher, G.H. (1980) *Textbook of Radiotherapy*, Philadelphia, PA: Lea and Febiger

Floyd, C.E., Jaszczak, R.J., Greer, K.L. and Coleman, R.E. (1986) Inverse Monte Carlo as a unified reconstruction algorithm for ECT, *J. Nucl. Med.*, **27**, 1577-1585

Ford, R.L. and Nelson, W.R. (1978) *The EGS Code System (Version 3)*, Stanford Linear Accelerator Centre Report SLAC-210

Galbraith, D.M. and Rawlinson, J.A. (1984) Partial bolussing to improve the depth doses in the surface region of low energy electron beams, *Int. J. Radiat. Oncol. Biol. Phys.*, **10**, 313-317

Gass, S.I. (1969) *Linear Programming*, (3rd edn) New York, NY: McGraw Hill.

Geman, S. and Geman, D. (1984) Stochastic relaxation, Gibbs distributions, and Bayesian restoration of images, *IEEE Trans. Patt. Anan. Mach. Int.*, **PAMI6**, 721-741

Giarratano, J.C., Duerkes, R.J. and Almond, P.R. (1975) Lead shielding thickness for dose reduction of 7-28 MeV electrons, *Med. Phys.*, **2**, 336-337

Gibon, D., Rousseau, J., Castelain, B., Blond, S., Vasseur, C. and Marchandise, X. (1995) Treatment planning optimization by conjugate gradients and simulated annealing methods in stereotactic radiosurgery, *Int. J. Radiat. Oncol. Biol. Phys.*, **33**, 201-210

Goede, M.R., Gooden, D.S., Ellis, R.G. and Brickner, T.J. (1977) A versatile electron collimation system to be used with electron cones supplied with Varians Clinic 18, *Int. J. Radiat. Oncol. Biol. Phys.*, **2**, 791

Goldberg, D.E. (1989) *Genetic Algorithms in Search, Optimization and Machine Learning*, Addison-Wesley, Reading, MA

Goudsmit, S. and Saunderson, J.L. (1940) Multiple scattering of electrons, *Phys. Rev.*, **57**, 24

Graham, M.V., Jain, N.L., Kahn, M.G., Drzymala, R.E. and Purdy, J.A. (1996) Evaluation of an objective plan-evaluation model in the three dimensional treatment of nonsmall cell lung cancer, *Int. J. Radiat. Oncol. Biol. Phys.*, **34**, 469-474

Greening, J.R. (1985) *Fundamentals of Radiation Dosimetry* (2nd edn), Bristol, UK: Adam Hilger

Grusell, E., Montelius, A., Brahme, A., Rikner, G. and Russell, K. (1994) A general solution to charged particle beam flattening using an optimised dual-foil-scattering technique, with application to proton therapy beams, *Phys. Med. Biol.*, **39**, 2201-2216

Gustafsson, A., Lind, B.K. and Brahme, A. (1994) A generalised pencil beam algorithm for optimization of radiation therapy, *Med. Phys.*, **21**, 343-356

Gustafsson, A., Lind, B.K., Sveneeon, R. and Brahme, A. (1995) Simultaneous optimization of dynamic multileaf collimation and scanned patterns or compensation filters using a generalised pencil beam algorithm, *Med. Phys.*, **22**, 1141-1156

Halbleib, J.A. and Mehlhorn, T.A. (1986) ITS: The integrated TIGER series of coupled electron/photon Monte Carlo transport codes, *Nucl. Sci. Eng.*, **92**, 338

Han, K., Ballon, D., Chui, C. and Mohan, R. (1987) Monte Carlo simulation of a Cobalt-60 beam, *Med. Phys.*, **14**, 414-419

Hartmann-Siantar, C.L., Chandler, W.P., Hornstein, S.M., Cox, L.J., Rathkopf, J.A., Svatos, M.M., Weaver, K.A., Albright, N.W., Verhey, L.J., Mohan, R. and Wu, Q. (1996) Validation and performance assessment of the PEREGRINE dose calculation system for photon beam therapy, *Med. Phys.*, **23**, 1128-1129 (abstract)

Harvey, D.A., Haas, L.L. and Laughlin, J.S. (1952) Effects of X-ray and electron beam from the betatron on head and neck cancer, in *Proceedings of the Second National Cancer Conference*, American Cancer Society Inc., National Cancer Institute, American Assoc. for Cancer Research, New York, NY, Vol 1, 440-444

Haselow, R.E., Khan, F.M., Sharma, S.C. and Williamson, J. (1982) Water bag bolus in external cavities to produce dose homogeneity, *Int. J. Radiat. Oncol. Biol. Phys.*, **8**, 137-139

Heydarian, M., Hoban, P. and Beddoe, A. (1996) Comparison of dosimetric techniques in stereotactic radiosurgery, *Phys. Med. Biol.*, **41**, 93-110

Higgins, P.D., Sohn, J.W., Fine, R.M. and Schell, M.C. (1995) Three-dimensional conformal pancreas treatment: Comparison of four- to six-field techniques, *Int. J. Radiat. Oncol. Biol. Phys.*, **31**, 605-609

Hoban, P.W., Murray, D.C., Metcalfe, P.E. and Round, W.H. (1990) Superposition dose calculation in lung for 10 MV photons, *Aust. Phys. Eng. Sci. Med.*, **13**, 81-92

Hodes, L. (1974) Semiautomatic optimization of external beam radiation treatment planning, *Radiol.*, **110**, 191-196

Hogstrom, K.R. (1995) *Commissioning the Electron Component of a Treatment Planning System*, AAPM refresher course, 1995 AAPM Annual Meeting, Boston, MA

Hogstrom, K.R., Mills, M.D. and Almond, P.R. (1981) Electron beam dose calculations, *Phys. Med. Biol.*, **26**, 445-459

Hogstrom, K.R., Mills, M.D., Meyer, J.A., Palta, J.R., Mellenberg, D.E., Meoz, R.T. and Fields, R.S. (1983) Dosimetric evaluation of a pencil-beam algorithm for electrons employing a two-dimensional heterogeneity correction, *Int. J. Radiat. Oncol. Biol. Phys.*, **10**, 561-569

Hogstrom, K.R., Kurup, R.G., Shiu, A.S. and Starkschall, G. (1989) A two-dimensional pencil-beam algorithm for calculation of arc electron dose distributions, *Phys. Med. Biol.*, **34**, 315-341

Holmes, T.W. (1993) *A Model for the Physical Optimization of External Beam Radiotherapy*, PhD Thesis, University of Wisconsin, Madison, Wisconsin

Holmes, T. and Mackie, T.R. (1994a) A comparison of three inverse treatment planning algorithms, *Phys. Med. Biol.*, **39**, 91-106

Holmes, T. and Mackie, T.R. (1994b) A filtered backprojection dose calculation method for inverse treatment planning, *Med. Phys.*, **21**, 303-313

Holmes, T., Mackie, T.R., Simpkin, D. and Reckwerdt, P. (1991) A unified approach to the optimization of brachytherapy and external beam dosimetry, *Int. J. Radiat. Oncol. Biol. Phys.*, **20**, 859-873

Holmes, T.W., Mackie, T.R. and Reckwerdt, P. (1995) An iterative filtered backprojection inverse treatment planning algorithm for tomotherapy, *Int. J. Radiat. Oncol. Biol. Phys.*, **32**, 1215-1225

Horwich, A. (1990) The future of radiotherapy, *Radiotherapy and Oncology*, **19**, 353-356

Hope, C.S. and Cain, O. (1972) A computer program for optimized stationary beam treatment planning using score functions, *Comp Prog. Biomed.*, **2**, 221-231

Hope, C.S. and Orr, J.S. (1965) Computer optimization of 4 MeV treatment planning, *Phys. Med. Biol.*, **10**, 365-570

Hope, C.S., Laurie, J., Orr, J.S. and Halnan, K.E. (1967) Optimization of x-ray treatment planning by computer judgement, *Phys. Med. Biol.*, **12**, 531-542

Hsieh, C.L. and Uhlmann, E.M. (1956) Experimental evaluation of the physical characteristics of a 45 MeV medical linear electron accelerator, *Radiol.*, **67**, 263-272

Hugtenburg, R., Turner, J. and Butler, P. (1995) *Numerical reconstruction of spectra for electron therapy beams, Med. Phys.*, **22**, 948 (abstract)

Huizenga, H. and Storchi, P.R.M. (1989) Numerical calculation of energy deposition by broad high-energy electron beams, *Phys. Med. Biol.*, **34**, 1371-1396

Hyödynmaa, S., Gustaffson, A. and Brahme, A. (1996) Optimization of conformal electron beam therapy using energy- and fluence-modulated beams, *Med. Phys.*, **23**, 659-666

ICRU (1970) *Specification of High Activity Gamma-ray Sources,* International Commision on Radiation Units and Measurements Report 18, Bethesda, MD: ICRU

ICRU (1984) *Radiation Dosimetry: Electrons with initial energies between 1 MeV and 50 MeV*, International Commision on Radiation Units and Measurements Report 35, Bethesda, MD: ICRU

Ingber, L. (1989) Very fast simulated reannealing, *Math. Comput. Model.*, **12**, 967-973

Ingber, L. and Rosen, B. (1992) Genetic algorithms and very fast simulated reannealing: A comparison, *Math. Comput. Model.*, **16**, 87-100

Jackson, J.D. (1975) *Classical Electrodynamics* (2nd edn), New York, NY: Wiley

Janssen, J.J., Reideman, D.E.J., Morawska-Kaczynska, M., Storchi, P.R.M. and Huizenga, H. (1994) Numerical calculation of energy deposition by high-energy electron beams III. Three-dimensional heterogeneous media, *Phys. Med. Biol.*, **39**, 1351-1366

Jeffrey, W. and Rosner, R. (1986) Optimisation algorithms: Simulated annealing and neural network processing, *Astrophys. J.*, **310**, 473-481

Jenkins, T.M., Nelson, W.R. and Rindi, A. (eds) (1988) *Monte Carlo Transport of Electrons and Photons*, New York, NY: Plenum Press

Jette, D. (1988) Electron dose calculation using multiple scattering theory: A Gaussian multiple scattering theory, *Med. Phys.*, **15**, 123-137

Jette, D. (1995) Incorporation of single scattering into Gaussian multiple scattering theory, *Med. Phys.*, **22**, 1006 (abstract)

Jette, D. (1996) Electron dose calculation using multiple scattering theory: A new theory of multiple scattering, *Med. Phys.*, **23**, 459-477

Jette, D. and Walker, S. (1992) Electron dose calculation using multiple scattering theory: Evaluation of a new model for inhomogeneities, *Med. Phys.*, **19**, 1241-1254

Jette, D., Pagnamenta, A., Lanzl, L.H. and Rozenfeld, M. (1983) The application of multiple scattering theory to therapeutic electron dosimetry, *Med. Phys.*, **10**, 141-146

Johns, H.E. and Cunningham, J.R. (1983) *The Physics of Radiology*, (4th edn), Springfield, IL: Thomas

Johns, P.C. and Yaffe, M.J. (1983) Coherent scatter in disgnostic radiology, *Med. Phys.*, **10**, 40-50

Johnson, M.E. (ed) (1988) Simulated annealing (SA) and optimization: modern algorithms with VLSI, optimal design, and missile defense applications, *Am. J. Math. Mgmt. Sci.*, **8**, 4

Källman, P., Lind, B.K., Eklöf, A. and Brahme, A. (1988) Shaping of arbitrary dose distributions by dynamic multileaf collimation, *Phys. Med. Biol.*, **33**, 1291-1300

Källman, P., Lind, B.K. and Brahme, A. (1992) An algorithm for maximising the probability of complication-free tumour control in radiation therapy, *Phys. Med. Biol.*, **37**, 871-890

Karlsson, M. and Zackrisson, B. (1993) Matching of electron and photon beams with a multi-leaf collimator, *Radiotherapy and Oncology*, **29**, 317-326

Karlsson, M., Nyström, H. and Svensson, H. (1992) Electron beam characteristics of the 50 MeV racetrack microtron, *Med. Phys.*, **19**, 307-315

Karzmark, C.J. and Morton, M.S. (1989) *A Primer on Theory and Operation of Linear Accelerators in Radiation Therapy*, Medical Physics Publishing Corp.

Karzmark, C.J., Nunan, C.S. and Tanabe, E. (1993) *Medical Electron Accelerators*, New York, NY: M°Graw Hill Inc.

Kassaee, A., Altschuler, M.D., Ayyalsomayajula, S. and Bloch, P. (1994) Influence of cone design on the electron beam characteristics on clinical accelerators, *Med. Phys.*, **21**, 1671-1676

Kawachi, K. (1975) Calculation of electron dose distributions for radiotherapy treatment planning, *Phys. Med. Biol.*, **20**, 571-577

Kawrakow, I., Fippel, M. and Friedrich, K. (1996) 3D electron dose calculation using a Voxel-based Monte Carlo algorithm (VMC), *Med. Phys.*, **23**, 445-457

Keall, P. (1994) *The Angular and Energy Distribution of a 15 MeV Electron Beam*, Msc Thesis, University of Adelaide, Australia

Keall, P.J. (1996) *Electron Transport in Photon and Electron Beam Modelling*, PhD Thesis, University of Adelaide, Australia

Keall, P.J. and Hoban, P.W. (1994) The angular and energy distribution of the primary electron beam, *Aust. Phys. Eng. Sci. Med.*, **17**, 116-123

Keall, P.J. and Hoban, P.W. (1995) Accounting for primary electron scatter in X-ray beam convolution calculations, *Med. Phys.*, **22**, 1413-1418

Keall, P.J. and Hoban, P.W. (1996a) A review of electron beam dose calculation algorithms, *Aust. Phys. Eng. Sci. Med.*, **19**, 111-130

Keall, P.J. and Hoban, P.W. (1996b) Superposition dose calculation incoporating Monte Carlo generated electron track kernels, *Med. Phys.*, **23**, 479-485

Keall, P.J. and Hoban, P.W. (1996c) Calculating the angular standard deviation of electron beams using Fermi-Eyges theory, *Phys. Med. Biol.*, **41**, 1511-1515

Keall, P.J. and Hoban, P.W. (1996) Super-Monte Carlo for electron beam planning, *Med. Phys.*, In press

Khan, F.M. (1994) *The Physics of Radiation Therapy* (2nd edn), Baltimore, MD: Williams and Wilkins

Khan, F.M., Dopke, K.P., Hogstrom, K.R., Kutcher, G.J., Nath, R., Prasad, S.L., Purdy, J.A., Rozenfeld, M. and Werner, B.L. (1991) Clinical electron beam dosimetry: Report of the AAPM radiation therapy committee task group 25, *Med. Phys.*, **18**, 73-109

Kirkpatrick, S., Gelatt, C.D. and Vecchi, M.P. (1983) Optimization by simulated annealing, *Science*, **220**, 671-680

Klein, E.E., Low, D.A. and Purdy, J.A. (1995) Changes in electron beam dosimetry with a new scattering foil applicator system on a Clinac 2100C, *Int. J. Radiat. Oncol. Biol. Phys.*, **32**, 483-490

Klevenhagen, S.C. (1985) *Physics of Electron Beam Therapy*, Bristol, UK: Adam Hilger Ltd

Klevenhagen, S.C. (1994) An algorithm to include the bremsstrahlung contamination in the determination of the absorbed dose in electron beams, *Phys. Med. Biol.*, **39**, 1103-1112

Knuth, D.E. (1981) *Seminumerical Algorithms* (2nd edn), Vol. 2 of *The Art of Computer Programming*, Reading, MA: Addison Wesley

Koch, H.W. and Motz, J.W. (1959) Bremsstrahlung cross-section formulas and related data, *Rev. Mod. Phys.*, **31**, 920-955

Kooy, H.M. and Barth, N.H. (1990) The verification of an inverse problem in radiation therapy, *Int. J. Radiat. Oncol. Biol. Phys.*, **18**, 433-439

Kooy, H.M. and Rashid, H. (1989) A three-dimensional electron pencil-beam algorithm, *Phys. Med. Biol.*, **34**, 229-243

Korevaar, E.W., Janssen, J.J., Storchi, P.R.M. and Huizenga, H. (1995) Description of a clinical electron beam. The initial phase space as input of the phase space evolution model, *Med. Phys.*, **22**, 948 (abstract)

Kozlov, A.P. and Shisov, V.A. (1976) Forming of electron beams from a betatron by foil scatterers, *Acta Radiol. Ther. Phys. Biol.*, **15**, 493-512

Kubsad, S.S., Mackie, T.R., Gehring, M.A., Misisco, D.J., Paliwal, B.R., Mehta, M.P. and Kinsella, T.J. (1990) Monte Carlo and convolution dosimetry for stereotactic radiosurgery, *Int. J. Radiat. Oncol. Biol. Phys.*, **19**, 1027-1035

Kurup, R.G., Glasgow, G.P. and Leybovich, L. (1995) Output factors for irregularly shaped electron fields, *Medical Dosimetry*, **20**, 155-159

Kutcher, G.J., Burman, C., Brewster, L., Goitein, M. and Mohan, R. (1991) Histogram reduction method for calculating complication probabilities for three-dimensional treatment planning evaluations, *Int. J. Radiat. Oncol. Biol. Phys.*, **21**, 137-146

Lambert, G.D., Sandland, M.R., Whitton, A.C. and Doughty, D. (1985) Combining backscattered electrons and low energy photons to improve the dose distribution to an eyelid, *Int. J. Radiat. Oncol. Biol. Phys.*, **11**, 617-620

Langer, M. and Leong, J. (1987) Optimization of beam weights under dose-volume restrictions, *Int. J. Radiat. Oncol. Biol. Phys.*, **13**, 1255-1260

Langer, M., Brown, R., Urie, M., Leong, J., Stracher, M. and Shapiro, J (1990) Large scale optimization of beam weights under dose-volume restrictions, *Int. J. Radiat. Oncol. Biol. Phys.*, **18**, 887-893

Lax, I. (1986) Inhomogeneity corrections in electron-beam dose planning. Limitations with the semi-infinite slab approximation, *Phys. Med. Biol.*, **31**, 879-892

Lax, I. and Brahme, A. (1980) Collimation of high energy electron beams, *Acta Radiol. Oncol.*, **19**, 199-207

Lax, I. and Brahme, A. (1982) Rotation therapy using a novel high-gradient filter, *Radiol.*, **145**, 473-478

Lax, I. and Brahme, A. (1985) Electron beam dose planning using Gaussian beams: Energy and spatial scaling with inhomogeneities, *Acta Radiol. Oncol.*, **24**, 75-85

Leavitt, D.D., Peacock, L.M., Gibbs, F.A. and Stewart, J.R. (1985) Electron arc therapy: Physical measurements and treatment planning techniques, *Int. J. Radiat. Oncol. Biol. Phys.*, **11**, 987-999

Leavitt, D.D., Stewart, J.R. and Earley, L. (1990) Improved dose homogeneity in electron arc therapy achieved by a multiple-energy technique, *Int. J. Radiat. Oncol. Biol. Phys.*, **19**, 159-165

Lefkopoulos, D., Levrier, M., Bendada, S. and Touboul, E. (1995a) A general optimization procedure for stereotactic small-beam multi-isocentric radiotherapy, *Int. J. Imag. Syst. Technol.*, **6**, 114-123

Lefkopoulos, D., Grandjean, P., Laouar, A. and Schlienger, M. (1995b) Study of the degree of ill conditioning of the phase space of pencil-beam radiotherapy using singular value desomposition, *Int. J. Imag. Syst. Technol.*, **6**, 104-113.

Legras, J., Legras, B. and Lambert, J.-P. (1982) Software for linear and nonlinear optimization in external beam radiotherapy, *Comp Prog. Biomed.*, **15**, 233-242

Leibel, S.A., Ling, C.C., Kutcher, G.J., Mohan, R., Cordon-Cordo, C. and Fuks, Z. (1991) The biological basis for conformal three-dimensional radiation therapy, *Int. J. Radiat. Oncol. Biol. Phys.*, **21**, 805-811

Lennernäs, B., Isaksson, U. and Nilsson, S. (1995) The use of artificial intelligence neural networks in the evaluation of treatment plans for external beam radiotherapy, *Oncology Reports*, **2**, 863-869

Lief, E.P., Humm, J.L., Larsson, A. and Kutcher, G.J. (1994) Electron beam penumbra shaping using a scanned elementary beam, *Med. Phys.*, **21**, 946 (abstract)

Lief, E.P., Larsson, A. and Humm, J.L. (1995) Electron scanning beam intensity modulation, *Med. Phys.*, **22**, 930 (abstract)

Lief, E.P., Larsson, A. and Humm, J.L. (1996) Electron dose profile shaping by modulation of a scanning elementary beam, *Med. Phys.*, **23**, 33-44

Lillicrap, S.C., Wilson, P. and Boag, J.W. (1975) Dose distributions in high energy electron beams: Production of broad beam distributions from narrow beam data, *Phys. Med. Biol.*, **20**, 30-38

Lind, B.K. (1990) Properties of an algorithm for solving the inverse problem in radiation therapy, *Inv. Prob.*, **6**, 415-426

Lind, B.K. and Brahme, A. (1987) Optimization of radiation therapy dose distributions using scanned electron and photon beams and multileaf collimators, *Proc. 9th Int. Conf. on Computers in Radiotherapy*, Amsterdam: Elsevier, 235-239

Lind, B.K. and Kallman, P. (1990) Experimental verification of an algorithm for inverse radiation therapy planning, *Radioth. Oncol.*, **17**, 359-368

Lind, B.K. and Brahme, A. (1992) Photon field quantities and units for kernel based radiation therapy planning and treatment optimization, *Phys. Med. Biol.*, **37**, 891-909

Lind, B. and Brahme, A. (1995) Development of treatment techniques for radiotherapy optimization, *Int. J. Imag. Syst. Technol.*, **6**, 33-42

Liu, S., Lind, B.K. and Brahme, A. (1993) Two accurate algorithms for calculating the energy fluence profile in inverse radiation therapy planning, *Phys. Med. Biol.*, **38**, 1809-1824

Loevinger, R., Karzmark, C.J. and Weissbluth, M. (1961) Radiation therapy with high energy electrons, *Radiololgy*, **77**, 906

Lovelock, D.M.J., Chui, C.S., Kutcher, G.J. and Mohan, R. (1994) Analysis of the photon beam treatment planning data for a scanning beam machine, *Med. Phys.*, **21**, 1969-1977

Lovelock, D.M.J., Chui, C.S. and Mohan, R. (1995) A Monte Carlo model of photon beams used in radiation therapy, *Med. Phys.*, **22**, 1387-1394

Low, D.A., Starkschall, G., Bujnowski, S.W., Wang, L.L. and Hogstrom, K.R. (1992) Electron bolus design for radiotherapy treatment planning: Bolus design algorithms, *Med. Phys.*, **19**, 115-124

Low, D.A., Starkschall, G., Sherman, N.E., Bujnowski, S.W., Ewton, J.R. and Hogstrom, K.R. (1995) Computer-aided design and fabrication on an electron bolus for treatment of the paraspinal muscles, *Int. J. Radiat. Oncol. Biol. Phys.*, **33**, 1127-1138

Luxton, G. and Astrahan, M.A. (1988) Characteristics of the high energy photon beam of a 25 MV accelerator, *Med. Phys.*, **15**, 82-87

M^{c}Call, R.C., M^{c}Intyre, R.D. and Turnbull, W.G. (1978) Improvement of linear accelerator depth dose curves, *Med. Phys.*, **5**, 518-524

M^{c}Donald, S.C. and Rubin, P. (1977) Optimization of external beam radiation therapy, *Int. J. Radiat. Oncol. Biol. Phys.*, **2**, 307-317

M^{c}Lellan, J., Papiez, L., Sandison, G.A., Huda, W. and Therrien, P. (1992) A numerical method for electron transport calculations, *Phys. Med. Biol.*, **37**, 1109-1125

M^{c}Lellan, J., Sawchuk, S., Battista, J.J., Sandison, G.A. and Papiez, L.S. (1994) A method for the calculation of electron energy-straggling spectra, *Med. Phys.*, **21**, 367-378

M^{c}Naney, D., M^{c}Neese, M.P., Guillamondegui, O.M., Flatecher, G.H. and Oswald, M.J. (1983) Postoperative irradiation in malignant epithelial tumors of the parotid gland, *Int. J. Radiat. Oncol. Biol. Phys.*, **9**, 1289-1295

M^{c}Parland, B.J. (1989) A method of calculating the output factors of arbitrarily shaped electron fields, *Med. Phys.*, **16**, 88-93

Ma, C.M., Rogers, D.W.O., Faddegon, B.A., Ding, G.X, Wei, J.S., Bielajew, A.F. and Mackie, T.R. (1995) Simplified models of electron beams from a Clinac 2100C accelerator, *Med. Phys.*, **22**, 1295 (abstract)

Mackie, T.R. (1987) Calculating electron dose using a convolution/superposition method, in Bruinvis, I.A.D., van der Giessen, P.H., van Kleffens, H.J. and Wittkemper, F.W. (eds) *The Use of Computers in Radiation Therapy*, North Holland: Elsevier Science, 445-448

Mackie, T.R., Scrimger, J.W. and Battista, J.J. (1985) A convolution method of calculating dose for 15-MV X rays, *Med. Phys.*, **12**, 188-196

Mackie, T.R, Bielajew, A.F., Rogers, D.W.O. and Battista, J.J. (1988) Generation of photon energy deposition kernels using the EGS Monte Carlo code, *Phys. Med. Biol.*, **33**, 1-20

Mackie, T.R., Kubsad, S.S., Rogers, D.W.O. and Bielajew, A.F. (1990) The OMEGA project: Electron dose planning using Monte Carlo simulation, *Med. Phys.*, **17**, 730 (abstract)

Mackie, T.R., Holmes, T.W., Swerdloff, S., Reckwerdt, P.J., Deasy, J.O., Yang, J., Paliwal, B.R., and Kinsella, T.J. (1993) Tomotherapy: A new concept for the delivery of conformal therapy using dynamic compensation, *Med. Phys.*, **20**, 1709-1719

Mackie, T.R., Holmes, T.W., Reckwerdt, P.J. and Yang, J. (1995) Tomotherapy: Optimized planning and delivery of radiation therapy, *Int. J. Imag. Sci. Technol.*, **6**, 43-55

Mageras, G.S. and Mohan, R. (1993) Application of fast simulated annealing to optimization of conformal radiation treatments, *Med. Phys.*, **20**, 639-647

Mah, E., Antolak, J., Scrimger, J.W. and Battista, J.J. (1989) experimental evaluation of a 2D and 3D electron pencil beam algorithm, *Phys. Med. Biol.*, **34**, 1179-1194

Manfredotti, C., Nastasi, U., Marchisio, R., Ongaro, C., Gervino, G., Ragona, R., Anglesio, S. and Sannazzari, G. (1990) Monte Carlo simulation of dose distribution in electron beam radiotherapy planning, *Nucl. Instr. Meth.*, **A291**, 646-654

Marbach, J.R. and Almond, P.R. (1981) Optimization of field flatness and depth-dose for therapy electron beams, *Phys. Med. Biol.*, **26**, 435-443

Mantel, J., Perry, H. and Weinkam, J.J. (1977) Automatic variation of field size and dose rate in rotation therapy, *Int. J. Radiat. Oncol. Biol. Phys.*, **2**, 697-704

Metropolis, N., Rosenbluth, A.W., Rosenbluth, M.N., Teller, A.H. and Teller, E. (1953) Equations of state calculations by fast computing machines, *J. Chem. Phys.*, **21**, 1087-1092

Marion, J.B. and Zimmerman, B.A. (1967) Multiple scattering of charged particles, *Nucl. Instr. Meth.*, **51**, 93

Meyer, J.A., Palta, J.R. and Hogstrom, K.R. (1984) Demonstration of relatively new electron dosimetry measurement techniques on the Mevatron 80, *Med. Phys.*, **11**, 670-677

Mills, M.D., Hogstrom, K.R. and Almond, P.R. (1982) Prediction of electron beam output factors, *Med. Phys.*, **9**, 60-68

Mohan, R. (1988) Monte Carlo simulation of radiation treatment machine heads, in Jenkins *et al.* (1988), 453-468

Mohan, R. and Wang, X. (1996) Response to Bortfeld et al. Re: Physical vs. biological objectives for treatment plan optimization, *Radiotherapy and Oncology*, **40**, 186-187

Mohan, R., Chui, C. and Lidofsky, L. (1985) Energy and angular distributions of photons from medical linear accelerators, *Med. Phys.*, **12**, 592-596

Mohan, R., Chui, C., Fontenla, D., Han, K. and Ballon, D. (1988) The effect of angular spread on the intensity distribution of arbitrarily shaped electron beams, *Med. Phys.*, **15**, 204-210

Mohan, R., Mageras, G.S., Baldwin, B., Brewster, L.J., Kutcher, G.J., Leibel, S., Burman, C.M., Ling, C.C. and Fuks, S. (1992) Clinically relevant optimization of 3-D conformal treatments, *Med. Phys.*, **19**, 933-944

Mohan, R., Wang, X., Jackson, A., Bortfeld, T., Boyer, A.L., Kutcher, G.J., Leibel, S.A., Fuks, Z. and Ling, C.C. (1994) The potential and limitations of the inverse radiotherapy technique, *Radiotherapy and Oncology*, **32**, 232-248

Moliere, G. (1947) Theorie der Streuung schneller geladener Teilchen I: Einzelstreuung am abgesschirmter Coulomb-Feld, *Z. Naturforsch*, **2a**, 133

Møller, C. (1932) Zur theorie der durchgangs schneller elektronen durch materie, *Ann. Phys.*, **14**, 531

Morawska-Kaczynska, M. and Huizenga, H. (1992) Numerical calculation of energy deposition by broad high-energy electron beams: II. Multi-layered geometry, *Phys. Med. Biol.*, **37**, 2103-2116

Morrill, S.M., Lane, R.G. and Rosen, I.I. (1990) Constrained simulated annealing for optimized radiation therapy treatment planning, *Comp. Meth. Prog. Biomed.*, **33**, 135-144

Morrill, S.M., Lane, R.G. and Rosen, I.I. (1991a) Treatment planning optimization using constrained simulated annealing, *Phys. Med. Biol.*, **36**, 1341-1361

Morrill, S.M., Lane, R.G., Wong, J.A. and Rosen, I.I. (1991b) Dose-volume considerations with linear programming optimization, *Med. Phys.*, **18**, 1201-1210

Morril, S.M., Langer, M.L., Lane, R.G. and Rosen, I.I. (1994) Tissue heterogeneity effects in treatment plan optimization, *Int. J. Radiat. Oncol. Biol. Phys.*, **30**, 699-706

Morrill, S.M., Shing Lam, K. Lane, R.G., Langer, M. and Rosen, I.I. (1995) Very fast simulated reannealing in radiation therapy treatment plan optimization, *Int. J. Radiat. Oncol. Biol. Phys.*, **31**, 179-188

Moyer, R.F., King, G.A. and Hauser, J.F. (1986) Lead as surface bolus for high-energy photon and electron therapy, *Med. Phys.*, **13**, 263-266

Muller-Runkel, R., Ovadia, J., Borger, F., Culbert, H. and Rohinsky, B. (1985) A shaping device for irregular electron fields for the Therac-20 accelerator, *Med. Phys.*, **12**, 90-92

Murray, D. (1990) Using EGS4 Monte Carlo in medical radiation physics, *Aust. Phys. Eng. Sci. Med.*, **13**, 132-147

Murray, D.C. (1991) *The Application of Parallel Processing to Radiotherapy Dose Computation*, PhD Thesis, University of Waikato, New Zealand

Nahum, A.E., Dearnaley, D.P. and Steel, G.G. (1994) Prospects for proton-beam radiotherapy, *Eur. J. Cancer*, **30A**, 1577-1583

Nair, R.P., Nair, T.K.M. and Wrede, D.E. (1983) Shaped field electron dosimetry for a Philips SL25/10 linear accelerator, *Med. Phys.*, **10**, 356-360

Nelms, A.T. (1956) *Energy Loss and Range of Electrons and Positrons*, National Bureau of Standards Circular 577

Nelms, A.T. (1958) *Energy Loss and Range of Electrons and Positrons*, Supplement to National Bureau of Standards Circular 577

Nelson, W.R. and Jenkins, T.M. (eds) (1980) *Computer Techniques in Radiation Transport and Dosimetry*, New York, NY: Plenum Press

Nelson, W.R. and Rogers, D.W.O. (1988) Structure and operation of the EGS4 code system, in Jenkins *et al.*, (1988), 287-306

Nelson, W.R., Hirayama, H. and Rogers, D.W.O. (1985) *The EGS4 Code System*, Stanford Linear Accelerator Centre Report 265, Stanford University, Stanford, CA

Neuenschwander, H. and Born, E.J. (1992) A macro Monte Carlo method of electron beam dose calculation, *Phys. Med. Biol.*, **37**, 107-125

Neuenschwander, H., Mackie, T.R. and Reckwerdt, P.J. (1995) MMC - A high performance Monte Carlo code for electron beam treatment planning, *Phys. Med. Biol.*, **40**, 543-574

Niemierko, A. (1992) Random search algorithm (RONSC) for optimization of radiation therapy with both physical and biological end points as constraints, *Int. J. Radiat. Oncol. Biol. Phys.*, **25**, 135-145

Niemierko, A. (1996) Optimization of intensity modulated beams: Local or global optimum? *Med. Phys.*, **23**, 1072 (abstract)

Niemierko, A. and Goitein, M. (1990) Random sampling for evaluating treatment plans, *Med. Phys.*, **17**, 753-762

Niemierko, A., Urie, M. and Goitein, M. (1992) Optimization of 3D radiation therapy with both physical and biological end points and constraints, *Int. J. Radiat. Oncol. Biol. Phys.*, **23**, 99-108

Nilsson, B. and Brahme, A. (1981) Contamination of high-energy photon beams by scattered photons, *Strahlenther.*, **157**, 181-186

Okumura, Y., Kitagawa, T. and Kitabatake, T. (1969) Scattering foil device for high energy electron-beam therapy, *Radiol.*, **93**, 667

Oldham, M. and Webb, S. (1995) The optimization and inherent limitations of 3D conformal radiotherapy treatment plans of the prostate, *Brit. J. Radiol.*, **68**, 882-893

Oldham, M., Neal., A. and Webb, S. (1995) A comparison of conventional 'forward planning' with inverse planning for 3D conformal radiotherapy of the prostate, *Radiotherapy and Oncology*, **35**, 248-262

Ovadia, J. and Ullmann, E.M. (1960) Isodose distribution and treatment planning with electrons of 20-35 MeV for deep seated tumours, *Radiol.*, **84**, 754-760

Pages, L., Bertel, E., Joffre, H. and Sklavenitis, L. (1972) Energy loss, range and bremsstrahlung yield for 10-keV to 100 MeV electrons in various elements and chemical compounds, *Atom. Data*, **4**, 1

Papanikolaou, N. and Paliwal, B. (1995) A study of the effect of cone shielding in intraoperative radiotherapy, *Med. Phys.*, **22**, 571-575

Patau, J.P., Pandelle, R. and Terrisol, M. (1975) Simulation des transport des electrons de radiotherpie dans un milieu irradie a travers un cache diffuseur, *Medical Dosimetry*, **IAEA-SM-193**, Vienna, Austria, IAEA, 293-313

Paxman, R.G., Barrett, H.H., Smith, W.E. and Milster, T.D. (1985) Image reconstruction from coded data. 2: Code design, *J. Optical. Soc. Amer.*, **A2**, 501-509

Pennington, E.C., Jani, S.K. and Wen, B.-C. (1988) Leakage radiation from electron applicators on a medical accelerator, *Med. Phys.*, **15**, 763-765

Perry, D.J. and Holt, G.J. (1980) A model for calculating the effects of small inhomogeneities on electron beam dose distributions, *Med. Phys.*, **7**, 207-215

Petti, P.L., Goodman, M.S., Gabriel, T.A. and Mohan, R. (1983a) Investigation of build-up dose from electron contamination of clinical photon beams, *Med. Phys.*, **10**, 18-24

Petti, P.L., Goodman, M.S., Sisterson, J.M., Biggs, B.J., Gabriel, T.A. and Mohan, R. (1983b) Sources of electron contamination for the Clinac 35 25-MV photon beam, *Med. Phys.*, **10**, 856-861

Popp, F.A., Bothe, B. and Goedecke, R. (1975) Prinzipien zur optimierung der bestrahlungsplanung, *Strahlenther.*, **150**, 389-401

Powlis, W.D., Altschuler, M.D., Censor, Y. and Buhle, E.L. (1989) Semi-automated radiotherapy treatment planning with a mathematical model to satisfy treatment goals, *Int. J. Radiat. Oncol. Biol. Phys.*, **16**, 271-276

Press, W.H. and Teukolsky, S.A. (1991) Simulated annealing optimisation over continuous spaces, *Comput. Phys.*, **5**, 426-429

Press, W.H., Flannery, B.P., Teukolsky, S.A. and Vetterling, W.T. (1986) *Numerical Recipes: The Art of Scientific Computing*, Cambridge: Cambridge University Press

Press, W.H., Teukolsky, S.A., Vetterling, S.A. and Flannery, B.P. (1992) *Numerical Recipes in C: The Art of Scientific Computing*, 2nd edn, Cambridge University Press, NY

Purdy, J.A., Choi, M.C. and Feldman, A. (1980) Lipowitz metal shielding thickness for dose reduction of 6-20 MeV electrons, *Med. Phys.*, **7**, 251-253

Radcliffe, N. and Wilson, (1990) Natural solutions give their best, *New Scientist*, **14th April**, 47-50

Redpath, A.T., Vickery, B. and Wright, D.H. (1976) A new technique for radiation therapy planning using quadratic programming, *Phys. Med. Biol.*, **21**, 781-791

Rogers, D.W.O. and Bielajew, A.F. (1986) Differences in electron depth-dose curves calculated with EGS and ETRAN and improved energy-range relationships, *Med. Phys.*, **13**, 687-694

Rogers, D.W.O., Ewart, G.M., Bielajew, A.F. and van Dyk, G. (1985) *Calculation Of Contamination Of The Co-60 Beam From An AECL Therapy Source*, National Research Council of Canada Report PXNR-2710

Rogers, D.W.O., Ewart, G.M., Bielajew, A.F. and van Dyk, G. (1988) Calculation of electron contamination in a Co-60 therapy beam, in *Proceedings of the IAEA International Symposium on Dosimetry in Radiotherapy*, Vol 1, Vienna, Austria: IAEA 303-312

Rogers, D.W.O., Faddegon, B.A., Ding, D.X., Ma, C.-M., Wei, J. and Mackie, T.R. (1995) BEAM: A Monte Carlo code to simulate radiotherapy treatment units, *Med. Phys.*, **22**, 503-524

Rosen, I.I., Loyd, M.D. and Lane, R.G. (1990) Collimator scatter in modelling radiation beam profiles, *Med. Phys.*, **17**, 422-428

Rosen, I.I., Lane, R.G., Morrill, S.M. and Belli, J.A. (1991) Treatment plan optimization using linear programming, *Med. Phys.*, **18**, 141-152

Rosen, I.I., Lam, K.S., Lane, R.G., Langer, M. and Morrill, S.M. (1995) Comparison of simulated annealing algorithms for conformal therapy treatment planning, *Int. J. Radiat. Oncol. Biol. Phys.*, **33**, 1091-1099

Rossi, B. (1952) *High Energy Particles*, Englewood Cliffs, NJ

Rustgi, S.N. and Rodgers, J.E. (1987) Analysis of the bremsstrahlung component in 6-18 MeV electron beams, *Med. Phys.*, **14**, 884-888

Sandberg, G. (1973) Electron beam flattening with an annular scattering foil, *IEEE Trans. Nucl. Sci.*, **20**, 1025

Sandison, G.A. and Huda, W. (1987) Application of Fermi scattering theory to a magnetically scanned electron linear accelerator, *Med. Phys.*, **15**, 498-510

Schafer, R.W., Russel, M. and Richards, M.A. (1981) Constrained iterative restoration algorithms, *Proc. IEEE*, **69**, 432-450

Scheib, S. and Pedroni, E. (1992) Dose calculation and optimization for 3D conformal voxel scanning, *Rad. Envir. Biophys.*, **31**, 247-256

Schreider, Y.A. (ed) (1966) *The Monte Carlo Method*, New York, NY: Pergamon Press

Schultheiss, T.E., Hanks, G.E., Hunt, M.A., Lee, W.R. and Hanlon, A.L. (1996) The difficulty in validating optimization using bioeffect models, *Med. Phys.*, **23**, 1112 (abstract)

Scott, W.T. (1963) The theory of small-angle multiple scattering of fast charged particles, *Rev. Mod. Phys.*, **35**, 231

Seltzer, S.M. (1987) An overview of ETRAN Monte Carlo methods, in Jenkins *et al.* (1988), 153-182

Shiu, A.S. and Hogstrom, K.R. (1991) Pencil beam redefinition algorithm for electron dose distributions, *Med. Phys.*, **18**, 7-18

Shiu, A.S., Tung, S., Hogstrom, K.R., Wong, J.W., Gerber, R.L., Harms, W.B., Purdy, J.A., Ten Haken, R.K., M°Shan, D.L. and Fraass, B.L. (1992) Verification data for electron beam dose algorithms, *Med. Phys.*, **19**, 623-636

Short, K.R., Ross, C.K., Bielajew, A.F. and Rogers, D.W.O. (1986) Electron beam dose distributions near standard inhomogeneities, *Phys. Med. Biol.*, **31**, 235-249

Sibata, C.H., Mota, H.C., Beddar, A.S., Higgins, P.D. and Shin, K.H. (1991) Influence of detector size in beam profile measurements, *Phys. Med. Biol.*, **36**, 621-631

Simpkin, D. and Mackie, T.R. (1990) EGS4 Monte Carlo determination of the beta dose kernel in water, *Med. Phys.*, **17**, 179-186

Sixel, K.E. and Faddegon, B.A. (1995) Calculation of X-ray spectra for radiosurgical beams, *Med. Phys.*, **20**, 1657-1661

Sloboda, R.S. (1992) Optimization of brachytherapy dose distributions by simulated annealing, *Med. Phys.*, **19**, 955-964

Smith, A.R. (1990) Evaluation of new radiation oncology technology, *Int. J. Radiat. Oncol. Biol. Phys.*, **18**, 701-703

Smith, W.E., Paxman, R.G. and Barrett, H.H. (1985) Image reconstruction from coded data. 1: Reconstruction algorithms and experimental results, *J. Optical Soc. Amer.*, **A2**, 491-500

Söderström, S. (1995) *Radiobiologically Based Optimization of External Beam Radiotherapy Techniques Using a Small Number of Fields*, PhD Thesis, University of Stockholm, Sweden

Söderström, S. and Brahme, A. (1992) Selection of suitable beam orientations in radiation therapy using entropy and fourier transfrom measures, *Phys. Med. Biol.*, **37**, 911-924

Söderström, S. and Brahme, A. (1993) Optimization of a multiple field techniques using radiobiological objective functions, *Med. Phys.*, **20**, 1201-1210

Söderström, S. and Brahme, A. (1995) Which is the most suitable number of photon beam portals in coplanar radiation therapy?, *Int. J. Rad. Oncol. Biol. Phys.*, **33**, 151-159

Söderström, S., Gustafsson, A. and Brahme, A. (1993) The clinical value of different treatment objectives and degrees of freedom in radiation therapy optimization, *Radiotherapy and Oncology*, **29**, 148-163

Söderström, S., Gustafsson, A. and Brahme, A. (1995) Few field radiation therapy optimization in the phase space of complication free tumor control, *Int. J. Imag. Syst. Technol.*, **6**, 91-103

Sonderman, D. and Abrahamson, P.G. (1985) Radiotherapy design using mathematical programming models. *Oper. Res.*, **33**, 705-725

Spirou, S.V. and Chui, C.-S. (1996) Generation of arbitrary intensity profiles by combining the scanning beam with dynamic multileaf collimation, *Med. Phys.*, **23**, 1-8

Starkschall, G. (1984) A constrained least-squares optimization method for external beam radiation therapy treatment planning, *Med. Phys.*, **11**, 659-665

Starkschall, G. (1996) 2D versus 3D radiotherapy treatment planning, in Palta, J.R. and Mackie, T.R. (eds) *Teletherapy: Present and Future*, Proceedings of the 1996 AAPM Summer School, Vancouver BC

Starkschall, G. and Eifel, P.J.(1992) An interactive beam-weight optimization tool for three-dimensional radiation therapy treatment planning, *Med. Phys.*, **19**, 155-163

Starkschall, G., Henkelmann, G.C. and Ang, K.K. (1990) An interactive system for point dose optimization, *Int. J. Radiat. Oncol. Biol. Phys.*, **18**, 957-964

Starkschall, G., Shiu, A.S., Bujnowski, S.W., Wang, L.L., Low, D.A. and Hogstrom, K.R. (1991) Effect of dimensionality of heterogeneity corrections on the implementation of a three-dimensional electron pencil beam algorithm, *Phys. Med. Biol.*, **36**, 207-227

Steidley, K.D., Gamper, L., Greener, A. and Caggiano, A. (1994) A Clarkson's sector integration routine for personal computers, *Med. Phys.*, **21**, 61-64

Stein, J., Mohan, R., Wang, X.-H., Bortfeld, T., Wu, Q., Preiser, K., Schlegel, W. and Ling, C.C. (1996) Optimum number and orientations of beams for intensity-modulated treatments, *Med. Phys.*, **23**, 1063 (abstract)

Storchi, P.R.M. and Huizenga, H. (1985) On a numerical approach of the pencil beam model, *Phys. Med. Biol.*, **30**, 467-473

Sutter, J.M. and Kalivas, J.H. (1991) Convergence of generalised simulated annealing with variable step size with application towards parameter estimations of linear and nonlinear models, *Ann. Chem.*, **63**, 2383-2386

Svatos, M.M., Chandler, W.P., Mackie, T.R., Rathkopf, J. and Hartmann-Siantar, C. (1996) Creeping towards the macro response Monte Carlo (MRMC) method for electron transport, *Med. Phys.*, **23**, 1141 (abstract)

Svensson, H. (1971) Influence of scattering foils, transmission monitors and collimating system on the absorbed dose distribution from 10 to 35 MeV electron radiation, *Acta Radiol. Ther. Phys. Biol.*, **10**, 443

Svensson, H. and Hittinger, G. (1967) Influence of collimating systems on dose distributions from 10 to 35 MeV electron radiation, *Acta Radiol. Oncol.*, **6**, 404-409

Svensson, H. and Hittinger, G. (1971) Dosimetric measurements at the Nordic medical accelerators. Part 1. Characteristics of the radiation beam, *Acta Radiol. Ther. Phys. Biol.*, **10**, 369

Szu, H. (1987) Fast simulated annealing, *AIP Conf. Proc. Neural Networks for Computing*, Snowbird, UT, April 1986, 420-425

Szu, H. and Hartley, R. (1987) Fast simulated annealing, *Phys. Lett.*, **A122**, 157-162

Takai, M., Nishimura, T. and Kaneko, M. (1987) Optimization of the conformal radiotherapy, in Bruinvis, I.A.D., van der Giessen, P.H., van Kleffens, H.J. and Wittkämper, F.W. (eds), *The Use of Computers in Radiation Therapy*, 9th ICCR, North-Holland: Elsevier Science

Ten Haken, R.K, Frass, B.A. and Lam, K.L. (1996) Dosimetry and data acquisition, in Palta, J.R. and Mackie, T.R. (eds) *Teletherapy: Present and Future*, Proceedings of the 1996 Summer School of the AAPM, Vancouver, Canada

Thomason, C. and Higgins, P. (1989) Radial dose distribution of ^{192}Ir and ^{137}Cs seed sources, *Med. Phys.*, **11**, 659-665

Ting, J.Y., Yankelvich, R., Goswami, G., Fiedler, J.A. and Hordek, P.V. (1994) Scattered radiation from linear accelerator and Cobalt-60 collimator jaws, *Int. J. Radiat. Oncol. Biol. Phys.*, **30**, 985-992

Tulovsky, V., Ringor, M. and Papiez, L. (1995) Optimization of rotational radiotherapy treatment planning, *Int. J. Radiat. Oncol. Biol. Phys.*, **32**, 1205-1214

Udale, M. (1988) A Monte Carlo investigation of surface doses for broad electron beams, *Phys. Med. Biol.*, **33**, 939-953

Udale-Smith, M. (1990) *A Monte Carlo Investigation of High Energy Electron Beams Used in Radiotherapy*, PhD Thesis, Leeds University, UK

Udale-Smith, M. (1992) Monte Carlo calculations of electron parameters for three Philips linear accelerators, *Phys. Med. Biol.*, **37**, 85-105

van de Geijn, J., Chin, B., Pochobradsky, J. and Miller, R.W. (1987) A new model for computerised clinical electron beam dosimetry, *Med. Phys.*, **14**, 577-584

van der Laarse, R. and Strackee, J. (1976) Pseudo optimization of radiotherapy treatment planning, *Brit. J. Radiol.*, **49**, 450-457

van der Laarse, R., Bruinvis, I.A.D. and Farid Nooman, M. (1978) Wall-scattering effects in electron beam collimation, *Acta Radiol. Onc.*, **17**, 113-124

Wang, X,-H, Mohan, R., Jackson, A., Leibel, S.A., Fuks, Z. and Ling, C.C. (1995) Optimization of intensity-modulated 3D conformal treatment plans based on biological indices, *Radiotherapy and Oncology*, **37**, 140-152

Webb, S. (1989a) Optimisation of conformal radiotherapy dose distributions by simulated annealing, *Phys. Med. Biol.*, **34**, 1349-1370

Webb, S. (1989b) SPECT reconstruction by simulated annealing, *Phys. Med. Biol.*, **34**, 259-281

Webb, S. (1991a) Optimization of conformal radiotherapy dose distributions by simulated annealing: 2. Inclusion of scatter in the 2D technique, *Phys. Med. Biol.*, **36**, 1227-1237

Webb, S. (1991b) Optimisation by simulated annealing of three-dimensional conformal treatment planning for radiation fields defined by a multileaf collimator, *Phys. Med. Biol.*, **36**, 1201-1226

Webb, S. (1992) Optimisation by simulated annealing of three-dimensional conformal treatment planning for radiation fields defined by a multileaf collimator: 2. Inclusion of two-dimensional modulation of the X-ray intensity, *Phys. Med. Biol.*, **37**, 1689-1704

Webb, S. (1993) *The Physics of Three-Dimensional Radiation Therapy: Conformal Radiotherapy, Radiosurgery and Treatment Planning*, Bristol, UK: Institute of Physics Publishing

Webb, S. (1994) Optimizing the planning of intensity-modulated radiotherapy. *Phys. Med. Biol.*, **39**, 2229-2246

Webb, S. (1995) Optimizing radiation therapy inverse planning using the simulated annealing techique, *Int. J. Imag. Syst. Technol.*, **6**, 71-79

Weeks., K.J. and Sontag, M.R. (1991) 3D dose-volume compensation using a nonlinear least squares regression technique, *Med. Phys.*, **18**, 474-480

Werner, B.L., Khan, F.M. and Diebel, F.C. (1982) A model for calculating electron beam scattering in treatment planning, *Med. Phys.*, **9**, 180-187

White, D.R. (1978) Tissue substitutes in experimental radiation physics, *Med. Phys.*, **5**, 467-479

Williams, P.C. and Hendry, J.H. (1978) The RBE of megavoltage photon and electron beams, *Br. J. Radiol.*, **51**, 220

Willie, L.T. (1986) Searching potential energy surfaces by simulated annealing, *Nature*, **324**, 46-48

Willoughby, T.R., Starkschall, G., Janjan, N.A. and Rosen, I.I. (1996) Evaluation and scoring of radiotherapy treatment plans using an artificial neural network, *Int. J. Radiat. Oncol. Biol. Phys.*, **34**, 923-930

Woo, M.K. and Cunningham, J.R. (1987) The convolution method of dose calculation applied to electron beams, *Med. Phys.*, **14**, 705 (abstract)

Woo, M.K. and Cunningham, J.R. (1988) Comments on a unified electron/photon dosimetry approach, *Phys. Med. Biol.*, **33**, 981-982

Woo, M.K. and Cunningham, J.R. (1990) The validity of the density scaling method in primary electron transport for electron and photon beams, *Med. Phys.*, **17**, 187-194

Yu, C.X., Ge, W.S. and Wong, J.W. (1988) A multiray model for calculating electron pencil beam distribution, *Med. Phys.*, **15**, 662-670

Zackrisson, B. and Karlsson, M. (1996) Matching of electron beams for conformal therapy of target volumes at moderate depths, *Radiotherapy and Oncology*, **39**, 261-270

Zatz, L.M., von Essen, C.F. and Kaplan, H.S. (1961) Radiation therapy with high energy electrons, *Radiol.*, **77**, 928-939

Zefkili, S., Kappar, C. and Rosenwald, J.C. (1994) On-axis and off-axis primary dose component in high energy photon beams, *Med. Phys.*, **21**, 799-808

Zheng-Ming, L. and Brahme, A. (1993) An overview of the transport theory of charged particles, *Radiat. Phys. Chem.*, **41**, 673-703

Zink, S. (1989) The promise of a new technology: Knowledge-based systems in radiation oncology and diagnostic radiology, *Comp. Med. Imag. Graph.*, **13**, 281-293